Biomaterial study with polyisocyanide hydrogel

Proefschrift

Ter verkrijging van de graad van doctor aan de Radboud Universiteit Nijmegen op gezag van de rector magnificus prof. dr. J.H.J.M. van Krieken, volgens besluit van het college van decanen in het openbaar te verdedigen om 14:30 uur op maandag 3 oktober 2016

door

Zaskia Hillét Eksteen Akeroyd

geboren in Windhoek, Namibia

op woensdag 7 april 1982

Promotor:

Prof. dr. A. E. Rowan

Copromotoren:

Dr. E. Oosterwijk

Dr. C. Wilson

Manuscriptcommissie:

Dr. P.Y.W Dankers (Technische Universiteit Eindhoven)

Prof. dr. ir. J.C.M. van Hest

Prof. dr. B. Klumperman (Universiteit Stellenbosch, Zuid-Afrika)

Paranimfen:

Dr. F. Janssen

Emilia Grad

Press: Ipskamp Drukkers B.V., Enschede

ISBN:

Biomaterial study with polyisocyanide hydrogel

Doctoral Thesis

To obtain the degree of doctor from Radboud University Nijmegen on the authority of the Rector Magnificus prof. dr. J.H.J.M. van Krieken, according to the decision of the Council of Deans, to be defended in public on Monday, October 3, 2016 at 14:30 hours

by

Zaskia Hillét Eksteen Akeroyd

Born in Windhoek, Namibia

on Wednesday April 7, 1982

Supervisor:

Prof. dr. A. E. Rowan

Co-supervisors

Dr. E. Oosterwijk

Dr. C. Wilson

Doctoral Thesis Committee:

Dr. P.Y.W Dankers (Eindhoven University of Technology)

Prof. dr. ir. J.C.M. van Hest

Prof. dr. B. Klumperman (Stellenbosch University, South Africa)

Defence Assistants:

Dr. F. Janssen

Emilia Grad

Table of Contents

“Even if I knew that tomorrow the world would go to pieces,

I would still plant my apple tree.”

Martin Luther

Chapter 1 : Towards artificial extracellular matrix and controlled cellular fate in 3D

Abstract
The design parameters required for artificial extracellular matrix (ECM) that successfully induce pre-vascularisation will be defined and evaluated. The importance of stiffness in controlling cellular fate will be evaluated and redefined to highlight the importance of a previously ignored mechanical signalling queue, which is present in natural ECM, namely strain stiffening.

The ultimate goal in tissue engineering is to control cellular fates. In order to do this one needs to precisely mimic the behaviour of the extracellular matrix (ECM) *in vitro* so as to elicit cellular responses that are identical to those induced naturally. If cells behaved as if in native tissue it would be possible to obtain more accurate tissue and wound healing models that would make it possible to obtain tissue that more closely resembles native tissue [1]. Once generated, newly formed tissue must be sustainably supported meaning it must be properly vascularised to facilitate the efficient transfer of oxygen, nutrients and waste products [2]. The search for tissue mimetic environments is advancing at a rapid pace [3]. Functional biomimetic materials that mimic the ECM are expected to play a pivotal role in the field of tissue engineering and regenerative medicine. The level of complexity required in such tissue mimetic environments varies from the interplay of chemical triggers (cell adhesion ligands), to the material properties (stiffness) and micro architectures [4-5] (porosity), all of which affect cellular fates. In nature the decision of a cell to differentiate, proliferate, migrate, apoptose or perform other specific functions is as a result of a coordinated response to the complex spatio-temporal biochemical and biomechanical cues

from the cellular microenvironment [6]. The cellular microenvironment is a self assembled network composed of a mixture of insoluble hydrated fibrillar, helical, finite bundled, strain stiffening polymers such as fibrinogen and collagen in the ECM, and intermediate filaments, actin filaments and microtubules in the intracellular matrix (ICM) (Figure 1). Within this self assembled network there are also soluble macromolecules (chemokines) in combination with larger molecules imbedded on the surfaces of neighbouring cells (proteins and cell adhesion ligands) to provide chemical signals within the intercellular environment (Figure 1b).

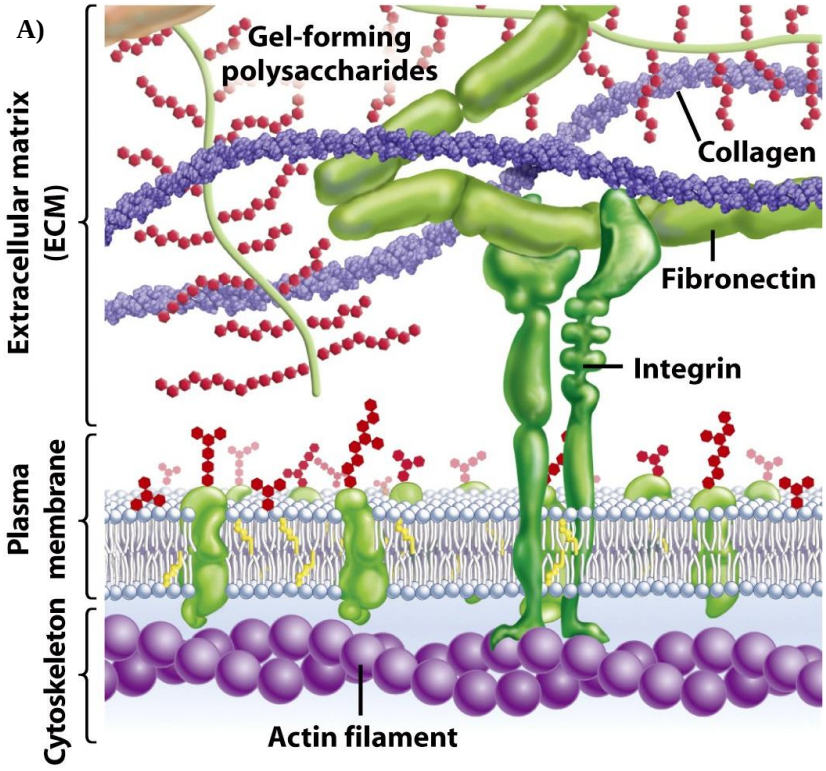

B)

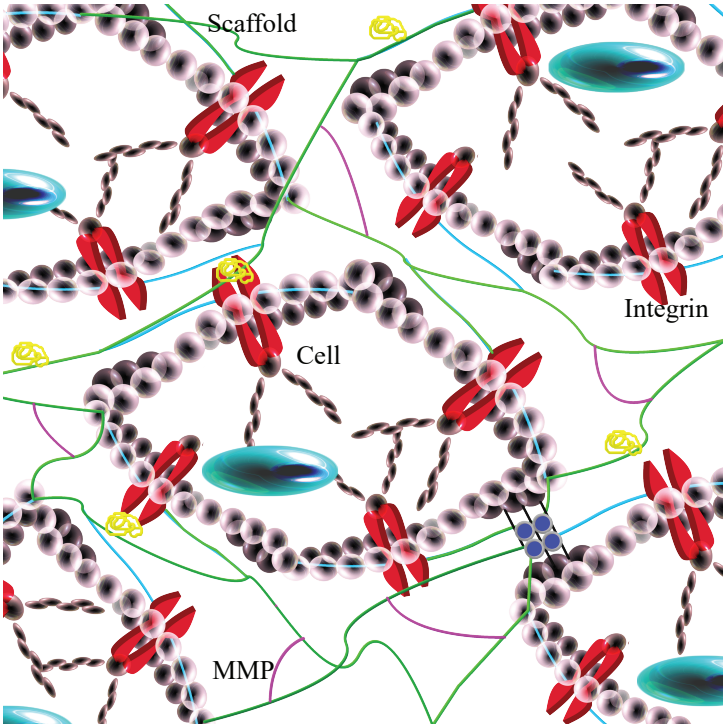

Figure 1. a) An artistic representation of the cellular microenvironment demonstrating the interconnectivity of the intracellular (intermediate fibres, actin fibres l_p=15 μm, microtubules l_p=6000 μm) and extracellular matrix (collagen, fibronectin l_p=1000 μm) [7] b) Model of self assembled components in the cellular microenvironment: cell-cell (calcium bridges); cell-ECM interactions; matrix metalloproteinase (MMP) cleavable peptides (pink); fibrous scaffold (green) with cell adhesion ligands (yellow); cell excreted ECM in blue[8].

The primary design inputs identified by Hubbell and Lutolf required for a synthetic ECM-like scaffold include: high water retention capacity, tenacity for holding cells in a stretched position, porosity allowing cells to grow/migrate in 3D, the free flow of nutrients and oxygen, the presentation of chemical signals like receptor-binding ligands, biodegradability or rather the ability to be remodelled by cells to create space for newly formed tissue [3].

The influence of matrix stiffness on cellular fate is generally accepted to be directly related to its stiffness [9-10]. This is beautifully illustrated in Figure 2 by the image illustrating breast tumor cellular fate once exposed to different matrix stiffness could be reverted into non-malignant phenotype by adjusting the matrix stiffness [11].

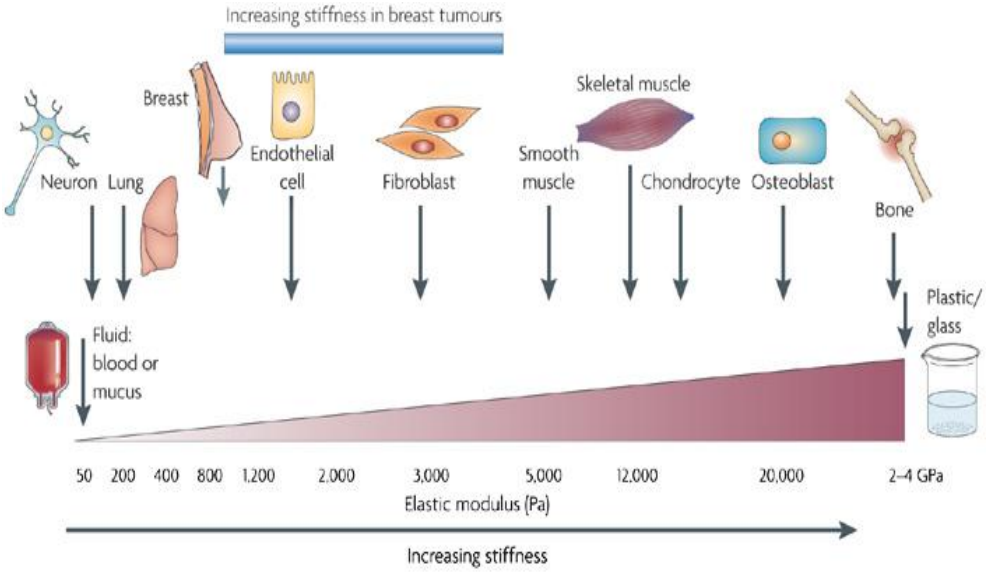

Figure 2. All cells, including those in traditionally mechanically static tissues, such as the breast or the brain, are exposed to isometric force or tension that is generated locally at the nanoscale level by cell–cell or cell–extracellular matrix interactions and that influences cell function. By changing the stiffness of the matrix it is possible to tune phenotype [11].

In this chapter the state of the art relating to the development of synthetic ECM materials for vasculogenesis, the analysis of the gaps in current knowledge and the identification of the key hurdles to be overcome in realising completely synthetic ECM mimics capable of predetermining cellular fate will be discussed.

Why use hydrogels as tissue mimetic materials: Hydrogels are uniquely suited in their material properties for tissue scaffolds, because of their innate similarities to the ECM, high water content, easy transport of oxygen, nutrients and waste [12] and the potential to act as a 3D scaffold for cells. A plethora of hydrogels have been screened for their ability to function as tissue mimetic materials amassing a vast pool of knowledge that relates to scaffold properties such as cellular attachment, molecular response, structural integrity, biodegradability, biocompatibility and solute transport designed to meet the proliferative demands of the newly formed tissue [13]. To not overcomplicate the comparison of different tissue mimetic materials and purely focus on material properties (design parameters of the artificial ECM), the effect of soluble factors in cell culture media was ignored. It is however known that the addition of soluble growth factors and various salts does affect cellular fate [14]. The various hydrogels used as tissue mimetic materials can be classified into three categories: natural, hybrid or purely synthetic.

Natural hydrogels or materials from a natural sources used as tissue mimetic materials, *e.g.*, collagen with stiffness of ca 7.5 kPa and pore sizes of 2-15 μm [15-21], gelatin [22-26], cellulose [27], hyaluronic acid (HA) [28], HA-collagen [29], alginate [30-31], fibrin with stiffness of 200 Pa at a concentration of 2 mg/mL and pore sizes of 2 - 4 μm [[32-38]], PureCol [39], Matrigel™ with pore sizes in the nm range [39-45], have all been used as tissue mimetic materials. Natural materials (collagen, fibrin, hyaluronic acid) inherently contain biological signals (cell adhesion ligands), hydrogels formed from these materials tend to be mechanically weak and manipulation of their chemical and physical properties requires chemical crosslinking reactions. Matrigel is a hydrogel derived from mouse

sarcoma, which has a low stiffness (440 Pa at 8.2 mg/ml) [46], suffers from batch to batch variation and is chemically ill-defined, inherently confounding observations made in this system as the matrix itself can influence the results.

Fully synthetic hydrogels based on the following polymers were used as tissue mimetic materials: polyethylene (glycol) (PEG) with a stiffness of 192 Pa with pore sizes of 23 nm [47-49], polyethylene (glycol) diacrylate (PEGDA) [50], PEG-PEGDA-KQGDV [51], fibrous self-assembling peptide amphiphile or PuraMatrix with stiffnesses ranging from 46 - 15 000 Pa and pore sizes of 50-200 nm [39,52-53], polyalanine-poly(propylene glycol)-PEG-poly(propylene glycol)-polyalanine [54], poly(N,N-diethylacrylamide)-YIGSR [55], poly (2-hydroxyethyl methacrylate)-polyethylene terephthalate [56-57], poly(N-isopropylacrylamide)-co-PEG-GRGDS [58], PEG-polypeptide [59]. The polymers are well defined chemically and mechanically, but without modification biologically inert. To make synthetic materials more biologically active the addition of cell regularity cues to guide cell function e.g. cell adhesion ligands (GRGDS) and growth factors are needed [1].

Hybrid hydrogels consisting of synthetic and naturally derived materials, *e.g.*, poly(caprolactone)-collagen & HA[60], PEGDA-HA-gelatin or Extracel^{TM} with stiffnesses between 4-100 kPa [28,39], PEG-fibrinogen with stiffness of upto 45 kPa and pore sizes of 100-150 μm[61-63], polylactide-chitosan [64], PLA-gelatin spheres [65], PEG-gelatin-MA [66], poly(N-isopropylacrylamide) (PNIPAM)-chitosan [67], PLGA-alginate [68], cellulose-polyvinyl alcohol (PVA) [69], poly(epsilon-caprolactone): -chitosan [70]; -collagen [71]; -fibronectin [72]; -fibrin [72]; -gelatin [73]. Hybrid materials encounter the same issues as natural materials that although cellular signals are available, the inherent

nature of the naturally sourced material could result in batch to batch variation and potential contaminations so it is difficult to quantify what parameters control cell behaviour.[74]. Another problem is that by varying the ratio of the synthetic to natural components the cellular responses will be affected further complicating interpretation of results. If the mechanical stiffness would increase by increasing the concentration of the synthetic material simultaneously resulting in a decrease in cellular signals from the natural source, a change in porosity and consequently the cellular fate could be induced.

As can be seen in the previous section, hydrogels as artificial ECM may vary in stiffness from 200 – 100,000 Pa and pore sizes from 23 – 150,000 nm. These values are for tissue mimetic materials used for everything from tissue culture to injectable materials that facilitate wound healing. Still it does seriously challenge the theory that matrix stiffness alone effects cellular fate. Before any hard conclusions can be drawn however, let us narrow the focus to tissue mimetic materials specifically used to induce vasculogenesis.

What tissue mimetic materials have specifically been used for vasculogenesis? As discussed earlier, it is not enough to simply affect cellular fate in tissue mimetic environments, but the environment also needs to direct cells (human umbilical vein endothelial cells (HUVEC) and endothelial progenitor cells) in combination with smooth muscle cells to undergo vasculogenesis (formation of vasculature). Its role is ultimately to form a pre-vascularised construct that will survive to bridge between native tissue and an implanted organ, construct or implant.

A naturally sourced hydrogel that has been used to induce vasculogenesis is a fibrin hydrogel that induced myoblast tube formation of human myoblast cells [32]. Another

naturally sourced hydrogel Matrigel was used to both inhibit and induce the sprouting of HUVEC [75]. The stiffness of both these natural tissue mimetic materials were in the Pa range [46], but the pore sizes of fibrin gels are 2-4 μm whereas those of Matrigel are in the nm range [37,76] the relevance of pore size will be discussed later in this chapter, but briefly in the case of Matrigel the cells were able to remodel the matrix to enable migration through the matrix.

Hybrid hydrogels consisting of dextran-gelatin have also been used as a matrix to co-culture smooth muscle cells and human umbilical artery endothelial cells, again the cells were seen to sprout and deposit their own ECM [77]. In a similar dextran-gelatin hydrogel with stiffness of 800-3000 Pa, human umbilical artery smooth muscle cells were seen to spread, proliferate and form extensive cellular networks [78]. Hyaluronic acid-collagen hydrogels were used to line a microfluidic device, coated with HUVEC, the addition of growth factor and RGD resulted in some migration and the onset of tube formation, but detachment from the device/hydrogel occurred within five days [29]. An *in vivo* tissue mimetic model was created by co-culturing retinal stem cells and progenitor cells (RSPC) with endothelial cells in agarose covalently labelled with GRGDS and a gradient of vascular endothelial growth factor (VEGF), it was possible to both induce and inhibit sprouting of the RSPC [79]. In a hybrid PEG-fibrin hydrogel migration and sprouting of smooth muscle cells was observed [61]. An interpenetrating network of porous (100-150 μm) PEG and fibrin was implanted subcutaneously into mice to obtain vascularised structures over a 3 week period [63]. A poly(Ɛ-caprolactone)-collagen and hyaluronic acid tissue mimetic material was used to study the co-cultured of HUVEC and lung fibroblast

cells *in vitro*, exposed to VEGF and platelet derived growth factor over a five weeks primitive capillary networks and HUVEC infiltration was observed [60].

Therefore in hybrid hydrogels various cellular fates were observed from sprouting to vasculogenesis, but it is difficult to define which parameter caused this as there are covalently immobilized cell adhesion ligands (variable concentrations), broad stiffness ranges and in some cases even covalently immobilized growth factors.

A synthetic hydrogel consisting of PEG and biologically degradable MMP bonds was used to co-culture mesenchymal stem cells and smooth muscle cells, resulting in the differentiation of stem cells into more natural smooth muscle cell phenotypes than those obtained on conventional 2D surfaces and the proliferation of both cell types over 3 weeks [48]. This would suggest that the dynamic nature of matrix and decomposition over time could be important material properties. A synthetic block copolymer consisting of PEG containing proteolytically cleavable peptides (collagenease and elastase) and cell adhesion ligands RGD and KQAGDV was used to investigate SMC migration and degradation of the synthetic tissue mimetic material [51]. In another system based on PEG containing RGD and a transforming growth factor peptide β1 was used to induce sprouting and the up regulation of MMP in HUVEC in 2D cell culture environment [49]. Smooth muscle cells (SMC) were cultured on top of PEG hydrogels containing gradients of basic fibroblast growth factor and over a time span of 48 h, SMC were seen to align and migrate preferentially in the direction of the increasing growth factor gradient when compared to controls [80]. From this it is safe to conclude that covalently attached growth factors and cell adhesion ligands in a artificial ECM are critical to successful vasculogenesis.

Angiogenesis of HUVEC and human microvasculature endothelial cells was investigated by culturing cells on top of PEG covalently modified with VEGF and RGDS, showing that the cells were able to proliferate, migrate and survive apoptosis in the synthetic environment [81]. Other synthetic systems of interest are those based on ionic self assembling peptide gels or PuraMatrix^{TM}, which are thought to gelate through the formation of a network of peptide β-sheets filaments [82]. HUVEC cultured in 3D inside this synthetic tissue mimic with stiffness lower than 100 Pa, elongated and formed interconnected capillary networks within two days [52]. This is surprising as the current accepted theory of matrix stiffness affecting cellular fate would suggest that this result should only be possible at matrix stiffness of ca 3000 Pa (Figure 2), perhaps the effect of matrix stiffness cannot be so easily defined. This would suggest that equally important factors such as the presence of covalently immobilized growth factors, cell adhesion ligands and topography must be included in designing artificial ECM for vascularisation.

Some conclusions based on the current state of the art on tissue mimetic materials used for vasculogenesis: Natural and hybrid hydrogels always induce a cellular response, whereas synthetic hydrogels require the presence of covalently bound ligands that can interact with the cells. The stiffness that resulted in successful sprouting *in vitro* varied over several orders of magnitude between 46 – 3000 Pa. The pore sizes were known to vary from nm – μm range.

Hybrid materials however appear to have more success in eliciting cellular responses when compared to the purely synthetic systems which leaves the author to postulate that not all the design parameters required for tuneable cellular fates which are present in naturally

derived materials have been clearly identified and built into the synthetic systems. Not one individual element is responsible for guiding cellular fate but perhaps a somewhat neglected essential element is the mechanical response of cell-matrix bond, which for natural systems or hybrid systems would be the strain stiffening behaviour of the scaffold, which is not present in most synthetic materials. Therefore it is fair to assume that not only microenvironment, architecture, porosity and stiffness play a role in cellular fate but also the behaviour under strain either linear or non linear has an effect on cellular fate.

Synthetic design parameters identified from state of the art: The design parameters for a synthetic tissue mimetic material for vasculogenesis are: the presence of cell adhesion ligands (RGD); variable bulk stiffness and fibre stiffness that responds to mechanical stimuli in a similar fashion as natural material (strain stiffening) in that it requires very little force to rapidly stiffen (to be discussed in more detail see Figure 7) soft gel 100 Pa to 1000-10000 Pa; porosity, mesh size and permeability in the μm range and if pore size is in the nm range the network itself must be sufficiently soft to enable cellular remodelling and ultimately the degradation of the scaffold to make room for newly formed tissue over time.

In this chapter these design parameters and their ability to induce cellular fate (stem cells, endothelial cells, smooth muscle cells) will be evaluated starting with mechanical aspects, i.e. bulk and fibre stiffness, non linear behaviour fibre and its effect on effective stiffness, pore size which affects bulk stiffness, chemical signals/ligands cell-matrix interactions and matrix topology. From all this information, an attempt will be made to define the design parameters required to mimic the ECM successfully and control cellular fate. Firstly we will look in depth at the effect of all the stiffness present in the tissue

mimetic material (Figure 2), biological triggers and finally topology to which the cells are exposed and how these factors effect cellular fate.

So what is stiffness and how do you control it? Stiffness is the rigidity of an object and the extent to which it resists deformation in response to an applied force [83].

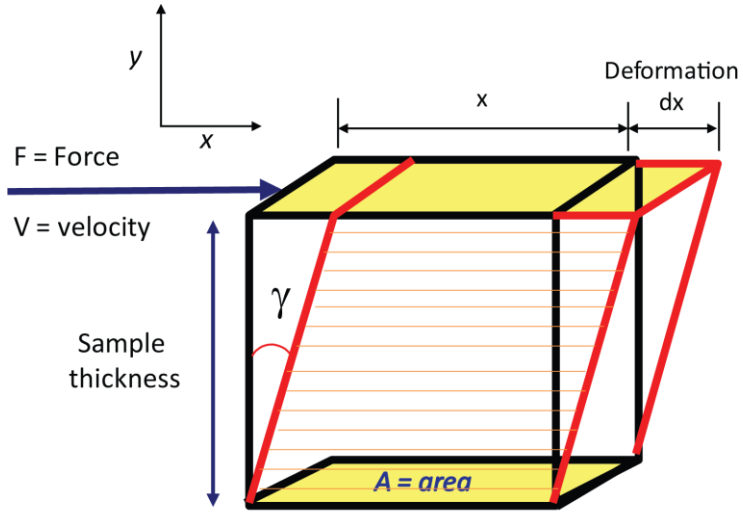

Shear Stress: $\sigma = F/A$
Strain: $\gamma = dx/y_o$
Shear Rate: $\dot{\gamma} = d\gamma/dt = V/y_o$

Figure 3. Illustration of the concept of stiffness, an external force is applied to a cube, the distance the cube is deformed (dx) is related to its stiffness, i.e. a larger dx meaning a lower stiffness. Where y_0 is the sample thickness.

The stiffness (k) of an object can be defined as its resistance to deform (displacement dx) under an applied force (F), i.e. the value required to bend or stretch the fibre.

$$k = \frac{F}{dx}$$

In this thesis bulk stiffness is a value determined through rheology. It is a general term referring to the dynamic modulus G of a viscoelastic network that consists of many individual fibres much like the ropes of a fisherman's net. The stiffness here refers to a value required to deform the network under oscillating shear, but because the material behaves as both a liquid (loss modulus G") and a solid (storage modulus G') the more solid like its behaviour the stiffer it will be.

$$\text{Bulk stiffness = dynamic modulus } \mathrm{G} = \frac{stress}{strain}$$

$$\text{But } \mathrm{G} = \mathrm{G}' + i\mathrm{G}''$$

$$\text{Where } i^2 = -1$$

$$\text{Stress: } \mathrm{G}' = \frac{\sigma_0}{\varepsilon_0}\cos\delta_*$$

$$\text{Strain:} \mathrm{G}'' = \frac{\sigma_0}{\varepsilon_0} sin\delta_*$$

Where σ_0 and $\varepsilon_0$are the amplitudes of stress and strain and $\delta_*$is the phase shift between them.

In Figure 4 the various stiffness and force elements present in the matrix that affect cellular fate are illustrated. The bulk stiffness in most hydrogels is affected by the degree of crosslinking. Therefore the bulk stiffness in terms of the cell is how hard the cell has to pull on or push, to squeeze through the hydrogel as a whole. Fibre stiffness affects the cells more directly as it affects the mechanical response of the fibre to external stimuli, which in turn affects the forces experienced at the cellular surface. Therefore the force the cell experiences at the cellular membrane via the fibre/ECM is affected by the type of material the ECM consists of e.g. elastic linear response or a non-linear strain stiffening response. Cell-matrix forces measured in natural systems (non-linear fibrillar matrix) are approximately 43 pN [84]. This force affects the degree of focal adhesions and variations of

this force (12 -55 pN) results in tuneable cellular fates [84]. In designing the perfect synthetic ECM, this effect on cell-matrix forces via bulk stiffness and fibre stiffness should not be ignored and may even be used to actually direct cellular fate.

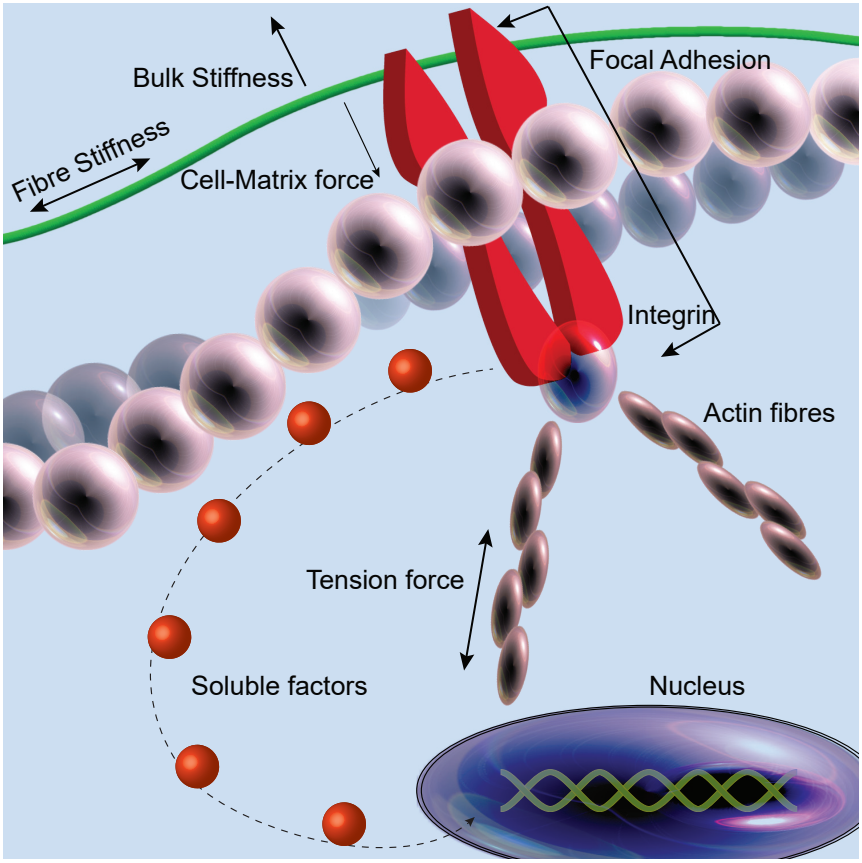

Figure 4. Image of the mechanotransduction forces and stiffness involved in cellular fate, the grey balls depict the cellular membrane; the green fibre depicts the network component; orange balls depict the chemical soluble factors produced by the cell as a result of mechanical forces either with the network or other cells [85-87].

What is the effect of stiffness in 2D on cell fate? The bulk stiffness of the ECM is thought to have an important influence in the function of cells, the seminal study in this field by Engler *et al.* elucidated the profound effect of substrate stiffness on the fate of stem

cells in 2D culture conditions. Mesenchymal stem cells (MSCs) were cultured on polyacrylamide hydrogels of varying stiffness, coated with collagen I. At a gel stiffness mimicking that of brain tissue (0.1 – 1.0 kPa), differentiation into neuronal cells was induced. In gels of intermediate stiffness (8.0 – 17.0 kPa), muscle cells were formed (myogenesis). When the gels were even stiffer (25.0 – 40.0 kPa), close to the stiffness of the collagenous bone tissue, the MSCs differentiated into bone cells (osteogenesis). Thus, it was clear from this study that a substrate having stiffness resembling a particular tissue would induce differentiation into that particular cell lineage [88].

An important point to note in the context of the stiffness of 2D substrates is that, in 2D cell culture condition, cells are seeded on the surface of a substrate that has been either coated with ECM fibrillar material (*e.g.*, collagen I), or, functionalized with cell-interactive ligands, in which case, these ligands are presented on the surface of the substrate for cell-substrate interaction. In order for the cell to sense the substrate stiffness, there should be a mechanical coupling between cell, mediator (ECM or cell interactive ligand) and substrate. In this event, when the cells pull the ECM material, the mechanical feedback of the material will include the information of material-substrate interaction. In the case of cell-interactive ligands the feedback should directly reflect the mechanical properties of the substrate however in the case of ECM coated substrates it is necessary to de-convolute the feedback of substrate and mediator. Huck and co-workers have recently demonstrated that MSCs cultured on collagen coated PDMS substrates of different stiffnesses did not show any difference in cell attachment and differentiation as a function of stiffness [89]. This is because collagen cannot penetrate into PDMS therefore the coupling and transfer of

information between mediator and substrate is highly inefficient. However, when PDMS was replaced with polyacrylamide (PAAm) gels, the stiffness of the gels affected differentiation of the cells. Unlike PDMS, PAAm gels are porous, and the porosity decreases as the stiffness of the hydrogel is increased, resulting in smaller distance between the anchoring points of the collagen, and thus eliciting greater mechanical feedback required for integrin clustering, affecting the morphology of the cells.

What is the effect of bulk stiffness in a 3D matrix on cell fate? The question therefore has arisen how does this knowledge of the role of matrix stiffness in 2D cell culture conditions translate into 3D? This question is important, since in reality cells are immersed and interact within a 3D space. To fully understand the role of the mechanical properties relating to the ECM cell interaction there must be a translation of the current state of the art 2D data into 3D applicability. Not surprisingly dimensionality has a fundamental role that can influence cell response in a significant way; let's say the cell is like a scuba diver, our diver would be much happier under water surrounded by water than slithering on top of a shallow puddle. Keeping in mind that both the cell shape and degree of spreading have an important role in cell signalling and the eventual cell fate, care must be exercised in applying the knowledge from the 2D system in the 3D microenvironment. Elucidating the exact role of stiffness in regulating cells in **natural** hydrogels is a difficult proposition, as modifying stiffness is non-trivial. While the bulk mechanics of natural hydrogel can be made effectively more stiff by increasing concentration [90-91], this results in a decrease in mesh size, an increase in cellular confinement, resistance to transport, and a change to the local concentration of ligands presented to cells cultured within [92]. In

hybrid hydrogels such as PEG-fibrinogen or collagen-agarose [93] it is possible to tune stiffness independent from ligand concentration [61-62], however, the mesh size of hybrid hydrogels is commonly much smaller than that of natural hydrogels, thus increasing both resistance to transport and cellular confinement.

One clear example of the above problem of translating the effect of bulk stiffness on cellular spreading from 2D into 3D was recently observed by Mooney *et al.* [94]. They explored the effect of stiffness on tuning MSC fate in PEG-RGD and alginate-G_4RGDASSK[TAMRA]Y hydrogels. A clear correlation of MSC differentiation with the matrix stiffness was observed in these hydrogels, in agreement with the original finding from Engler's [95-96] work on 2D polyacrylamide substrates. Unlike the stretched and elongated cell structures found on 2D; the cells in 3D retained almost spherical morphology in hydrogels of varied stiffnesses, and the differentiation showed a biphasic response to the stiffness of the matrix. Mooney proposed that cells employed traction forces to dynamically remodel the matrix for integrin-RGD clustering and that this is what ultimately decides cellular fate and not the stiffness of the matrix it finds itself in [94]. A complicating factor to this theory of reorganization for synapse formation is the inherent strain stiffening behaviour of natural fibres [97], as even at very low forces the matrix will once passing its critical stress, rapidly increase in stiffness hampering cluster formation. We therefore propose that remodelling of the ECM to induce cluster formation would be possible only if the rate of remodelling is slow enough to ensure cluster formation prior to entering into the non-linear stiffness regime.

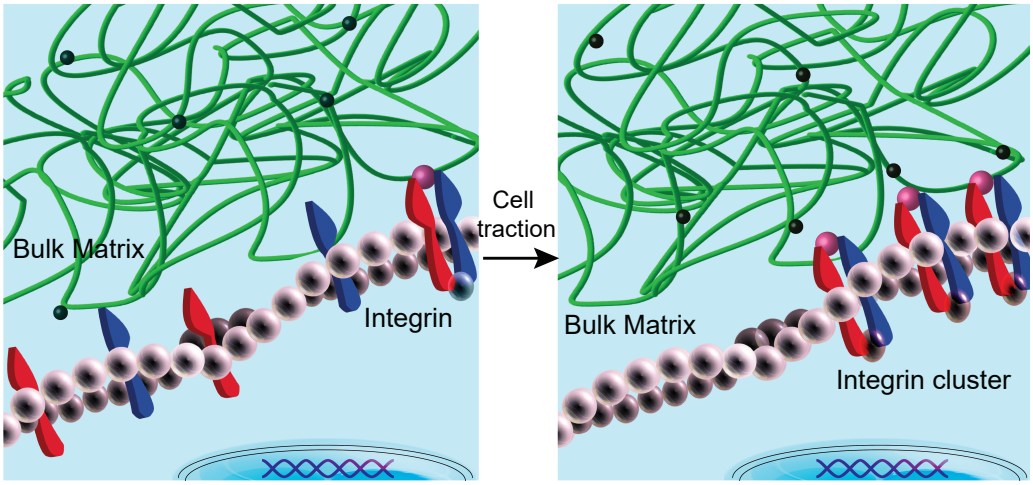

Figure 5. Schematic demonstrating concept of cell employed traction forces to dynamically remodel the matrix (green fibres) for integrin-RGD (red and blue Y) clustering [94].

Thus, from the results of Mooney's work, it is intuitive to conclude that traction force induced deformation of the matrix in concert with the inherent matrix stiffness, is the guiding parameter for cell fate in 3D tissue mimetic materials. However, the situation in 3D environment is highly complex and perhaps such a simplistic explanation is too trivial. Indeed, Burdick and co-workers have demonstrated that, in covalently cross-linked gels based on alginate, dextran or hyaluronic acid, adipogenesis was preferred over osteogenesis over a wide range of gel stiffness (4-90 kPa) [28]. This result directly contrasted the finding from Mooney's work, where osteogenesis was the preferred differentiation lineage at 20 kPa gel stiffness. This difference can be attributed to the fact that covalent cross-linking prevented structural mobility in Burdick's gels, unlike the ionically crosslinked hydrogels in Mooney's work, thus resisting the matrix remodelling required for integrin clustering and osteogenesis. The bulk stiffness in terms of crosslink bond strength, as the dissociation constant of a covalently cross-linked system would be much higher than that of an ionically

cross-linked system, affected the cell-matrix forces that the tissue mimetic material could withstand before deforming or breaking.

The argument that integrin clustering and synaps formation guides cellular fate was further supported by the work of Kotlarchyk *et al.* who observed that by generating stiffness gradients in natural (fibrin) hydrogels by directly altering the tensile stress state of the hydrogel's fibre network through the application of shear strain the micro-mechanical gradients formed directly affected the morphology of aortic smooth muscle cells cultured in this tissue mimetic material [38].

Some specific examples of bulk stiffness on cell fate in hybrid hydrogel systems: Hyaluronic acid (HA) hydrogels have been used extensively to study the effect of varying gel stiffness on cell response. It is clear that surfaces like glass or polyurethane membranes coated with a functional ligands are purely 2D, but once a surfaces is coated with a fibrin or polyacrylamide hydrogel layer, this changes to a pseudo 2 1/2 D layer that does not completely encapsulate the cells (resulting in a limited dimensionality as the cells are exposed to air on the one side and a soft wet hydrogel on the other side). The HA based systems have been investigated both as 2 1/2D and completely 3D systems. Such HA based systems also generally contain gelatin and PEGDA crosslinkers to refine the material properties. Prestwich *et al.* synthesized HA membranes with different ratios of thiolated HA, thiolated gelatin, and crosslinkers. A wide range of gel stiffness (11 Pa - 3500 Pa) could be accessed by varying the concentration of the thiolated HA and the cross-linking density. In essence, addition of thiol-modified gelatin reduced bulk stiffness by diluting the thiolated HA concentration, increasing the percentage of gelatin (an ECM material that

promotes cell adhesion) decreased the overall stiffness, which led to a change in fibroblast phenotype (from rounded to fully spread) [98-99]. In another study, HA (1 wt%) gels with increasing PEGDA (cross-linker) and constant concentration of covalently bound fibronectin domains, adult human dermal fibroblasts (HDFs) modified their mechanical response in order to match hydrogel stiffness, meaning that the cells on stiffer substrates, had more organized actin cytoskeletons and more extended morphology [100-101]. Similarly, in the migration studies of HDFs, traction stresses correlated to the stiffness of the hydrogel, and high stresses led to nuclear distortion [102]. Young *et al.* found that the time-dependent stiffening of thiol-modified HA hydrogels enhanced cardiomyocyte differentiation in vitro. The increase of the elastic modulus mimicked the increase in modulus during embryo heart development, suggesting that time dependent dynamic material properties could enhance cell maturation in engineered tissues. This is an example of the mechanical feedback mechanism affecting directly cellular fate [95]. In another study, MSCs were cultured on Extracel^{TM} at elastic moduli that matched muscle (20 kPa) or brain (2 kPa) tissue stiffness and over ninety MSC-secreted cytokines and growth factors were assayed, many of them exhibiting stiffness-dependent expression at constant ECM concentrations [103].

The complex nature of hybrid hydrogels, hint at some design elements that are not present in current synthetic hydrogels such as: strain stiffening elements and combinations of cell adhesion ligands (not yet defined). The perfect synthetic system would therefore not only have variable bulk stiffness, but also variable fibre stiffness that can strain stiffen and be easily decorated with various cell adhesion ligands.

Fibre stiffness and its effect on cell fate, the stiffness of the fibre can be defined as its resistance to deformation under an applied force. Whereas strain stiffening describes the way a fibre's stiffness increases either linearly or non-linearly under an applied force.

What is strain stiffening? The major component of the ECM is composed of filamentous polymers attached to each other and to cells by a series of molecular links. A key property of these polymers such as fibrin and collagen is their tendency to stiffen with stretching. Importantly, cellular traction forces are sufficient to locally deform the ECM [104], whose stiffness is strain-dependent [105]. It is known that when a force (shear stress) is applied to the extracellular-matrix fibres, the networks stiffen and resist additional deformation, as a result of fibre entanglement (in which the displacement of one fibre is impeded by another) and the entropic elasticity of individual fibres [97]. Indeed, Kotlarchyk *et al.* demonstrated that the stiffness of the ECM can be tuned by external mechanical loads alone to study the effects of ECM stiffness on cell physiology in 3D [38]. Nonlinear stiffening means that the ECM can operate over stiffness regimes of several orders of magnitude, covering the entire mechanical spectrum with only a few materials [97,106].

The current proposed mechanisms of strain stiffening in natural, synthetic and hybrid hydrogels: Two different models are used to describe networks under strain. In general synthetic polymers experience linear stress to strain response while natural biopolymers experience non-linear stress to strain response (Figure 6).

In the linear model it states that the network (polymers with short persistance lengths) follow the classical theory of rubber elasticity, which assumes uniform deformation due to

similar stretching of each fibre in a network of flexible fibres. In this model network elasticity comes from the entropic elasticity of individual Gaussian like coiled fibres, and the linear force extension relation of Gaussian coils gives rise to the linear elasticity of flexible polymer fibre networks [36,106].

In the non linear model, force extension of individual polymers (long persistance lengths) leads to strain stiffening of the semi flexible polymer network. The fibres deform initially by **bending** at small strains and then by stretching at larger strains when their **end-to-end vectors align** in the shear field [97,107]. This can also be described by fibre **bending** and enthalpic **stretching** which states that fibres with linear force–extension relationships produce strain stiffening in networks owing to the **geometrical changes as they align in shear** (Figure 6b) [108-110]. Essentially all this means is that in a network of polymers with long persistance lengths the deformation as a result to external force is additive and the deformation non uniform.

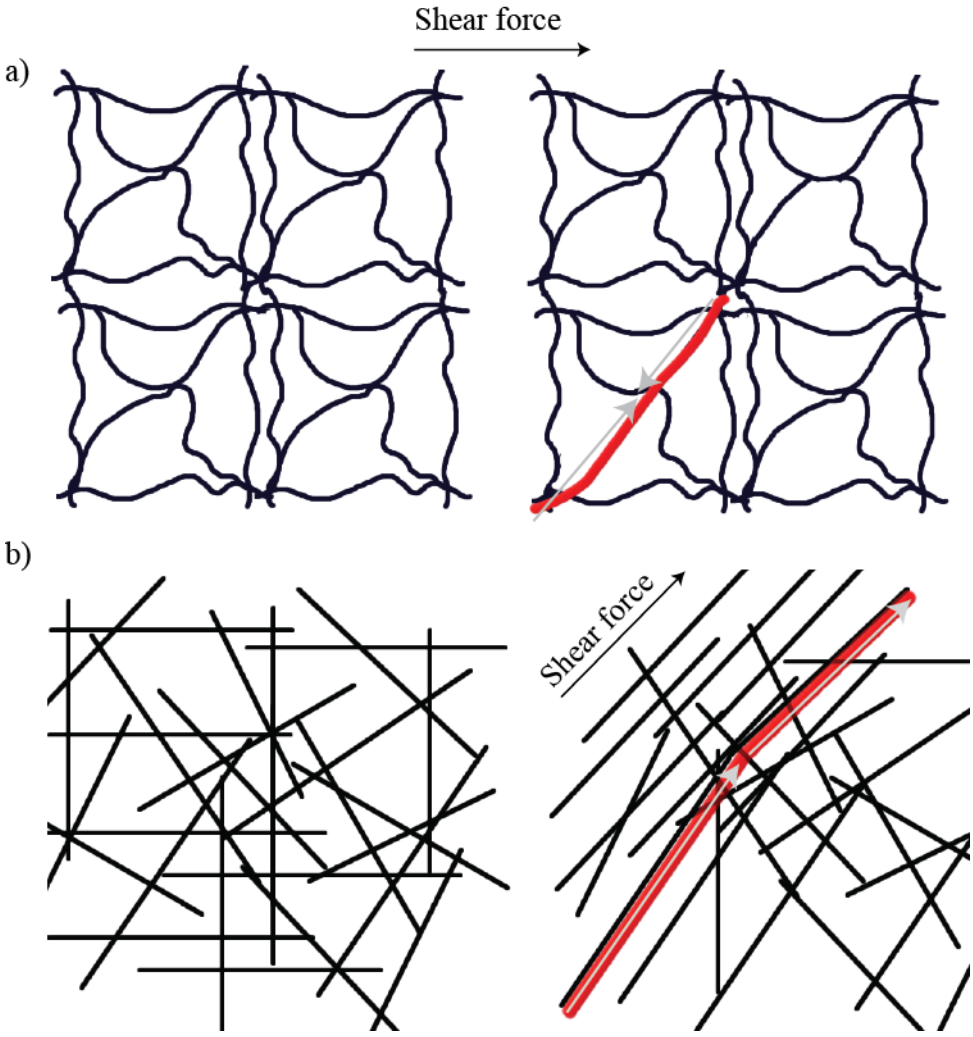

Figure 6. Schematics for two different mechanisms of network deformation on the application of an external force.(a) elastic or linear stress response, upon the application of external force the network deforms uniformly (not additive), (b) non-linear stress response as a result of cumulative alignment of fibres upon the application of external force the network deforms in the direction of shear (additive)[36]

What is the effect of strain stiffening on cell-cell interactions? Cells exert forces on the ECM [106]. The resistance of the ECM to these forces and to the strain field that cells

generate within the ECM subsequently affect the cellular fate. Cell-generated force was first observed in fibrin gels, where cells generated traction fields and the effected cellular alignment in low density cultures to spontaneously polarize cells towards each other within 400-600 μm [111]. In the work of Rudnicki *et al.* both fibrin and collagen hydrogels with varying stiffness and degrees of non-linearity were investigated. They observed that cell-induced mechanical signals transmit hundreds of microns within the network to influence cell behaviour due to simultaneously non-linear strain stiffening and the topology within the fibrous network [112]. Therefore it is safe to conclude that mechanical deformation is locally distributed to induce/trigger cell emission as mechanical signals are affine and the transfer of cellular signalling occurs over micrometers but that the cell's chemical emissions spread much further due to diffusion.

State of the art on hydrogels that show strain stiffening: In Figure 7, the stiffness of a variety of networks, quantified by their differential moduli is plotted as a function of applied strain. The change in storage modulus may be defined by the differential modulus (K'). At low stress, the differential modulus ($K' \equiv \mathrm{d}\sigma/\mathrm{d}\gamma$) equals the plateau modulus G_0, but beyond a critical stress σ_c, K' becomes stress dependent. The systems considered here vary over orders of magnitude in stiffness and in the strains they tolerate without breaking. Synthetic elastomer polymers that strain stiffen are extremely rare. One example is of poly(methyl methacrylate) (PMMA) end blocks separated by a poly(n-butyl acrylate) (PnBA) midblock, a physically associating synthetic triblock co-polymer, shows strain stiffening behaviour at high degrees of strain. This synthetic material is however not suitable for biological applications due to insolubility in biologically relevant media [113].

A biologically relevant strain stiffening synthetic hydrogel **polyisocyanopeptide** will be discussed in detail during this thesis. An example of its strain stiffening behaviour can be seen in Figure 7 by the differential modulus under increasing strain.

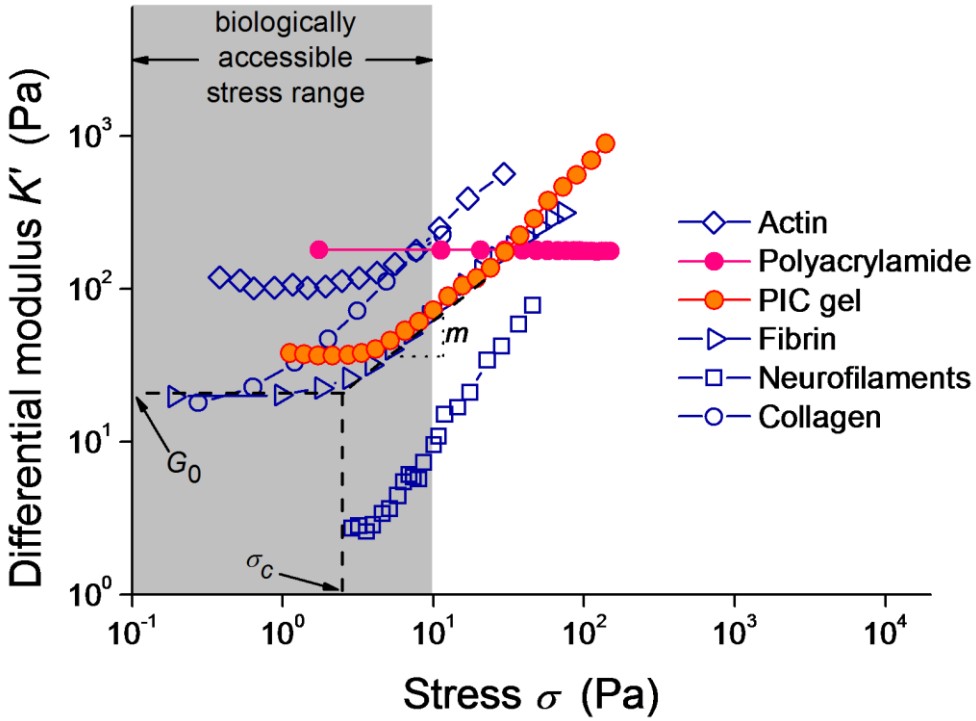

Figure 7. Strain stiffening behaviour of natural and synthetic polymers, differential modulus K' against shear stress [97,113-114], K'= $\partial\sigma/\partial\gamma$, where γ is the shear strain, against shear stress. PIC falls well within the biologically accessible stress ranges and closely resembles natural ECM fibres with regards to strain stiffening behaviour.

Apart from stiffness, the other parameter that effect cellular fate are: pore size, biological cues such as adhesion ligands, cellular landscape or topography. These factors will now be discussed.

How does pore size and bulk stiffness effect cellular mobility? In 3D systems successful tissue engineering hydrogels should be at least 90% porous [115], pores should be 50 – 200 μm in size [116] and inter-connected [117]. These pre-requisites enable the free diffusion of oxygen, nutrients, metabolites and the migration of cells themselves. Interestingly Zaman *et al.* observed cellular mobility though Matrigel a naturally sourced hydrogels that have nm pore sizes, no necking was observed indicating that cells move through the pores by deforming the matrix and creating open spaces to migrate through [76]. This was also observed in experiments with endothelial cells forming 3D networks in synthetic peptide hydrogels, the motility mechanism through sub-micrometer pores is therefore concluded to be dependent on the cells ability to remodel the tissue mimetic material hydrogel and on the pore size [52].

The influence of cell-matrix interaction and the resulting biological triggers on cellular fate: All the important cellular events, for example, adhesion, spreading, proliferation and differentiation, are governed by the interactions of the cells with their surrounding matrix. In the process of integrin mediated cellular adhesion a cascade of events occurs (Figure 8), these are attachment, spreading, organization of actin cytoskeleton and the formation of focal adhesions [118].

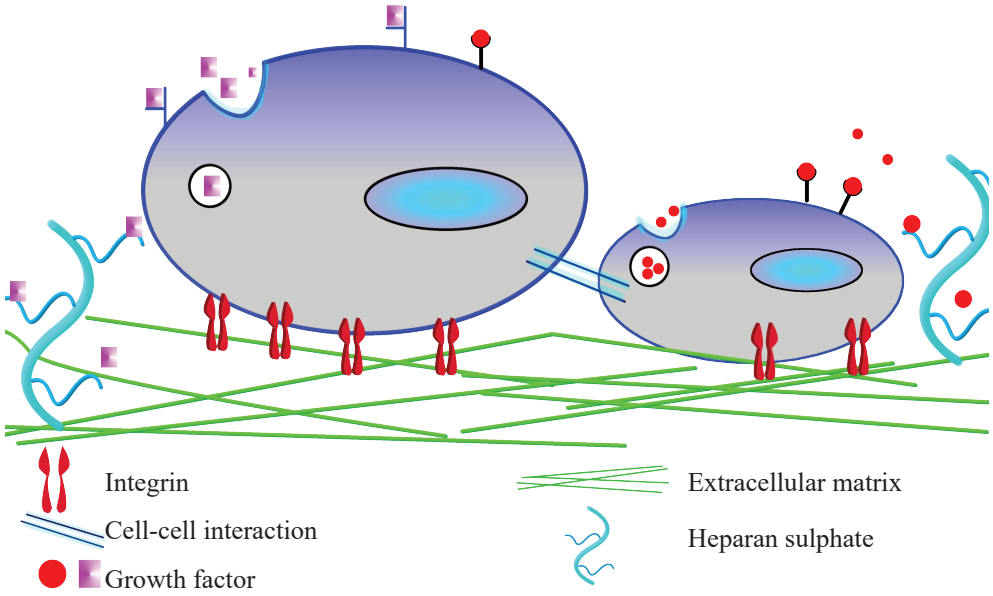

Figure 8. Cells interact with the ECM, the ECM fibres provide cells with topographical features that trigger morphogenesis. Adhesion proteins such as fibronectin and laminin located on the fibres interact with the cells through their integrin receptors to initiate intracellular signalling cascades, which affect most aspects of cell behaviour [119].

In the initial stages of cell-matrix interaction, focal adhesion complex formation occurs between the integrins and the extracellular matrix ligands (for example, RGD). It is through this complex that the mechanical information of the matrix is transmitted to the cytoskeletal

actin. Simultaneously, chemical signals are also received through the focal adhesions (for example, in the case of integrin-growth factor binding). This event is basically the equivalent of the cells 'sensing' their surrounding microenvironment. Several cytoskeletal proteins, such as, talin, filamin, *etc.* that interact with integrin αβ cytodomain, are believed to be recruited in the focal adhesion complex [120]. Although the mechanisms of the force transmission pathway are still not well understood, talin binding to the integrin β cytoplasmic domain is believed to be the crucial step for the activation of integrins and to establish ECM-integrin-talin-actin link in the early stages of focal adhesion complex formation [121-123]. A key role for another protein, vinculin, in the stabilization of the focal adhesion complex and the effective force transmission from the matrix to the cytoskeletal actin, has been established [124].The globular head of talin connects to integrin in the focal adhesion complex and the rod-like tail is attached to actin in cytoskeleton. The transmission of signals (both mechanical as well as chemical) through the focal adhesion complex into the cytoskeleton initiates cascades of events and controls specific gene expression in the nucleus. Phosphorylation of non-muscle myosin II, a cytoskeletal motor, takes place which then leads to actin bundle formation and stress actin fiber generation. It has been speculated that this actomyosin contraction event unfolds the talin rod and exposes the buried binding sites for vinculin, which is then recruited into the focal adhesion complex through talin-vinculin interaction [125]. A feedback mechanism operates in executing the whole process of matrix mechanics 'sensing' by the cells. Thus, when the focal adhesions develop, the **cells pull on the matrix** by force generated through actomyosin contraction. If the matrix (fibre) is stiff, it will resist this deformation at the adhesion sites, the focal adhesions mature through the clustering of integrins and the cells

subsequently pull on the matrix with **greater force** than if the matrix was soft. Therefore the mechanical and chemical signals from the matrix operate in tandem in determining cellular fate.

Cell adhesion complexes (integrin-ligand), what type of integrins are used in vasculogenesis? Cells are decorated with adhesion receptors that when bound to the relevant ligands impact on the cells anchoring, behaviour and survival. The most versatile of these adhesion receptors are the integrin family. Integrins play an important role as anchors and are involved in important cellular processes such as embryogenesis, differentiation, immune responses, wound healing and hemostasis [126]. Integrins consist of two supramolecular transmembrane subunits termed the α and β. Various combinations of these hetero dimers are known with the subunits defining the ligand specificity of the integrins. From a tissue engineering perspective however only the most promiscuous integrins are of interest e.g. αvβ3 integrin which binds to fibronectin, von Willebrand factor and many others.

The optimum concentration of ligands inside the tissue mimetic material to affect cellular morphology has not been clearly defined in the past as the density in 3D can at best be described in concentration and not in a unit per/cm^2, in Table 1 a few tissue mimetic hydrogels are summarized. The optimum concentration of ligand in 2D was in the pmol-μmol/cm^2 range. In 3D the concentrations ranged in the μM-mM range.

Another interesting aspect is the spacer length between the ligand (RGD) and its scaffold (polymer backbone). This length should influence the efficacy with which the ligand will bind into the active pocket of the integrins on cell surface. Figure 9 shows a

schematic of the polyisocyanide decorated with the ligand GRGDS; the polymer fibre core (pink), the spacer length between the adhesion ligand and the polymer fibre (black) and the ligand itself (GRGDS in purple), the measured distance between the fibre core and the start of the ligand is approx 21 Å.

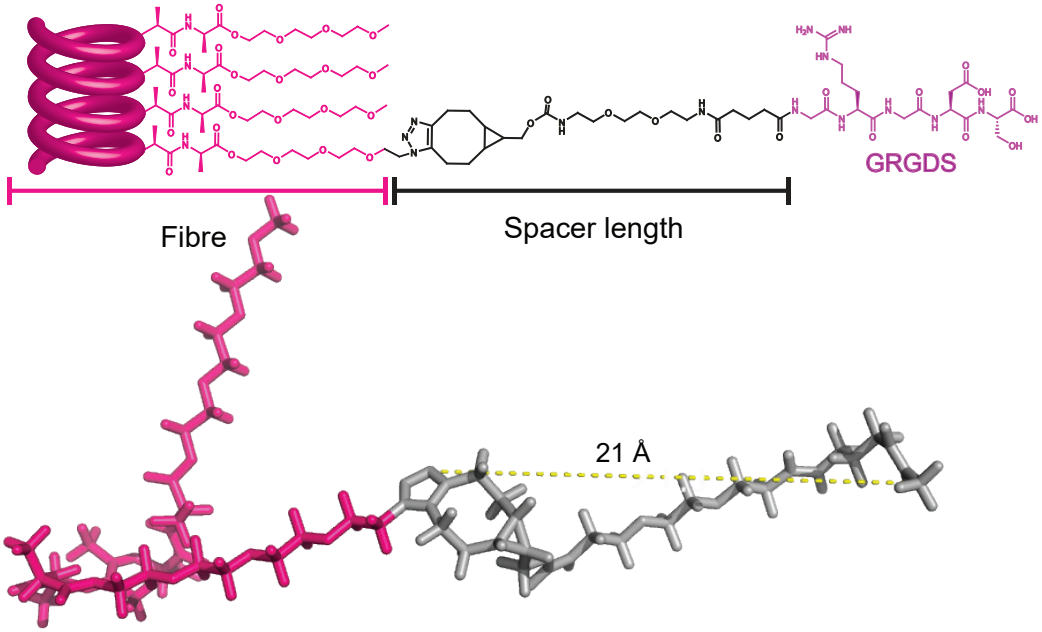

Figure 9. Schematic representation of oligoethylene glycol polyisocyanopeptide polymer fibre decorated with adhesion ligand GRGDS. The oligoethylene glycol core is represented in pink, the spacer in grey, and the peptide in lilac.

A summary of hydrogels used for vasculogenesis was collated and the spacer length between fibre and RGD calculated using a simplified chemical structures energy minimization algorithm in ChemBioDraw3D software (see, Table 1). The spacer length of the fibre-ligands ranged between 2 –19 Å, regardless of whether the hydrogel was used for or a 2D or 3D cell culture. From this table it was concluded that in designing a synthetic

hydrogel for vasculogenesis, the spacer length between scaffold and adhesion ligand should be between 3-20 Å.

Table 1. Overview of synthetic/hybrid hydrogels, the adhesion ligands used in the culture of cells

Adhesion Ligand	**Tissue mimetic material**	**Spacer length (Å)**	**Concentration**
2D			
GRGDS [127-128]	PLA, PLGA; PCU, PHBA	10.0; 6.2	0.3-3.0 µM
YRGDG [129-131]	PEG	2.4	66.0 pmol/cm2
GRGDSY [132]	PU	4.2	pmol/cm2
GRGDVY [132]	PU	4.2	pmol/cm2
GRGDSPK [133]	PS, STARCH	6.2	0.7 nmol/cm2
RGDSPASSKP [129-131]	PEG-based	2.4	66.0 pmol/cm2
3D			
RGDS [15,81]	PEG	2.7	3.7 µM/mL
GRGDS [79]	AGAROSE	10.1	2.1 µM
RGDSP [134]	GGGSSPHSRN(SG)5RGDSP	15.1-18.6	6.0 mM (dense)

What is the influence of the hydrogels topography on cell fate? The optimum spacing (for cell adhesion) between RGD ligands of adsorbed cell adhesion proteins have been estimated to range from 15-30 nm for globular proteins such as vitronectin and from 25-50 nm for rod shaped fibronectin molecules [135]. The role of nano scale surface topology appears to play a role in 2D culture of stem cells. Cellular responses were observed with nanoscale surface humps based on polymer demixing [136], ordered gold bundle arrays [137], clusters of adhesive ligands [138] or nanotubes [96,139] at distinct length scales. Nano/Micro-patterned surfaces also significantly influence the cellular fate. For example, PDMS surfaces containing nanogratings induced preferential neurogenic differentiation of mesenchymal stem cells [140]. In another recent example, culture of endothelial cells on polymer substrates micro-patterned with angiogenesis inducing peptide

sequence SVVYGLR led to tubulogenesis in 10-50 μm patterns, whereas, wider patterns (100 μm) failed to activate tubular differentiation [141]. Fibrous structures and finite bundling is present in all natural ECM fibres. It has been hinted at that the fibrillar nanoscale topological organization of fibrin and collagen gels play a role in cell activity and differentiation [112].

What is the best bioconjugation strategy for the introduction of ligands into tissue mimetic materials? It is important to decouple the ligand concentration from the polymer concentration as to avoid issues with changing mechanical properties and mesh sizes [76]. Slightly outdated methods for introducing reactive groups such as streptavidin-biotin [142-144]; thiols [145]; amines [146]; azides [147] may be used to introduce bioactive ligands into hydrogels. However the development of cyto-compatible, strain promoted azide-alkyne cycloaddition (SPAAC) reaction, a non toxic aqueous "click" chemistry results in a modular method for the introduction of bioactive ligands in a controlled manner e.g. the coupling of bicyclononynes to azides [148-150] without being affected by the hydrogel concentration. The use of SPAAC bioconjugation strategies and its effect on PIC will be investigated in Chapter 6 and the streptavidin-biotin bioconjugation in Chapter 5.

Conclusion

The following parameters were identified in the design of synthetic extra cellular matrix for vasculogenesis. Ligands form cell adhesion sites with integrins that are located on the cellular surface. The conjugation strategy for ligand introduction into the synthetic extra cellular matrix should be modular, non-toxic and should not alter the pore sizes. For vasculogenesis in 3D the density of ligands in 3D should be at a concentration in the μM range and at a distance from the fibre to effectively penetrate the integrin binding pocket (*ca* 3 - 20 Å). Cell adhesion is required not only to provide chemical cues between cells but also to enable the formation of biomechanical sensors that dictate the density of focal adhesion which in turn effect the intra cellular chemical signals that are transported to the nucleus and dictate cellular fate. The pore size must be in the μm range or the hydrogel itself must be bioresponsive enough that the cells can remodel it to enable cellular mobility. The effect of aspect ratios in 2D confirmed the need for well defined structures that enable control over focal adhesion formation with one every 15 - 50 nm and that vasculogenesis is enhanced in systems consisting of a finite bundled topology. The bulk stiffness or storage modulus of the tissue mimetic extracellular matrix for vasculogenesis must be tuneable in the range 100 - 3000 Pa. To truly mimic nature the inclusion of strain stiffening elements in the synthetic extra cellular matrix is strongly advised. This is because cells encapsulated in hydrogels with similar bulk stiffness and ligand densities will have varied cellular fate dependent on the nature of the fibres stress strain response.

A synthetic hydrogel that meets these design characteristics is **polyisocyanopeptide oligoethylene glycol, a new class of tissue mimetic material.** This new class of tissue mimetic material consists of finite fibre bundles, that gelate at extremely low concentrations above their lower critical solution temperature, the fibres exhibit strain stiffening behaviour and have a storage modulus range that spans10 - 1000 Pa. This means that water soluble polyisocyanopeptides, have similar stiffnesses as those observed for fibrin hydrogels at 2 mg/mL (200 Pa) [38] and Matrigel 8 mg/mL (440 Pa) [46] and similar fibre stiffness behaviour as natural fibres (strain stiffening). Polyisocyanopeptido oligoethylene glycols have pore sizes of 100-150 nm at 1 mg/mL similar to those observed for Matrigel [76] and ionic peptide stacking gels [52]. Cell adhesion ligands can easily be introduced by strain promoted acetylene azide “click” reaction through synthesis of copolymers with functional handles e.g. azides to enable decoration with ligands decorated with bicyclononyne functionalities, without altering the concentration of the polymer in solution.

Aim & Outline

The aim of this thesis is to explore the possible biomedical applications of polyisocyanopeptide oligoethylene glycol. The biomedical applications to be investigated include the material in its gelled state as an artificial ECM and in a diluted solution as a therapeutic carrier.

In this thesis research is presented to answer the following questions: Is it possible to synthesize water soluble PIC? Can the gelation temperature be tuned? Is PIC biologically inert? Is it possible to add copolymers with functional handles and what densities of handles are tolerable? Can PIC be used as a therapeutic carrier and how do they compare to the current state of the art? Is it possible to change the bulk stiffness of PIC hydrogels? Can a PIC hydrogel containing GRGDS be used as aECM for vasculogenesis (under cell culture conditions) e.g. what loading of GRGDS is required to induce vasculogenesis, what concentration of PIC results in a hydrogel that is strong enough to suspend cells in 3D, does the hydrogel itself survive, do cells survive in it and if the cells survive is vasculogenesis observed? In an animal model PIC is subcutaneously injected, is this a suitable technique for administration of the PIC and was the cellular response similar to that of observed *in vivo*?

In Chapter 1 the current state of the art for artificial ECM was discussed and the design parameters for the ultimate aECM defined. In Chapter 2, the design, synthesis and characterization of isocyanide monomers for the synthesis of polyisocyanodipeptide oligoethylene glycol polymers will be performed. In Chapter 3, the monomers synthesized in Chapter 2 will be used to synthesize a broad range of (homo-;co-; ter-) polymers. Briefly,

homopolymers with di-alanine repeat units in *LL*, *DL*, *LD* tri- or tetra- ethylene glycol; copolymers of tri- and tetra- ethylene glycol (varied ratios of ethylene glycol sub units should affect the LCST [151]), tri- or tetra-co-azide- ethylene glycol (varied densities of functional handle), tri- or tetra-co-acetylene- ethylene glycol (varied densities of functional handle), the homopolymers of Abz-tetra-, and finally the terpolymers of tri-tetra-azide ethylene glycol (targeted LCST temperatures with functional handle) will be synthesized. The synthesized polymers will be characterized and the differences in material properties compared among them. Once the polymers are available the effect of crosslinking on the material properties to obtain for example higher bulk stiffness will be investigated in Chapter 4. Specifically covalent, dynamic, physical and ionic crosslinking strategies will be explored. The effect of the different crosslinking strategies on the hydrogels material properties will be analyzed. The second biomedical application PIC as therapeutic carrier will be investigated in Chapter 5. In a dilute model system, PIC decorated with streptavidin-biotin-antibodies will be used to activate T-cells through the formation of an "immune synaps". The copolymers of polyisocyanopeptide tetra ethylene glycol will be compared to short persistence length, spherical molecules similarly decorated with antibodies, to elucidate the effect of shape, stiffness and multivalency on T-cell activation. In Chapter 6, PIC hydrogels, decorated with varying densities of the cell adhesion ligand GRGDS will be investigated as a new type of artificial ECM both *in vivo* and *in vitro*. In Chapter 7, the main findings of Chapters 2-6 will be discussed and any potential future work briefly highlighted.

References:

1 Fisher, S. A., Tam, R. Y. & Shoichet, M. S. Tissue Mimetics: Engineered Hydrogel Matrices Provide Biomimetic Environments for Cell Growth. *Tissue Engineering Part A*, **20**, 895-898, (2014).

2 Griffith, L. G. & Naughton, G. Tissue Engineering--Current Challenges and Expanding Opportunities. *Science*, **295**, 1009-1014, (2002).

3 Lutolf, M. P. & Hubbell, J. A. Synthetic biomaterials as instructive extracellular microenvironments for morphogenesis in tissue engineering. *Nat Biotechnol*, **23**, 47-55, (2005).

4 Annabi, N. *et al.* Controlling the Porosity and Microarchitecture of Hydrogels for Tissue Engineering. *Tissue Engineering Part B: Reviews*, **16**, 371-383, (2010).

5 Harley, B. A. C. *et al.* Microarchitecture of Three-Dimensional Scaffolds Influences Cell Migration Behavior via Junction Interactions. *Biophysical journal*, **95**, 4013-4024, (2008).

6 Owen, S. C. & Shoichet, M. S. Design of three-dimensional biomimetic scaffolds. *Journal of Biomedical Materials Research Part A*, **94A**, 1321-1331, (2010).

7 Freeman, S. in *Biological Science, 2/E* (ed Benjamin Cummings) Ch. 8. Cell-Cell Interactions (Prentice Hall, 2005).

8 Zhu, J. Bioactive modification of poly(ethylene glycol) hydrogels for tissue engineering. *Biomaterials*, **31**, 4639-4656, (2010).

9 Even-Ram, S., Artym, V. & Yamada, K. M. Matrix Control of Stem Cell Fate. *Cell*, **126**, 645-647, (2006).

10 Discher, D. E., Mooney, D. J. & Zandstra, P. W. Growth Factors, Matrices, and Forces Combine and Control Stem Cells. *Science*, **324**, 1673-1677, (2009).

11 Butcher, D. T., Alliston, T. & Weaver, V. M. A tense situation: forcing tumour progression. *Nat Rev Cancer*, **9**, 108-122, (2009).

12 Tibbitt, M. W. & Anseth, K. S. Hydrogels as extracellular matrix mimics for 3D cell culture. *Biotechnology and Bioengineering*, **103**, 655-663, (2009).

13 Slaughter, B. V. *et al.* Hydrogels in Regenerative Medicine. *Advanced Materials*, **21**, 3307-3329, (2009).

14 Discher, D. E., Mooney, D. J. & Zandstra, P. W. Growth factors, matrices, and forces combine and control stem cells. *Science (New York, N.Y.)*, **324**, 1673-1677, (2009).

15 Leslie-Barbick, J. E., Moon, J. J. & West, J. L. Covalently-Immobilized Vascular Endothelial Growth Factor Promotes Endothelial Cell Tubulogenesis in Poly(ethylene glycol) Diacrylate Hydrogels. *Journal of Biomaterials Science, Polymer Edition*, **20**, 1763-1779, (2009).

16 Xu, T. *et al.* Electrophysiological characterization of embryonic hippocampal neurons cultured in a 3D collagen hydrogel. *Biomaterials*, **30**, 4377-4383, (2009).

17 Yang, Y.-l., Motte, S. & Kaufman, L. J. Pore size variable type I collagen gels and their interaction with glioma cells. *Biomaterials*, **31**, 5678-5688, (2010).

18 Flynn, L. E. The use of decellularized adipose tissue to provide an inductive microenvironment for the adipogenic differentiation of human adipose-derived stem cells. *Biomaterials*, **31**, 4715-4724, (2010).
19 Mirsadraee, S. *et al.* Development and Characterization of an Acellular Human Pericardial Matrix for Tissue Engineering. *Tissue Engineering*, **12**, 763-773, (2006).
20 Mirsadraee, S. *et al.* Biocompatibility of Acellular Human Pericardium. *Journal of Surgical Research*, **143**, 407-414, (2007).
21 Fujisato, T. *et al.* Effect of basic fibroblast growth factor on cartilage regeneration in chondrocyte-seeded collagen sponge scaffold. *Biomaterials*, **17**, 155-162, (1996).
22 Tabata, Y., Hijikata, S. & Ikada, Y. Enhanced vascularization and tissue granulation by basic fibroblast growth factor impregnated in gelatin hydrogels. *Journal of Controlled Release*, **31**, 189-199, (1994).
23 Kawai, K. *et al.* Accelerated tissue regeneration through incorporation of basic fibroblast growth factor-impregnated gelatin microspheres into artificial dermis. *Biomaterials*, **21**, 489-499, (2000).
24 Tabata, Y. *et al.* De Novo Formation of Adipose Tissue by Controlled Release of Basic Fibroblast Growth Factor. *Tissue Engineering*, **6**, 279-289, (2000).
25 Tabata, Y. *et al.* Bone regeneration by basic fibroblast growth factor complexed with biodegradable hydrogels. *Biomaterials*, **19**, 807-815, (1998).
26 Tabata, Y. *et al.* Skull bone regeneration in primates in response to basic fibroblast growth factor. *Journal of Neurosurgery*, **91**, 851-856, (1999).
27 Sohier, J. *et al.* Hydrogel/calcium phosphate composites require specific properties for three-dimensional culture of human bone mesenchymal cells. *Acta Biomaterialia*, **6**, 2932-2939, (2010).
28 Khetan, S. *et al.* Degradation-mediated cellular traction directs stem cell fate in covalently crosslinked three-dimensional hydrogels. *Nat Mater*, **12**, 458-465, (2013).
29 Jeong, G. *et al.* Microfluidic assay of endothelial cell migration in 3D interpenetrating polymer semi-network HA-Collagen hydrogel. *Biomed Microdevices*, **13**, 717-723, (2011).
30 Edelman, E. R. *et al.* Controlled and modulated release of basic fibroblast growth factor. *Biomaterials*, **12**, 619-626, (1991).
31 Peters, M. C. *et al.* Release from alginate enhances the biological activity of vascular endothelial growth factor. *Journal of Biomaterials Science, Polymer Edition*, **9**, 1267-1278, (1998).
32 Chiron, S. *et al.* Complex Interactions between Human Myoblasts and the Surrounding 3D Fibrin-Based Matrix. *PLoS ONE*, **7**, e36173, (2012).
33 Shaikh, F. M. *et al.* Fibrin: A Natural Biodegradable Scaffold in Vascular Tissue Engineering. *Cells Tissues Organs*, **188**, 333-346, (2008).
34 Birla, R. K. *et al.* Myocardial Engineering in Vivo: Formation and Characterization of Contractile, Vascularized Three-Dimensional Cardiac Tissue. *Tissue Engineering*, **11**, 803-813, (2005).

35 DeBlois, C., Côté, M.-F. & Doillon, C. J. Heparin-fibroblast growth factorfibrin complex: in vitro and in vivo applications to collagen-based materials. *Biomaterials*, **15**, 665-672, (1994).
36 Janmey, P. A., Winer, J. P. & Weisel, J. W. Fibrin gels and their clinical and bioengineering applications. *Journal of The Royal Society Interface*, **6**, 1-10, (2009).
37 Okada, M. *et al.* Fibronectin and fibrin gel structure. *Journal of Biological Chemistry*, **260**, 1811-1820, (1985).
38 Kotlarchyk, M. A. *et al.* Concentration Independent Modulation of Local Micromechanics in a Fibrin Gel. *PLoS ONE*, **6**, e20201, (2011).
39 Serban, M. A., Liu, Y. & Prestwich, G. D. Effects of extracellular matrix analogues on primary human fibroblast behavior. *Acta Biomaterialia*, **4**, 67-75, (2008).
40 Kleinman, H. K. *et al.* Basement membrane complexes with biological activity. *Biochemistry*, **25**, 312-318, (1986).
41 Anderl, J. N. *et al.* Retention and biodistribution of microspheres injected into ischemic myocardium. *Journal of Biomedical Materials Research Part A*, **88A**, 704-710, (2009).
42 Copland, I. B. *et al.* Coupling erythropoietin secretion to mesenchymal stromal cells enhances their regenerative properties. *Cardiovascular Research*, **79**, 405-415, (2008).
43 Giraud, M.-N. *et al.* Hydrogel-based Engineered Skeletal Muscle Grafts Normalize Heart Function Early After Myocardial Infarction. *Artificial Organs*, **32**, 692-700, (2008).
44 Kutschka, I. *et al.* Collagen Matrices Enhance Survival of Transplanted Cardiomyoblasts and Contribute to Functional Improvement of Ischemic Rat Hearts. *Circulation*, **114**, I-167-I-173, (2006).
45 Hansen, A. *et al.* Development of a Drug Screening Platform Based on Engineered Heart Tissue. *Circulation Research*, **107**, 35-44, (2010).
46 Reed, J. *et al.* In Situ Mechanical Interferometry of Matrigel Films. *Langmuir*, **25**, 36-39, (2009).
47 Hill-West, J. L. *et al.* Inhibition of thrombosis and intimal thickening by in situ photopolymerization of thin hydrogel barriers. *Proceedings of the National Academy of Sciences of the United States of America*, **91**, 5967-5971, (1994).
48 Adelöw, C. *et al.* The effect of enzymatically degradable poly(ethylene glycol) hydrogels on smooth muscle cell phenotype. *Biomaterials*, **29**, 314-326, (2008).
49 Seliktar, D. *et al.* MMP-2 sensitive, VEGF-bearing bioactive hydrogels for promotion of vascular healing. *Journal of Biomedical Materials Research Part A*, **68A**, 704-716, (2004).
50 An, Y. & Hubbell, J. A. Intraarterial protein delivery via intimally-adherent bilayer hydrogels. *Journal of Controlled Release*, **64**, 205-215, (2000).
51 Mann, B. K. *et al.* Smooth muscle cell growth in photopolymerized hydrogels with cell adhesive and proteolytically degradable domains: synthetic ECM analogs for tissue engineering. *Biomaterials*, **22**, 3045-3051, (2001).

52 Sieminski, A. L. *et al.* Primary sequence of ionic self-assembling peptide gels affects endothelial cell adhesion and capillary morphogenesis. *Journal of Biomedical Materials Research Part A*, **87A**, 494-504, (2008).
53 Sieminski, A. L. *et al.* The Stiffness of Three-dimensional Ionic Self-assembling Peptide Gels Affects the Extent of Capillary-like Network Formation. *Cell Biochem Biophys*, **49**, 73-83, (2007).
54 Choi, B. G. *et al.* In situ thermal gelling polypeptide for chondrocytes 3D culture. *Biomaterials*, **31**, 9266-9272, (2010).
55 Horák, D. *et al.* Pentapeptide-modified poly(N,N-diethylacrylamide) hydrogel scaffolds for tissue engineering. *Journal of Biomedical Materials Research Part B: Applied Biomaterials*, **98B**, 54-67, (2011).
56 Allder, M. A. *et al.* A Hydrogel Pericardial Patch. *ASAIO Journal*, **36**, M572-574, (1990).
57 Walker, A. S. *et al.* Performance of a Hydrogel Composite Pericardial Substitute After Long-term Implant Studies. *ASAIO Journal*, **38**, M550-M554, (1992).
58 Park, K.-H., Na, K. & Chung, H.-M. Enhancement of the adhesion of fibroblasts by peptide containing an Arg-Gly-Asp sequence with poly(ethylene glycol) into a thermo-reversible hydrogel as a synthetic extracellular matrix. *Biotechnol Lett*, **27**, 227-231, (2005).
59 Goktas, M. *et al.* Self-Assembled Peptide Amphiphile Nanofibers and PEG Composite Hydrogels as Tunable ECM Mimetic Microenvironment. *Biomacromolecules*, **16**, 1247-1258, (2015).
60 Ekaputra, A. K. *et al.* The three-dimensional vascularization of growth factor-releasing hybrid scaffold of poly (ε-caprolactone)/collagen fibers and hyaluronic acid hydrogel. *Biomaterials*, **32**, 8108-8117, (2011).
61 Dikovsky, D., Bianco-Peled, H. & Seliktar, D. The effect of structural alterations of PEG-fibrinogen hydrogel scaffolds on 3-D cellular morphology and cellular migration. *Biomaterials*, **27**, 1496-1506, (2006).
62 Kim, P. D. *et al.* The influence of ascorbic acid, TGF-β1, and cell-mediated remodeling on the bulk mechanical properties of 3-D PEG–fibrinogen constructs. *Biomaterials*, **30**, 3854-3864, (2009).
63 Jiang, B. *et al.* Fibrin-Loaded Porous Poly(Ethylene Glycol) Hydrogels as Scaffold Materials for Vascularized Tissue Formation. *Tissue Engineering Part A*, **19**, 224-234, (2012).
64 Wan, Y. *et al.* Porous polylactide/chitosan scaffolds for tissue engineering. *Journal of Biomedical Materials Research Part A*, **80A**, 776-789, (2007).
65 Liu, X., Won, Y. & Ma, P. X. Porogen-induced surface modification of nano-fibrous poly(l-lactic acid) scaffolds for tissue engineering. *Biomaterials*, **27**, 3980-3987, (2006).
66 Daniele, M. A. *et al.* Interpenetrating networks based on gelatin methacrylamide and PEG formed using concurrent thiol click chemistries for hydrogel tissue engineering scaffolds. *Biomaterials*, **35**, 1845-1856, (2014).
67 Wang, J. *et al.* Cell adhesion and accelerated detachment on the surface of temperature-sensitive chitosan and poly(N-isopropylacrylamide) hydrogels. *J Mater Sci: Mater Med*, **20**, 583-590, (2009).

68 Richardson, T. P. *et al.* Polymeric system for dual growth factor delivery. *Nat Biotech*, **19**, 1029-1034, (2001).
69 Appel, E. A. *et al.* Sustained release of proteins from high water content supramolecular polymer hydrogels. *Biomaterials*, **33**, 4646-4652, (2012).
70 Mei, N. *et al.* Biocompatibility of Poly(ε-caprolactone) Scaffold Modified by Chitosan—The Fibroblasts Proliferation in vitro. *Journal of Biomaterials Applications*, **19**, 323-339, (2005).
71 Dai, N. T. *et al.* Composite cell support membranes based on collagen and polycaprolactone for tissue engineering of skin. *Biomaterials*, **25**, 4263-4271, (2004).
72 Pankajakshan, D., Krishnan V, K. & Krishnan, L. K. Vascular tissue generation in response to signaling molecules integrated with a novel poly(ε-caprolactone)–fibrin hybrid scaffold. *Journal of Tissue Engineering and Regenerative Medicine*, **1**, 389-397, (2007).
73 Ma, Z. *et al.* Grafting of gelatin on electrospun poly(caprolactone) nanofibers to improve endothelial cell spreading and proliferation and to control cell Orientation. *Tissue Engineering*, **11**, 1149-1158, (2005).
74 Hansen, K. C. *et al.* An In-solution Ultrasonication-assisted Digestion Method for Improved Extracellular Matrix Proteome Coverage. *Molecular & Cellular Proteomics*, **8**, 1648-1657, (2009).
75 Kong, D. *et al.* Inhibition of Angiogenesis and Invasion by 3,3′-Diindolylmethane Is Mediated by the Nuclear Factor–κB Downstream Target Genes MMP-9 and uPA that Regulated Bioavailability of Vascular Endothelial Growth Factor in Prostate Cancer. *Cancer Research*, **67**, 3310-3319, (2007).
76 Zaman, M. H. *et al.* Migration of tumor cells in 3D matrices is governed by matrix stiffness along with cell-matrix adhesion and proteolysis. *Proceedings of the National Academy of Sciences*, **103**, 10889-10894, (2006).
77 Liu, Y. *et al.* Impact of Endothelial Cells on 3D Cultured Smooth Muscle Cells in a Biomimetic Hydrogel. *ACS Applied Materials & Interfaces*, **4**, 1378-1387, (2012).
78 Liu, Y. & Chan-Park, M. B. A biomimetic hydrogel based on methacrylated dextran-graft-lysine and gelatin for 3D smooth muscle cell culture. *Biomaterials*, **31**, 1158-1170, (2010).
79 Aizawa, Y. & Shoichet, M. S. The role of endothelial cells in the retinal stem and progenitor cell niche within a 3D engineered hydrogel matrix. *Biomaterials*, **33**, 5198-5205, (2012).
80 DeLong, S. A., Moon, J. J. & West, J. L. Covalently immobilized gradients of bFGF on hydrogel scaffolds for directed cell migration. *Biomaterials*, **26**, 3227-3234, (2005).
81 Porter, A. M., Klinge, C. M. & Gobin, A. S. Biomimetic Hydrogels with VEGF Induce Angiogenic Processes in Both hUVEC and hMEC. *Biomacromolecules*, **12**, 242-246, (2011).
82 Zhang, S. *et al.* Self-complementary oligopeptide matrices support mammalian cell attachment. *Biomaterials*, **16**, 1385-1393, (1995).

83 Stiffness — an unknown world of mechanical science? *Injury*, **31, Supplement 2**, 14-84, (2000).
84 Wang, X. & Ha, T. Defining Single Molecular Forces Required to Activate Integrin and Notch Signaling. *Science*, **340**, 991-994, (2013).
85 Watt, F. M. & Huck, W. T. S. Role of the extracellular matrix in regulating stem cell fate. *Nat Rev Mol Cell Biol*, **14**, 467-473, (2013).
86 Swift, J. *et al.* Nuclear Lamin-A Scales with Tissue Stiffness and Enhances Matrix-Directed Differentiation. *Science*, **341**, (2013).
87 Dupont, S. *et al.* Role of YAP/TAZ in mechanotransduction. *Nature*, **474**, 179-183, (2011).
88 Engler, A. J. *et al.* Matrix Elasticity Directs Stem Cell Lineage Specification. *Cell*, **126**, 677-689, (2006).
89 Trappmann, B. *et al.* Extracellular-matrix tethering regulates stem-cell fate. *Nat Mater*, **11**, 642-649, (2012).
90 Behravesh, E., Sikavitsas, V. I. & Mikos, A. G. Quantification of ligand surface concentration of bulk-modified biomimetic hydrogels. *Biomaterials*, **24**, 4365-4374, (2003).
91 Ghajar, C. M. *et al.* The Effect of Matrix Density on the Regulation of 3-D Capillary Morphogenesis. *Biophysical journal*, **94**, 1930-1941, (2008).
92 Pathak, A. & Kumar, S. Biophysical regulation of tumor cell invasion: moving beyond matrix stiffness. *Integrative Biology*, **3**, 267-278, (2011).
93 Ulrich, T. A. *et al.* Probing cellular mechanobiology in three-dimensional culture with collagen–agarose matrices. *Biomaterials*, **31**, 1875-1884, (2010).
94 Huebsch, N. *et al.* Harnessing traction-mediated manipulation of the cell/matrix interface to control stem-cell fate. *Nat Mater*, **9**, 518-526, (2010).
95 Young, J. L. & Engler, A. J. Hydrogels with time-dependent material properties enhance cardiomyocyte differentiation in vitro. *Biomaterials*, **32**, 1002-1009, (2011).
96 Oh, S. *et al.* Stem cell fate dictated solely by altered nanotube dimension. *Proceedings of the National Academy of Sciences*, **106**, 2130-2135, (2009).
97 Storm, C. *et al.* Nonlinear elasticity in biological gels. *Nature*, **435**, 191-194, (2005).
98 Shu, X. Z. *et al.* Disulfide-crosslinked hyaluronan-gelatin hydrogel films: a covalent mimic of the extracellular matrix for in vitro cell growth. *Biomaterials*, **24**, 3825-3834, (2003).
99 Vanderhooft, J. L. *et al.* Rheological Properties of Cross-Linked Hyaluronan–Gelatin Hydrogels for Tissue Engineering. *Macromolecular Bioscience*, **9**, 20-28, (2009).
100 Ghosh, K. *et al.* Cell adaptation to a physiologically relevant ECM mimic with different viscoelastic properties. *Biomaterials*, **28**, 671-679, (2007).
101 Ghosh, K. *et al.* Fibronectin Functional Domains Coupled to Hyaluronan Stimulate Adult Human Dermal Fibroblast Responses Critical for Wound Healing. *Tissue Engineering*, **12**, 601-613, (2006).

102 Pan, Z. *et al.* Traction Stresses and Translational Distortion of the Nucleus During Fibroblast Migration on a Physiologically Relevant ECM Mimic. *Biophysical journal*, **96**, 4286-4298, (2009).
103 Seib, F. P. *et al.* Matrix elasticity regulates the secretory profile of human bone marrow-derived multipotent mesenchymal stromal cells (MSCs). *Biochemical and Biophysical Research Communications*, **389**, 663-667, (2009).
104 Bloom, R. J. *et al.* Mapping Local Matrix Remodeling Induced by a Migrating Tumor Cell Using Three-Dimensional Multiple-Particle Tracking. *Biophysical journal*, **95**, 4077-4088, (2008).
105 Winer, J. P., Oake, S. & Janmey, P. A. Non-Linear Elasticity of Extracellular Matrices Enables Contractile Cells to Communicate Local Position and Orientation. *PLoS ONE*, **4**, e6382, (2009).
106 Wen, Q. & Janmey, P. A. Effects of non-linearity on cell–ECM interactions. *Experimental Cell Research*, **319**, 2481-2489, (2013).
107 MacKintosh, F. C., Käs, J. & Janmey, P. A. Elasticity of Semiflexible Biopolymer Networks. *Physical Review Letters*, **75**, 4425-4428, (1995).
108 Žagar, G., Onck, P. R. & Van der Giessen, E. Elasticity of Rigidly Cross-Linked Networks of Athermal Filaments. *Macromolecules*, **44**, 7026-7033, (2011).
109 van Dillen, T., Onck, P. R. & Van der Giessen, E. Models for stiffening in cross-linked biopolymer networks: A comparative study. *Journal of the Mechanics and Physics of Solids*, **56**, 2240-2264, (2008).
110 Onck, P. R. *et al.* Alternative Explanation of Stiffening in Cross-Linked Semiflexible Networks. *Physical Review Letters*, **95**, 178102, (2005).
111 Lo, C.-M. *et al.* Cell Movement Is Guided by the Rigidity of the Substrate. *Biophysical journal*, **79**, 144-152, (2000).
112 Rudnicki, M. S. *et al.* Nonlinear Strain Stiffening Is Not Sufficient to Explain How Far Cells Can Feel on Fibrous Protein Gels. *Biophysical journal*, **105**, 11-20, (2013).
113 Erk, K. A., Henderson, K. J. & Shull, K. R. Strain Stiffening in Synthetic and Biopolymer Networks. *Biomacromolecules*, **11**, 1358-1363, (2010).
114 Jaspers, M. *et al.* Ultra-responsive soft matter from strain-stiffening hydrogels. *Nat Commun*, **5**, 1-8, (2014).
115 Freed, L. E. *et al.* Biodegradable Polymer Scaffolds for Tissue Engineering. *Nat Biotechnol*, **12**, 689-693, (1994).
116 Lee, M., Wu, B. M. & Dunn, J. C. Y. Effect of scaffold architecture and pore size on smooth muscle cell growth. *Journal of Biomedical Materials Research Part A*, **87A**, 1010-1016, (2008).
117 van Tienen, T. G. *et al.* Tissue ingrowth and degradation of two biodegradable porous polymers with different porosities and pore sizes. *Biomaterials*, **23**, 1731-1738, (2002).
118 LeBaron, R. G. & Athanasiou, K. A. Extracellular Matrix Cell Adhesion Peptides: Functional Applications in Orthopedic Materials. *Tissue Engineering*, **6**, 85-103, (2000).
119 Dvir, T. *et al.* Nanotechnological strategies for engineering complex tissues. *Nat Nanotechnol*, **6**, 13-22, (2011).

120 Liu, S., Calderwood, D. A. & Ginsberg, M. H. Integrin cytoplasmic domain-binding proteins. *Journal of Cell Science*, **113**, 3563-3571, (2000).
121 Tadokoro, S. *et al.* Talin Binding to Integrin ß Tails: A Final Common Step in Integrin Activation. *Science*, **302**, 103-106, (2003).
122 Calderwood, D. A. *et al.* Competition for Talin Results in Trans-dominant Inhibition of Integrin Activation. *Journal of Biological Chemistry*, **279**, 28889-28895, (2004).
123 Jiang, G. *et al.* Two-piconewton slip bond between fibronectin and the cytoskeleton depends on talin. *Nature*, **424**, 334-337, (2003).
124 Tolbert, C. E., Burridge, K. & Campbell, S. L. Vinculin regulation of F-actin bundle formation: What does it mean for the cell? *Cell Adhesion & Migration*, **7**, 219-225, (2013).
125 del Rio, A. *et al.* Stretching Single Talin Rod Molecules Activates Vinculin Binding. *Science*, **323**, 638-641, (2009).
126 Lowell, C. & Mayadas, T. in *Integrin and Cell Adhesion Molecules* Vol. 757 *Methods in Molecular Biology* (ed Motomu Shimaoka) Ch. 22, 369-397 (Humana Press, 2012).
127 Anderheiden, D. *et al.* Surface modification of a biocompatible polymer based on polyurethane for artificial blood vessels. *J Mater Sci: Mater Med*, **3**, 1-4, (1992).
128 Yang, X. B. *et al.* Human osteoprogenitor growth and differentiation on synthetic biodegradable structures after surface modification. *Bone*, **29**, 523-531, (2001).
129 Kao, W. J., Hubbell, J. A. & Anderson, J. M. Protein-mediated macrophage adhesion and activation on biomaterials: a model for modulating cell behavior. *J Mater Sci: Mater Med*, **10**, 601-605, (1999).
130 Drumheller, P. D. & Hubbell, J. A. Densely crosslinked polymer networks of poly(ethylene glycol) in trimethylolpropane triacrylate for cell-adhesion-resistant surfaces. *Journal of Biomedical Materials Research*, **29**, 207-215, (1995).
131 Kao, W. J. & Hubbell, J. A. Murine macrophage behavior on peptide-grafted polyethyleneglycol-containing networks. *Biotechnology and Bioengineering*, **59**, 2-9, (1998).
132 Lin, H.-B. *et al.* Endothelial cell adhesion on polyurethanes containing covalently attached RGD-peptides. *Biomaterials*, **13**, 905-914, (1992).
133 Holland, J. *et al.* Culture of human vascular endothelial cells on an RGD-containing synthetic peptide attached to a starch-coated polystyrene surface: comparison with fibronectin-coated tissue grade polystyrene. *Biomaterials*, **17**, 2147-2156, (1996).
134 Shroff, K. *et al.* Fibronectin-mimetic peptide-amphiphile nanofiber gels support increased cell adhesion and promote ECM production. *Soft Matter*, **6**, 5064-5072, (2010).
135 Danilov, Y. N. & Juliano, R. L. (Arg・Gly・Asp)n-Albumin conjugates as a model substratum for integrin-mediated cell adhesion. *Experimental Cell Research*, **182**, 186-196, (1989).
136 Dalby, M. J. *et al.* Nucleus alignment and cell signaling in fibroblasts: response to a micro-grooved topography. *Experimental Cell Research*, **284**, 272-280, (2003).

137 Boyen, H.-G. *et al.* Oxidation-Resistant Gold-55 Clusters. *Science*, **297**, 1533-1536, (2002).
138 Cavalcanti-Adam, E. A. *et al.* Lateral spacing of integrin ligands influences cell spreading and focal adhesion assembly. *European Journal of Cell Biology*, **85**, 219-224, (2006).
139 Park, J. *et al.* Nanosize and Vitality: TiO2 Nanotube Diameter Directs Cell Fate. *Nano Letters*, **7**, 1686-1691, (2007).
140 Yim, E. K. F., Pang, S. W. & Leong, K. W. Synthetic nanostructures inducing differentiation of human mesenchymal stem cells into neuronal lineage. *Experimental Cell Research*, **313**, 1820-1829, (2007).
141 Lei, Y. *et al.* Modulation of Lumen Formation by Microgeometrical Bioactive Cues and Migration Mode of Actin Machinery. *Small*, **9**, 1086-1095, (2013).
142 Dundas, C., Demonte, D. & Park, S. Streptavidin–biotin technology: improvements and innovations in chemical and biological applications. *Appl Microbiol Biotechnol*, **97**, 9343-9353, (2013).
143 Laitinen, O. H. *et al.* Brave new (strept)avidins in biotechnology. *Trends in Biotechnology*, **25**, 269-277, (2007).
144 Hermanson, G. T. in *Bioconjugate Techniques (Second Edition)* (ed Greg T. Hermanson) 900-923 (Academic Press, 2008).
145 Stenzel, M. H. Bioconjugation Using Thiols: Old Chemistry Rediscovered to Connect Polymers with Nature's Building Blocks. *ACS Macro Letters*, **2**, 14-18, (2013).
146 Hermanson, G. T. in *Bioconjugate Techniques (Second Edition)* (ed Greg T. Hermanson) 169-212 (Academic Press, 2008).
147 Schoffelen, S. *et al.* Metal-free and pH-controlled introduction of azides in proteins. *Chemical Science*, **2**, 701-705, (2011).
148 Dommerholt, J. *et al.* Readily Accessible Bicyclononynes for Bioorthogonal Labeling and Three-Dimensional Imaging of Living Cells. *Angewandte Chemie International Edition*, **49**, 9422-9425, (2010).
149 Nimmo, C. M., Owen, S. C. & Shoichet, M. S. Diels−Alder Click Cross-Linked Hyaluronic Acid Hydrogels for Tissue Engineering. *Biomacromolecules*, **12**, 824-830, (2011).
150 van Dongen, S. F. M. *et al.* Reactive protein-repellent surfaces for the straightforward attachment of small molecules up to whole cells. *Chemical Science*, **3**, 3000-3006, (2012).
151 Lutz, J.-F. Polymerization of oligo(ethylene glycol) (meth)acrylates: Toward new generations of smart biocompatible materials. *Journal of Polymer Science Part A: Polymer Chemistry*, **46**, 3459-3470, (2008).

Chapter 2 : Monomer Synthesis

Abstract
Alanine-alanine triethylene glycol isocyanide monomers with varied enantiomers of alanine-alanine (*LD;DL*) were synthesized. Alanine-alanine (*LD*) tetraethylene glycol isocyanide monomer was synthesized. Isocyanide monomers of alanine-alanine (*LD*) oligoethylene glycol containing a functional handle appendage of either acetylene or azide were synthesized. A monomer containing non-natural amino acid of aminobenzoic acid-alanine tetra ethylene glycol was synthesized successfully.

Introduction

Isocyanide monomers, from which polyisocyanides are synthesized, were first reported by Lieke in 1859 [1]. Later in 1867 Gautier published the synthesis of isocyanides from silver cyanide and alkyl iodides [2], whilst Hofmann found that isocyanides could be prepared by the reaction of an amine with chloroform [3]. One of the first indications of a successful synthesis of a (liquid) isocyanide is the characteristic pungent and repulsive odour of this compound [4] which hindered their widespread use. These rather toxic and cumbersome methods were not suitable for the large scale production of isocyanides, further limiting the research on isocyanides entirely. This all changed when Hagedorn and Ugi reported the facile synthesis of isocyanides from formamides using a dehydration reaction with diphosgene [5-8].

The isocyanide monomers required to synthesize polymers that are biocompatible ECM mimics must form β-sheets and be soluble in water. Therefore the isocyanide monomer must contain a dipeptide and a water soluble element e.g. oligoethylene glycol.

Another important element that is required for most biomimetic materials are functional handles that can be used to attach biologically relevant signals e.g. RGD or growth factors.

The functional handle of choice was the azide, as Cu^{I}-catalyzed Huisgen 1,3-dipolar cycloaddition simply known as click chemistry [9] is modular, wide in scope, high in yield, has little side products that are easily removed, is regioselective but not necessarily enantio selective, uses simple reaction conditions, is not sensitive to oxygen or water. In addition it uses easily accessible reagents, requires no solvent or a solvent that is easily removed or benign like water, enables simple product isolation, has a high thermodynamic driving force (greater than 20 kcal mol^{-1}) and goes rapidly to completion [9-12]. A more recent click strategy that avoids Cu^{I} completely (which is ideal for biomedical materials), uses strain promoted acetylene azide cycloaddition (SPAAC) [13-16].

A wide variety of different amino acids have been used in the past e.g. alanine, leucine [17] and glutamic acid [18] to prepare polyisocyanides. However the best results in terms of tertiary structure and helix stability were obtained with alanine di and tri peptide variants. It was hypothesized that by substituting one of the alanine subunits in the oligoethylene di-alanine monomer with aminobenzoic acid it would be possible to obtain higher persistance length water soluble polymers. Yashima *et al.* polymerized an enantiomerically pure 4-isocyanobenzoic acid derivative bearing an L-alanine group substituted with a *n*-decyl chain with the objective to generate polymeric liquid crystals [19]. When this monomer was polymerized with a Ni catalyst, a polymer with a broad molecular weight distribution was obtained. When the same monomer was polymerized with the μ-ethynediyl Pt-Pd catalyst, a polymer with a narrow molecular weight distribution was formed [20]. Once synthesized it

would be possible to compare the water soluble polyisocyanides from the Ni catalyst with the Pt-Pd catalyst in terms of material properties and dispersity (Đ).

In this chapter, the synthesis of isocyanide monomers that contain different lengths of oligoethylene glycol, different chiralities with regards to the dipeptide alanine-alanine core and functionalizable handles that consist of acetylene or azides will be investigated (Figure 1&2).

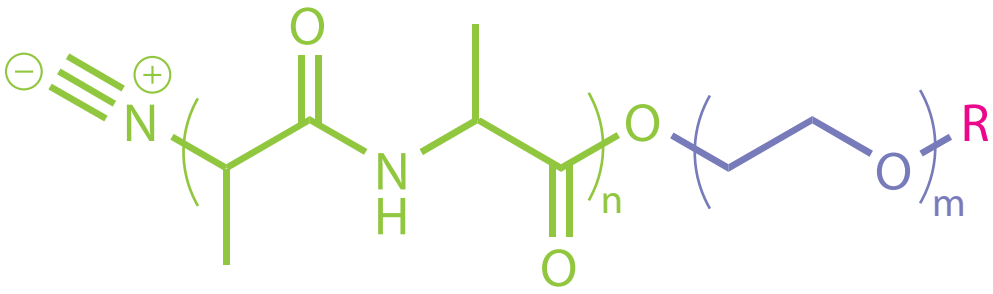

m= 3 or 4
n = *DL* or *LL* or *LD* alanine-alanine
R= azide or acetylene or CH3

Figure 1: Oligo(ethylene glycol) substituted polyisocyanopeptides. The isocyanide monomer with alanine-alanine dipeptide core, oligoethylene spacer and functionalizable chain end.

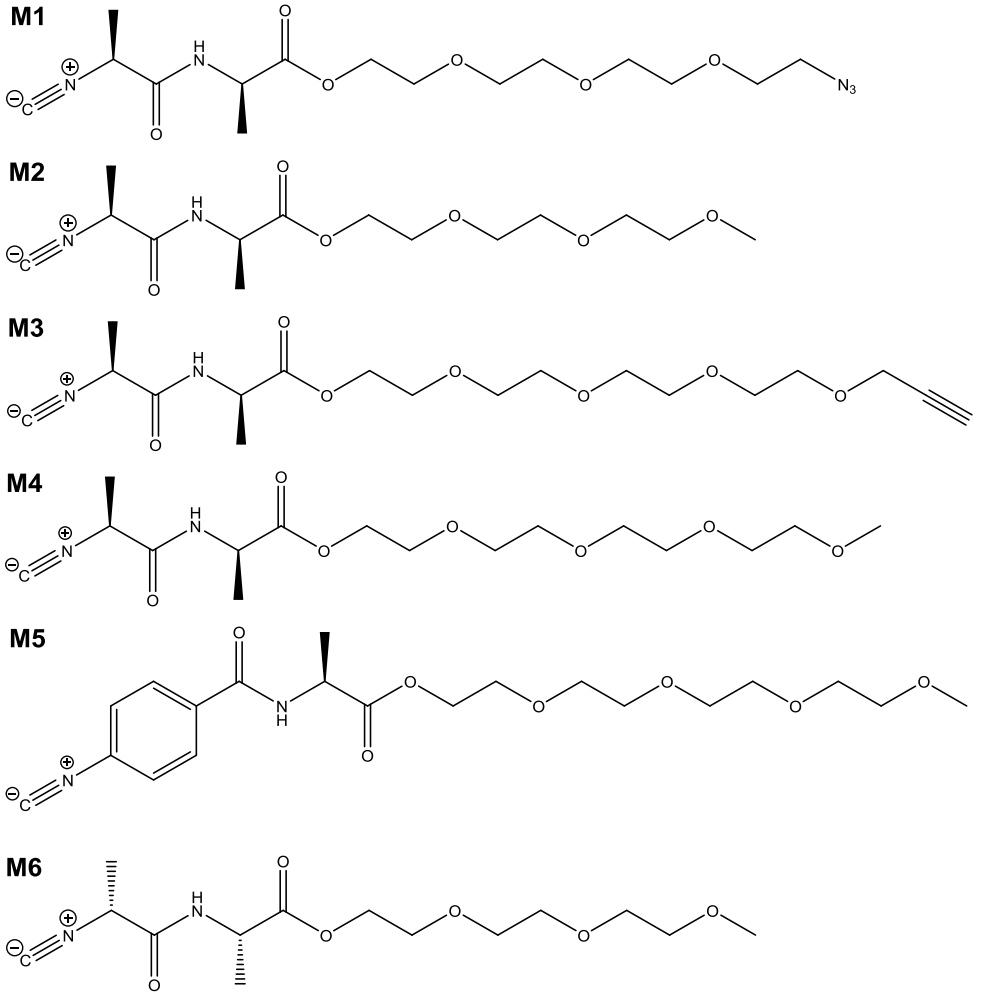

Figure 2. A schematic summary of the monomers synthesized in this chapter.

.

Results and discussion

1. Monomer synthesis

1.1. 2-(2-(2-(2-azidoethoxy)ethoxy)ethoxy)ethyl-(*L*)-alaninyl-(*D*)-isocyanoalanine (M1)

Tetraethylene glycol was mono-tosylated in the presence of pyridine by the addition of one equivalent of 4-toluenesulfonyl chloride. The remaining alcohol group was coupled to *tert*-butyloxycarbonyl (BOC)-*L*-alanine using the Steglich esterification [21]. The purified compound was deprotected yielding the free amine. The free amine was used in a DCC coupling with BOC-*D*-alanine in the presence of dicyclohexylcarbodiimide (DCC) and hydroxybenzotriazole (HOBt) to limit racemization. The free amine was obtained after de-BOCylation. It was found that higher yields were obtainable if the amine was first converted to the formyl prior to nucleophilic substitution of tosyl with sodium azide. The dehydration reaction of **5** with diphosgene at -40 °C was the lowest yielding step of the entire synthesis. The azide monomer **M1** was synthesized over six steps with an overall yield of 1.3% (Figure 3).

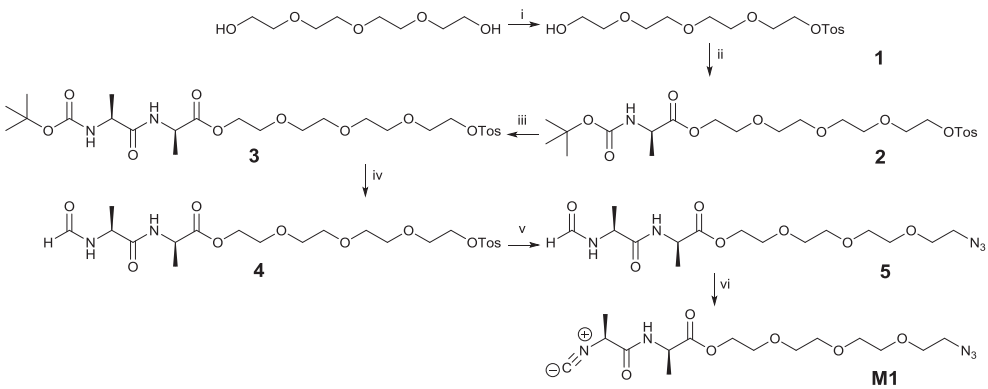

Figure 3. Synthesis of M1: i)pTosCl, pyridine, 0 °C rt, 12 h, 29 % ; ii) Boc-L-Ala, DCC, DMAP, CH_2Cl_2, 0 °C room temperature, 4 h, 76 % ; iii a) ~2 M HCl in ethyl acetate, CH_2Cl_2 room temperature, 1 h, quantitative yield b) Boc-D-Ala-OH, DIPEA, HOBt, CH_2Cl_2, 0 °C room temperature, 14 h, 60% , iv a) 2 M HCl in ethyl acetate, CH_2Cl_2 room temperature, 1 h, quantitative yield b) ethyl formate/sodium formate was refluxed for 8 h at 66 °C 54 % v) absolute EtOH, sodium azide was refluxed 16 h , 78% vi) N-methylmorpholine (NMM) -40 °C diphosgene (0.04 M) over 2 h 27% .

1.2. Synthesis of 2-(2-(2-methoxyethoxy)ethoxy)ethyl (*L*)-alaninyl-(*D*)-isocyanoalanine (M2)

The commonly used route in our group for obtaining **6**, was a DCC coupling of Boc-*L*-alanine to triethylene glycol monomethyl ether under alkaline conditions [22]. The alternative synthetic route depicted in Figure 4, was prefered as the starting compounds *L*-alanine and *p*-toluene sulfonic acid (PTSA) were significantly cheaper , similar yields were obtained and the synthesis time was significantly shortened.

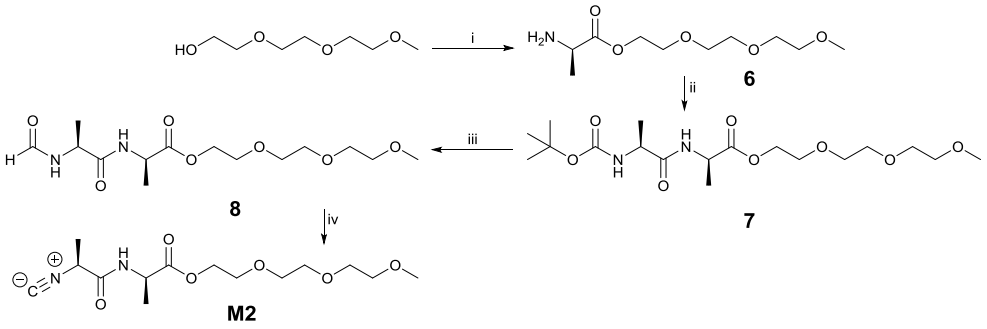

Figure 4. Synthetic scheme for synthesis of M2 i) *L*-Ala, PTSA, 126 °C, 4h, 62%; ii) Boc-*D*-Ala, DCC, HOBt, DIPEA, 0 °C →rt, 16 h, 52 % ; iii) a. HCl in dioxane, ethyl acetate, 2h, quantitative b. Sodium formate/Ethyl formate 66 °C, o/n, 56 % ; iv) diphosgene/NMM, CH_2Cl_2, - 40 °C, 2 h, 51%.

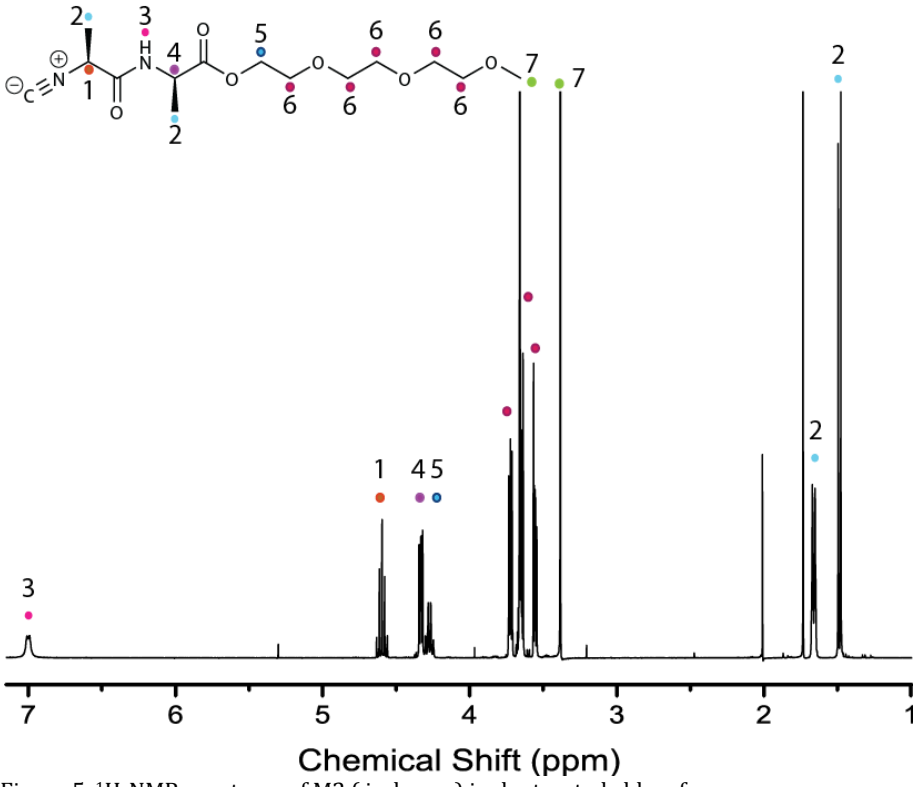

Figure 5. ^{1}H-NMR spectrum of M2 (in-house) in deuterated chloroform.

Since large quantities of compound **M2** were required it was decided to outsource the synthesis of the compound as the low overall yield and a turnaround time of two to three weeks from starting the synthesis till obtaining the monomer was deemed too slow to generate large batches of polymers. The **M2** monomer was purchased from Chiralix B.V. as 95 % pure; the synthetic strategy used to produce their monomer was not disclosed to me. It was however important to compare the two monomers **M2** Chiralix with **M2** in-house (synthesized by me) before using them as reactants. **M2** Chiralix required an additional silica column purification step prior to use. After purification the monomer was light yellow in colour whereas the in-house monomer was colourless. The LC-MS was the same for both monomers. The optical rotation of **M2** from Chiralix after purification via silica column chromatography was -0.44° and that of in-house **M2** was -0.34°. The occurrence of a low percentage of racemisation is therefore likely for both monomers as the optical rotation should be zero for a *D*-*L*-monomer. Upon closer inspection of the nuclear magnetic resonance spectra, the two monomers differ slightly in the range (1.7-1.4 ppm) for the alanine CH_3 (2 from Figure 5) doublet of doublets (Figure 6). A broad doublet is visible for the Chiralix monomer at 1.6 ppm, which could be indicative of a trace racemic impurity of around 0.09 % according to ^{1}H-NMR. The in-house monomer contains some unidentified possible starting material or racemic impurities at 1.40- 1.45 ppm of around 0.07%. Both types of monomers were deemed pure enough to continue.

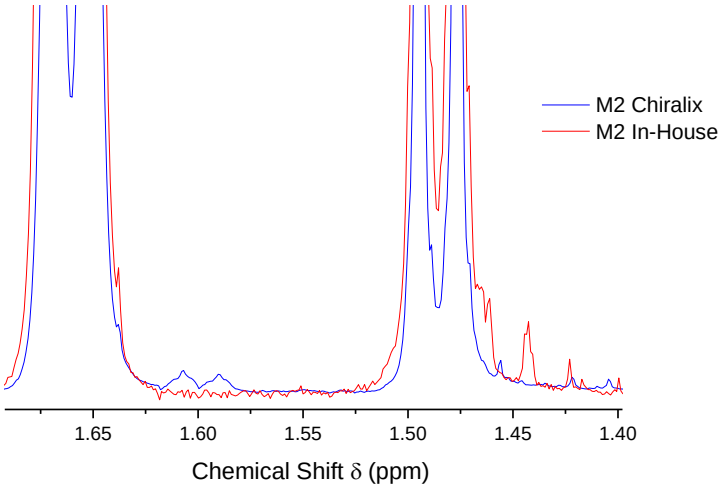

Figure 6. Zoom in of ^{1}H-NMR spectra of M2 Chiralix vs in house in deuterated chloroform.

1.3. Synthesis of 3,6,9,12-tetraoxapentadec-14-yn-1-yl (*L*)alaninyl-(*D*)-isocyanoalanine (M3)

Mono-functionalization of tetraetylene glycol was achieved using a SN_2 nucleophilic substitution reaction with 3-bromoprop-1-yne in dry THF with good yields. The rest of the synthetic route towards **M3** was similar to that of **M1** (Figure 7). The rate limiting step for the entire synthesis was again the final dehydration step in the presence of diphosgene. The acetylene monomer **M3** was synthesized over seven steps with an overall yield of ~5%.

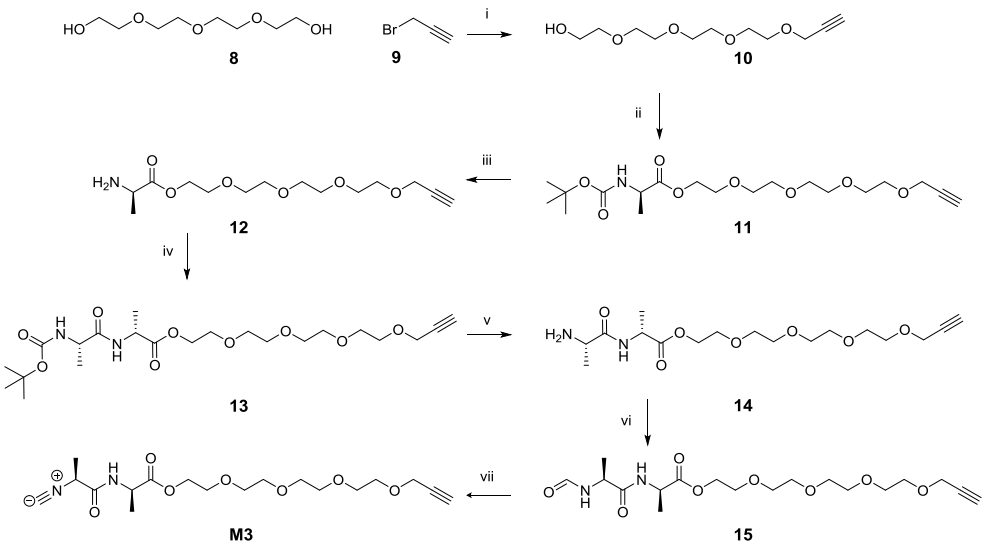

Figure 7. Synthesis of M3: i) NaH, THF, rt, 17 h, 73%; ii) Boc-*L*-Ala-OH, DMAP, DCC, CH_2Cl_2, 0 °C→rt, 16 h, 82%; iii) 2 M HCl in dioxane, CH_2Cl_2, rt, 1 h, quantitative yield; iv) Boc-*D*-Ala-OH, D*i*PEA, HOBt, DCC, DMAP, CH_2Cl_2, 0 °C→rt, 14 h, 60%; v) 2 M HCl in dioxane, CH_2Cl_2, rt, 1 h, quantitative yield; vi) sodium formate, ethyl formate, reflux, 18 h, 47%; vii) NMM, diphosgene, CH_2Cl_2, Ar, -50 °C, 40 min, 31% .

1.4. Synthesis of 2-(2-(2-(2-methoxyethoxy)ethoxy)ethoxy)ethyl-(*L*)-alaninyl-(*D*)-isocyanoalanine (M4)

The Fischer esterification was performed between the alcohol group of tetraethylene glycol monomethyl ether and the carboxylic acid group of *L*-alanine catalysed by p-toluene sulfonic acid, the reaction was driven to completion by using a Dean-Stark setup in which water was continuously removed from the reaction mixture. This intermediate strategy enabled the use of cheaper starting products and increased yields as it removed the need for an additional deprotection and purification via silica column chromatography step. The

reaction steps ii-v was similar as to those previously described for monomer **M2.** Monomer **M4** was synthesized over five steps with an overall yield of 4 % (Figure 8).

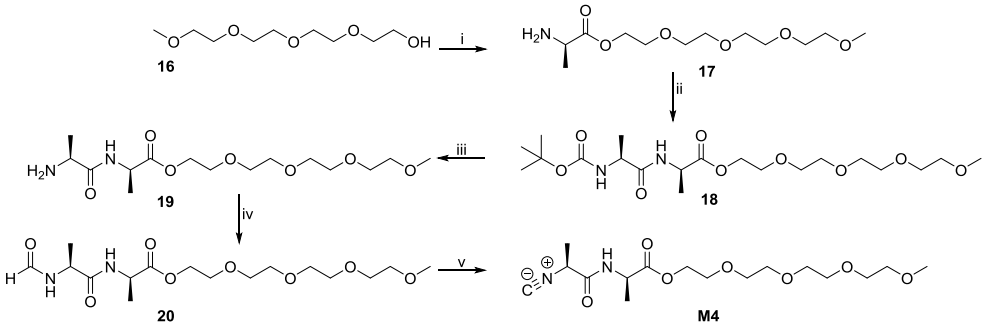

Figure 8. Reagents and conditions: i) *L*-alanine, p-toluene sulfonic acid, toluene, reflux, 4 h, 46%; ii) Boc-*D*-Ala-OH, DMAP, DCC, DIPEA, HOBt CH_2Cl_2, 0 °C→rt, 16 h, 68%; iii) HCl in dioxane, CH_2Cl_2, rt, 2 h, quantitative yield; iv) sodium formate, ethyl formate, reflux, 16 h, 33%; v) NMM, diphosgene, CH_2Cl_2, Ar, -70 °C, 35 min, 43% .

1.5. Synthesis of 2-(2-(2-methoxyethoxy)ethoxy)ethyl (*D*)-alaninyl-(*L*)-isocyanoalanine (M6)

The enantiomeric inverse of **M2** was synthesized to see what effect the inverse chirality would have on polymer synthesized from this monomer. The same synthesis route as that for **M2** was followed with the only difference being that *D*-alanine was esterified with triethylene glycol monomethyl ether in the presence of p-toluene sulfonic acid and after purification, **24** was combined with *L*-alanine through nucleophilic substitution in the presence of DCC. Monomer **M6** was synthesized over four steps with an overall yield of 3 % (Figure 9).

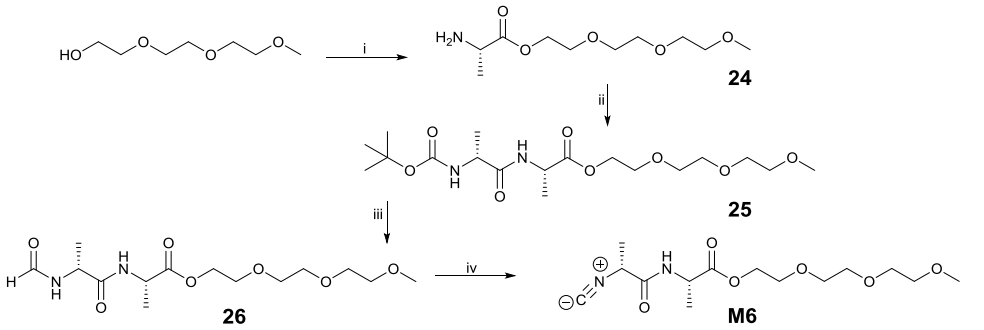

Figure 9. Reagents and conditions: i) *D*-alanine, p-toluene sulfonic acid, toluene, reflux, 4 h, 44 %; ii) Boc-*L*-Ala-OH, DMAP, DCC, HOBt, CH_2Cl_2, 0 °C→rt, 16 h; iii) a. HCl in dioxane, CH_2Cl_2, rt, 2 h, quantitative yield, b. Sodium formate, ethyl formate, reflux, 8 h, 13 %; iv) NMM, diphosgene, CH2Cl2, -40 °C, 120 min, 53 % .

2. Synthesis of 2-(2-(2-(2-methoxyethoxy)ethoxy)ethoxy)ethyl (*L*)-alaninyl-4-isocyanobenzamine (M5)

N-boc-4 aminobenzoic acid (Boc-4Abz-OH) was activated with DCC and underwent nucleophilic substitution with **17** to obtain **22**. After de-protection and standard formylation compound **23** was obtained in excellent yield. The dehydration of formyl to isocyanide was also successful. Monomer **M5** was synthesized over four steps with an overall yield of 20 % (Figure 10; Figure 11), the higher yields with regards to the other monomers is probably due to the larger hydrophobicity of **22-23** compared to **18** and **20**, resulting in lower product losses during purification step using multiple extractions with water.

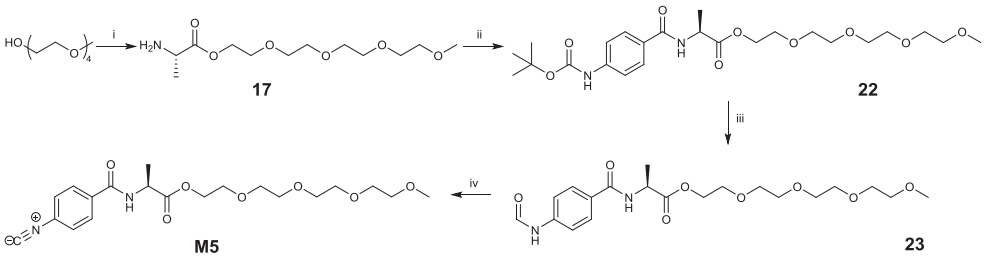

Figure 10. Reagents and conditions: i) L-alanine, p-toluene sulfonic acid, toluene, reflux, 3 h, 85 %; ii) Boc-4Abz-OH, DIPEA, DMAP, DCC, HOBt CH_2Cl_2, 0 °C rt, 16 h, 37 %; iii) a. HCl in dioxane, CH_2Cl_2, rt, 2 h, quantitative yield, b. Sodium formate, ethyl formate, reflux, 16h, 94 %; iv) NMM, diphosgene, CH_2Cl_2, Ar, -35 °C, 90 min, 70 % .

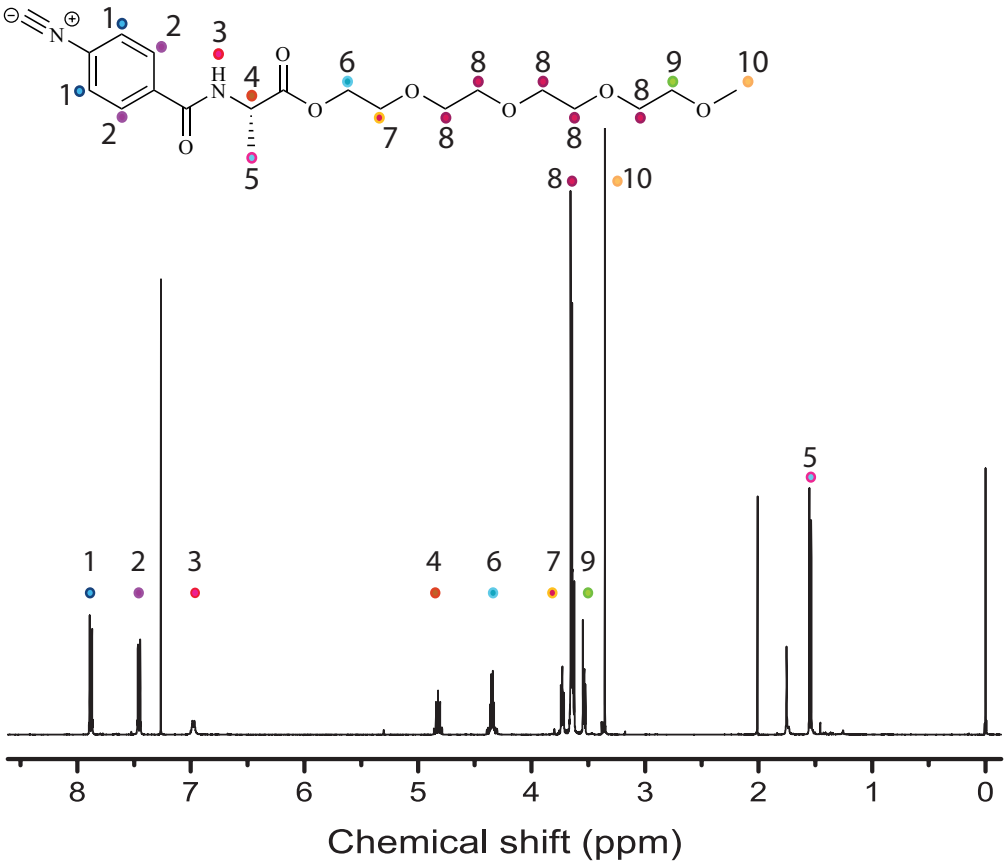

Figure 11. ^{1}H-NMR spectrum of M5 in deuterated chloroform, unassigned peaks are acetone (2.0 ppm), water (1.67 ppm) and TMS (0.0 ppm).

Conclusion/Discussion

As a whole, all the functional isocyanide monomers were synthesized successfully with overall yields comparable to the conventional alanine-alanine monomers with an average total yield of 5%. To increase the yields it would be advisable to investigate the use of a different dehydration method (Figure 12). For example, McCarthy *et al.* [23] and Mal with co-workers [24] reported on the use of Burgess Reagent, and Fuchs *et al.* [25] used phosphoryl trichloride as dehydration agent. Other reported dehydration agents include thionyl chloride [26-27] and cyanuric chloride [28-29].

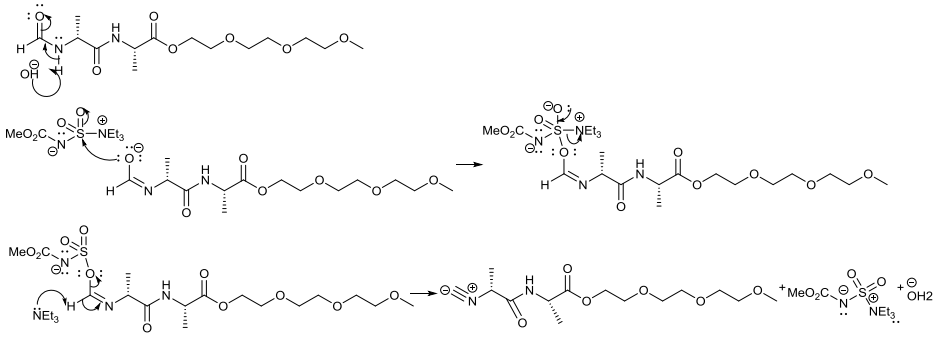

Figure 12. The proposed mechanism for the dehydration of **8** to obtain **M2** by using Burgess Reagent in a basic solvent system.

Experimental:

Instrumental: ^{1}H NMR and ^{13}C NMR spectra were recorded on a Bruker AC-300 MHz instrument operating at 300 MHz and 75 MHz, respectively. *J* values are given in Hz and chemical shifts are reported in ppm. TMS was used as the internal standard. The used abbreviations are s = singlet, d = doublet, bs = broad singlet, t= triplet q =quartet, dd= doublet of doublets. FT-infrared spectra of the compounds were measured using a Thermo Nicolet IR300 FT-IR spectrometer (Thermo Fisher Scientific, Breda, The Netherlands) equipped with a Harrick ATR unit. UV-VIS measurements were done using a Varian Cary 50 spectrometer (Agilent Technologies, Amstelveen, The Netherlands). For mass spectrometry a LCQ Advantage MAX instrument (Thermo Fisher Scientific) was used.

Materials: Toluene was distilled over sodium. Dichloromethane was distilled over phosphorous pentoxide. *N*-methylmorpholine was freshly distilled over sodium prior to use. Water was purified with a Milipore MiliQ system, (mQ water 18.2 MΩ). All the other chemicals were used as received. Column chromatography was performed using silica gel (0.060–0.200 mm) provided by Baker. Thin layer chromatography (TLC) analyses were carried out on silica 60 F_{254} coated glass obtained from Merck and the compounds were visualised using Ninhydrine or basic aqueous $KMnO_4$ solutions. All glassware was soaked in a 0.5 M aqueous NaOH solution prior to use. Alumina Brokman grade III was used in all cases unless stated otherwise.

Synthesis

2. Monomer synthesis

2.1) Preparation of the comonomer M1

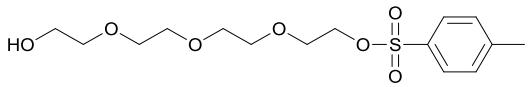

Tetraethylene glycol (28.5 mL, 164.3 mmol) was dissolved in 50 mL pyridine. The solution was subsequently cooled to 0 °C while stirring. Argon was bubbled through the solution for 15 minutes. Tosylchloride (21.9 g, 115 mmol) was added portion wise to the stirring solution. The mixture was further stirred at room temperature for 12 hours. The reaction mixture was diluted with 50 mL of a 10 % aqueous citric acid solution. The mixture was extracted three times with 250 mL of chloroform. The combined organic layers were dried over anhydrous Na_2SO_4, filtered and the solvent was evaporated. The resulting yellow oil was purified using column chromatography (SiO_2, 0.060 - 0.200 mm; ethyl acetate as eluent) to yield **1** as a pale yellow oil (11.7 g, 33.6 mmol, 29 %)[30]

R_f = 0.4 (ethyl acetate); **^{1}H NMR δ_H ($CDCl_3$, 300 MHz) =** 7.8 (dd, J = 7.81 Hz, 2H, -C$\underline{H}_{Ar}$-), 7.33 (d, J = 7.8 Hz, 2H, -C$\underline{H}_{Ar}$-S), 4.17 (m, 2H, HO-C$\underline{H}_2$-CH_2-), 3.65 (m, 16H, -C$\underline{H}_2$-), 2.45 (s, 3H, -C$\underline{H}_3$); **^{13}C NMR δ_C ($CDCl_3$, 75 MHz) =** 21.16 (1C, C*C*H_3), 61.0 (1C, *C*OH), 68.13(1C, *C*OS), 69.0 (1C, O*C*H_2), 70.0, 70.1, 70.1, 70.2 (4C, O*C*H_2), 70.8, 72.0 (2C, O*C*H_2), 127.5 (2C, CH*C*CH), 129.5 (2C, *C*HC*C*H), 139.7 (1C, *C*CH_3), 144.5 (1C, CH*C*S); **FT-IR υ (cm^{-1}, ATR) =** 3442 (O-H), 2870 (C-H), 1597 (C=C_{Ar}), 1453 (C-H), 1352 (S=O), 1175 (S=O), 1096 (C-O).

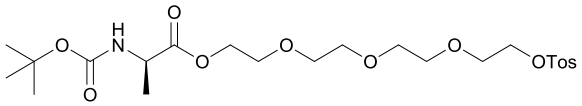

Compound **1** (5.2 g, 15.0 mmol), *N*-Boc-(*L*)-alanine (2.9 g, 15.0 mmol) and 4-dimethylaminopyridine (DMAP) (0.2 g, 1.6 mmol) were dissolved in 25 mL of freshly distilled CH_2Cl_2 and cooled to 0 °C while stirring. *N*,*N'*-dicyclohexylcarbodiimide (DCC) (3.1 g, 15.0 mmol) was added portion wise. The mixture turned yellow and was stirred for 1 h at 0 °C and thereafter it was stirred for 3 h at room temperature. The precipitated dicyclohexyl urea was removed by filtration and washed with ethyl acetate (3 x 20 mL) to remove any possible product that was adsorbed to it. The organic layer and ethyl acetate washings were concentrated under vacuum. The crude product was purified using column chromatography (SiO_2, 0.060 - 0.200 mm; 1% MeOH/CH_2Cl_2 as eluent) to yield **2** as a light orange oil (5.5 g, 11.4 mmol, 76%)

R_f = 0.4 (10 % MeOH/CH_2Cl_2); **^{1}H NMR δ_H ($CDCl_3$, 300 MHz) =** 7.79 (d, J = 8.4 Hz, 2H, -C$\underline{H}_{Ar}$-), 7.33 (d, J = 8.1 Hz, 2H, -C$\underline{H}_{Ar}$-), 5.02 (s, 1H, -N$\underline{H}$), 4.28 (m, 3H, -C$\underline{H}$(CH_3), COOC$\underline{H}_2$-), 4.15 (m, 2H, O-C$\underline{H}_2$-CH_2), 3.69 (m, 14H, O-C$\underline{H}_2$-CH_2), 2.44 (s, 3H, --C$\underline{H}_3$), 1.44 (s, 9H, -OC(C$\underline{H}_3$)$_3$), 1.37 (d, J = 7.2 Hz, 3H, -CH(C$\underline{H}_3$)); **^{13}C NMR δ_C ($CDCl_3$, 75 MHz) =** 18.8 (1C, CH*C*H_3), 21.7 (1C, C*C*H_3), 28.4 (3C, C(*C*H_3)$_3$), 49.4 (1C, O(C=O)*C*HNH), 64.5 (1C, Boc-O*C*H_2), 68.9 (2C, O*C*H_2), 69.4 (1C, O*C*H_2), 70.7 (4C, O*C*H_2), 80.3 (1C, *C*(CH_3)$_3$), 128.2 (2C, CH*C*CH), 130.0 (2C, *C*HC*C*H), 145.0 (1C, *C*CH_3), 155.4 (1C, CH*C*S), 173.6 (1C, CH(*C*=O)NH), 176.7 (1C, CH(*C*=O)O); **FT-IR υ (cm^{-1}, ATR) =** 2924 (C-H), 1745 (C=O ester), 1712 (C=O amide), 1597 (N-H), 1452 (C-H), 1352 (S=O), 1173 (S=O), 1120 (C-O) **MS (ESI) m/z [M+Na]$^+$** ($C_{23}H_{37}NO_{10}SNa$) calcd 542.2; found 542.2.

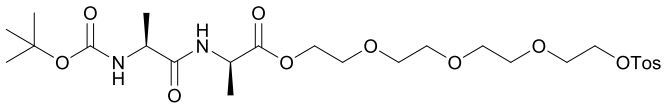

Compound **2** (5.9 g, 11.4 mmol) was dissolved in 60 mL HCl saturated ethyl acetate and stirred for 2 h at room temperature. The solvent was evaporated under vacuum and the excess HCl was removed by adding 30 mL CH_2Cl_2 and 1 mL *n*-BuOH followed by evaporation. The residual *n*-BuOH was removed via azeotropic distillation with 3x 30 mL CH_2Cl_2. The resulting HCl salt of **2**, *N*-Boc-(*D*)-alanine (2.1 g, 11.4 mmol) and *N*-hydroxybenzotriazole monohydrate (1.7 g, 11.4 mmol) were dissolved in 40 mL freshly distilled CH_2Cl_2. DIPEA (2.0 mL, 11.4 mmol) was added dropwise and the mixture was stirred at room temperature until everything was dissolved. The solution was cooled to 0 °C and DCC (2.4 g, 11.4 mmol) was added portion wise. A white precipitate was formed and the mixture was stirred for 1 h at 0 °C followed by 3 h of stirring at room temperature. The precipitate which was identified as a mixture of DCU and starting compounds was filtered off, and subsequently washed with ethyl acetate (3 x 30 mL) to remove any possible product that was adsorbed to its surface. The filtrate and ethyl acetate washings were evaporated under vacuum. The crude product was purified using column chromatography (SiO_2, 0.060 - 0.200 mm; 2 % MeOH/CH_2Cl_2 as eluent) to yield **3** as a pale yellow oil (3.4 g, 5.7 mmol, 52 %);

R_f = 0.3 (10 % MeOH/CH_2Cl_2); **^{1}H NMR δ_H ($CDCl_3$, 300 MHz)** 7.80 (d, J = 8.4, 2H, -C<u>H</u>$_{Ar}$- C-S), 7.36 (d, J = 8.1, 2H, -C<u>H</u>$_{Ar}$-), 6.91 (s, 1H, -N<u>H</u>), 5.00 (s, 1H, -N<u>H</u>), 4.58 (m, 1H, -NHC<u>H</u>(CH_3)-), 4.28 (m, 2H, -COOC<u>H</u>$_2$-), 4.14 (m, 2H, O-C<u>H</u>$_2$-CH_2-), 3.61 (m, 12H, -C(O)OCH_2C<u>H</u>$_2$O(C<u>H</u>$_2$CH_2O)$_3$-), 2.45 (s, 3H, -C<u>H</u>$_3$), 1.45 (s, 9H, -OC(C<u>H</u>$_3$)$_3$), 1.40 (d, J = 7.2, 3H, -CH(C<u>H</u>$_3$)-), 1.35 (d, J = 7.2, 3H, -CH(C<u>H</u>$_3$)-); **^{13}C NMR δ_C ($CDCl_3$, 75 MHz)** 18.2 (2C, CH*C*H_3), 21.7 (1C, *C*CH_3), 28.4 (3C, C(*C*H_3)$_3$), 47.2 (1C, NCH), 50.0 (1C, NCH), 64.5 (1C, Boc-O*C*H_2), 68.7 (2C, O*C*H_2), 69.3 (1C, O*C*H_2), 70.6 (4C, O*C*H_2), 80.2 (1C, *C*(CH$_3$)$_3$), 128.0 (2C, *C*HC*C*H), 129.9 (2C, *C*HC*C*H), 133.1 (1C *C*CH_3), 144.9 (1C, CHCS), 172.7 (2C, C=O); **FT-IR υ (cm^{-1}, ATR)** 2876 (C-H), 1740 (C=O ester), 1718 (C=O amide), 1667 (N-H), 1522 (N-H), 1452 (C-H), 1365 (S=O), 1161 (S=O), 1105 (C-O); **MS (ESI) m/z $[M+Na]^+$** ($C_{26}H_{42}N_2O_{11}SNa$) calcd 613.2; found 613.1.

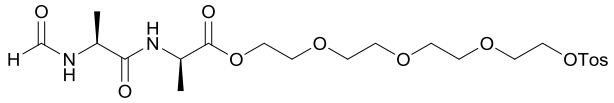

Compound **3** (1.7 g, 2.9 mmol) was deprotected following the same procedure as described for compound **2** and used without further purification. The crude product was dissolved in 25 mL ethyl formate. Sodium formate (1.0 g, 14.3 mmol) was added and the mixture was refluxed for 8 hours at 66 °C. The mixture was cooled to room temperature and the excess sodium formate filtered-off. The filtrate was concentrated under reduced pressure. The crude product was purified using column chromatography (SiO_2, 0.060 - 0.200 mm; 4 % MeOH/CH_2Cl_2 as eluent) to yield **4** as a light yellow oil (0.8 g, 1.5 mmol, 54 %)
R_f = 0.3 (10 % MeOH/CH_2Cl_2); **^{1}H NMR δ_H ($CDCl_3$, 300 MHz)** 8.18 (s, 1H, <u>H</u>C(O)NH-), 7.79 (d, J = 8.3, 2H, -C<u>H</u>$_{Ar}$- C-S), 7.35 (d, J = 8.4, 2H, -C<u>H</u>$_{Ar}$-), 6.78 (s, 1H, -N<u>H</u>-), 6.55 (s, 1H, -N<u>H</u>-), 4.55 (m, 2H, -NHC<u>H</u>(CH$_3$)), 4.30 (m, 2H,- COOC<u>H</u>$_2$-), 4.13 (m, 2H, O-C<u>H</u>$_2$-CH_2), 3.61 (m, 12H, (C<u>H</u>$_2$C<u>H</u>$_2$O)$_3$), 2.44 (s, 3H, -C<u>H</u>$_3$), 1.42 (m, 6H, -CH(C<u>H</u>$_3$)); **^{13}C NMR δ_C ($CDCl_3$, 75 MHz)** 17.9 (1C, CH*C*H_3), 18.2 (1C, CH*C*H_3), 21.7 (1C, C*C*H_3), 47.2 (1C, O(C=O)HN*C*H), 48.1 (1C, HNHC(C=O)), 64.5 (1C, O*C*H_2), 68.7 (2C, O*C*H_2), 69.3 (1C, O*C*H_2), 70.6 (4C, O*C*H_2), 128.0 (2C, *C*HC*C*H), 129.9 (2C, *C*HC*C*H), 133.1 (1C, *C*CH_3), 144.9 (1C, CH*C*CH), 161.0 (1C, H(*C*=O)NH)), 172.6 (1C, CH(*C*=O)NH), 173.2 (1C, CH(*C*=O)O); **FT-IR υ (cm^{-1}, ATR)** 2873 (C-H), 1738 (C=O), 1653 (N-H), 1532 (N-H), 1452 (C-H), 1352 (S=O), 1174 (S=O), 1097 (C-O); **MS (ESI) m/z $[M+Na]^+$** ($C_{22}H_{34}N_2O_{10}SNa$) calcd 541.2; found 541.2.

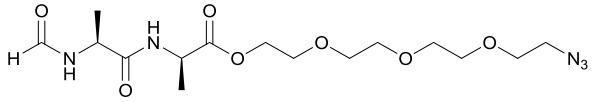

Compound **4** (0.6 g, 1.1 mmol) was dissolved in 40 mL absolute EtOH. Sodium azide (0.4 g, 5.9 mmol) was added and the mixture was refluxed overnight. Once cooled to room temperature, the solids were removed by filtration and the filtrate was dried under vacuum. The crude product was purified using column chromatography (SiO_2, 0.060 - 0.200 mm; 4% MeOH/CH_2Cl_2 as eluent) to yield **5** as a pale orange oil (0.3 g, 0.8 mmol, 78%)
R_f = 0.4 (10% MeOH/CH_2Cl_2); **^{1}H NMR δ_H ($CDCl_3$, 300 MHz)** 8.20 (s, 1H, <u>H</u>C(O)NH-), 6.84 (s, 1H, -N<u>H</u>), 6.60 (s, 1H, -N<u>H</u>), 4.60 (m, 2H, NHC<u>H</u>(CH$_3$)), 4.26 (m, 2H, -C(O)OC<u>H</u>$_2$-), 3.68 (m, 12H, -(C<u>H</u>$_2$C<u>H</u>$_2$O)$_3$-), 3.40 (m, 2H, N$_3$C<u>H</u>$_2$-), 1.42 (m, 6H, -

CH(C<u>H</u>$_3$)-); **^{13}C NMR δ_C (CDCl$_3$, 75 MHz)** 17.9 (1C, CH_3), 18.2 (1C, CH_3), 47.4 (1C, *C*H_2N_3), 48.4 (1C, H(C=O)HN*C*H), 50.7 (1C, HN*C*(CH_3)C=O), 69.0 (1C, CH_2*C*H_2O), 70.1 (1C, O*C*H_2CH_2), 70.6 (2C, O*C*H_2), 70.7 (2C, O*C*H_2), 161.4 (1C, H(*C*=O)NH), 172.7 (1C, CH(*C*=O)NH), 172.9 (1C, CH(*C*=O)O); **FT-IR υ (cm^{-1}, ATR)** 3309 (N-H), 2875 (C-H), 2105 (N_3), 1737 (C=O), 1651 (N-H), 1529 (N-H), 1453 (C-H), 1133 (C-O); **MS (ESI) m/z [M+Na]$^+$** ($C_{15}H_{27}N_5O_7Na$) calcd 412.2; found 412.2.

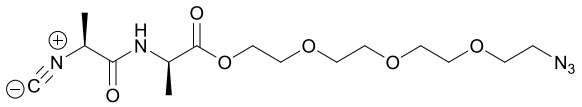

Compound **5** (221.0 mg, 0.6 mmol) and *N*-methylmorpholine (NMM) (0.2 mL, 2.3 mmol) were dissolved in 150 mL freshly distilled CH_2Cl_2 and cooled down to -40 °C (dry acetone bath) under an argon atmosphere. A solution of diphosgene (0.1 mL, 0.4 mmol) in 10 mL freshly distilled CH_2Cl_2 was added dropwise over 1 h while maintaining the argon atmosphere. While adding diphosgene, the mixture was stirred and kept strictly at -40 °C. Once the mixture began to turn yellow, the reaction was rapidly quenched with an excess of sodium bicarbonate (5.0 g). The quenched mixture was stirred for 5 minutes at -40 °C. The reaction mixture was passed over a short silica column (SiO_2, 0.060 - 0.200 mm). The column was packed using CH_2Cl_2 as eluent, but the desired compound was eluted with CH_2Cl_2/acetonitrile (3:1) to yield **M1** as a pale yellow oil (48.1 mg, 0.5 mmol, 27%); **R_f** = 0.5 (10% MeOH/CH_2Cl_2); **^{1}H NMR δ_H (CDCl$_3$, 300 MHz)** 7.00 (bd, 1H, -N<u>*H*</u>-), 4.59 (m, 1H, -NHC<u>*H*</u>(CH_3)C(O)O-), 4.32 (m, 3H, (-C(O)OC<u>*H*</u>$_2$CH$_2$O-), -C≡NC<u>*H*</u>(CH_3)C(O)NH-), 3.67 (m, 12H, -(OC<u>*H*</u>$_2$C<u>*H*</u>$_2$)$_3$), 3.39 (m, 2H, N_3C<u>H</u>$_2$-), 1.65 (d, J = 7.2, 3H, C≡NCH(C<u>*H*</u>$_3$)C(O)-), 1.48 (d, J = 7.2, 3H, C≡NCH(C<u>*H*</u>$_3$)C(O)-); **^{13}C NMR δ_C (CDCl$_3$, 75 MHz)** 170.69 (1C, CH(CH_3)*C*(O)OCH_2), 165.72 (1C, CH(CH_3)*C*(O)NH), 70.69, 70.65, 70.61, 70.56, 70.02, 68.81 (1 C, *C*H_2*C*H_2O), 50.66 (1C, *C*H_2N_3), 48.56 (C≡N*C*H), 19.66, 18.04 (1C, CH(*C*H_3)CO); **FT-IR υ (cm^{-1}, ATR)** 3318 (N-H), 2875 (C-H), 2142 (C≡N), 2105 (N_3), 1744 (C=O), 1540 (N-H), 1453 (C-H), 1123 (C-O); **MS (ESI) m/z [M+Na]$^+$** ($C_{15}H_{25}N_5O_6Na$), calcd 394.17; found 394.1.

2.2) Preparation of the comonomer M2

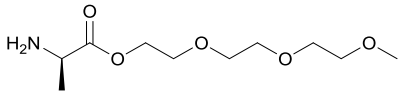

Triethylene glycol monomethyl ether (25.0 mL, 156.2 mmol), *L*-alanine (13.9 g, 156.2 mmol), *p*-toluene sulfonic acid (32.7 g, 171.8 mmol) and 250 mL toluene were added in a round bottom flask. The reaction mixture was refluxed at 126 °C for 4 h in a Dean-Stark setup and 3 mL water was collected. The excess *p*-toluene sulfonic acid was filtered off, and the filtrate was evaporated under reduced pressure. The crude product was dissolved in 300 mL chloroform, and the organic layer was extracted three times with a saturated aqueous solution of $NaHCO_3$. Thereafter, the basic water layer was extracted twice more with chloroform. The organic layers were combined, dried with Na_2SO_4, and the solvent was evaporated under reduced pressure, obtaining 22.7 g of **6** in a 62% yield. No further purification was performed.

^{1}H NMR ($CDCl_3$, 300 MHz): 4.29-4.26 (t, J=4.8 Hz, 1H, -C<u>H</u>(CH_3)-); 3.71-3.52 (m, 12H, (-OC<u>H</u>$_2$C<u>H</u>$_2$-)$_3$); 3.37 (s, 3H, -C<u>H</u>$_3$); 1.35-1.32 (d, J=7 Hz, 2H, -N<u>H</u>$_2$).

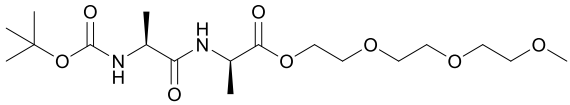

Boc-*D*-Ala-OH (18.3 g, 96.4 mmol), DCC (21.9 g, 106.1 mmol) and 100 mL DCM were combined in a separate container to form a white paste. The DMAP (0.1 g, 0.8 mmol), DIPEA (1.7 mL, 9.6 mmol), HOBt (14.8 g, 96.4 mmol), **6** (22.7 g, 96.4 mmol) and 150 mL CH_2Cl_2 were mixed together. The mixture was stirred at room temperature to ensure the HOBt was completely dissolved before being cooled in an ice bath to 0 ^oC. The pH of the cooled mixture was checked to be above 8.0. Once confirmed pH and temperature were reached the white slurry of DCC-Boc-Ala-OH was added and the reaction was stirred for 16 hours. The excess starting material and dicyclohexylurea side product was filtered off. The filtrate was diluted with 200 mL chloroform, and the mixture was extracted three times with a saturated aqueous citric acid solution. These acidic water washings in turn were combined and extracted with chloroform (1 x 200 mL). The now slightly acidic filtrate was washed twice with a saturated aqueous $NaHCO_3$ solution. The alkaline water washings were combined and extracted twice more with chloroform. All the organic layers were combined, dried over Na_2SO_4, and concentrated under reduced pressure. At this point the resulting crude product oil was covered with a 2 cm layer of ethyl acetate and placed in the fridge for a few hours to remove any residual starting compounds and dicyclohexylurea, which crystallized out. Once the side product was filtered off the filtrate was concentrated and the crude product purified with column chromatography (2% MeOH in CH_2Cl_2), obtaining 20.4 g of **7** in a 52% yield.

R_f = 0.53 (10% MeOH/CH_2Cl_2)) **^{1}H NMR ($CDCl_3$, 400 MHz)**: δ = 6.77 (s, 1H, -N<u>H</u>CH-); 5.09 (s, 1H, - N<u>H</u>CH) -; 4.60 (quin, *J* = 7.4, 1H, -NHC<u>H</u>(CH_3)-); 4.31-4.28 (m, 3H, -C(O)OC<u>H</u>$_2$CH$_2$O-, -C<u>H</u>(CH_3)COO-); 3.70-3.56 (m, 10H, -C(O)OCH$_2$C<u>H</u>$_2$O(C<u>H</u>$_2$C<u>H</u>$_2$O)$_2$-); 3.38 (s, 1H, -OC<u>H</u>$_3$); 1.46 (s, 9H, -OC(C<u>H</u>$_3$)$_3$); 1.41 (d, *J* = 7.2, 3H, -NHCH(C<u>H</u>$_3$)-; 1.38 (d, J = 7.2, 3H, -NHCH(C<u>H</u>$_3$)-); **^{13}C NMR ($CDCl_3$, 75 MHz)**: δ =172.9 (CH(CH_3)*C*OO); 172.3 (CH(CH_3)*C*ONH); 156.0 (NH*C*OO); 79.9 (O*C*(CH_3)$_3$) ; 71.9; 70.6; 70.5; 70.3; 68.9; 64.5 (COO*C*H$_2$CH$_2$); 59.2 (O*C*H$_3$);49.7; 48.2 (*C*H(CH_3)); 28.0 (OC(*C*H$_3$)$_3$); 18.0 (CH(*C*H$_3$)CONH; CH(*C*H$_3$)COO)

To obtain the HCl salt, compound **7** (13.2 g, 32.4 mmol) was dissolved in 20 mL of ethyl acetate and treated with 20 mL 4 M HCl in dioxane. The mixture was stirred for 1 hour at room temperature. After checking via TLC with starting compound another 20 mL 4 M HCl in dioxane was added and the solution was stirred further for 1 hour at room temperature. The residual *t*-BuOH was removed by addition of 20 mL of CH_2Cl_2 and azeotropic distillation under reduced pressure. Another 60 mL CH_2Cl_2 was added in 20 mL aliquots and removed under reduced pressure.

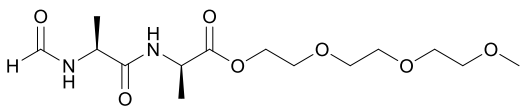

The HCl salt of **7** (13.2 g, 32.3 mmol) and sodium formate (8.8 g, 129.3 mmol) were dissolved in 250 mL ethyl formate. The reaction mixture was boiled for 14 h at 66 °C. A precipitate was filtered off, and the filtrate was concentrated by removing excess solvent under reduced pressure. Column chromatography (4% MeOH in CH_2Cl_2) was used to purify the crude product, obtaining 6.0 g of oil of **8** in a 56% yield.
R_f = 0.54 (10% MeOH/CH_2Cl_2) **^{1}H NMR (CDCl$_3$, 400 MHz)**: δ = 8.23 (s, 1H, HC(O)NH-); 6.94 (br.d, *J* = 7.8, 1H, -NHCH-); 6.79 (br.d, *J* = 8.1, 1H, -NHCH-; 4.57 (m, 2 H, NHCH(CH$_3$)-, -NHCH(CH$_3$)-); 4.26 (m, 2H, -C(O)OCH$_2$-); 3.67-3.54 (m, 10H, -C(O)OCH$_2$CH$_2$O(CH$_2$CH$_2$O)$_3$-); 3.43 (s, 3H, -OCH$_3$); 1.45 (m, 6H, -NHCH(CH$_3$)-, -NHCH(CH$_3$); **^{13}C NMR (CDCl$_3$, 75 MHz)**: δ = 172.4 (CH(CH$_3$)*C*OO); 171.4 (CH(CH$_3$)*C*ONH); 161.3;160.6 (NH*C*HO); 71.8; 70.5; 70.5; 70.1; 68.8; 64.5 (COO*C*H$_2$CH$_2$); 59.0 (O*C*H$_3$); 48.2; 46.8 (*C*H(CH$_3$); 18.4 (CH(*C*H$_3$)CONH); 17.6 (CH(*C*H$_3$)COO)

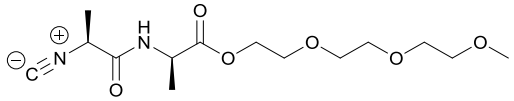

Compound **8** (6.0 g, 18.1 mmol) was degassed for 1 hour with N_2. Then NMM (5 mL, 45.2 mmol) was dissolved with freshly distilled CH_2Cl_2 (50 mL), and added to the solution. The reaction mixture was cooled to -40 °C (dry ice/ isopropanol). A solution of diphosgene (1.5 mL, 12.6 mmol) in CH_2Cl_2 (50 mL) was added drop wise over 2 h. The reaction mixture was stirred until it turned to a yellow-orange colour, and quenched with $NaHCO_3$ (3.0 g). The product was purified by column chromatography. The column was packed with DCM (0.3% triethylamine) and the product was eluted with (1:2 ACN/CH_2Cl_2), obtaining 3.3 g of **M2** in a 51% yield. Optical rotation -0.34
R_f = 0.50 (10% MeOH/CH_2Cl_2) **^{1}H NMR (CDCl$_3$, 400 MHz)**: δ = 7.00 (br.d, *J* = 7.0, 1H, -NH-); 4.58 (m, 1H, C≡NCH(CH$_3$)C(O)NH-); 4.28 (m, 2H, -C(O)OCH$_2$CH$_2$O-); 4.26 (m, 1H, -NHCH(CH$_3$)C(O)O-); 3.74-3.53 (m, 10H, -OCH$_2$CH$_2$(OCH$_2$CH$_2$)$_3$OCH$_3$); 3.41 (s, 3H, -OCH$_3$); 1.67 (d, *J* = 7.0, 3H, C≡NCH(CH$_3$)C(O)-); 1.49 (d, *J* = 7.0, 3H, -NHCH(CH$_3$)C(O)O-); **^{13}C NMR (CDCl$_3$, 75 MHz):** δ = 171.94 (CH(CH$_3$)*C*OO); 165.71 (CH(CH$_3$)*C*ONH); 161.25 (N*C*); 71.88; 70.51; 70.51; 68.77; 64.66 (COO*C*H$_2$CH$_2$); 58.98 (O*C*H$_3$); 53.26; 48.53 (*C*H(CH$_3$)); 19.62 (CH(*C*H$_3$)CONH); 18.00 (CH(*C*H$_3$)CONH) **MS (ESI):** m/z ([M+Na]$^+$: $C_{14}H_{24}N_2O_6Na$), calcd 339.15; found 339.2

2.3) Preparation of the comonomer M3

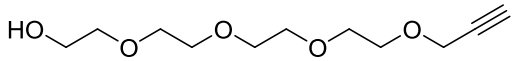

NaH (2.8 g, 46.7 mmol, 60% mineral oil) was added to a solution of **8** (12.0 mL, 69.5 mmol) in dry THF (250 mL). A solution of **9** (5.0 mL, 56.1 mmol) in dry THF was added dropwise and the reaction mixture was stirred for 17 h. The side product was filtered off and the residue was washed with water (1 × 15 mL), brine (3 × 15 mL) and dried with Na_2SO_4. After the solvent was removed, the crude product was purified by column chromatography using ethyl acetate as eluent. The product **10** was obtained as a yellow oil (8.5 g, 73%).
R_f = 0.2 (EtOAc) **^{1}H NMR (CDCl$_3$, 300 MHz)**: δ = 4.18 (d, *J* = 2.3 Hz 2H, -OCH$_2$C≡CH); 3.65-3.42 (m, 16H,C(O)OCH$_2$CH$_2$O(CH$_2$CH$_2$O)$_3$-); 2.84 (br.s, 1H, HO-CH$_2$-); 2.42 (t, *J* =

2.4 Hz 1H, -$OCH_2C{\equiv}C\underline{H}$) **^{13}C NMR ($CDCl_3$, 75 MHz)**: δ = 80.8 (*C*≡CH); 75.9 (C≡*C*H); 73.6; 71.6; 71.7; 71.7; 71.7; 70.2 (*C*H_2); 62.7(HO*C*H_2); 59.6 (*C*H_2C≡CH); **FT-IR (cm^{-1}, ATR)**: 3429 (O-H); 3251 (C≡C); 1455 (C-H); 1349; 1089(C-O) **MS (ESI):** m/z ([M+H]$^+$: $C_{11}H_{20}O_5$), calcd 232.13; found 233.13

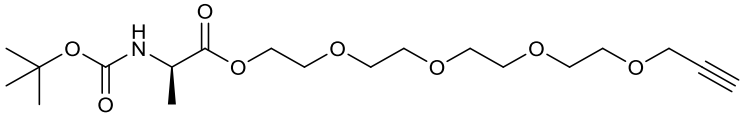

DMAP (0.5 g, 4.1 mmol), Boc-*L*-Ala-OH (8.5 g, 44.9 mmol) and DCC (9.3 g, 44.9 mmol) were added to a cooled solution (0 °C, ice bath) of **3** (9.5 g, 40.9 mmol) in CH_2Cl_2 (300 mL). The reaction mixture was stirred at 0 °C for 4 h and subsequently at room temperature for 12 h. A white solid was filtered off and the residue (colourless) was washed with water (3 × 100 mL) and the water layer was extracted with DCM (1 × 100 mL). The combined organic layers were dried with Na_2SO_4 and concentrated. The excess starting product and DCU was filtered off and the filtrate was concentrate under reduced pressure. The crude product was purified using column chromatography using a 1% MeOH in CH_2Cl_2 as eluent. The product **11** was obtained as a yellow oil (13.4 g, 82%).
R_f = 0.3 (5% MeOH/CH_2Cl_2) **^{1}H NMR ($CDCl_3$, 300 MHz)**: δ = 5.08 (bd, *J* = 7.4 Hz, 1H, -N$\underline{H}$CH-); 4.29-4.25 (m, 3H, -NHC$\underline{H}$-, -C(O)OC$\underline{H}_2$CH_2O-); 4.18 (d, *J* = 2.3 Hz, 2H, -OC$\underline{H}_2$C≡CH); 3.70-3.63 (m, 14H, -C(O)OCH_2C$\underline{H}_2$O(C$\underline{H}_2$CH_2O)$_3$-); 2.42 (t, *J* = 2.4 Hz, 1H -$OCH_2C{\equiv}C\underline{H}$); 1.42 (s, 9H, -OC(C$\underline{H}_3$)$_3$); 1.39 (d, *J* = 7.3 Hz, 3H, -NHCH(C$\underline{H}_3$)-)) **^{13}C NMR ($CDCl_3$, 75 MHz)**: δ = 173.5 (CH(CH_3)*C*OO); 74.6 (C≡*C*H); 70.8; 70.6; 69.2; 69.1; 64.5 (*C*H_2); 58.6 (*C*H_2C≡CH); 49.5(*C*H(CH_3); 28.5 (OC(*C*H_3)$_3$); 18.8 (CH(*C*H_3)NH); **FT-IR (cm^{-1}, ATR)**: 2869 (C-N), 1710 (C=O), 1164, 1100 (C-O), 609 **MS (ESI):** m/z ([M+Na]$^+$: $C_{19}H_{33}NO_8Na$), calcd 426.22; found 426.21

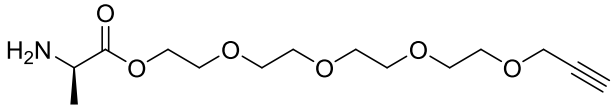

Compound **11** (13.4 g, 33.3 mmol) was dissolved in 20 mL DCM and to this 20 mL 4 M HCl/dioxane was added. The mixture was stirred for 1 h. The progress of the deprotection was followed by thin layer chromatography and staining with ninhydrine solution. Upon completion of the deprotection, 1 mL of *n*-BuOH and 20 mL of CH_2Cl_2 was added to the crude product. The excess solvent was evaporated under reduced pressure. Subsequently 60 mL CH_2Cl_2 was added in 20 mL aliquots and evaporated under reduced pressure to obtain compound **12** (quant. yield) as a yellow oil.
R_f = 0.1 (0.1% Et_3N 5% MeOH/CH_2Cl_2) **^{1}H NMR ($CDCl_3$, 300 MHz)**: δ = 4.30-4.22 (m, 1H, -NHC$\underline{H}$(CH_3)-); 4.20 (d, *J* = 2.4 Hz, 2H, -OC$\underline{H}_2$C≡CH); 3.70-3.60 (m, 14H, -C(O)OCH_2C$\underline{H}_2$O(C$\underline{H}_2$CH_2O)$_3$-); 2.47 (t, *J* = 2.4 Hz, 1H, -$OCH_2C{\equiv}C\underline{H}$) **^{13}C NMR ($CDCl_3$, 75 MHz):** δ=169.37 (CH(CH_3)*C*OO); 79.08(*C*≡CH); 74.32(C≡*C*H); 74.03; 70.09; 69.96; 69.91; 69.7; 68.52; 57.89; 48.78 (*C*H_2); 27.81 (*C*H_2O); 15.58(CH(*C*H_3)CONH); **FT-IR (cm^{-1}, ATR)**: 2873 (C-N); 1745 (C=O); 1246; 1207; 1098; 1030 (C-N); 909; 728 **MS (ESI):** m/z ([M+Na]$^+$: $C_{14}H_{25}NO_6Na$), calcd 326.34; found 326.3

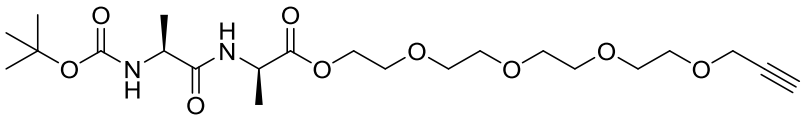

DMAP (0.4 g, 3.3 mmol), Boc-*D*-Ala-OH (6.9 g, 36.6 mmol), DIPEA (66.2 mL, 389.0 mmol) and DCC (7.6 g, 36.7 mmol) were added to a cooled solution (0 °C, ice bath) of the HCl salt of **12** (10.1 g, 33.3 mmol) in CH_2Cl_2 (250 mL). The reaction mixture was stirred at 0 °C for 3 h and subsequently at room temperature for 14 h. A white solid was filtered off and the residue (colourless) was washed with a saturated aqueous citric acid solution (3 × 75 mL). The water layer was backwashed with chloroform (1 × 100 mL). A white side product was filtered and washed with ethyl acetate, the filtrate and ethyl acetate washings were concentrated under reduced pressure. Two consecutive columns were performed, first the crude product was eluted with 2% MeOH in CH_2Cl_2 similar R_f fractions combined and concentrated under reduced pressure. The second column was eluted with ethyl acetate to yield compound **6** (9.4 g, 60%) as a yellow oil.
R_f = 0.2 (2% MeOH/CH_2Cl_2) **^{1}H NMR (CDCl$_3$, 300 MHz)**: δ = 7.25 (s, 1H, NHCH); 5.1 (br.s., 1H, NHCH); 4.58 (q, *J* = 7.5 Hz 1H, NHC<u>H</u>(CH_3)); 4.27 (m, 3H, C(O)OC<u>H</u>$_2$$CH_2$O); 4.19 (d, *J* = 2.4 Hz, 2H, OC<u>H</u>$_2$C≡CH); 3.72-3.65 (m, 14H, C(O)OCH$_2$C<u>H</u>$_2$O(C<u>H</u>$_2$C<u>H</u>$_2$O)$_3$); 2.42 (t, *J* = 2.4 Hz, 1H, C≡C<u>H</u>); 1.44 (s, *J* = 7.2 Hz 9H, OC(C<u>H</u>$_3$)$_3$); 1.40 (d, 3H, NHCH(C<u>H</u>$_3$); 1.34 (d, 3H, NHCH(C<u>H</u>$_3$)) **^{13}C NMR (CDCl$_3$, 75 MHz)**: δ = 172.2 (CH(CH_3)*C*OO); 171.8 (CH(CH_3)*C*OO); 155.0 (NH*C*OO); 74.1; 70.1; 68.6; 68.4; 63.9; 57.9; 49.5; 47.6 (*C*H$_2$); 27.8 (OC(*C*H$_3$)$_3$); 17.7 (CH(*C*H$_3$)NH) **MS (ESI):** m/z ([M+Na]$^+$: $C_{22}H_{38}N_2O_9Na$), calcd 497.25; found 497.24

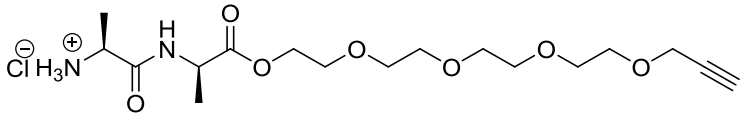

A solution of **13** (9.4 g, 19.9 mmol) in 20 mL DCM was treated with 30 mL 4M HCl in dioxane. The mixture was stirred for 1 h. The mixture was concentrated by removing excess solvent under reduced pressure. The oil was diluted with 20 mL DCM and any residual t-BuOH removed via azeotropic distillation, this procedure was repeated three times. Once dry, a yellow oil **14** was obtained with quantitative yield.
R_f = 0.06 (5% MeOH/CH_2Cl_2) **^{1}H NMR (CDCl$_3$, 300 MHz)**: δ = 4.50-4.30 (m, 4H, -NHC<u>H</u>(CH_3), -NHC<u>H</u>(CH_3), -C(O)OC<u>H</u>$_2$CH$_2$O-); 4.25 (d, *J* = 2.4 Hz, 2H, -OC<u>H</u>$_2$C≡CH); 3.79-3.61 (m, 14H, -C(O)OCH$_2$C<u>H</u>$_2$O(C<u>H</u>$_2$CH$_2$O)$_3$); 2.46 (t, *J* = 2.4 Hz, 1H, -OCH$_2$C≡C<u>H</u>); 1.54 **FT-IR (cm^{-1}, ATR)**: 3235 (C-H$_{alkyne}$) ; 2880; 2245; 1736 (C=O); 1681 (C=O); 1099 (C-O); 910; 730 **MS (ESI):** m/z ([M+Na]$^+$: $C_{17}H_{30}N_2O_7Na$), calcd 397.42; found 397.5

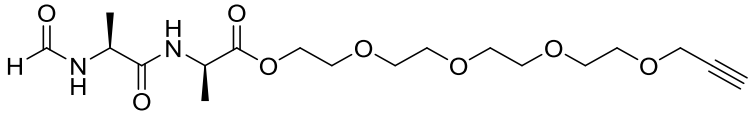

To a solution of 5g (13.5 mmol) of product **7** in ethyl formate (25 mL) was added sodium formate (3.7 g, 53.8 mmol). The reaction mixture was refluxed for 18 h at 70 °C. The excess sodium formate was filtered off and the filtrate was evaporated under reduced pressure. The crude product was purified with column chromatography using 5% methanol

in ACN/CH_2Cl_2 as eluent. From the column a red-brown oil was obtained and to remove the colour, the oil was filtered over basic alumina. The oil was concentrated on top of a 10 cm alumina plug in a glass filter and carefully washed with ethyl acetate. The ethyl acetate was removed under reduced pressure. An amount of 2.3 g of pure **15** (slightly yellow-colourless oil) was obtained with a yield of 42%.
R_f = 0.2 (5% MeOH in ACN/CH_2Cl_2 (1:2, v/v)) **^{1}H NMR ($CDCl_3$, 300 MHz)**: δ = 8.18 (s, 1H, HC(O)NH-); 6.86 (bd, 1H, -NHCH-); 6.66 (bd, 1H, -NHCH-; 4.58 (m, 2 H, -NHCH(CH_3), -NHCH(CH_3)); 4.25 (m, 2H, -C(O)OCH_2-); 4.18 (d, 2H, -OCH_2C≡CH); 3.72-3.59 (m, 14H, -C(O)O$CH_2CH_2O(CH_2CH_2O)_3$-); 2.42 (t, 1H, -OCH_2C≡CH); 1.39 (t, 6H, -NHCH(CH_3), -NHCH(CH_3)) **^{13}C NMR ($CDCl_3$, 75 MHz)**: δ = 172.0 (*C*(O)OCH_2); 171.0 (*C*(O)NH); 160.9 (*C*(O)H); 74.2; 70.0; 69.8; 68.6; 68.5 63.9; 57.9 (*C*H_2); 47.9 (*C*H(CH_3)); 46.7 (*C*H(CH_3)); 17.4 (CH(*C*H_3)); **FT-IR (cm^{-1}, ATR)**: 3282 (C-H_{alkyne}); 2872 (C-$H_{formamide}$); 1738 (C=O); 1654 (C=O); 1100 (C-O) **MS (ESI):** m/z ($[M+Na]^+$: $C_{18}H_{30}N_2O_8Na$), calcd 425.19; found 425.2

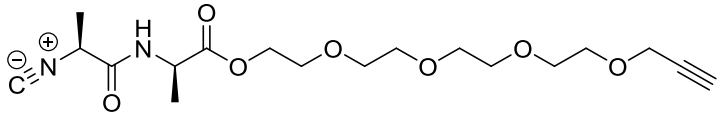

To a solution of **15** (2.3 g, 5.7 mmol) in freshly distilled CH_2Cl_2 (40 mL), NMM (1.6 mL, 14.2 mmol) was added. The reaction mixture was cooled to -80 °C (dry ice/acetone). A solution of diphosgene (0.5 mL, 3.7 mmol) in CH_2Cl_2 (30 mL) was added dropwise very slowly to the cooled alkaline mixture of **15**. The reaction mixture was stirred for 60 min, quenched with an excess of solid $NaHCO_3$ and poured directly on a silica plug (0.3% Et_3N in DCM). The plug was eluted with 0.3% Et_3N in 1:2 ACN/$CHCl_3$. The product **M3** was obtained (1.1 g, 3.1 mmol, 55%) as a yellow oil.
R_f = 0.5 (10% MeOH/DCM)) **^{1}H NMR ($CDCl_3$, 300 MHz)**: δ = 7.00 (bd, 1H, -NH-); 4.58 (m, 1H, -NHCH(CH_3)C(O)O); 4.32 (m, 2H, -C(O)OCH_2CH_2O); 4.25 (m, 1H, C≡NCH(CH_3)); 4.19 (d, 2H, -OCH_2C≡CH); 3.72-3.61 (m, 14H, -O$CH_2CH_2(OCH_2CH_2)_3OCH_2$C≡CH); 2.42 (t, 1H, -C≡CH); 1.65 (d, 3H, C≡NCH(CH_3)C(O)-); 1.49 (d, 3H, -NHCH(CH_3)C(O)O-) **^{13}C NMR ($CDCl_3$, 75 MHz)**: δ = 171.5 (*C*(O)OCH_2); 165.3 (*C*(O)NH); 160.9 (*C*≡N); 74.6 (-CH_2*C*CH); 73.9 (-CH_2C≡*C*H); 70.4, 70.8, 70.8, 70.8, 69.8, 68.3, 68.0; 64.2; 57.9 (*C*H_2); 48.2 (C≡N*C*H(CH_3)); 48.0 (-NH*C*H(CH_3)); 19.3 (CH(*C*H_3)CONH); 19.0 (CH(*C*H_3)CONH) **FT-IR (cm^{-1}, ATR)**: 3250 (N-H); 2890 (C-H); 2140 (C≡N); 1750 (C=O); 1690 (C=O); 1095 (C-O) **MS (ESI):** m/z ($[M+Na]^+$: $C_{18}H_{39}N_2O_7Na$), calcd 407.18; found 407.2.

2.4) Preparation of the comonomer M4

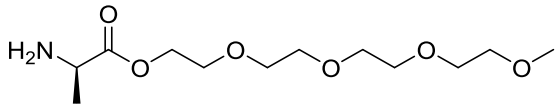

L-Ala-OH (5.0 g, 89.0 mmol), *p*-toluene sulfonic acid (11.9 g, 62.6 mmol), tetraethylene glycol monomethyl ether (**10**) (12 mL, 56.9 mmol) and 200 mL of toluene were added in a round bottom flask. The mixture was refluxed for 4 h using a Dean-Stark trap (~3 mL of

water was collected).The residual *p*-toluene sulfonic acid was filtered off and the filtrate was concentrated under reduced pressure. The concentrated crude product was re-dissolved in 100 mL CH_2Cl_2 and then three extractions with a saturated aqueous solution of $NaHCO_3$ were done. The organic washings were combined and was dried over Na_2SO_4. The product was purified via filtration over alumina with CH_2Cl_2 as eluent to obtain 7.3 g of **17** as a colourless oil in a 46% yield.
^{1}H NMR ($CDCl_3$, 300 MHz): 4.28-4.25 (t, J=4.81 Hz, 1H, -C<u>H</u>(CH_3)-); 3.73-3.53 (m, 16H, (-OC<u>H</u>$_2$C<u>H</u>$_2$-)$_4$); 3.37 (s, 3H, -C<u>H</u>$_3$); 1.35-1.32 (d, J=6.9 Hz, 2H, -N<u>H</u>$_2$) **FT-IR (cm^{-1}, ATR):** 3462 (N-H); 2872 (C-H); 1734 (C=O ester); 1104 (C-O ether).

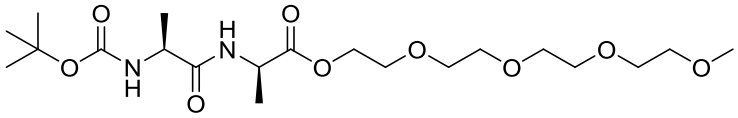

DMAP (0.1 g, 0.8 mmol), Boc-*D*-Ala-OH (4.9 g, 26.1 mmol), DIPEA (0.5 mL, 2.6 mmol), HOBt (4.0 g, 26.1 mmol) and DCC (5.9 g, 28.7 mmol) were added to a cooled solution (0 °C, ice bath) of **17** (7.3 g, 26.1 mmol) in CH_2Cl_2 (250 mL). The reaction mixture was stirred at 0 °C for 3 h and subsequently at room temperature for 15 h. Residual starting compounds and DCU was filtered off. The filtrate was washed with a 10 % aqueous citric acid solution (3 × 50 mL) and the water washings extracted with chloroform (1 × 75 mL). All the organic layers were combined and dried with Na_2SO_4. The dried organic layer was filtered and concentrated under reduced pressure. The crude product was purified with column chromatography using alumina with chloroform as the eluent. The product **18** was yielded (8.0 g, 68%) as a yellow oil.
R_f = 0.5 (10% MeOH/CH_2Cl_2) **^{1}H NMR ($CDCl_3$, 300 MHz)**: δ = 6.80 (s, 1H, -N<u>H</u>CH-); 5.11 (br.s, 1H, - N<u>H</u>CH) -; 4.60 (quin, *J* = 7.2, 1H, -NHC<u>H</u>(CH_3)-); 4.28-4.28 (m, 3H, -C(O)OC<u>H</u>$_2$C<u>H</u>$_2$O-, -C<u>H</u>(CH_3)COO-); 3.73-3.64 (m, 14H, -C(O)OC<u>H</u>$_2$C<u>H</u>$_2$O(C<u>H</u>$_2$C<u>H</u>$_2$O)$_3$-); 3.39 (s, 1H, -OC<u>H</u>$_3$); 1.46 (s, 9H, -OC(C<u>H</u>$_3$)$_3$); 1.43 (d, *J* =7.0, 3H, -NHCH(C<u>H</u>$_3$)-; 1.36 (d, *J* = 7.4, 3H, -NHCH(C<u>H</u>$_3$)-) **FT-IR (cm^{-1}, ATR)**: 3317 (N-H); 2876 (C-H); 1739 (C=O ester); 1671 (N-H); 1517 (N-H); 1452 (C-H); 1163 (C-O)

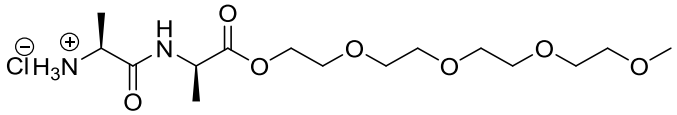

A solution of **18** (8.0 g, 17.7 mmol) in 20 mL ethyl acetate was treated with 20 mL 4 M HCl in dioxane solution. The mixture was stirred for 1 h. TLC still showed the presence of compound **18**, and therefore another 20 mL HCl in dioxane was added and the stirring continued for an additional 1 h. The solvent was evaporated under reduced pressure to obtain **19** (quant. yield) as a yellow oil.
R_f = 0.8 (10% MeOH/CH_2Cl_2)

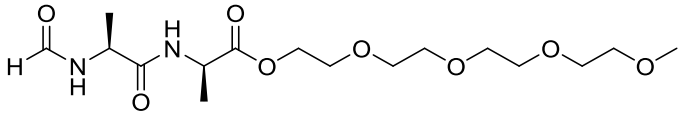

To a solution of **19** (6.2 g 17.7 mmol) in ethyl formate (50 mL) sodium formate (4.8 g, 70.8 mmol) was added. The reaction mixture was refluxed for 14 h at 70 °C. The excess sodium

formate was filtered off and the solvent was evaporated under reduced pressure. The crude product was a red oil. Column chromatography (4% MeOH in CH_2Cl_2,) was used to purify the product yielding **20** as a light yellow oil (2.2 g, 33%).
^{1}H NMR ($CDCl_3$, 300 MHz): δ = 8.21 (s, 1H, HC(O)NH-); 6.96 (bd, J=7.5Hz, 1H, -NHCH-); 6.79 (bd, J=7.5Hz, 1H, -NHCH-; 4.58 (m, 2 H, -NHCH(CH$_3$), -NHCH(CH$_3$)); 4.31 (m, 2H, -C(O)OCH$_2$); 3.67-3.56 (m, 14H, -C(O)OCH$_2$CH$_2$O(CH$_2$CH$_2$O)$_3$); 3.39 (s, 3H, -OCH$_3$); 1.43 (t, 6H, -NHCH(CH$_3$), -NHCH(CH$_3$) **^{13}C NMR ($CDCl_3$, 75 MHz)**: δ =172.42 (*C*(O)NH); 171.42(*C*(O)OCH$_2$); 161.32 (H*C*(O)); 160.55; 71.82; 70.51; 70.11; 68.76; 64.47; 61.65; 59.01 (*C*H$_2$); 48.24 (*C*H(*C*H$_3$)CONH); 46.78 (*C*H(*C*H$_3$)CONH); 18.42 (CH(*C*H$_3$)CONH); 17.63 (CH(*C*H$_3$)CONH) **FT-IR (cm^{-1}, ATR)**: 3297 (N-H); 2875(C-H); 1739 (C=O ester); 1653 (N-H); 1529(N-H), 1452 (C-H), 1101 (C-O)

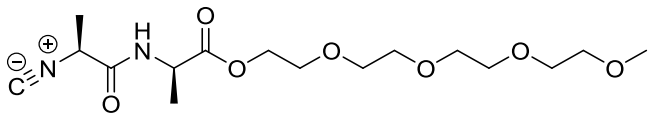

To a solution of **20** (3.2 g, 8.5 mmol) in freshly distilled CH_2Cl_2 (40 mL), NMM (2.3 mL, 21.2 mmol) was added. The reaction mixture was cooled to -78 °C (dry ice/acetone). A solution of diphosgene (0.7 mL, 5.9 mmol) in CH_2Cl_2 (30 mL) was added dropwise over the course of 2 h to the cooled alkaline solution of **20**. The reaction mixture was quenched with solid $NaHCO_3$ (3 g) and poured directly on a silica plug (0.3% Et_3N in DCM). The compound was eluted with 1:2 ACN/CH_2Cl_2 to obtain 1.3 g of **M4** (3.6 mmol, 43%) as a colourless oil.
R_f = 0.4 (10% MeOH/DCM)) **^{1}H NMR ($CDCl_3$, 300 MHz)**: δ = 6.99 (bd, 1H, -NH-); 4.58 (quin, *J* = 7.2, 1H, -NHCH(CH$_3$)); 4.32 (m, 2H, -C(O)OCH$_2$CH$_2$O-); 4.25 (m, 1H, C≡NCH(CH$_3$)C(O)NH-); 3.73-3.53 (m, 14H, -OCH$_2$CH$_2$(OCH$_2$CH$_2$)$_3$OCH$_3$); 3.37 (s, 3H, -OCH$_3$); 1.64 (d, *J* = 7.0, 3H, C≡NCH(CH$_3$)C(O)); 1.49 (d, *J* = 7.0, 3H, -NHCH(CH$_3$)C(O)O); **^{13}C NMR ($CDCl_3$, 75 MHz)**: δ = 171.98 (CH(CH$_3$)*C*(O)OCH$_2$); 165.73 (CH(CH$_3$)*C*(O)NH); 160.9 (*C*≡N); 71.92 (-CH$_2$*C*CH); 70.60, 70.60, 70.60, 70.51, 70.51, 68.8, 65.55; 64.72 (*C*H$_2$); 59.00 (O*C*H$_3$); 48.58 (C≡N*C*H(CH$_3$)CON-); 48.58 (NH*C*H(CH$_3$)C(O)O); 19.66 (CH(*C*H$_3$)CNH); 18.02 (CH(*C*H$_3$)C(O)O) **FT-IR (cm^{-1}, ATR)**: 3250 (N-H, amide); 2875 (C-H); 2140 (C≡N, isocyanide); 1741 (C=O, ester); 1682 (C=O, amide); 1100 (C-O, ether) **MS (ESI):** m/z ([M+Na]$^+$: $C_{18}H_{39}N_2O_7Na$), calcd 383.18; found 383.2

2.5) Preparation of the comonomer M5

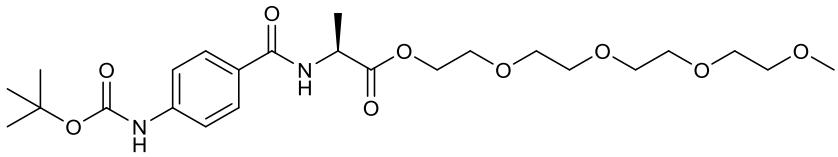

Compound **21** (5.0 g, 17.9 mmol), HOBt (2.7 g, 17.9 mmol), DIPEA (0.3 mL) and DMAP (spatula tip) were dissolved in CH_2Cl_2 (100 mL) and stirred until all the solids were dissolved. The solution was cooled to 0 ºC and a mixture of Boc-4Abz-OH (4.3 g, 17.9 mmol) and DCC (4.1 g, 19.7 mmol) in CH_2Cl_2 (~50 mL) was added portion wise. The

reaction was stirred o/n and allowed to slowly warm up to room temperature. The DCU was filtered off and the filtrate concentrated under reduced pressure. The crude product was subsequently dissolved in $CHCl_3$, washed with a 10% aqueous solution of citric acid (3x) and a saturated aqueous solution of $NaHCO_3$. The water layers were combined and extracted with $CHCl_3$ (3x). All the organic layers were combined and dried over Na_2SO_4. The solvent was removed under reduced pressure and the crude product was purified via column chromatography (SiO_2 0.060-0.200 mm) using $CHCl_3$ as eluent to yield a yellow oil (3.3 g, 6.6 mmol, 37%).

^{1}H NMR ($CDCl_3$, 300 MHz): 7.66 (m, 2H, -C$\underline{H}_{Ar}$-); 7.38 (m, 2H, -C$\underline{H}_{Ar}$-); 6.75 (s, 1H, -N$\underline{H}$-); 6.60 (s, 1H, -N$\underline{H}$-); 4.65 (m, 1H, -C$\underline{H}$(CH_3)), 4.23 (m, 2H, -COOC$\underline{H}_2$-); 3.61 (m, 2H, -COOCH$_2$C$\underline{H}_2$-), 3.55-3.47 (m, 10H, -OC$\underline{H}_2$C$\underline{H}_2$OC$\underline{H}_2$C$\underline{H}_2$OC$\underline{H}_2$-); 3.43-3.40 (m, 2H, -C$\underline{H}_2$OCH$_3$); 3.25 (s, 3H, -OC$\underline{H}_3$); 1.42 (m, 12H, C(C$\underline{H}_3$)$_3$, CH(C$\underline{H}_3$)). **FT-IR (cm^{-1}, ATR):** 3286 (N-H); 2880 (C-H); 1726 (C=O ester); 1640 (amide I); 1523 (amide II); 1236 (C-O ester); 1158 (C-O ester); 1052 (C-O ether); 771 (Ar-H).

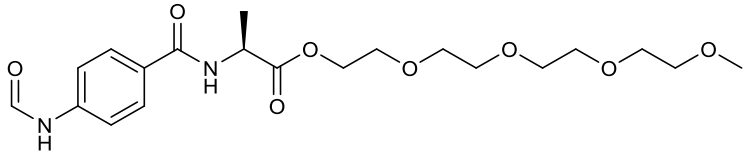

Compound **22** (3.3 g, 6.6 mmol) was treated with 20 mL 4M HCl in dioxane at room temperature. The deprotection was followed by TLC. When the deprotection was completed (1 h), the solvent was evaporated. The compound was dissolved in *n*-BuOH (0.5 mL) and $CHCl_3$ (20 mL) and evaporated under reduced pressure. The crude product was used without further purification.

The deprotected compound was dissolved in ethyl formate (~100 mL) and sodium formate (1.8 g, 26.6 mmol) was added. The mixture was refluxed o/n. The excess sodium formate was filtered off and the filtrate concentrated via evaporation under reduced pressure. The crude product was purified using column chromatography (SiO_2 0.060-0.200 mm) with CH_2Cl_2/10% MeOH as eluent. After evaporation of the solvent under reduced pressure, the product was obtained as a yellow oil (2.7 g, 6.2 mmol, 94%).

^{1}H NMR ($CDCl_3$, 300 MHz): 8.40 (d, J=1.8 Hz, 1H, C$\underline{H}$O); 7.87-7.78 (m, 2H, -C$\underline{H}_{Ar}$-); 7.68-7.65 (m, 2H, -C$\underline{H}_{Ar}$-); 7.17-7.14 (d, J=8.7 Hz, 1H, -N$\underline{H}$-); 6.84-6.82 (d, J=6.9 Hz, 1H, -N$\underline{H}$-); 4.79-4.69 (q, J=7.4 Hz, 1H, -C$\underline{H}$(CH_3)); 4.31 (m, 2H, -COOC$\underline{H}_2$-); 3.70 (t, J=4.7 Hz, 2H, -COOCH$_2$C$\underline{H}_2$-); 3.62-3.54 (m, 10H, -OC$\underline{H}_2$C$\underline{H}_2$OC$\underline{H}_2$C$\underline{H}_2$OC$\underline{H}_2$-); 3.53-3.50 (m, 2H, -C$\underline{H}_2$OCH$_3$); 3.34 (s, 3H, -OC$\underline{H}_3$); 1.53-1.51 (d, J=7.2 Hz 3H, -CH(C$\underline{H}_3$)) **^{13}C NMR ($CDCl_3$, 75 MHz):** 199.1 (*C*(O)OCH$_2$), 187.6 (*C*(O)NH); 155.0 (*C*(O)NH) ; 148.1 (C_{Ar}); 143.5(C_{Ar}); 141.4(C_{Ar}); 135.1(C_{Ar}); 122.5(C_{Ar}); 112.2(C_{Ar}); 111.6(C_{Ar}); 110.9(C_{Ar}); 110.2(C_{Ar}); 101.3; 99.4; 53.9; 52.5; 50.9; 46.5; 40.6; 36.2; 35.8; 35.5; 35.1(*C*H$_2$); 34.7(CH(*C*H$_3$); 30.8(O*C*H$_3$); **FT-IR (cm^{-1} ATR):** 3278 (N-H); 3053 (Ar-H); 2875 (C-H); 1739 (C=O ester); 1640 (amide I, formamide I); 1526 (amide II, formamide II); 1256 (C-O ester); 1171 (C-O ester); 1095 (C-O ether); 731 (Ar-H) **MS (ESI):** m/z ([M +Na]$^+$: $C_{20}H_{30}N_2O_8Na$), calcd 449.5; found 449.3.

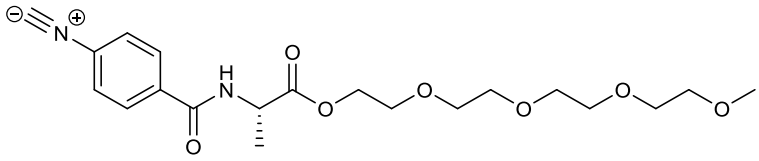

Compound **23** (1.0 g, 2.3 mmol) was dissolved in 200 mL dry CH_2Cl_2, NMM (591.4 mg, 645 µL, 5.9 mmol) was added and the mixture was cooled to -35 ºC in a dry ice/isopropanol bath. The setup was flushed with argon prior to and during the reaction. Diphosgene (324.7 mg, 197 µL, 1.6 mmol) was diluted in 50 mL of CH_2Cl_2 and added dropwise over a period of 90 min to the cooled alkaline mixture of **23** under vigorously stirring. The reaction was quenched with ~5.0 g of solid $NaHCO_3$ and stirred for an additional 10 min. The mixture was poured directly onto a column (SiO_2 0.065 - 0.200 mm, CH_2Cl_2) and allowed to concentrate at the top. The eluent was switched to acetonitrile/CH_2Cl_2 (1:2) to obtain a dark yellow oil (670.0 mg, 1.6 mmol, 70%).

^{1}H NMR ($CDCl_3$, 400 MHz): 7.89-7.87 (m, 2H, -C$\underline{H}_{Ar}$-); 7.47-7.45 (m, 2H, -C$\underline{H}_{Ar}$-); 6.99-6.97 (d, J=7.4 Hz, 1H, -N$\underline{H}$-); 4.86-4.79 (q, J=7.1 Hz, 1H, -C$\underline{H}$(CH_3)); 4.39-4.30 (m, 2H, -COOC$\underline{H}_2$-); 3.74-3.72 (t, J=5.1 Hz, 2H, -COOCH$_2$C$\underline{H}_2$-); 3.66-3.62 (m, 10H, -OC$\underline{H}_2$C$\underline{H}_2$OC$\underline{H}_2$C$\underline{H}_2$OC$\underline{H}_2$-); 3.55-3.52 (m, 2H, -C$\underline{H}_2$OCH$_3$); 3.38-3.35 (s, 3H, -OC$\underline{H}_3$); 1.55-1.54 (d, J=7 Hz, 3H, -CH(C$\underline{H}_3$)) **FT-IR (cm^{-1} ATR):** 3323 (N-H); 2877 (C-H); 2123 (C$\underline{\equiv}$N); 1742 (C=O ester); 1659 (amide I); 1538 (amide II); 1173 (C-O ester); 1107 (C-O ether); 859 (Ar-H); 615 (Ar-H) **MS (ESI):** m/z ([M +Na +K]$^+$: $C_{20}H_{28}N_2O_7NaK$), calcd 470.54; found 469.0.

2.6) Preparation of the comonomer M6

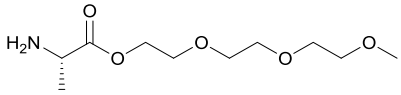

Triethylene glycol monomethyl ether (22.0 mL, 156.2 mmol), *D*-alanine (12.0 g, 134.6 mmol), *p*-toluene sulfonic acid (28.2 g, 163.5 mmol) and 250 mL toluene were added in a round bottom flask. The reaction mixture was refluxed at 126 ºC for 4 h in a Dean-Stark setup and 3 mL of water was collected. A solid precipitate was filtered off, and the solvent was evaporated under reduced pressure. The product was dissolved in 300 mL chloroform and was extracted three times with a saturated aqueous solution of $NaHCO_3$. Thereafter, the water layer was extracted twice with chloroform. The combined organic layers were dried with Na_2SO_4, and the solvent was evaporated under reduced pressure, obtaining 14.0 g of **24** with a 44% yield.

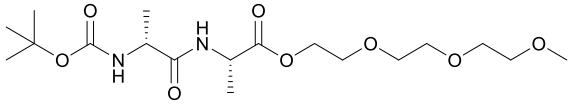

Boc-*L*-Ala-OH (11.2 g, 59.4 mmol), DMAP (spatula tip), HOBt (9.1 g, 59.4 mmol), DCC (13.5 g, 65.3 mmol), **24** (14.0 g, 59.4 mmol) and 250 mL of CH_2Cl_2 were mixed together, cooled in an ice bath to 0 ºC and stirred for 3 h. Thereafter, the mixture was allowed to reach room temperature and subsequently stirred for 15 h. The solid was filtered off, the product was dissolved with 200 mL chloroform, and the solution was extracted three times

with a saturated aqueous solution of citric acid. The water layer was extracted with chloroform (1 x 200 mL). The combined organic layers were washed twice with a saturated aqueous solution of $NaHCO_3$, and the water layer was extracted with chloroform two more times. All organic layers were combined and dried with Na_2SO_4, and the solvent was evaporated under reduced pressure. The crude product **25** was used for the next step without any further purification.

Compound **25** (24.2 g, 59.4 mmol) was dissolved in 20 mL ethyl acetate and treated with 20 mL 4 M HCl in dioxane. The mixture was stirred for 1 h at room temperature. TLC still showed the presence of starting compound, therefore, another 20 mL 4 M HCl in dioxane was added and the solution was stirred for 1 additional hour at room temperature. The residual *t*-BuOH was removed by addition of 20 mL DCM and azeotropic distillation under reduced pressure. This procedure was repeated three times.

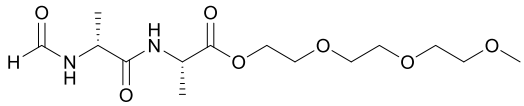

The HCl salt of **25** (13.2 g, 32.3 mmol) and sodium formate (8.8 g, 129.3 mmol) were dissolved into 250 mL ethyl formate. The reaction mixture was boiled for 14 h at 66 ºC. The residual sodium formate was filtered off, and the filtrate concentrated under reduced pressure. The crude product was purified by column chromatography (4% MeOH in CH_2Cl_2), followed by filtration over a short alumina grade III column using ethyl acetate as eluent, obtaining 2.5 g of **26** in a 13 % yield.

R_f = 0.5 (10% MeOH/CH_2Cl_2) **^{1}H NMR (CDCl$_3$, 400 MHz)**: δ = 8.19 (s, 1H, HC(O)NH); 7.02 (br.d, *J* = 7.8,1H, NHCH); 6.75 (br.d, *J* = 7.0, 1H, NHCH; 4.60 (m, 2 H, NHC$\underline{H}$(CH_3), NHC$\underline{H}$(CH_3)); 4.31 (m, 2H, C(O)OC$\underline{H}_2$); 3.67-3.54 (m, 10H, C(O)OCH$_2$C$\underline{H}_2$O(C$\underline{H}_2$C$\underline{H}_2$O)$_3$); 3.38 (s, 3H, OC$\underline{H}_3$); 1.42 (d, 3H, *J* = 7.0 , -NHCH(C$\underline{H}_3$); 1.39 (d, *J* = 7.0, 3H -NHCH(C$\underline{H}_3$)

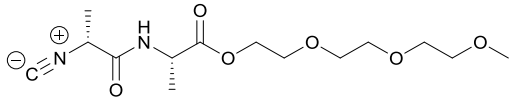

Compound **26** (2.5 g, 7.6 mmol) was degassed for 1 h with N_2. Then NMM (2.1 mL, 19.0 mmol) was dissolved in freshly distilled CH_2Cl_2 (100 mL), and added to the solution. The reaction mixture was cooled to -40 ºC (dry ice/ isopropanol). A solution of diphosgene (0.6 mL, 4.6 mmol) in CH_2Cl_2 (50 mL) was added dropwise over 2 h. The reaction mixture was stirred until it turned to a yellow-orange colour, and was quenched with solid $NaHCO_3$ (3.0 g). The quenched solution was immediately poured onto a silica column mixed with DCM (0.3% triethylamine) and eluted with (1:3 ACN/CH_2Cl_2), obtaining 1.3 g of **M6** in a 53% yield.

R_f = 0.5 (10% MeOH/CH_2Cl_2) **^{1}H NMR (CDCl$_3$, 400 MHz)**: δ = 7.01 (br.d, *J* = 7.4, 1H, N$\underline{H}$); 4.58 (quant, *J* = 7.2 , 1H, C≡NC$\underline{H}$(CH_3)C(O)NH); 4.33 (m, 2H, C(O)OC$\underline{H}_2$CH$_2$O); 4.26 (q, *J* = 7.0, 1H, NHC$\underline{H}$(CH_3)C(O)O); 3.74-3.53 (m, 10H, OCH$_2$C$\underline{H}_2$(OC$\underline{H}_2$C$\underline{H}_2$)$_3$OCH$_3$); 3.39 (s, 3H, OC$\underline{H}_3$); 1.67 (d, *J* = 7.4, 3H, C≡NCH(C$\underline{H}_3$)C(O)); 1.48 (d, *J* = 7.0, 3H, NHCH(C$\underline{H}_3$)C(O)O) **MS (ESI):** m/z ([M+Na]$^+$: $C_{14}H_{24}N_2O_6Na$), calcd 339.4; found 339.1

References

1 Lieke, W. Ueber das Cyanallyl. *Justus Liebigs Annalen der Chemie*, **112**, 316-321, (1859).

2 Gautier, A. Ueber die Einwirkung des Chlorwasserstoffs u. a. auf das Aethyl- und Methylcyanür. *Justus Liebigs Annalen der Chemie*, **142**, 289-294, (1867).

3 Hofmann, A. W. Observations on mixed contents. . *Berichte der Deutschen Chemischen Gesellschaft* **3**, 63, (1870).

4 Pirrung, M. C. & Ghorai, S. Versatile, Fragrant, Convertible Isonitriles. *Journal of the American Chemical Society*, **128**, 11772-11773, (2006).

5 Hagedorn, I., Eholzer, U. & Lüttringhaus, A. Beiträge zur Konstitutionsermittlung des Antibiotikums Xanthocillin. *Chemische Berichte*, **93**, 1584-1590, (1960).

6 Ugi, I. & Meyr, R. New method of preparing isonitriles. . *Angewandte Chemie International Edition*, **70**, 702-703 (1958).

7 Ugi, I. & Fetzer, U. Isonitrile, VII. Die Reaktion von Cyclohexyl-isocyanid mit Phenylmagnesiumbromid. *Chemische Berichte*, **94**, 2239-2243, (1961).

8 Metselaar, G. A. *et al.* Polyisocyanides Derived from Tripeptides of Alanine. *Chemistry – A European Journal*, **13**, 950-960, (2007).

9 Kolb, H. C., Finn, M. G. & Sharpless, K. B. Click Chemistry: Diverse Chemical Function from a Few Good Reactions. *Angewandte Chemie International Edition*, **40**, 2004-2021, (2001).

10 Huisgen, R. *et al.* 1.3-Dipolare Cycloadditionen, XXIII. Einige Beobachtungen zur Addition organischer Azide an CC-Dreifachbindungen. *Chemische Berichte*, **98**, 4014-4021, (1965).

11 Tornøe, C. W., Christensen, C. & Meldal, M. Peptidotriazoles on Solid Phase: [1,2,3]-Triazoles by Regiospecific Copper(I)-Catalyzed 1,3-Dipolar Cycloadditions of Terminal Alkynes to Azides. *The Journal of Organic Chemistry*, **67**, 3057-3064, (2002).

12 Rostovtsev, V. V. *et al.* A Stepwise Huisgen Cycloaddition Process: Copper(I)-Catalyzed Regioselective "Ligation" of Azides and Terminal Alkynes. *Angewandte Chemie International Edition*, **41**, 2596-2599, (2002).

13 Agard, N. J., Prescher, J. A. & Bertozzi, C. R. A Strain-Promoted [3 + 2] Azide−Alkyne Cycloaddition for Covalent Modification of Biomolecules in Living Systems. *Journal of the American Chemical Society*, **126**, 15046-15047, (2004).

14 Ning, X. *et al.* Visualizing Metabolically Labeled Glycoconjugates of Living Cells by Copper-Free and Fast Huisgen Cycloadditions. *Angewandte Chemie International Edition*, **47**, 2253-2255, (2008).

15 Lutz, J.-F. Copper-Free Azide–Alkyne Cycloadditions: New Insights and Perspectives. *Angewandte Chemie International Edition*, **47**, 2182-2184, (2008).

16 Dommerholt, J. *et al.* Readily Accessible Bicyclononynes for Bioorthogonal Labeling and Three-Dimensional Imaging of Living Cells. *Angewandte Chemie International Edition*, **49**, 9422-9425, (2010).

17 Wezenberg, S. J. *et al.* Synthesis, Characterization, and Folding Behavior of β-Amino Acid Derived Polyisocyanides. *Chemistry – A European Journal*, **12**, 2778-2786, (2006).

18 Hu, G. *et al.* Water-Soluble Chiral Polyisocyanides Showing Thermoresponsive Behavior. *Macromolecules*, **46**, 1124-1132, (2013).
19 Kajitani, T. *et al.* Helix-Sense Controlled Polymerization of a Single Phenyl Isocyanide Enantiomer Leading to Diastereomeric Helical Polyisocyanides with Opposite Helix-Sense and Cholesteric Liquid Crystals with Opposite Twist-Sense. *Journal of the American Chemical Society*, **128**, 708-709, (2006).
20 Onouchi, H. *et al.* Two- and Three-Dimensional Smectic Ordering of Single-Handed Helical Polymers. *Journal of the American Chemical Society*, **130**, 229-236, (2008).
21 Neises, B. & Steglich, W. Simple Method for the Esterification of Carboxylic Acids. *Angewandte Chemie International Edition in English*, **17**, 522-524, (1978).
22 Koepf, M. *et al.* Preparation and characterization of non-linear poly(ethylene glycol) analogs from oligo(ethylene glycol) functionalized polyisocyanopeptides. *European Polymer Journal*, **49**, 1510-1522, (2013).
23 Creedon, S. M., Crowley, K. H. & McCarthy, D. G. Dehydration of formamides using the Burgess Reagent: a new route to isocyanides. *Journal of the Chemical Society, Perkin Transactions 1*, 1015-1018, (1998).
24 Khalpi, S., Dey, S. & Mal, D. Burgess reagent in organic synthesis. . *J. Indian Inst. Sci.*, **81**, 461-476, (2001).
25 Böhme, H. & Fuchs, G. Über Darstellung und Umsetzungen von Formamidomethyl-aminen, -sulfiden und -sulfonen. *Chemische Berichte*, **103**, 2775-2779, (1970).
26 Walborsky, H. M. & Niznik, G. E. Synthesis of isonitriles. *The Journal of Organic Chemistry*, **37**, 187-190, (1972).
27 van der Eijk, J. M., Nolte, R. J. M. & Drenth, W. Polyisocyanides 5. Synthesis and polymerization of carbylhistidine and carbylhistamine. *Recueil des Travaux Chimiques des Pays-Bas*, **97**, 46-49, (1978).
28 Wittmann, R. Neue Synthese von Isonitrilen. *Angewandte Chemie*, **73**, 219-220, (1961).
29 Porcheddu, A., Giacomelli, G. & Salaris, M. Microwave-Assisted Synthesis of Isonitriles: A General Simple Methodology. *The Journal of Organic Chemistry*, **70**, 2361-2363, (2005).
30 Park, K. D., Liu, R. & Kohn, H. Useful Tools for Biomolecule Isolation, Detection, and Identification: Acylhydrazone-Based Cleavable Linkers. *Chemistry & Biology*, **16**, 763-772, (2009).

Chapter 3 : Polymer synthesis and characterization

Abstract
In Chapter 1, the network and fibre characteristics, which are desirable for a synthetic ECM, were discussed. A synthetic ECM material must be fibrous, have finite bundling, should exhibit strain stiffening mechanics and it should be able to form a cell supporting 3D biocompatible network. In this chapter we will take a closer look at the synthesis of helical stiff water-soluble polyisocyanide hydrogels. The synthesis of tri and tetra ethylene glycol isocyanide monomers with and without functional handles will be investigated. The difference between homo- and copolymers on the polymer characteristics will be presented. The effect of introducing monomers with functional handles (acetylene or azide) appended to the polymer backbone and the highest possible loading, whilst still retaining polymer characteristics similar to the non-functional polymer will be discussed. Finally in a route towards stiffer polymers, the inclusion of π-π stacking monomers into the polymer by the introduction of aminobenzoic acid instead of the conventional alanine and its effect on the polymerization will be investigated.

Introduction

As defined in Chapter 1, the mechanical properties of the ECM fibrous scaffolds are essential in translating the biomechanical environmental signals to cells suspended in it to stimulate a cellular response. These ECM fibres have very specific characteristics such as finite bundles of self-assembled helical fibrils with non-linear stress strain behaviour setting them apart from all current synthetic systems. In this chapter, a completely new class of synthetic ECM fibre mimic based on polyisocyanopeptides (PICs) will be discussed [1]. These helical polymers possess a 4_1 (four repeat units per turn) β-helical architecture, in which a hydrogen bond network is formed among the peptidic side groups parallel to the polymer backbone [2] (Figure 1), resulting in exceptionally stiff chains with persistence lengths l_p comparable to that of dsDNA [3]. Some derivatives of this family of polymers are amongst the stiffest manmade materials known to date with an l_p up to 200 nm [4]. In this

chapter homopolymers, copolymers and terpolymers will be synthesized from the monomers synthesized in Chapter 2. By modifying the monomer building blocks whilst keeping the monomer to catalyst molar ratio constant at 1:10,000, the ability to tune the properties of the synthesized polymers was studied. Changing the molar ratio of tri- and tetra-ethylene glycol sub units present in a polymer the sol to gel transition temperature can in principle be tailored. In addition, the effect of using different enantiomeric states of the alanine amino acid, *DL*, *LD* and *LL* upon the helicity of the individual fibres and how this chiral change would affect the bundling and eventually the hydrogels mechanical properties will be presented. In order to develop a genuine ECM, the introduction of functional handles to enable modular methods for bioconjugation of biologically relevant ligands to the polymers was studied. In the hope of varying the stiffness of the polymers, the effect of π-π stacking on the polymer fibre through the addition/substitution of alanine with the non natural 4- amino benzoic acid was investigated.

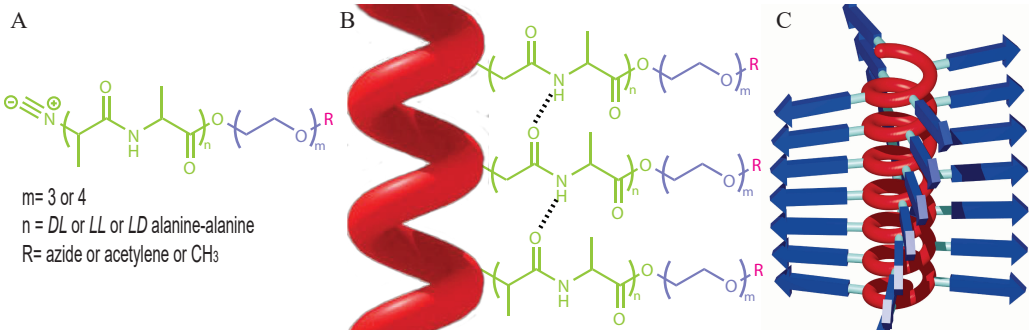

Figure 1. Oligo(ethylene glycol) substituted polyisocyanopeptides. (a) the isocyanide monomer with alanine-alanine dipeptide core, oligoethylene spacer and functionalizable chain end, (b) representation of the hydrogen-bond network that stabilises the secondary helical structure, (c) Schematic illustration of the 4_1 β–sheet helix. The arrow represents the peptide substituents.

Results and discussion

1. Polymer synthesis

1.1. Homopolymers

1.1.1. Poly(*DL*-isocyanopeptide)-graft-tri(ethylene glycol) (M2)

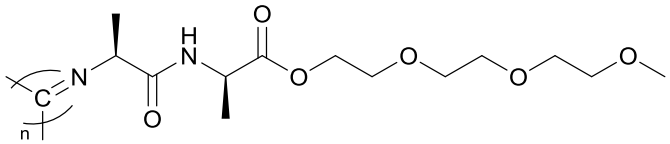

Polymers were synthesized from a triethylene glycol (M2) monomer derivative catalyzed with nickel in a dry environment for three days. Compound **M2** was dissolved in freshly distilled toluene. A volume of the 1 mM catalyst stock solution equivalent to 10^{-4} of the total **M2** mols was transferred via pipette into the mixture of **M2** and toluene. The flask was placed in an ice bath and fitted with a $CaCl_2$ drying tube. The mixture was diluted with distilled dry toluene to obtain a final concentration of 50 mg/mL monomer. After 2-3 h the mixture became extremely viscous and additional solvent was added to obtain a concentration of 25 mg/mL. This mixture was allowed to stir for a total of 72 h. The polymer was isolated via precipitation into diisopropylether. This precipitation cycle was repeated three times to obtain a broad range of yields. The polymers were analysed by measuring the intrinsic viscosity to determine molecular weight ($\overline{M_v}$), rheology (G') and circular dichroism. They were visualized by drop casting from solution onto freshly cleaved mica via atomic force microscopy (AFM).

During repetitive syntheses at the same monomer to catalyst molar ratio (1:10,000) it was observed that a broad range of yields and $\overline{M_v}$ were obtained within the group. To investigate the reproducibility of the method it was decided to keep the protocol constant and evaluate the reproducibility among different people. The obtained homopolymers had gravimetric yields ranging between 50-93 % and molecular weights ranging from 369 – 796 kg/mol (Table 1). It was therefore concluded that the synthetic method is extremely sensitive to slight variations.

Table 1. Homopolymer synthesis summary: molecular weight and yield.

Sample	$\overline{M_v}$ **(kg/mol)**	**Yield (%)**
P1	498	89
P2	590	50
P3*	491	~
P4	722	93
P5*	586	67
P6*	444	60
P7	796	78
P8*	369	72

*: Chiralix monomer

The only other known variable between synthesized polymers was the source of the monomer. By using statistical analysis software the molecular weights obtained using the same catalyst ratio per monomer source was compared. This comparison can be seen in Figure 2, overlaying the probability plots of the molecular weights per monomer source the distribution of molecular weight were normal. The average molecular weight per monomer source was determined along with the standard deviations. When the two averages were compared the standard deviation (error bars) overlapped meaning that although the

monomer sources were different there was no statistical difference between the obtained average molecular weights.

The two sets of data were also compared by performing a standard two-sample t test and it was found that P= 0.069 which means that there was no significant deviation between the molecular weight distributions (Table 15).

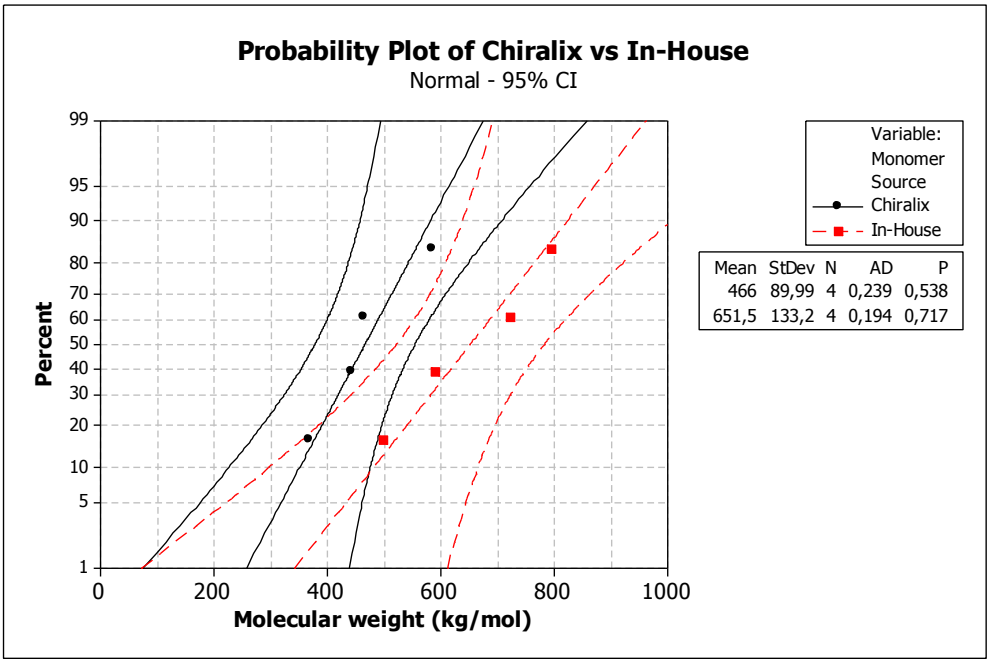

Figure 2. The probability plots at a 95% confidence interval of the molecular weights obtained from a 1:10,000 catalyst ratio, using isocyanide monomer M2 from two different sources.

Spectroscopic results

The resulting polymers, although of differing length were found to have similar CD spectra varying only in intensity as a function of the concentration. No difference in spectra of polymers obtained from in-house or Chiralix monomers was observed (Figure 3).

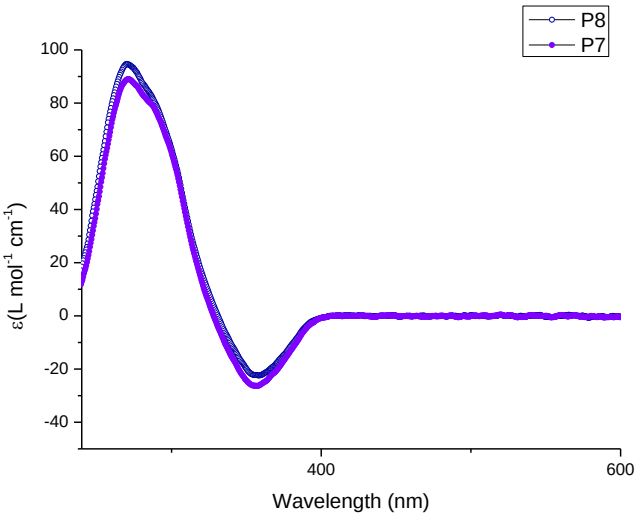

Figure 3. The CD spectra for P8 (M2 from Chiralix) vs P7 (M2 in-house) 4 mg/mL in DCM.

Therefore it was concluded that the only deviation in polymer behaviour was as a result of difference in molecular weight and that comparing all further results would be performed ignoring the monomer source.

Rheology

During linear rheology experiments it was observed that molecular weight affected the LCST temperature, a difference of up to 5 °C was possible as observed when comparing **P8** (369 kg/mol) 18 °C with **P7** 13 °C (796 kg/mol) (Figure 4).

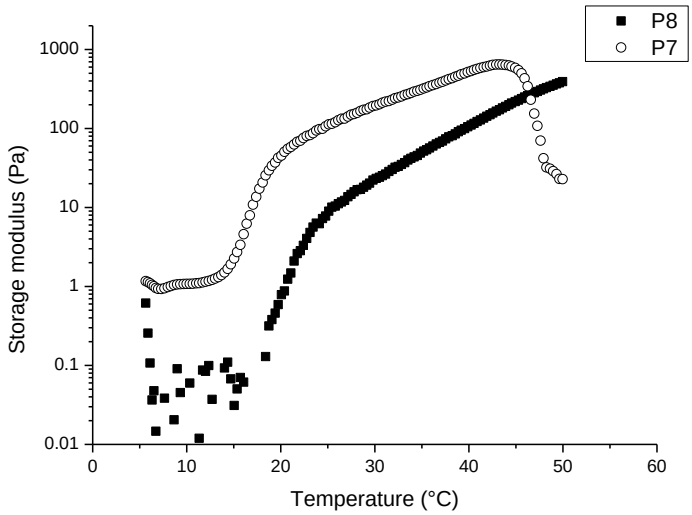

Figure 4. Storage modulus as a function of temperature of two homopolymers , **P8** with a molecular weight of 369 kg/mol and **P7** with a molecular weight of 796 kg/mol at 1.6 mg/mL in PBS.

The rheology of mixtures of these two polymers was also studied to see how the storage modulus of the low molecular weight polymer solution would change by the addition of high molecular weight polymer. To investigate this **P8** (369 kg/mol) was systematically enriched with increasing amounts of **P7** (796 kg/mol), see Figure 5. The stiffness of the resulting mixture gradually increased as the ratio of **P7** to **P8** was increased. The sol-gel transition temperature decreased with increasing percentages of **P7**. This earlier sol-gel transition temperature for the high molecular weight polymers is believed to occur because the longer the average polymer length the faster the rate of polymers entanglement resulting in polymer precipitation or the onset of an earlier sol-gel transition and therefore a lower sol-gel transition temperature is observed. The relationship between the percentage of **P7** by weight and the increase in storage modulus was found to be linear (Figure 5). This

rather surprising result reveals that it would be possible to combine polymers from different batches to obtain a uniform material with controlled bulk stiffness circumventing prior issues of batch variation in stiffness at the same sample concentration. This level of controlled material properties is important if the material should ever be used as a marketable material.

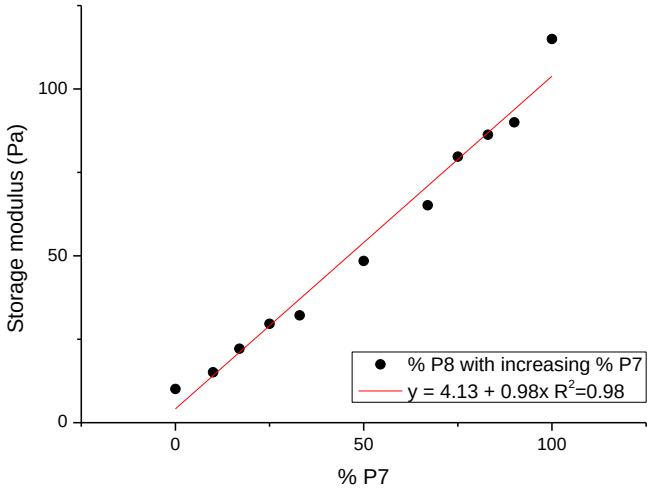

Figure 5. The stiffness of a mixture of P8 and P7 at 25 °C as determined with rheology measurements. On the x-axis the percentage of P7 in the mixture is plotted. All samples were at a concentration of 1.6 mg/mL. (y=4.13(2.96)+0.98(0.05)x; adj R^2=0.98)

AFM Analysis of the hydrogels

Bundle dimensions from AFM measurements.

As depicted in Figure 6, to measure bundle dimensions as a function of concentration, gels were prepared at concentrations ranging from 0.13−3.0 mg/mL were transferred to mica substrates and subjected to AFM [5].

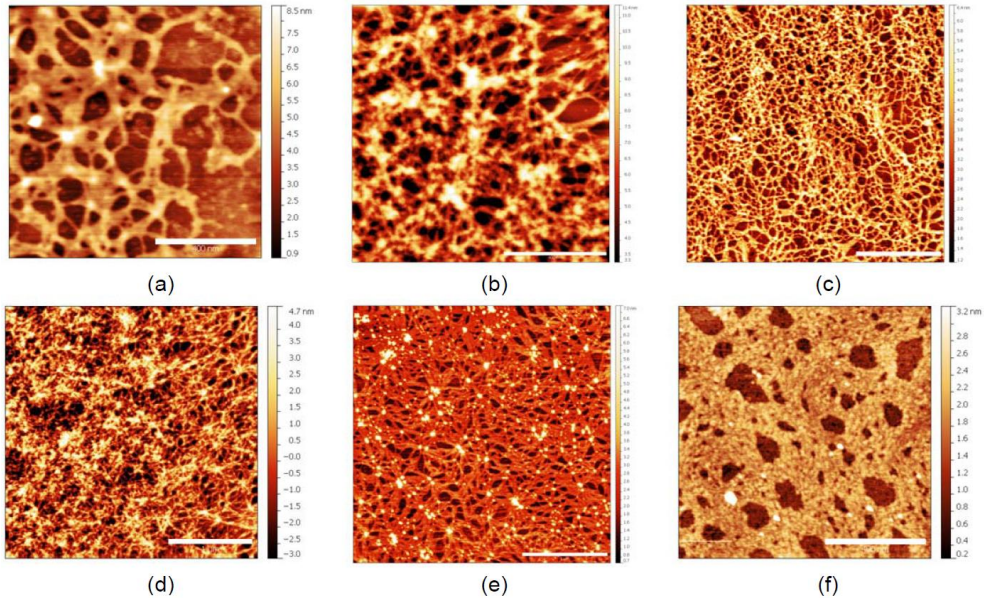

Figure 6. AFM images of **P1** obtained from samples of different polymer concentration: (A) 0.13 mg/mL(scale bar: 400 nm, height range 0.9–8.5 nm), (B) 0.25 mg/mL (scale bar: 400 nm, height range 3.3–11.4 nm), (C) 0.50 mg/mL (scale bar: 1.0 µm, height range 1.2–6.4 nm), (D) 0.75 mg/mL (scale bar: 1.0 µm, height range -3.0–4.7 nm), (E) 1.0 mg/mL (scale bar: 1.0 µm, height scale 0.7–7.0 nm), (F) 3.0 mg/mL (scale bar: 400 nm, height scale 0.2–0.2 nm).

Statistical analysis of the images yielded distributions of bundle heights and bundle widths, see Figure 7. The height profiles in samples prepared from a simple gel transfer showed strong variations with the position in the sample. The fibre height was used to define bundle properties as the z-axis measurements were more reliable than the data obtained from the xy width profiles. Despite the broad distributions per sample, the gels at all concentrations typically formed ~30 nm wide bundles with a possible tip broadening of

10 nm per edge that would mean ~20 nm originating solely from the tip broadening [6] and the residual 10 nm would be closer to 6-9 fibre thickness of ~7-10 nm.

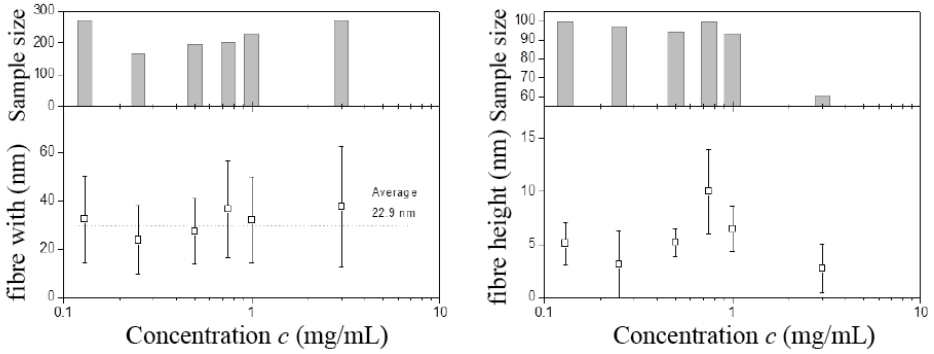

Figure 7. Fibre width (left) and height (right) determined from statistical analysis of AFM results at c = 0.13 – 3.0 mg/mL. The sample size of the analysis is shown in the top panel.

AFM Length

To analyze the difference in length between low molecular weight and high molecular weight polymers, the polymers were visualized by AFM and analyzed by measuring the length of individual polymers.

The polymer samples with low molecular weight as determined by viscometry had associated lower average lengths when observed by AFM when compared to the higher molecular weight sample. See, Figure 8 the histogram overlay of the AFM length data of **P8** vs. **P7**. It was possible to derive the dispersity (*Đ*) from the AFM lengths by dividing the weighted average polymer length by the number average polymer length (L_w/L_n). The *Đ* was determined to by 1.5 for **P8** and1.6 for **P7**.

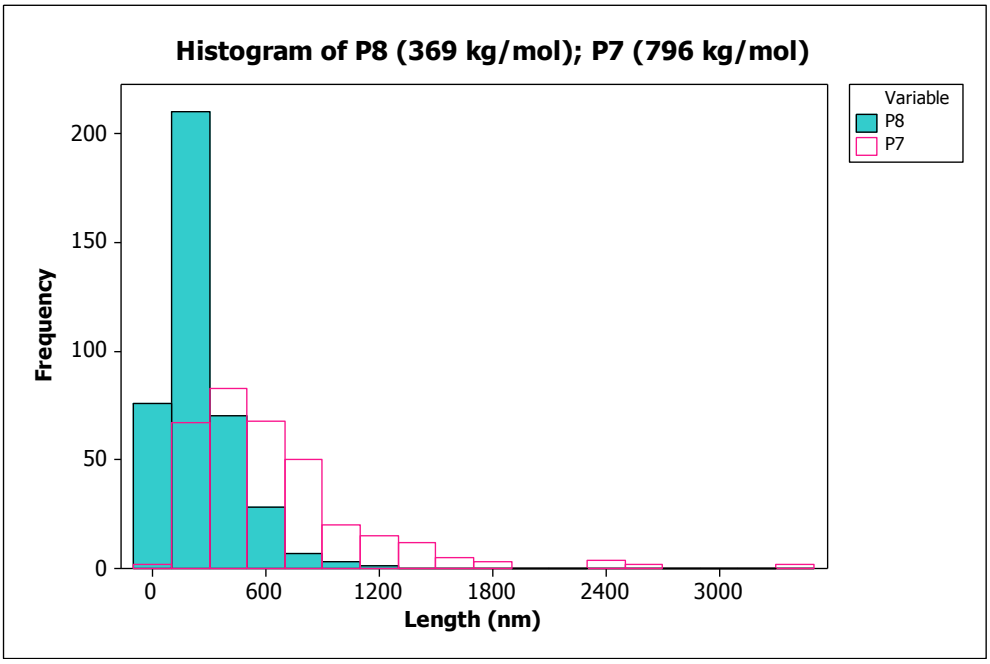

Figure 8. The histogram of polymer lengths as determined by analyzing AFM height profiles of P8 and P7.

Pore size analysis by single particle tracking.

The effect of concentration on the pore size of the PIC above the sol-gel transition temperature was investigated by tracking the Brownian movement of platinum nanoparticles of a known size (smaller than pore size as determined by AFM) for over 200 steps through a PIC solution of a known concentration, through a known volume. The PIC concentration was systematically increased and the effect of this on the movement of the particle measured. As the concentration increased the platinum particles diffusion coefficient decreased indicating that the pore size was decreasing with increasing concentration of polymer (Figure 9).

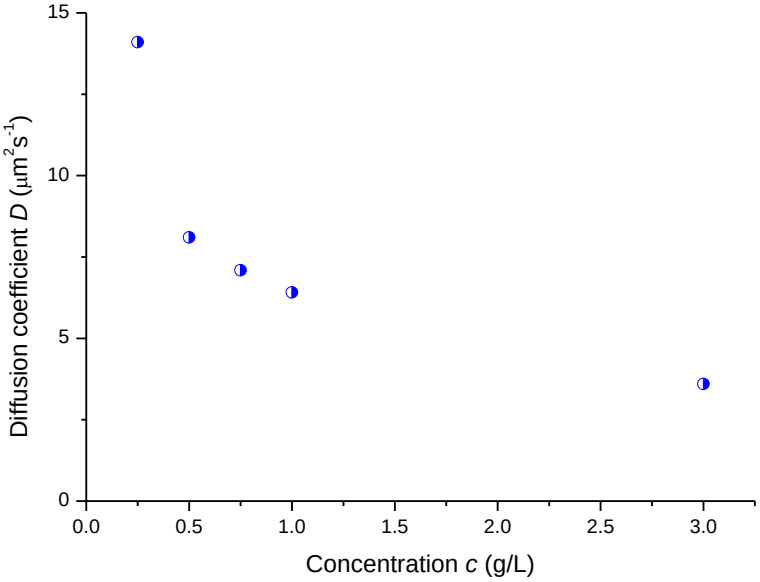

Figure 9. Tracking analysis. Average diffusion coefficient as a function of concentration of P1 at T = 22 °C.

From the data generated by the NanoTracking analysis, platinum nanoparticle of mean size of 184 nm in **P1** solutions with varying concentrations (0.13 – 3.0 mg/mL), it was possible to analyze the trajectory of individual platinum particles and calculate the mean square displacement per particle. A particle in a solution with large pores will exhibit isotropic random walk through Brownian motion. If the particle is inside a porous network where the pore size is equal to its own size this random walk will change to a confined random walk in which free movement is only possible in pores larger than its own diameter. It follows that if the pores are smaller than the particle diameter, the particle will become completely confined appearing to be "stuck" in a hole (Figure 10). MATLAB

software was used to automatically calculate the mean square displacement of the particles per PIC concentration, in Figure 10 one particle per concentration is highlighted for clarity. With increasing concentration of PIC, the mean square displacement of the particles decreases and the Brownian motion of the particles change from isotropic random walk (0.13 mg/mL), partially confined random walk (0.75 mg/mL) to a confined random walk (3.0 mg/mL) [7-8]. This confirmed that the pore size was slowly decreasing as the concentration of PIC was increased.

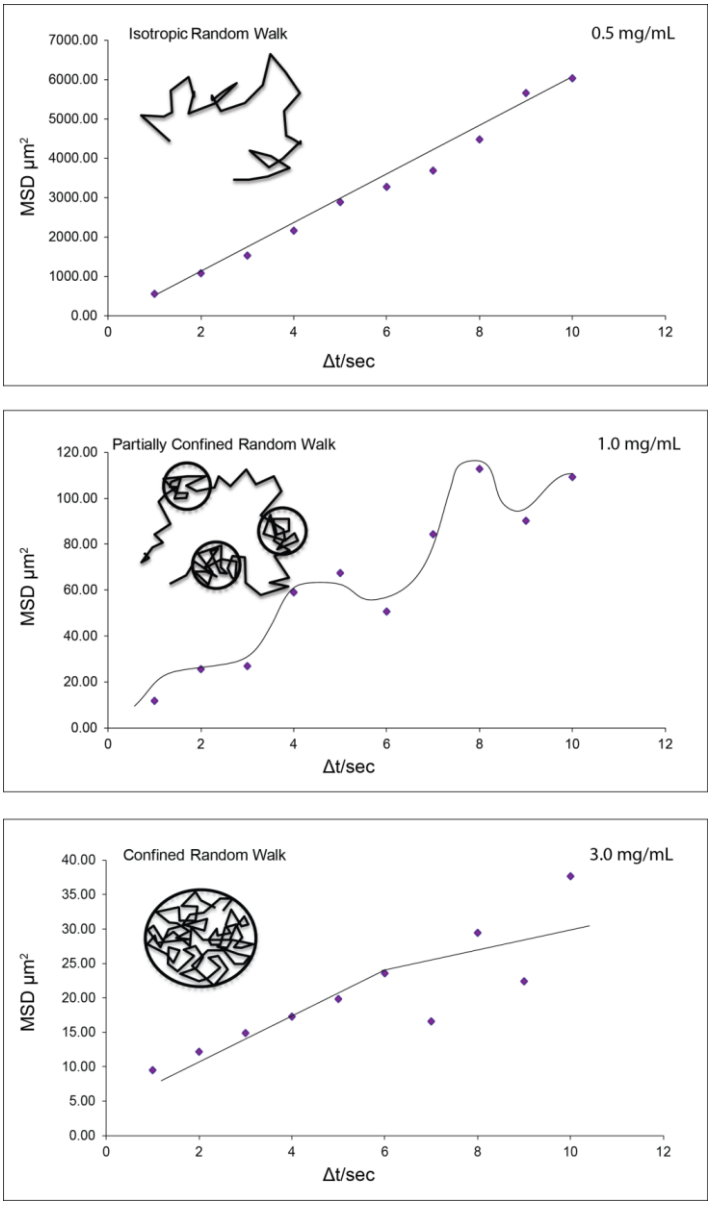

Figure 10. The platinum nanoparticles were visualized moving through the PIC hydrogel with increasing concentration of **P1** by Nanosight. In the above image one particle per concentration is highlighted and the mean square displacement in a defined space tracked over time.

1.1.2. Poly(*DL*-isocyanopeptide)-graft-tetra(ethylene glycol) (M4)

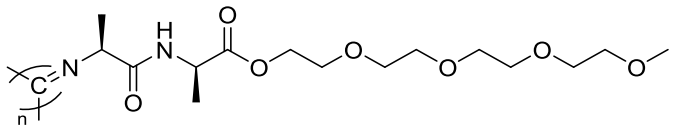

Homopolymers with the same chirality as in 1.1.1 but with one additional ethylene glycol subunit in the isocyanide monomer were synthesized to investigate the effect of the additional ethylene glycol unit on the polymers material properties. The same synthesis strategy and 1:10,000 catalyst ratio was used as in 1.1.1 with the only difference being the monomer used (see, Table 2 for details).

Table 2. Homopolymer synthesis summary: molecular weight and yield.

Sample	$\overline{M_v}$ **(kg/mol)**	**Yield (%)**
P9	430	55

Spectroscopic results

The polymer was dissolved in DCM at a concentration of 1 mg/mL and the circular dichroism measured over a range of 500 – 220 nm (see, Figure 11).

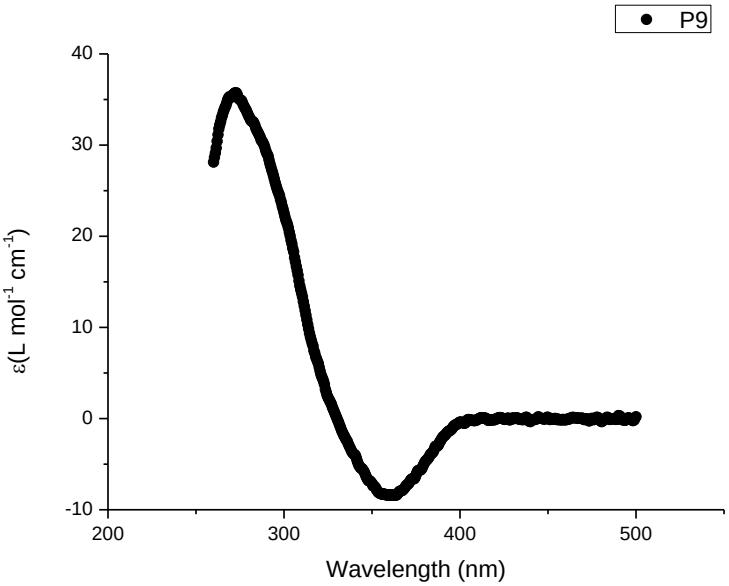

Figure 11. The CD spectrum for P9 at concentration of 1 mg/mL in DCM.

Rheology

Similar LCST behaviour was observed as for the homopolymers with triethylene glycol substitution, but the sol-gel transition was at a higher temperature of 42 °C (See Figure 16 for the temperature ramp of **P9**).

1.1.3. Poly(*LL*-isocyanopeptide)-graft-tetra(ethylene glycol) (M7)

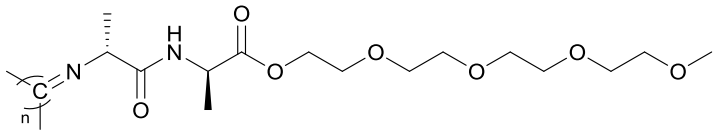

To investigate the effect of chirality on the homopolymer, the *LL*-di-alanine isocyanide monomer was polymerised using the same synthetic strategy as employed in 1.1.1. The

mixture was stirred at room temperature in a flask fitted with a $CaCl_2$ drying tube. The solution was left to stir over a series of days (see, Table 3). The length of stirring affected the molecular weight obtained. The polymer was isolated via precipitation into diisopropylether. The polymer was then re-dissolved in DCM and the precipitation cycle was repeated three times. The polymer was analysed by measuring the intrinsic viscosity and circular dichroism (see, Figure 12).

Table 3. Homopolymers synthesis summary: Molecular weight and Yield

Sample	**Reaction time (days)**	$\overline{M_v}$ **(kg/mol)**	**Yield (%)**
P10	4	22	16
P11	24	135	32

At four days the *LL* variant had a significantly lower molecular weight than the conventional *DL* **P9** (430 kg/mol). Even when the reaction time was increased to 24 days the molecular weight was still four times lower than the *DL* variant.

Spectroscopic results

CD spectra confirm that the appropriate *LL* polymer (**P10**; **P11**) was successfully synthesized as both peaks are now in –Ɛ as is characteristic for the *L* stereoisomer (see, Figure 12).

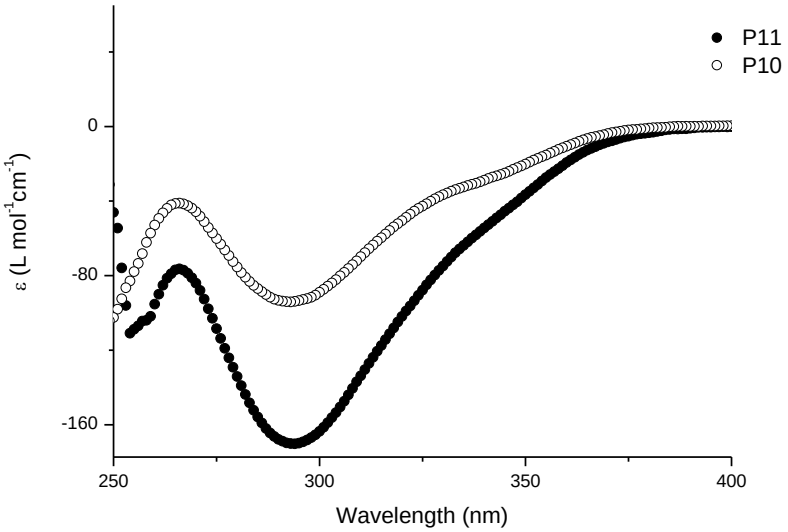

Figure 12. The CD spectra for homopolymers P10 and P11 at concentrations of 4 mg/mL in ACN.

In conclusion, the inverted monomer affected the polymerization kinetics negatively, possibly by limiting the initial self assembly structure that drives the polymerization forward. To better understand the nickel catalyzed polymer mechanism, this effect should be investigated in more detail in the future. However, for the goal of this thesis simply observing retarded polymer formation with limited to low monomer to polymer conversion was enough to discontinue this avenue of investigation.

1.1.4. Poly(*LD*-isocyanopeptide)-graft-tri(ethylene glycol) (M6)

Reversing the chirality of the alanine subunits in the isocyanide monomer would result in polymers with inverted helixes. The same synthesis strategy and monomer to catalyst ratio was used as in 1.1.1. but with monomer **M6** (see, Table 4 for details).

Table 4. Homopolymer synthesis summary: molecular weight and yield

Sample	$\overline{M_v}$ **(kg/mol)**	**Yield (%)**
P12	626	73

Spectroscopic results

The CD spectrum (see, Figure 13) confirmed that the inverse enantiomer polymer was synthesized.

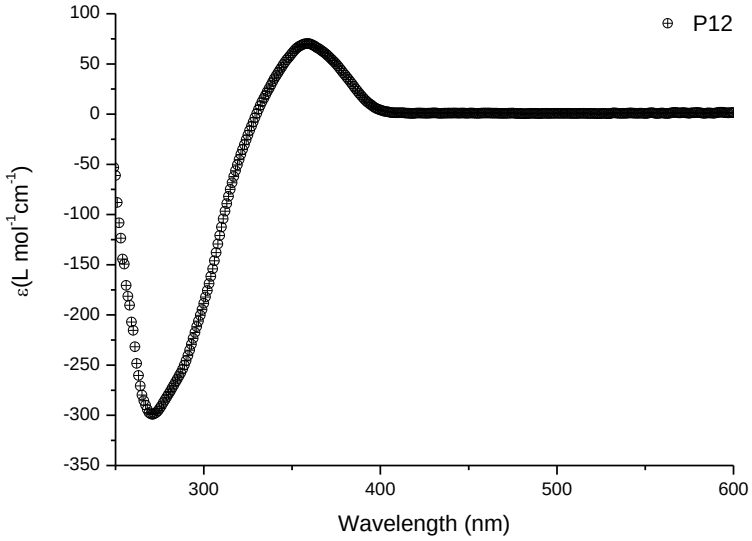

Figure 13. The CD spectrum for homopolymer P12 at a concentration of 4 mg/mL in ACN.

Rheology

To investigate the effect of 'handedness' on the gelation behaviour, a homopolymer with *LD* orientation was mixed with a homopolymer with *DL* orientation. It was postulated that the inverted handedness might affect bundling behaviour, which in turn may alter the gelation behaviour. The two polymers were combined 1:1 mass ratio 1 mg/mL in MQ. The

individual polymers went through a sol-gel transition upon heating (**P1** 18 °C vs. **P12** 22 °C) and the mixture showed an intermediate sol-gel transition temperature of 20 °C (see, Figure 14). This behaviour was observed previously in polymers with similar handedness but different molecular weights (Figure 4), which is probably the explanation in this case also as **P12** has a molecular weight of 626 kg/mol and **P1** 498 kg/mol. Therefore the effect of chirality on the PIC sol-gel transition seems negligible.

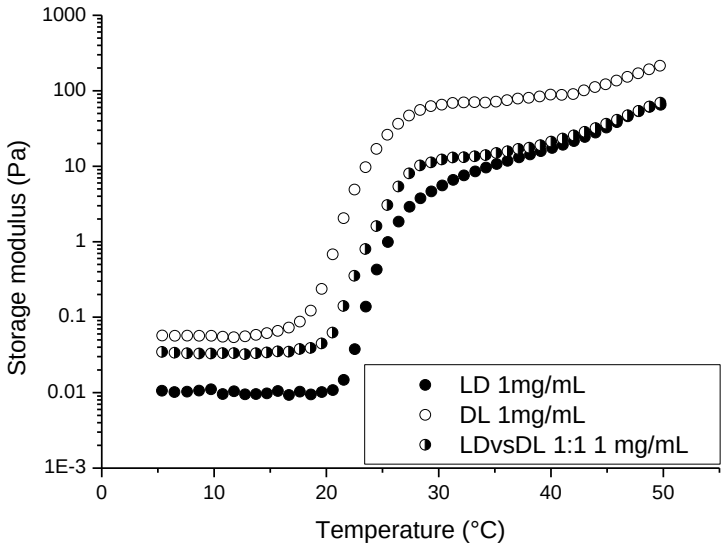

Figure 14. Storage modulus as a function of temperature for homopolymer *LD* (P12), *DL* (P1) and a 1:1 mixture of the two polymers (*LD*:*DL*) at 1,0 mg/mL in MQ.

To conclude the *LD* monomer did not inhibit the polymerization as was observed with the *LL* variant. Although the homopolymer **P12** did have an inverted handedness to the conventional *DL* polymer **P1** there was no clear difference in LCST behaviour neither in its pure form nor mixed in equal amounts with the *DL* variant. This would seem to suggest that

the two networks are completely miscible and that bundle formation is unaffected by the polymer fibres' handedness. In the future to verify whether the two polymers form a completely mixed system, two dyes (FRET pair) could be coupled to each polymer type, if sufficiently close to each other a FRET response would be observed, which would probably not occur in a phase-separated system.

1.2. Synthesis of Copolymers

1.2.1. Polymerization of Tri-Tetra ethylene glycol copolymers (M2:M4)

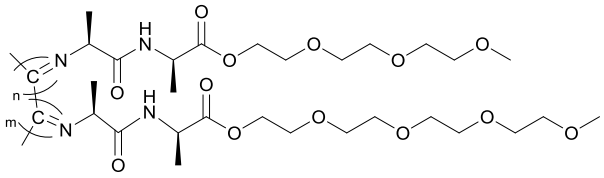

The same synthesis strategy was used as in 1.1.1 with the only difference being two different monomers were used. It was postulated that by varying the ratio of oligoethylene units it would be possible to control the LCST temperature [9] to obtain a targeted transition temperature between 18 °C and 42 °C.

Table 5. Copolymers synthesis summary: molar ratios, molecular weight and yield

Sample	**M2:M4 (mol ratios)**	**sol-gel (°C)**	$\overline{M_v}$ **(kg/mol)**	**Yield (%)**
P13	25:75	25	597	54
P14	50:50	30	551	57
P15*	38.9:61.1	39	296	18
P16*	27.9:72.1	30	523	61
P17*	20.8:79.2	32	525	44

*__M2__ from Chiralix

Spectroscopic results

The CD spectra (Figure 15) of all the copolymers described in Table 5 show a similar pattern. The **P15-17** polymers are at the same concentration of 4 mg/mL in ACN and it is clear that **P15** is lower in intensity.

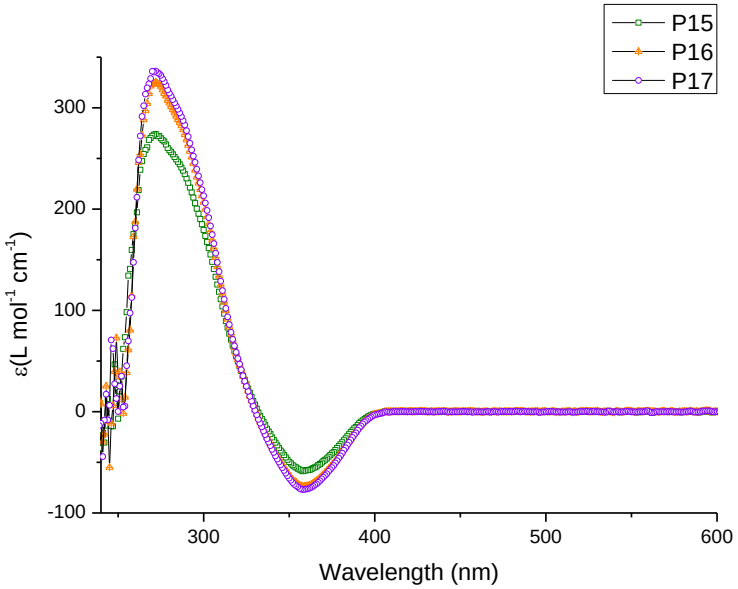

Figure 15. The CD spectra for copolymers separated into polymers from different monomer sources a) 4 mg/mL in ACN.

Rheology

It was observed that by changing the length of the polymers the sol-gel transition temperature could be modified but also by changing the ratios of oligoethylene monomers triethylene glycol (**M2**) to tetraethylene glycol (**M4**) (Figure 16) in a random copolymer it should be possible to change the sol-gel transition temperature between 18 - 42 °C [9].

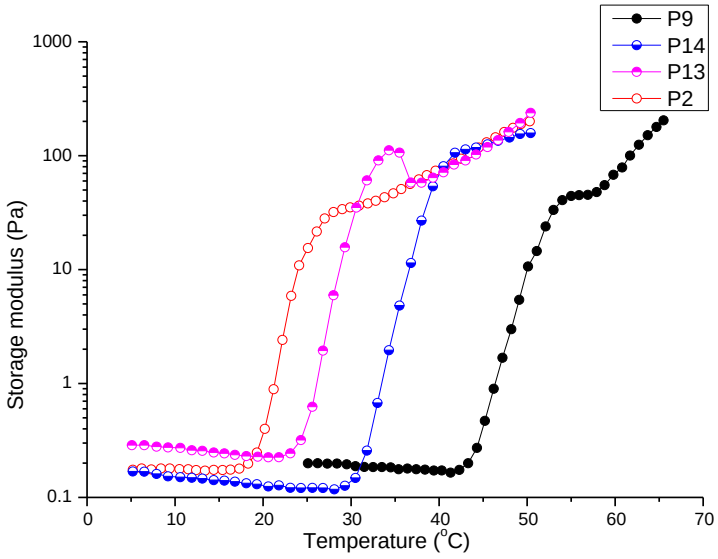

Figure 16. Storage modulus as a function of temperature for two copolymers and two homopolymers synthesized from the same monomer source for both M2 and M4 (in-house) and possessing similar molecular weights.

Care should be taken however when interpreting data such as seen in Figure 17, as the molecular weight also affects the gelation temperature (Figure 4 and Figure 23), therefore only copolymers with similar molecular weights may be compared in this way.

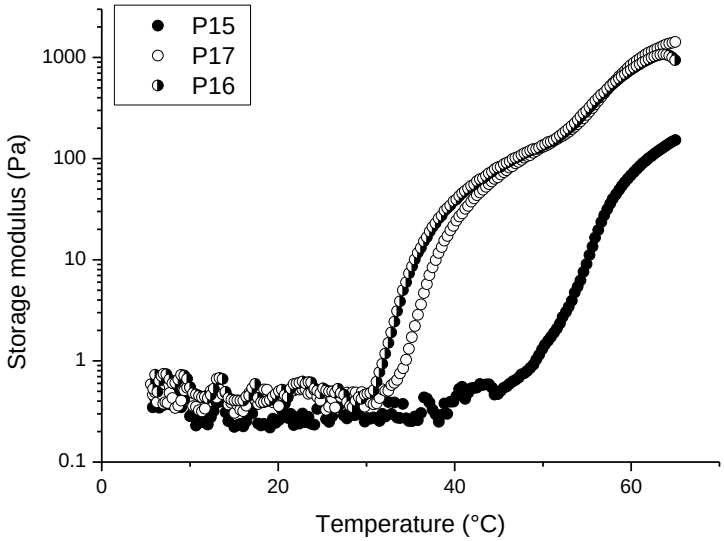

Figure 17. Storage modulus as a function of temperature for three copolymers synthesized from the same monomer source M2 (Chiralix) and M4 (in-house) but with dissimilar molecular weights.

The ball drop test [5] was used to confirm the sol-gel transitions observed in rheology. It is a very robust technique in which the gel is formed inside a temperature controlled water bath above its gel point. A small sphere with known diameter and weight is placed on top the gel. The water bath is cooled down and the exact temperature of gel-sol is noted as the sphere falls to the bottom of the gel container. In Figure 18 the result of this measurement is plotted against the rheology transitions. As rheology is more sensitive than the ball drop test, the sol-gel transition occurs at a slightly lower temperature. Nevertheless, both techniques show a linear dependency of sol-gel transition versus molar ratio of the comonomers. In the rheology data, the transition of **P17** and **P16** was included as it has a similar molecular weight as compared to the other polymers. From these experiments it was

possible to determine a linear relationship that could be used to tune the sol-gel transition of the hydrogels.

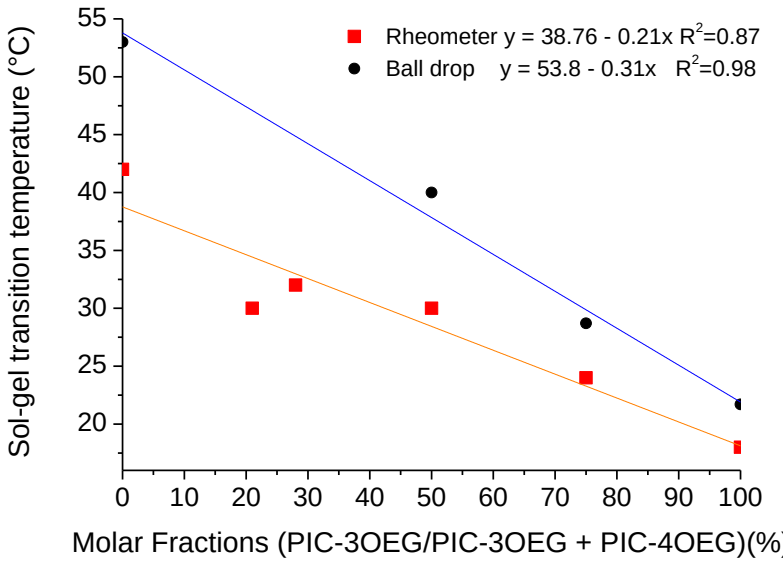

Figure 18. Sol-gel transitions of PIC copolymers with different % molar fractions of tri ethylene glycol monomer M2 to tetra ethylene glycol monomer M4, but similar molecular weight polymers.

1.2.2. Polymerization of azide functional tri or tetra ethylene co-polymers (M1:M2 and M1:M4)

As the polyisocyanides with biological relevant ligands were required, polymers with bioconjugation handles were needed. The bioconjugation strategy that seemed most promising in terms of ease, biological inertness, limited to no side products and high reactivity was the use of strain promoted acetylene-azide cycloaddition. Varying molar fractions of azide were introduced into the PIC backbone to create a library of possible

polymer scaffolds. The same synthetic strategy was used as in 1.1.1 with the only difference being the monomers used, i.e. the azide functional monomer (**M1**) and tri ethylene glycol (**M2**) or tetra ethylene glycol (**M4**) monomer.

Table 6. Azide appended copolymers synthesis summary: molar ratios, molecular weight and % yield.

Sample	**M1: M2 (mol)**	$\overline{M_v}$ **(kg/mol)**	**Yield (%)**
P18	1:100	688	57
P19	1:225	866	67
P20	1:400	1143	83
P21	1:570	948	83
P22	1:850	1042	47
P23	1:1140	1168	47
P24*	1:50	570	66
P25*	1:100	492	65
P26*	1:150	629	62
P27*	1:200	503	59
P28*	1:100	451	70
P29*	1:100	444	70
P30*	1:100	361	75
P31	1:50	755	72
P32	1:100	735	74
P33	1:200	714	68
P34	1:100	331	83
P35	1:400	378	62
P36	1:550	835	70
P37	1:1730	791	72
P38	1:25	733	87
P39	1:200	569	50
P40	1:100	674	50
P41	1:100	516	91
	M1:M4 (mol)		
P42	1:100	421	78
P43	1:100	616	88

*: monomer M2 source Chiralix

The ratio of azide to spacer monomer did not seem to affect the obtainable molecular weight (1:50 molar ratio of azide to spacer monomer). As observed previously

(homopolymers), the source of monomer affected the obtainable molecular weights (Figure 19).

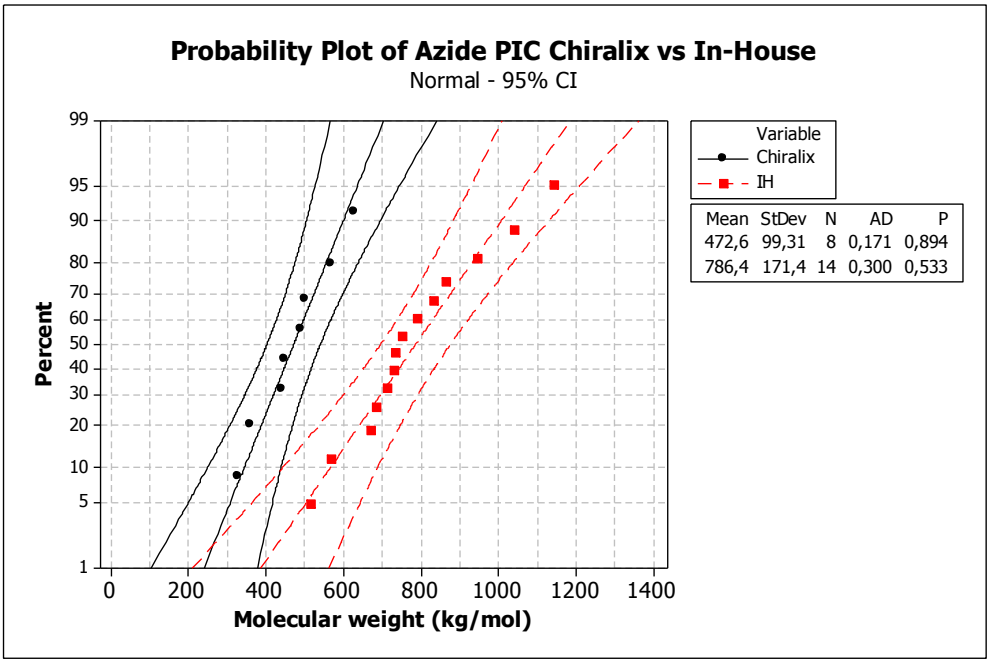

Figure 19. The probability plots at a 95% confidence interval of the molecular weights obtained from a 1:10,000 catalyst ratio, using isocyanide monomer M2 from two different sources and the same in-house azide monomer M1.

Per monomer source the molecular weights were normally distributed. The average molecular weight per monomer source was determined to be 473 kg/mol for Chiralix **M2** monomer and 786 kg/mol for in-house **M2**, when the standard deviation was added to the lowest average M_w and subtracted from the highest average M_w the two averages (error bars) did not overlap and therefore the difference between monomer sources was significant. The two ranges were also compared by using two-sample t-test, a t-value of -5.4

and resulting P-value of 0.00 was obtained for degrees of freedom = 19, this value is smaller than 0.05 and therefore the difference between the two ranges is significant.

Spectroscopic results

The quantification of azide loading on the backbone of PIC could not be performed accurately with ^{1}HNMR, therefore it was decided to label the PIC with a dye and determine the concentration of the dyes spectroscopically. For this strategy to be effective, a conjugation strategy with near quantitative yields and easy purification was required. It was opted to use the strain promoted acetylene-azide click (SPAAC) reaction as it is known to be rapid and efficient. The PIC itself has a slight absorption peak around 350 nm and therefore any dye used for quantification should not adsorb at this wavelength. The label opted for was the bicyclononyne functional fluorescein derivative, commonly known as TokyoGreen, which absorbs at 506 nm (Figure 20). The polymer dye conjugate did suffer from solubility issues and therefore a mixed solvent system of ACN:DMSO:MQ was required. The extinction coefficient in this solvent system was determined experimentally as seen in Figure 20.

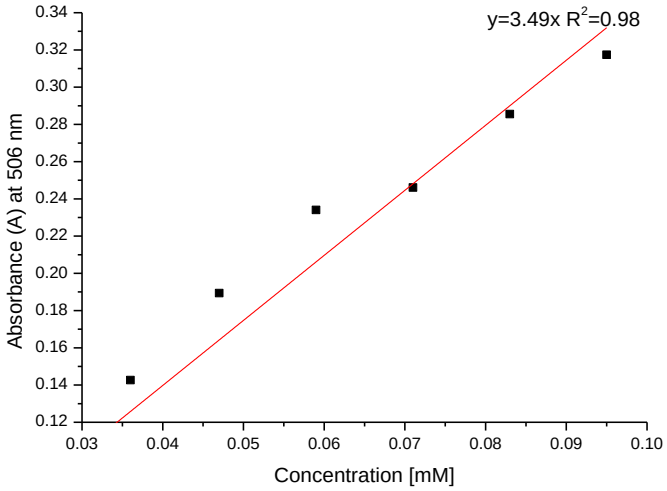

Figure 20. The calibration curve for TokyoGreen in ACN:DMSO:MQ (0.75:0.25:1.00) was constructed (y=3.49x adj. R^2=0.98) from the UV absorbance at 506 nm.

The polymers were dissolved in ACN, to which molar excess of TokyoGreen dissolved in DMSO was added. After conjugation the polymer-dye conjugate was purified via precipitation from diisopropyl ether until the diisopropyl ether solution no longer turned yellow. The polymer was dried under nitrogen flow. A known mass of the labelled polymer was dissolved in DMSO:ACN:MQ and the UV spectrum measured. The absorbance at λ = 506 nm was used to determine the concentration of dye in mol/L, based on the extinction coefficient 35493 M^{-1} cm^{-1} experimentally determined in the same solvent system (Figure 20). The azide ratio was determined by dividing the dye concentration by the monomer concentration (polymer weight divided by average monomer weight per L Table 7).

Table 7. A comparison between the targeted molar ratio (m/n) and that obtained from the dye test.

Sample	**M1: M2 (mol)**	**Molar ratio m/n** [#]
P18	1:100	1:85
P19	1:225	1:187
P21	1:570	1:494
P24	1:50	1:63
P25	1:100	1:107
P26	1:150	1:475
P27	1:200	1:219
P28	1:100	1:98
P29	1:100	1:95
P30	1:100	1:128
P31	1:50	1:62
P32	1:100	1:98
P33	1:200	1:556
P36	1:550	1:360
P38	1:25	1:50
P39	1:200	1:250
P40	1:100	1:126
P41	1:100	1:144

#: As determined by the dye test

IR spectroscopy was used to follow the depletion of the isocyanides around $\upsilon = 2100$ cm^{-1} during polymerization. The azide peak around $\upsilon = 2150$ cm^{-1} is very weak due to the relatively low concentration of azide dangling off the polymer backbone. The azide peak was therefore not used to determine the amount of reacted azide after conjugation quantitatively (Figure 21).

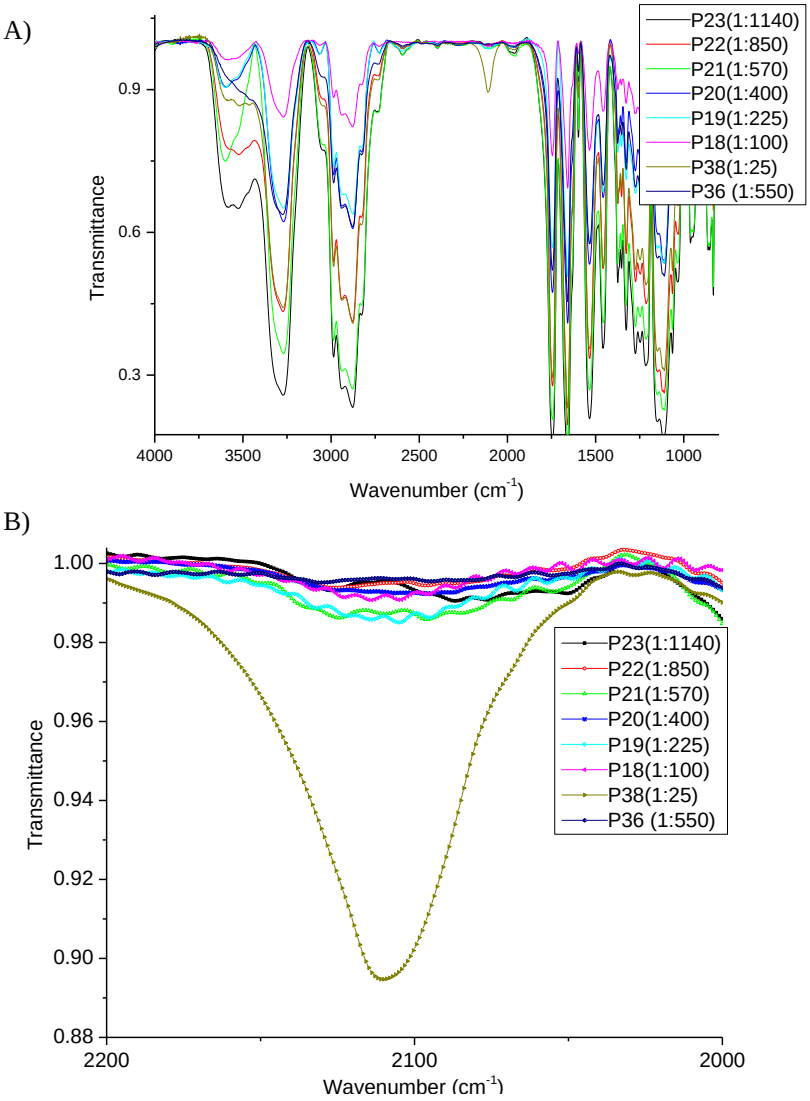

Figure 21. IR spectra of various ratios of azide PIC (a) 4000-850 cm^{-1} (b) 2200-2000 cm^{-1}.

Circular dichroism spectroscopy was used to investigate the secondary structure of the polymers. The CD spectra in phosphate buffered saline (PBS) were similar to those found in previous studies of the same material [10] and showed a Cotton effect with a maximum

around λ = 270 nm and a minimum around λ = 360 nm, indicating that the polymers form the secondary left handed helix structure (see, Figure 22). The azide ratio did not affect the CD signal. This indicates that the azide and the conjugations on the outside of the polymer do not influence the helical backbone structure that causes the CD signal.

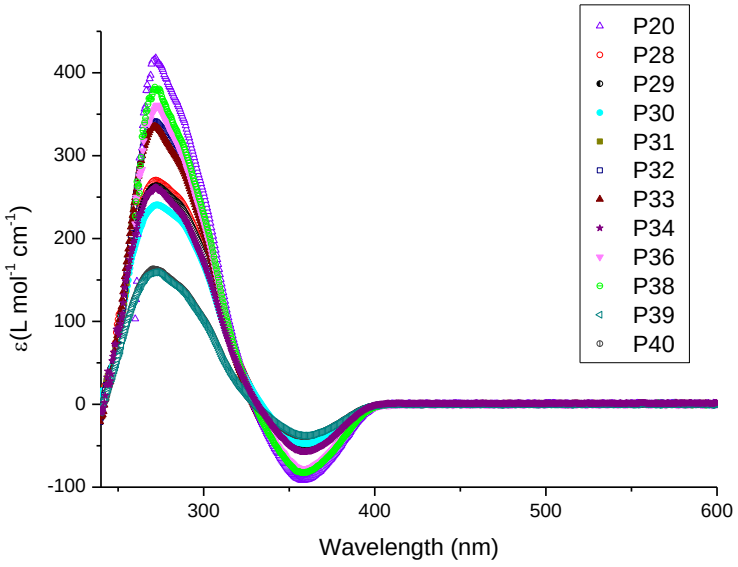

Figure 22. CD spectra of azide functiona PICs in ACN at: a) 4 mg/mL P20, P33-32, P36-38; b) 2 mg/mL P28-30, P34; c) 1 mg/mL P39-40.

Linear Rheology results

As the hydrogels are intended for biological applications, their mechanical properties in biologically relevant media need to be fully characterized e.g. phosphate buffered saline (PBS). To investigate the thermo responsive gel properties, the rheology of samples dissolved in PBS was measured with a standard temperature ramp (Figure 23). The storage modulus was observed to increase at the sol-gel transition temperature around 15-18 °C and

continues to rise with increasing temperature. This behaviour is in accordance with the rheological behaviour for similar polymers in MQ [5]. What has not been reported before is the sudden drop of the storage modulus that can be seen for some samples in Figure 23 (Figure 4) at increased temperatures. Why this drop-off is observed predominantly in high molecular weight homo- and copolymers (714-796 kg/mol) remains unclear. Separation of the rheology plates shortly after the drop-off occurred showed that there was still an intact (shrunken) layer of gel in the rheometer, but also an excess of water was excreted. The plate-plate geometry of the rheometer would slip because of the excreted water which is why the storage modulus drops rapidly if too much water is excreted. Cooling the sample down in the rheometer to re-dissolve it did not restore the sample. Possibly this was because the water excreted from the hydrogel was lost by evaporation and the homogeneity of the sample permanently disturbed. The excretion of water was also observed when heating a gel sample to 37 °C (mimicking the temperature ramp conditions) in a closed vial. Cooling the sample down at 0 °C for 5 minutes restored the sample and the rheology temperature ramp looked the same as a similar sample that was not heated. This indicates that the water excretion is reversible as long as there is no loss of excreted water. The excretion of liquid from gels is common in both natural [11] and synthetic polymer [12-13] systems. This phenomenon is known as syneresis and is caused by changes in interaction between the liquid and solid components of the solution [14]. It is also known that strain stiffening networks consisting of crosslinked semi flexible filaments exhibit negative normal stress when deformed in simple shear geometry [15-16], if this is not sufficiently incorporated into the rheometer settings the sample will contract away from the plate geometry and give senseless results. It is expected that this phenomenon would also be

present in the PIC network resulting in the expulsion of water and the contraction of the network above its LCST.

Temperature ramps were performed on polymers with exactly the same sample history in terms of dissolving time and freeze thaw cycles. An overlay for all these polymers at 1.6 mg/mL is shown in Figure 23. High molecular weight polymers (**P31-33**) 714-755 kg/mol exhibited higher stiffness and lower sol-gel transition temperatures (~12 °C) than the lower molecular weight polymers (**P24-P28**; **P30**) 361-629 kg/mol (see, Table 8).

Table 8. Storage moduli of azide functional PIC 1.6 mg/mL PBS at 37 °C

Samples	**Storage modulus G' (Pa)**
P24	101
P25	109
P26	76
P28	61
P30	79
P31	481
P32	279
P33	395
P41	34

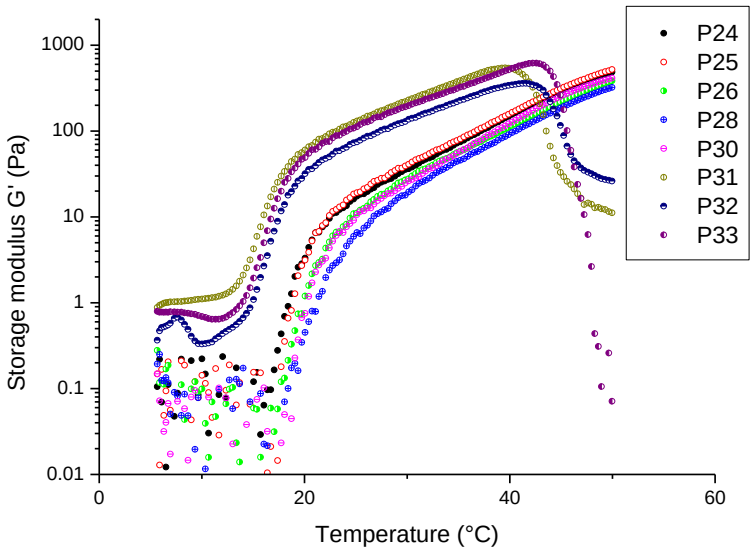

Figure 23. Storage modulus as a function of temperature for PICs at 1.6 mg/mL in PBS. Interestingly the a LCST of ~12 °C (P31-P33) high molecular weight and ~18 °C (P24-P28 and P30) low molecular weight PICs.

To avoid influencing the data by the effect of syneresis, the stiffness values at 25 °C were used to compare different samples. In Figure 24 it is observed that not only does the stiffness depend on concentration but on the molecular weight. The log of the modulus linearly with molecular weight (Figure 24) with adjusted R^2 values between 0.88-0.96.

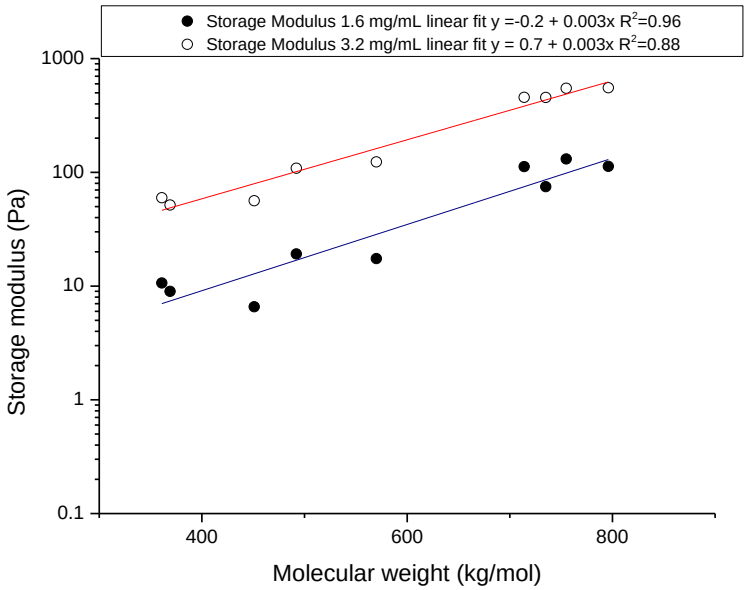

Figure 24. The storage modulus of the different molecular weights PICs in PBS at 25 °C at two different concentrations show similar trend in linear fit. (3.2 mg/mL: y=0.7(0.1)+0.003(1.9x10^{-4})x adj. R^2=0.96; 1.6 mg/mL: y=-0.2+0.003(3.7x10^{-4})x adj. R^2=0.88)

Non-linear rheology

As discussed in Chapter 1 most of the extracellular matrix proteins exhibit non linear strain stiffening behaviour under an applied force [6,12]. This behaviour was also observed in the synthetic PIC hydrogel system when exposed to similar strain conditions in the rheometer [7].

By plotting the differential modulus versus shear stress of a range of polymers the curves are not identical. In fact the critical stress (the point at which the differential modulus deviates from the linear regime) increases as molecular weight of the polymer increased (Figure 25).

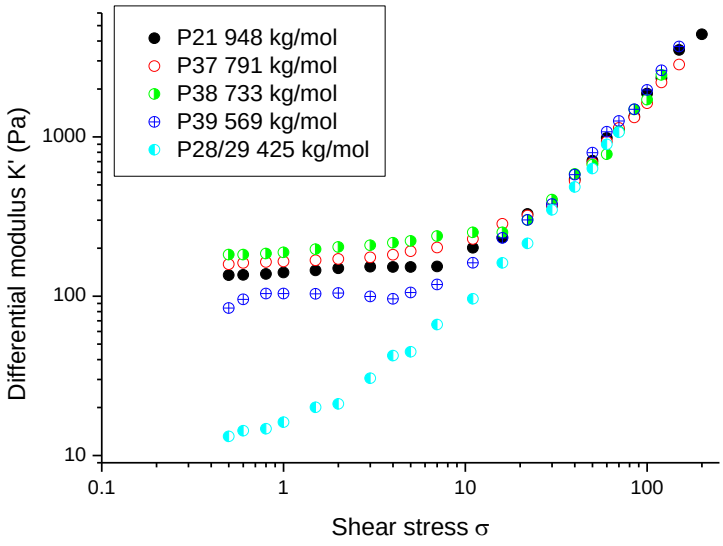

Figure 25. The differential modulus relative to the shear stress for a range azide functional PICs (1 mg/mL in MQ) with different molecular weights.

By plotting the critical stress values against the molecular weight, a linear relationship was observed. In the same graph the storage moduli of the same polymers were plotted against their molecular weight, here the relationship between stiffness and molecular weight is unclear (Figure 26). It would therefore appear that it would be possible to tailor the critical stiffness of the PIC by changing the molecular weight. It must be stated however that the polymers used to draw this conclusion were not synthesized from the same monomer sources.

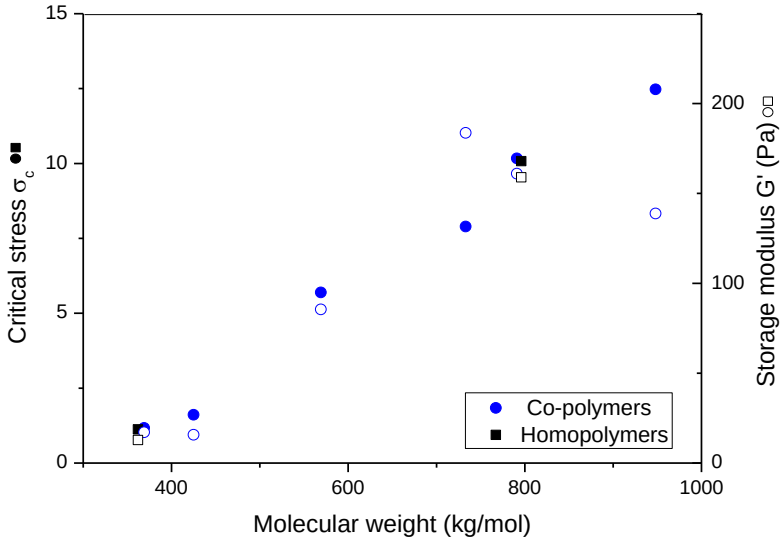

Figure 26. A graphical summary the of hydrogels mechanical properties: critical stress relative to the molecular weight and storage modulus relative to molecular weight. The homopolymers (P6 & P7) and the copolymers are shown. Polymers were freshly dissolved in MQ at 1 mg/mL for each measurement.

AFM length

To obtain a large enough batch of 1 in 100 azide polymer for both cell culture and animal studies it was investigated whether it would be possible to combine two relatively small batches of polymer to obtain one large batch with exactly the same characteristics as the individual batches. **P28** and **P29** were analyzed individually and as a combination by AFM. **P28** and **P29** showed mean lengths of 210 nm vs. 222 nm and the deviation between the median values was deemed small enough to be irrelevant 179 vs. 192 nm. After combination **P28/29** exhibited a slightly higher average length of 257 nm but the median was relatively unchanged 178 nm. This is clearly visualized by overlaying their individual

histograms (Figure 27). It was possible to calculate the $Đ$ from the AFM lengths by dividing the L_w/L_n : **P28** 1.4, **P29** 1.6, **P28/29** 1.7. It is therefore clear that the mixing of the two different batches did result in an increase in $Đ$.

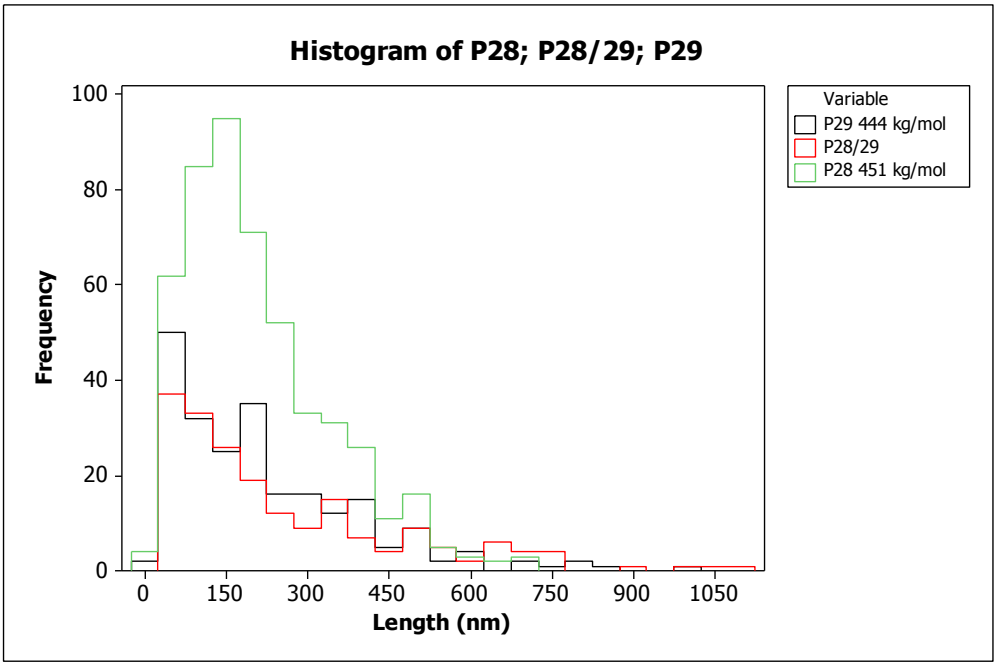

Figure 27. Histogram overlay of polymer lengths as determined by AFM height image analysis P28, P29 and the mixed sample P28/29 appear to have nearly the same mean and median distributions.

The high molecular weight polymers such as **P32** (azide: 1 in 100) and **P7** (homopolymer) exhibited a much large mean and median value compared to **P28/29** which is clearly visible by overlaying their histograms. Also by comparing two polymers of the same relative molecular weight **P7** ($Đ$ 1.6) with **P32** ($Đ$ 1.5) it is clear that the presence of 1 in 100 azides does not affect the $Đ$ adversely (Figure 28).

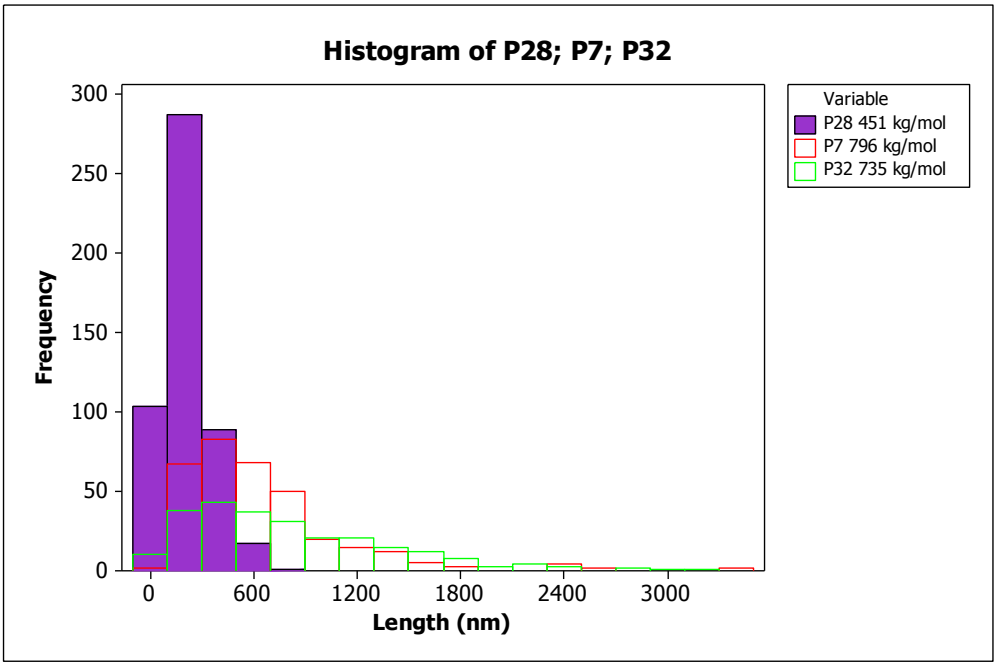

Figure 28. Histogram overlay of polymer lengths as determined by AFM height image analysis copolymer P28 ($Đ$ 1.4); homopolymer P7 ($Đ$ 1.6); azide copolymer m/n 1:100 P32 ($Đ$ 1.5).

1.2.3. Synthesis of terpolymers

The same synthesis strategy was utilized as previously mentioned with the only exception being the ratios of monomers used. The equivalents used were based on the equation determined in 1.1.1 and **M1** being deemed as equal to **M2** as its structure also consists of three ethylene glycol sub-units (see, Figure 29).

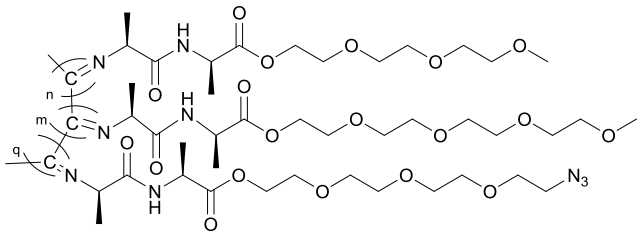

Figure 29. Oligo(ethylene glycol) isocyanopeptides terpolymers, the molar ratio of m/n/q was used to tailor the LCST.

Table 9. Terpolymer synthesis summary: molar fractions, molecular weight and yield.

Sample	**M2:M4 :M1 (mol) m/n/q**	**sol-gel (°C)**	$\overline{M_v}$ **(kg/mol)**	**Yield (%)**
P44	49.2:49.7:1	32	296	67
P45	41.1:57.9:1	35	304	63

Spectroscopic results

CD spectra (Figure 30) were consistent with those obtained from homopolymers and conventional copolymers.

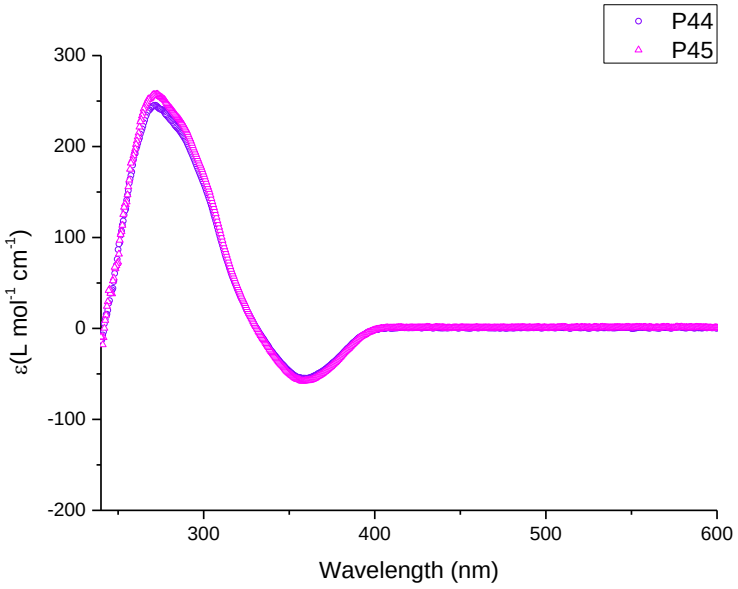

Figure 30. CD spectra of terpolymers (P44;P45) at 4 mg/mL in ACN.

Rheology

The rheological behaviour of the terpolymers was consistent with that of the copolymers (Figure 31).

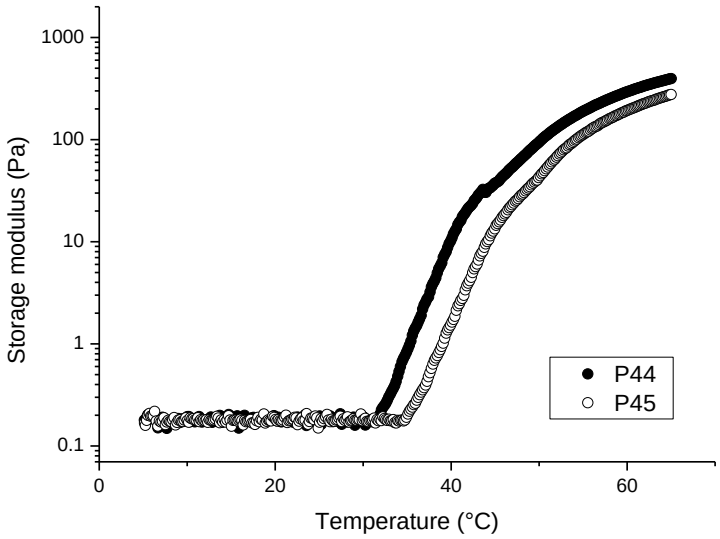

Figure 31. Storage modulus as a function of temperature for terpolymers (P44; P45) at 2 mg/mL in MQ.

The accuracy of the equation y=40.3-0.21x is summarized in the Table 10. The average deviation between the theoretical and actual sol-gel transition was 6.4 °C where the experimental value was consistently higher than the predicted value. As the equation was based on polymers synthesized from in-house monomer and with a high molecular weight (*ca* 500 kg/mol). The effect of molecular weight on sol-gel temperature was not incorporated in this equation, probably resulting in the observed systematic deviation of the calculated sol-gel temperature from the experimental one.

Table 10. Ratio of M2:M4 theoretical vs. Experimental Sol-Gel transition temperatures in °C

Samples	M2	M4	$\overline{M_v}$ (kg/mol)	sol-gel$_{Predicted}$ (y)	sol-gel$_{Actual}$	Difference
P15	61.1	38.9	296	27.5	39	11.5
P16	72.1	27.9	523	25.2	30	4.8
P17	79.2	20.8	525	23.7	32	8.3
P35	43.2	2.0	378	20.2	25	4.8
P44	49.7	50.2	296	29.9	32	2.1
P45	57.9	42.1	304	28.1	35	6.9

1.2.4. Acetylene copolymers

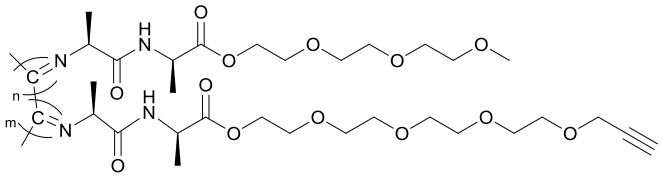

To introduce chemical handles that could later be used for the conjugation of specific dyes (e.g. Atto647N) through copper catalyzed Huisgen cycloaddition reactions copolymers with an acetylene functional isocyanide monomer **M3** were synthesized. These polymers would later be used for reptation and single molecule fluorescence studies. The molar ratio of acetylene (**M3**) to spacer monomer (**M4** or **M2**) was varied to create a library of possible polymers (Table 11). The same synthesis strategy was used as in 1.1.1 with the only difference being the monomers used.

Table 11. Copolymers synthesis summary: molar ratios, molecular weight and yield

Samples	**M3: M4 (mol)**	**$\overline{M_v}$ (kg/mol)**	**Yield (%)**
P46	1:1000	169	90
P47	1:1500	172	87
P48*	1:50	181	85
P49*	1:100	172	91
P54	1:50	99	34
	M3:M2 (mol)		
P55	1:100	352	73
P56	1:225	640	87
P57	1:400	677	53
P58	1:570	688	70
P59	1:850	669	70
P60	1:1140	642	70
P61	1:1000	571	

* Catalyst ratio of 1:1000, the rest of the polymers were all synthesized with a catalyst ratio of 1:10,000.

The molecular weight of the **P55-P60** was clearly affected by the addition of the acetylene functional monomer as the highest ratio of 1 in 100 resulted in a significantly different molecular weight with all monomers from the same source and prepared by the same person. It would therefore be fair to postulate that at densities higher than 1 in 100, acetylene incorporation into the polymer scaffold is possible but that this would result in chain termination, which would explain the lower average molecular weight at higher densities of acetylene.

Spectroscopic results

Surprisingly from comparing the CD of polymers with the same sample history but varied densities of acetylene monomer, no clear difference between the higher loading acetylene PIC was observed (Figure 32). In fact the highest density acetylene **P55** appeared slightly more intense than the other PIC in the series at the same concentration, which

suggests that although molecular weight was lowered due to the higher amount of acetylene functional monomer the helicity of the polymer was not affected.

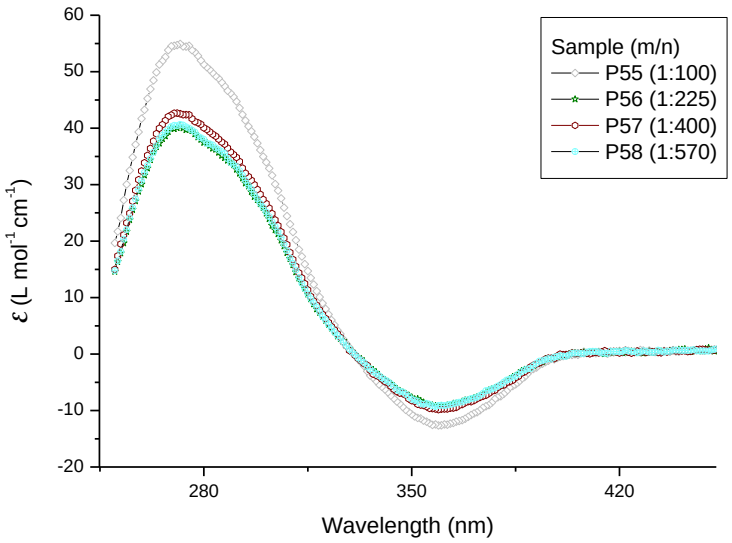

Figure 32. CD spectra of acetylene functional PIC at 1 mg/mL in DCM.

Rheology

The sol-gel transition seems to be unaffected by acetylene loadings since at m/n of 1 in 1500 and of 1 in 1000 tetra etylene glycol the transition temperature was 42 °C (**P47** and **P46**) and for 1 in 570 tri ethylene glycol (**P58**) it was 18 °C as was expected based on previous results obtained from the homopolymer of **M4** (tetra ethylene glycol 42 °C) and **M2** (tri ethylene glycol 18 °C) respectively (see, Figure 33).

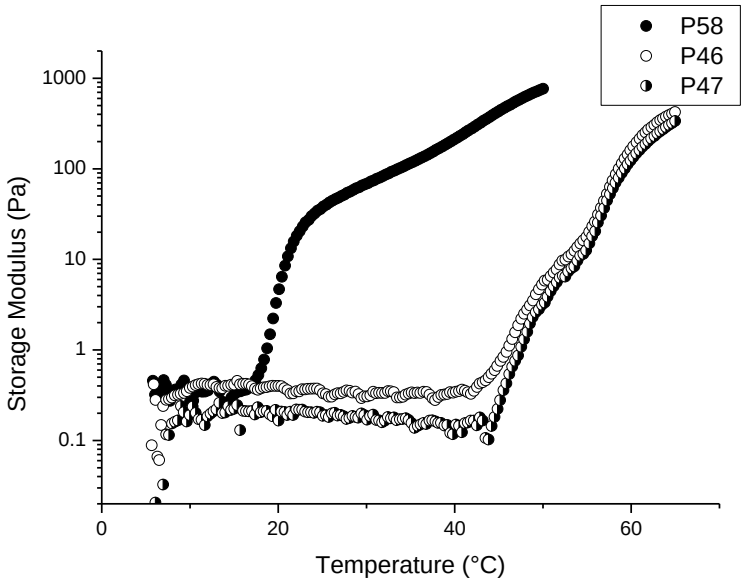

Figure 33. Storage modulus versus temperature for copolymers containing tetra ethylene glycol monomer (P46 and P47 1 mg/mL MQ) and copolymers containing tri ethylene glycol monomer (P58 at 1.8 mg/mL MQ) acetylene functional polymer.

Polymer chain length determined via AFM

Analysis of the acetylene functionalized polymer lengths indicate the same pattern as before, polymers with similar molecular weights have the same average length and shorter polymers have a lower average length. Polymer **P46** m/n 1:1000 had a *Đ* of 1.6, whereas polymers **P47** m/n 1:1500 had a *Đ* of 1.2 and **P54** m/n 1:50 had a *Đ* of 1.4. This can be visualized by overlaying the AFM length histograms (Figure 34).

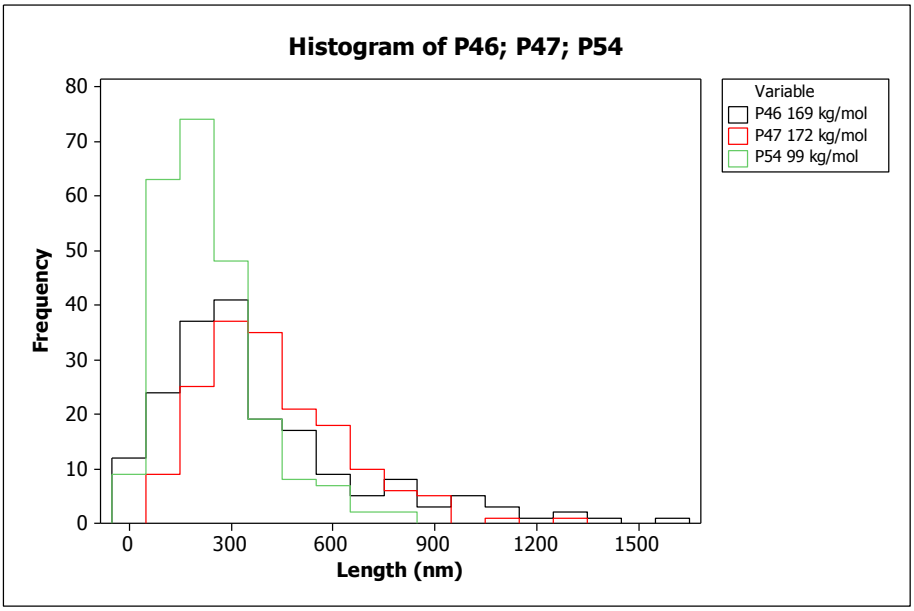

Figure 34. Histogram overlay acetylene functional polymer lengths as determined by AFM.

To conclude it was possible to vary the density of acetylene to spacer monomer up to a density m/n of 1:100 without adversely affecting the molecular weight at a catalyst ratio of 1:10,000. The lowered molecular weight did however not affect the *Đ* and therefore it is likely that although acetylene inclusion into the polymer scaffold is probable it results in chain end termination.

1.3. Synthesis of polymers with non natural aminoacids (M5)

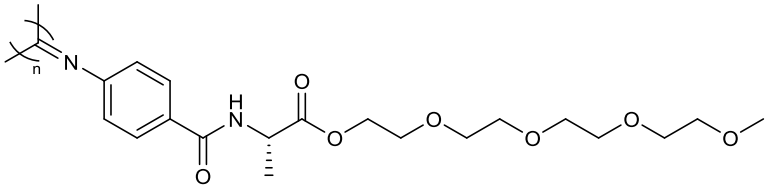

It would be very interesting to change stiffness of the PIC backbone especially when using it as a therapeutic carrier for biological applications as it would affect integrin clustering which is known to effect cellular fate [13]. In the group of Yashima *et al.* complex block-copolyisocyanides have been successfully synthesized in the presence of a platinum-palladium catalyst [14]. A monomer suitable for this system was designed that contains both the required para benzene isocyanide and the oligo ethylene glycol spacer to facilitate water solubility.

Compound **M5** (670 mg, 1.64 mmol) was dissolved in 5 mL dry toluene and a solution of $Ni(ClO_4)_2 \cdot 6H_2O$ (0.1 mM, 164 µL) was added. The reaction mixture was stirred for 5 days under air fitted with a $CaCl_2$ drying tube. This reaction was repeated in duplo, both times yielding dark brown, sticky solids with low yields.

Table 12. Homopolymers synthesis summary: molar ratios, molecular weight and yield

	$Ni(ClO_4)_2.6H_2O$ (mol): M (mol)	**Nanosight (nm)**	**$\overline{M_{AFM}}$ (kg/mol)**	**Yield (%)**
P62	1:100.000	228	226	22
P63	1:100.000	171	249	25

The polymers had no appreciable viscosity in either ACN or toluene at the concentration range used to analyse **P1-P61**. The solutions **P62-63** at 1 mg/mL in MQ did

not form hydrogels which is not uncommon for the homopolymers **M2** with a molecular weight of 200 kg/mol and lower. The low yield obtained for this polymerization indicates that this monomer suffered from some form of inhibition. Even though low molecular weight polymers were obtained, a substantial amount of time would be needed to optimize this system and it was decided that this would be outside the scope of this thesis.

Chain length distribution as determined via AFM

It is clear that the lengths of two different batches have the same mean and median, the polymers are short, but the synthesis was successful. The *Đ* for both were calculated by deviding L_w/L_n from the AFM lengths, **P62** 2.0 and **P63** 1.3.

Spectroscopic results

An intense Cotton effect centred at 364 nm in circular dichroism (CD) spectroscopy. Polymer **P62** showed a higher intensity than **P63** at the same concentration, indicating that the signal intensity increases with increasing molecular weight. Both spectra show a positive signal which is indicative of single handedness and the presence of a helical polymer (Figure 35).

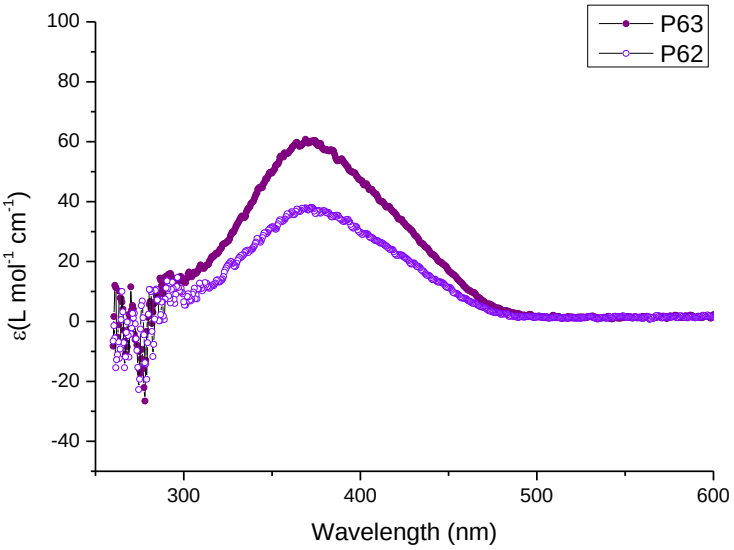

Figure 35: CD spectra of Abz-alanine homopolymers P62 and P63 at a concentration of 1 mg/mL in DCM.

In conclusion it was possible to synthesize a water soluble polyisocyanide di peptide based on the non natural aminobenzoic acid. In the future this monomer could be reacted using the platinum-palladium catalyst described in the work of Yashima *et al*.

2. Comparison of molecular weight determining techniques

Over the years it has become common practice in our group to determine the molecular weight of polyisocyanides from AFM image analysis and viscometry M_v. In general the polymer molecular weights are obtained from size exclusion chromatography (SEC) M_w. It was decided prudent to compare the molecular weight values obtained from the different techniques with each other. The viscometry technique is based on the flow rate of a dilute polymer solution over a known distance in a frictionless environment which after conversion with the Mark-Houwink equation was used to determine the molecular weight. The SEC technique relates to the hydrodynamic volume of a polymer and the time it takes the polymer to pass through a porous channel is relatable to its molecular weight as small polymers will permeate the porous medium more completely and therefore elute slower than larger polymers that will simply follow the path of least resistance.

By plotting the data obtained from SEC with viscometry a linear relationship between the molecular weights was obtained regardless of polymer composition (see Table 13 and Figure 36). The most noticeable difference was that the molecular weight obtained by SEC was consistently higher than that obtained by viscometry.

Table 13. Comparison of two molecular weight characterization techniques, viscometry vs. SEC

	Composition	$\overline{M_v}$ **(kg/mol)**	$\overline{M_w}$ **(kg/mol)**	**Difference**
P1	Homo tri	498	707	209
P64	Homo tri	571	786	215
P61	Acetylene tri	650	795	145
P65	Azide tetra	421	588	167
P36	Azide tri	835	967	132

The average M_v was 595 kg/mol with a standard deviation of 159 kg/mol and the average M_w was 769 kg/mol with a standard deviation of 139 kg/mol, which means that the the values from the two techniques were not statistically different from each other. The probability plot of each individual method was normally distributed and by comparing the two distributions with a standard two sample t-test a P value = 0.11 was obtained as this value is larger than 0.05 the two distributions are not statistically different from each other.

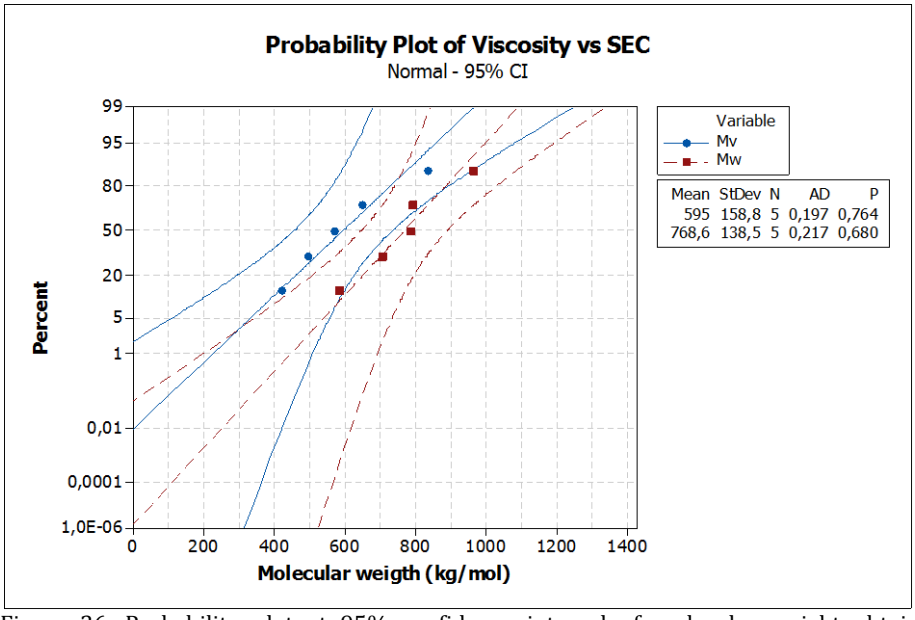

Figure 36. Probability plot at 95% confidence interval of molecular weight obtained by viscometery and SEC.

Comparing viscometery determined molecular weight (M_v) to molecular weight obtained by measuring the length of polymers visualized through atomic force microscopy (M_{AFM}), a more eratic comparison between techniques was observed (Table 14 and Figure 37).

Table 14. Comparison of two molecular weight characterization techniques, viscometry vs. AFM

Samples	**Composition**	$\overline{M_v}$ **(kg/mol)**	$\overline{M_{AFM}}$ **(kg/mol)**
P29	Azide tri	444	471
P28	Azide tri	451	502
P32	Azide tri	735	1752
P54	Acetylene tetra	99	652
P46	Acetylene tetra	169	940
P8	Homo tri	369	626
P7	Homo tri	796	1473

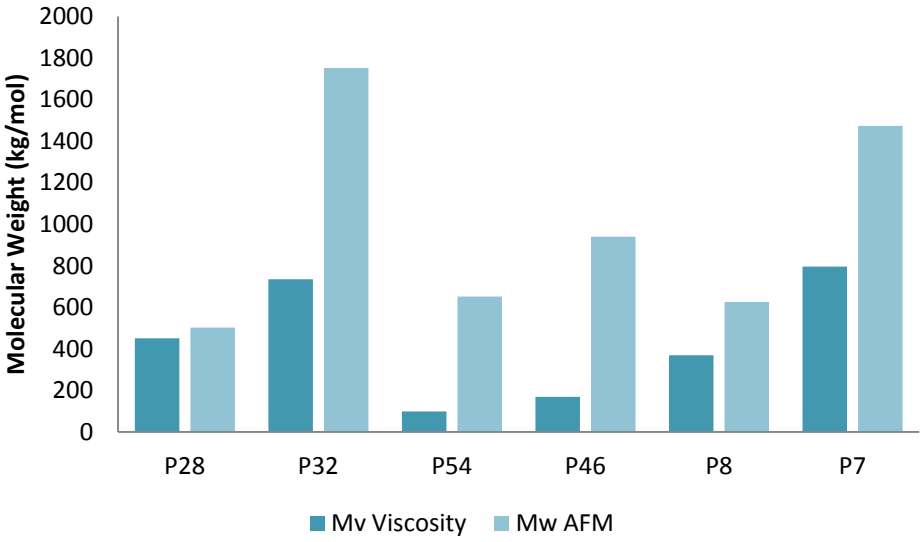

Figure 37. Box plot visual comparison of the molecular weights obtained from AFM and Viscometery.

The values obtained from manual AFM measurements are prone to human error as each polymer worm is measured manually by tracing the pixel length from the height image using Image J software. Based on a known scale bar these pixel values were converted to length values. The molecular weight range obtained by AFM measurement was also normally distributed. The average molecular weight obtained from M_{AFM} (916.6±505.5

kg/mol) and M_v (437.6±261.0 kg/mol) overlapped, which means that the average values from the two techniques were not statistically different from each other. When comparing the two data sets from AFM vs. viscometery using the two sample t-test a P value = 0.06 was obtained indicating that the two techniques is not statistically different from each other (see, Figure 38).

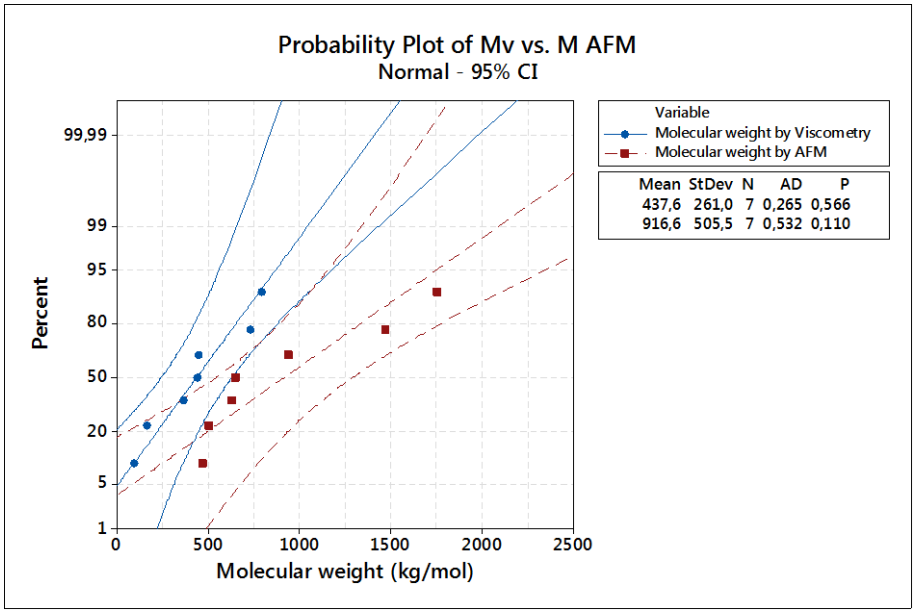

Figure 38. Probability distribution at 95% confidence interval of molecular weights obtained for the same samples using Viscometry and AFM.

3. Macrocopic observations of hydrogels

A rather unexpected observation of the polymer was made that during storage in its solvated state above its sol-gel temperature the hydrogels appear to shrink and expel water. It is proposed that this phenomenon is as a result of syneresis. Syneresis is a known to occur in synthetic PNIPAM hydrogels [9] and natural Agar hydrogels [8]. Syneresis is not

necessarily a negative phenomenon, but it does result in a dynamic environment which would affect cellular response as the forces the cells experience on their surfaces would be changing as the network they are attached to.

In the PIC system syneresis was quantified by measuring the loss of water from a hydrogel solvated in PBS over time. The water loss of gel samples in closed vials stored at 37 °C was measured by decanting at several time points and measuring the weight of the remaining sample. The results are shown in Figure 39 for gels of a low molecular weight (**P8** 369 kg/mol) and high molecular weight (**P7** 796 kg/mol) polymers at 1.6 and 3.2 mg/mL concentrations respectively. The expulsion of water was more pronounced in the beginning but never really ceased over the period of 8 days. At higher polymer concentrations and higher molecular weight this affect was more pronounced. Short polymers and lower concentrations provide more polymer mobility, which allows for enhanced macroscopic rearrangement that results in larger syneresis effect. Samples with higher molecular weight and higher concentrations would be less mobile, kinetically trapped resulting in reduced syneresis effect. In the PNIPAM system shrinking kinetics could be expressed in terms of the Tanaka-Fillmore equation Eq1and 2 [10]

$$\frac{|d(t)-d(\infty)|}{|d(0)-d(\infty)|} = \frac{|d(t)/d_0-d(\infty)/d_0|}{|d(0)/d_0-d(\infty)/d_0|} \approx \frac{6}{\pi^2} e^{\left(\frac{-t}{\tau}\right)} \text{ (Eq 1)}$$

Where, $d(t)$the gel diameter at time t and τ is the characteristic time of swelling. If it is assumed that a loss of solvent can be directly correlated to a loss in sample volume, therefore Eq 1 rearranged in terms of height yields Eq 2.

$$\frac{|h(t)-h(\infty)|}{|h(0)-h(\infty)|} = \frac{|h(t)/h_0-h(\infty)/h_0|}{|h(0)/h_0-h(\infty)/h_0|} \approx \frac{6}{\pi^2} e^{\left(\frac{-t}{\tau}\right)} \text{ (Eq 2)}$$

The proposed equation for the PIC hydrogel in terms of volume is:

$$\frac{\left|\frac{v}{\pi r^2}(t)-\frac{v}{\pi r^2}(\infty)\right|}{\left|\frac{v}{\pi r^2}(0)-\frac{v}{\pi r^2}(\infty)\right|} = \frac{\left|\frac{v}{\pi r^2}(t)/\frac{v_0}{\pi r^2{}_0}-\frac{v}{\pi r^2}(\infty)/\frac{v_0}{\pi r^2{}_0}\right|}{\left|\frac{v}{\pi r^2}(0)/\frac{v_0 v}{\pi r^2{}_0}-\frac{v}{\pi r^2}(\infty)/\frac{v_0}{\pi r^2{}_0}\right|} \text{ (Eq 3)}$$

This can be re organized as:

$$\frac{|v(t)-v(\infty)|}{|v(0)-v(\infty)|} = \frac{\left|r_t^2 h(t)-r_\infty^2 h(\infty)\right|}{\left|r_0^2 h(0)-r_\infty^2 h(\infty)\right|} \approx Ae^{\left(\frac{-t}{\tau}\right)} \text{ (Eq4)}$$

Where, A is a constant dependent on the volume change of the sample in terms of radius change. PIC hydrogel consists of 99.995 % solvent, the solvent is water which has a density of 1 mg/mL, therefore a change of volume can be defined as a loss in mass. The data was fitted to standard Exponential equation (Figure 39).

$$y = y_0 + Ae^{R_0 x} \text{ (Eq 5)}$$

Where, y_0 is the initial sample mass and $R_0 = \frac{1}{\tau}$ the rate of swelling. A negative R_0 would therefore be indicative of the rate of de-swelling.

Therefore, τ was equal to -48.1 for **P7** and -107.9 for **P8** (Figure 39), meaning **P8** (369 kg/mol) decreases in volume 2.24 times faster than **P7** (796 kg/mol). This is almost exactly the ratio of their molecular weight 2.16, further research in determining the rate of decay with regards to the molecular weight needs to be performed in the future to determine the statistical relevance of this mass loss result.

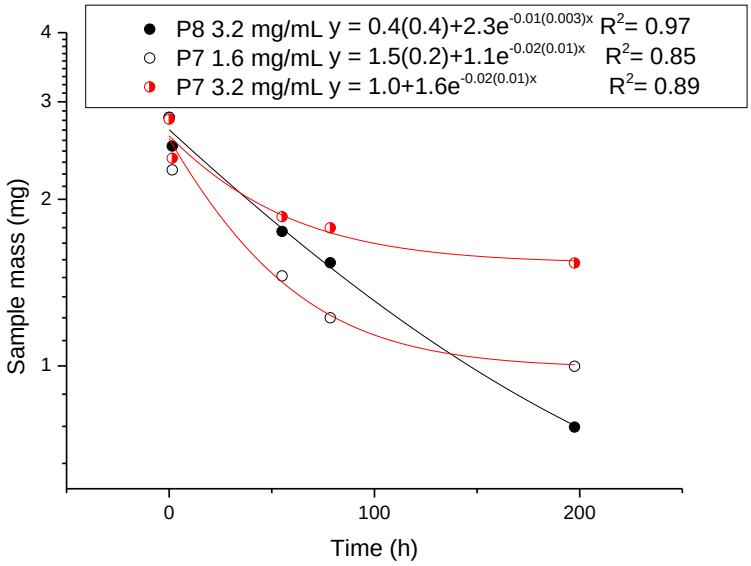

Figure 39. Loss of water from PIC hydrogels when stored at 37 °C. Sample mass after decanting excreted water is plotted against time.

For applications this effect should be taken into account when the polymers are used in a solvated hydrogel form e.g. cell culturing as this requires incubation at 37 °C for a prolonged time. The rate of syneresis decreases over time, perhaps a preconditioning incubation step would be advisable.

Rheology

The rheology of the PIC undergoing syneresis was measured by measuring the stiffness of three different polymers over the course of two weeks while storing the stock solutions in the refrigerator (4-7 °C). It was observed that the PIC hydrogels decrease in stiffness over time when stored in their liquid state. This meant that a PIC above its sol-gel

temperature would have a higher storage modulus on day one than the same stock solution of PIC measured after three days in the refrigerator. Comparing **P29**, **P8, P30** and **P32** was used to investigate the effect of molecular weight and azide ratio while exposed to the same environmental conditions. In Figure 40 the relative stiffness at 25 °C is plotted against the number of days stored in the refrigerator. The relative stiffness was determined by dividing the storage modulus of the sample on the day of the measurement by the storage modulus of the sample on the first day. **P8** homopolymer (369 kg/mol), **P30** 1:100 azides (361 kg/mol) and **P29** (444 kg/mol) exhibited a similar decrease in stiffness over time, indicating that azide ratio is not involved in this process. **P32** 1:100 azides (735 kg/mol) exhibited a smaller decrease in stiffness, indicating that higher molecular weight polymers may be less affected by syneresis. The storage effect was the most pronounced in the first four days and then seemed to stabilize. After two weeks the lower molecular weight polymers retained less than half of their original storage modulus. It was attempted to restore the hydrogels by re-dissolving them by stirring on ice, but the effect appears to be irreversible. The data was fitted by the exponential equation (Eq 5) and $R_0 = \frac{1}{\tau}$ in terms of stiffness determined for **P8**; **P29-30** to be average -0.3 compared to the -8.1×10^{-5}, which would suggest that the higher molecular weight polymers would take 4000 times longer to de-swell and reduce in stiffness when compared to their low molecular weight counterparts.

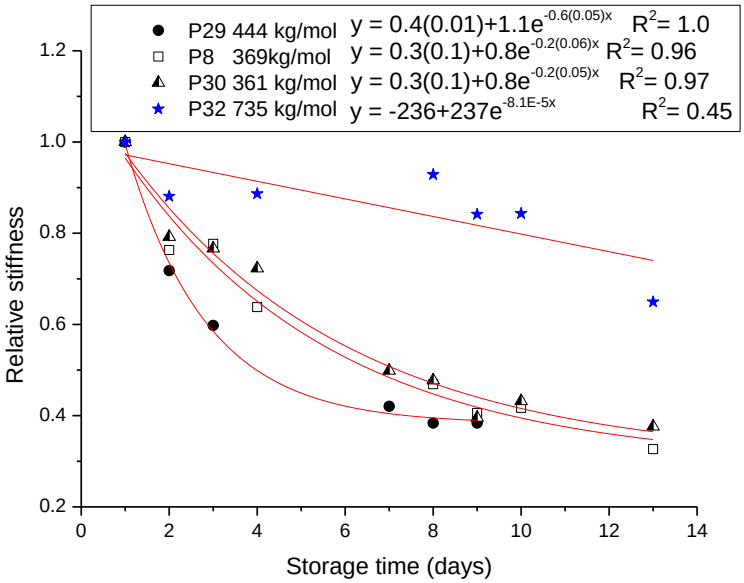

Figure 40. The relative stiffness of P29, P8 and P30 at 3.2 mg/mL at 25 °C, plotted against the storage time in days.

The decreased stiffness over time when stored in the solvated form is possibly caused by the increased flexibility of the individual polymer fibres below their sol-gel temperature causing increased mobility resulting in a higher probability of entanglement. These floppy pre-entangled fibres do not participate in bundle formation when finally heated above their sol-gel temperature decreasing the effective concentration of polymer present in the solution. This effect would critically effect the stiffness of the hydrogel as is clear from the following equations [7].

$$G_0(T) \propto N^3 \frac{c}{l_c^3} RT l_{p,0}^2(T) \quad \text{(Eq 6)}$$

$$c \approx \frac{G_0(T) l_c^3}{RT l_{p,0}^2(T) N^3} \text{ (Eq 7)}$$

Where c is the concentration, N is the bundle number which for this system was experimentally determined to be 9, $l_c^2$is the length between crosslinks (110 nm) and l_p^2 is the persistence length (460 nm); R is the gas constant (8.3 $LPaK^{-1}mol^{-1}$), and T is the absolute temperature at 25 °C (298 K). Therefore in the case of **P8** the initial stiffness at day one was 52 Pa and the stiffness after 13 days in the fridge was 17 Pa the concentration had effectively decreased from $1.8x10^{-13}$ mol/L to $5.9x10^{-14}$ mol/L which translates to a *3 fold decrease* in concentration over a two week time period which is in good agreement with the calculated average de-swelling value $R_0 = \frac{1}{\tau} = -0.3;\ \tau = -3.1.$

Conclusions

Several polyisocyanide homo-, co- and terpolymers were successfully synthesized. For the homo- and co-polymers containing tri ethylene glycol monomer, the range of molecular weights at a catalyst to monomer molar ratio of 1 in 10,000 was affected by the triethylene glycol monomer source. Statistically however the molecular weight ranges do not significantly deviate from each other and it can be concluded that even though the commercially sourced monomer does appear to result in polymers with lower average molecular weights this effect is consistent and the resulting polymers do not have any other difference in polymer properties that cannot be attributed to their lower average molecular weight.

The bulk stiffness and critical stress of homo- and co-polymers (at the same solution concentration) above their sol-gel transition temperature was shown to be linearly related to their molecular weights.

The sol-gel temperature of tri-ethylene glycol based homo and co-polymers were shown to be effected by up to 5 °C as a direct consequence of the average molecular weight. Polymers with molecular weights of <700 kg/mol showed LCST of ~12 °C and between 300-630 kg/mol showing LCST of 18 °C.

The addition of azide co monomer did not affect the overall mechanical characteristics of the polymer up to a density of 1:50. In co-polymers with acetylene handles, the highest loading of acetylenes that did not disrupt the obtainable molecular weight and mechanical properties was 1:100 acetylenes.

It was possible to synthesize co and tri-copolymers with targeted sol-gel transition (standard deviation 6.4 °C) temperatures by varying the ratio of tri- to tetra ethylene glycol monomer. The accuracy of this targeted sol-gel transition could be improved by synthesizing polymers with a lower average molecular weight to derive a new variable oligo ethylene glycol ratio for targeted LCST equation.

The effect of syneresis was observed in homo and co-polymer hydrogels with low and high molecular weights, above their LCST. The rate of de-swelling determined gravimetrically by measuring both the loss of sample mass and by using the rheometer to measure the reduction of stiffness over time. Regardless of the measuring technique the effect was more pronounced in low molecular weight polymers.

It was possible to synthesize a completely new PIC containing a non-natural aminobenzoic acid oligo ethylene glycol monomers.

Finally it was possible to reliably determine the molecular weight of the synthesized water soluble PIC with two non standard techniques (viscometry and AFM) that compared well with standard SEC technique.

Materials and Methods

Instrumental: The rheology measurements were performed on a TA Instruments Discovery HR-1fitted with a 40 mm Aluminium parallel plate geometry generally set to a gap of 750 µm for 1 mL of sample.

Procedure:

AFM

Hydrogels were deposited by direct contact with freshly cleaved HOPG or Muscovite Mica. All images were recorded with the AFM operating in Tapping Mode (TM) in air at room temperature, with a resolution of either 1024 x 1024 or 512 x 512 pixels, using scan rates of 1–1.5 lines/s. Commercial tapping-mode golden-coated silicon tips (NT-MDT) were used with a typical resonance frequency around 300 kHz.

Polymer chain lengths were evaluated using ImageJ (v1.43I) softwareS2 [17] to generate lengths in pixels, this could easily be converted to nm via scale bar on the original image. The length data was evaluated by Minitab16 statistical software (Minitab 16 Statistical Software (2010). State College, PA: Minitab, Inc. (www.minitab.com)).

The polymer chains heights and widths were measured using the Nanoscope software (v6.14r1) from Digital Instruments. Raw pictures were compensated for drift using the Nanoscope software (v6.14r1); no other processing was applied on the data used for the analysis.

Viscometry

To obtain the intrinsic viscosity of polymers, an Ubbelohde viscometer (Schott Instruments, Mainz, Germany) was used. A stock solution **(**4 mg/mL) of polymers was prepared in acetonitrile. From this stock solution, 4 mL of the following concentrations were prepared: 0.6; 0.5; 0.4; 0.3; 0.2 and 0.1 mg/mL. The solutions were loaded into a viscometry tube (nr. 1053431; Schott Instruments). The tube was placed into the water bath (25 °C) and allowed to equilibrate for 15 min before the measurement was started. The flow speed for each sample was measured four times and used to determine the kinematic viscosity ν. From this data, the reduced viscosity η_{red} and the inherent viscosity η_{inh} were calculated and plotted against the polymer concentration. The intrinsic viscosity $[\eta]$ represents the limiting value of η_{red} or η_{inh} at infinite dilution of the polymer, *i.e.*$[\eta] = \lim_{c\to 0} \eta_{inh}$. From extrapolation of η_{red} to c = 0, $[\eta]$ = could be obtained. Based on $[\eta]$, a molecular weight could be determined using the Mark-Houwink equation

$$[\eta] = K\overline{M_v}^{a} \quad \text{(Eq 8)}$$

Where $K = 1.4x10^{-9} dLmol^{a} g^{-(1+a)a)}$ and $a = 1.75$ [18]

Rheology

The polymer was dissolved in purified water (milliQ); PBS; cell culture medium by first swelling the polymer in a cooled solution before stirring for 16-72 hrs at 4 °C. Samples were inserted in the rheometer at 5 °C (i.e. as a liquid) and gelation occurred between the parallel plates by raising the temperature (2 °C/min). Drying of the sample was prevented by maintaining a moist atmosphere.
The measurements in the linear response regime were conducted at 2% strain at a frequency of 1 Hz. Temperature sweeps were recorded at a heating or cooling rate of 2 °C /min.
The measurements in the nonlinear regime were performed at 37 °C (25 minutes equilibrated) prior to starting measurement. Samples were exposed to a pre-stress protocol and superposing a small oscillatory stress with an amplitude of $|\delta\sigma| < 0.1\ \sigma$ at a frequency of $0.1 - 10$ Hz and allowed to equilibrate between consecutive steps for 3 min.

Single particle tracking analysis

Particle tracking studies were carried out on a Nanosight LM10 instrument equipped with an Electron Multiplication Charge Coupled Device (EMCCD) camera mounted on an optical microscopic system to track light scattered by particles that are present in a focused (80 μm) beam generated by a single mode laser diode with a 40 mW red laser illumination (640 nm). The cold polymer solutions containing platinum nanoparticles (average diameter 186 nm, concentration 106 particles/mL) were injected in a sample chamber of 0.5 mL size from which a volume of 120x80x20 microns was visualized under the microscope. The Brownian motion of the nanoparticles was tracked at 30 frames/s. NTA 2.3 software was used to evaluate the mean squared displacements of each visible particle (calibration 166 nm/pixel). Averaging over multiple particles (N > 50) yielded an average diffusion coefficient.

Mean square displacement (μm^2 vs $\Delta t/s$) was calculated by evaluating only the data of true particles with at least 30 steps. The mean square displacement of each particle was automatically calculated by using Matlab. The code for which can be supplied if needed.

Polymer Synthesis

Compound **M2** was dissolved in 2 mL of freshly distilled toluene. The catalyst stock solution of 1 mM was prepared by dissolving 39 mg of $Ni(ClO_4)_2 \cdot 6\ H_2O$ in 10 mL absolute ethanol and 90 mL of toluene. A volume of this stock solution equivalent to 10^{-4} of the total **M2** mols was transferred via pipette into the mixture of **M2** and toluene. The flask was placed in an ice bath and fitted with a $CaCl_2$ drying tube. The mixture was diluted with distilled dry toluene to obtain a final concentration of 50 mg/mL monomer. After 2-3 h the mixture became extremely viscous and additional solvent was added to obtain a concentration of 25 mg/mL. This mixture was allowed to stir for a total of 72 h. The polymer was isolated via precipitation into diisopropylether. This precipitation cycle was repeated three times to obtain a broad range of yields.

The dye test and how the azide concentration was determined by using UV:

A TokyoGreen stock solution was made by dissolving BCN-TokyoGreen (2.2 mg, 43.7 μmol) in DMSO (1 mL). The polymer to be tested was dissolved in ACN at a concentration around 3 mg/mL, with a total volume of 3 mL. The polymer solution was stirred for one hour at 5 °C to completely dissolve it. A volume of the TokyoGreen stock solution corresponding to 2 equivalent of BCN-TokyoGreen per azide was pipetted to the polymer solution. The mixture was stirred overnight at room temperature and was then precipitated in diisopropyl ether (40 mL). The diisopropyl ether was decanted of and the remaining polymer was air dried for one hour. This precipitation process was repeated two times. After the third precipitation the polymer was air dried over night under a nitrogen flow.

UV analysis protocol used for **P18-21;42**: PIC were dissolved in ACN:DMSO:MQ in a ratio of 0.75:0.25:1. The extinction coefficient of the TokyoGreen in this mixture was determined to be 35493 M^{-1} cm^{-1}.

The UV analysis protocol used on **P24-31**: An alkaline methanol solution was made by dissolving KOH (5 mg, 0.125 mmol) in methanol (100 mL) and diluted by pipetting 1 mL of this solution to 100 mL methanol. The pH of the resulting solution was around 9 as indicated by pH paper and was alkaline enough to make sure all the TokyoGreen that is added will be deprotonated. The polymer was weighed and dissolved in the alkaline methanol at 1.00 mg/mL and multiple UV-vis spectra were recorded, starting with this 1 mg/mL polymer solution and then diluting down until the TokyoGreen absorption at λ = 500 nm was in between an absorbance of 0.1 and 1 The absorption at λ = 500 nm of the dye conjugated polymer sample is then used to calculate dye concentration with the TokyoGreen extinction coefficient. The extinction coefficient of the deprotonated TokyoGreen in methanol was determined to be 87812 M^{-1} cm^{-1} by calculating the slope of the absorption at λ = 500 nm over concentration after measuring solutions of TokyoGreen in the alkaline methanol at different concentrations.

Statistical calculations

Homopolymers:

The two sample t-test was performed on two data sets obtained from homopolymers synthesized from **M2** from different sources using Minitab17 statistical software.

Table 15. Two sample t-test comparing homopolymers obtained from Chiralix vs. in-house M2.

Data Set	**N**	**Mean**	**StDev**	**Mean**
Chiralix	4	466	90	45
in-house	4	652	133	67

Difference = μ (Chiralix homo tri) - μ (in-house homo tri)

Estimate for difference: -185.5
95% CI for difference: (-392.1; 21.1)
t-test of difference = 0 (vs ≠): t-value = -2.31 P-value = 0.069 degrees of freedom (DF) = 5

Azide functional co-polymers:

The two sample t-test was performed on the molecular weight ranges obtained for azide functional co-polymer using different sources of **M2**.

Table 16. Two sample t-test comparing azide co-polymers from Chiralix vs. in-house M2.

Data Set	**N**	**Mean**	**StDev**	**Mean**
Chiralix	8	472.6	99.3	35
in-house	14	786	171	46

Difference = μ (Azide PIC Chiralix) - μ (Azide PIC in-house)
Estimate for difference: -313.7
95% CI for difference: (-434.5; -192.9)
t-test of difference = 0 (vs ≠): t-value = -5.44 P-value = 0,000 DF = 19

Molecular weight determination techniques

The two sample t-test was performed on the two methods of determining molecular weight viscometery and SEC.

Table 17. Two sample t-test comparing two techniques for determining molecular weight (M_v vs. M_w)

Data Set	**N**	**Mean**	**StDev**	**Mean**
viscometry	5	595	159	71
SEC	5	769	139	62

Difference = μ (viscometry) - μ (SEC)
Estimate for difference: -173.6
95% CI for difference: (-396.5; 49.3)
t-test of difference = 0 (vs ≠): t-value = -1.84 P-value = 0.108 DF = 7

The two sample t-test was performed on the two methods of determining molecular weight viscometery and AFM.

Table 18. Two sample t-test comparing two techniques for determining molecular weight (M_{AFM} vs. M_v)

Data Set	N	Mean	StDev	Mean
AFM	7	917	505	191
viscometry	7	438	261	99

Difference = μ (viscometry) - μ (AFM)
Estimate for difference: 479
95% CI for difference: (-17; 975)
t-test of difference = 0 (vs ≠): T-value = 2.23 P-value = 0.056 DF = 8

Mean square displacement: Analyzing the effect of changing polymer concentration on pore size

The cold solution of hydrogel with concentrations of either 3.0, 1.0, 0.75, 0.25 and 0.13 mg/mL polymer was doped with PtnP of an average size 186 nm in a final concentration of 10^6 particles/mL. The hydrogel PtnP mixture was injected in a sample chamber/gasket of 100 μl size from which a volume of 120x80x20 microns was visualized under the microscope. The Brownian motion of the nanoparticles was tracked at 30 frames/s. NTA 2.3 software was used to determine the average size of the particles based on the Strokes-Einstein equation. The mean square displacement of individual platinum nanoparticles was determined by Matlab the code can be supplied if required.

References

1 Schwartz, E. *et al.* Macromolecular multi-chromophoric scaffolding. *Chemical Society Reviews*, **39**, 1576-1599, (2010).

2 Cornelissen, J. J. L. M. *et al.* β-Helical Polymers from Isocyanopeptides. *Science*, **293**, 676-680, (2001).

3 Comstock, M. J., Ha, T. & Chemla, Y. R. Ultrahigh-resolution optical trap with single-fluorophore sensitivity. *Nat Methods*, **8**, 335-340, (2011).

4 van Buul, A. M. *et al.* Stiffness versus architecture of single helical polyisocyanopeptides. *Chemical Science*, **4**, 2357-2363, (2013).

5 Kouwer, P. H. *et al.* Responsive biomimetic networks from polyisocyanopeptide hydrogels. *Nature*, **493**, 651-655, (2013).

6 Malm, C. J., Genung, L. B. & Lapham, G. B. Cellulose Ester Viscosities by Ball-Drop Method. *Analytical Chemistry*, **22**, 656-661, (1950).

7 Wong, I. Y. *et al.* Anomalous Diffusion Probes Microstructure Dynamics of Entangled F-Actin Networks. *Physical Review Letters*, **92**, 178101, (2004).

8 Jeon, J.-H. & Metzler, R. Fractional Brownian motion and motion governed by the fractional Langevin equation in confined geometries. *Physical Review E*, **81**, 021103, (2010).

9 Lutz, J.-F. Polymerization of oligo(ethylene glycol) (meth)acrylates: Toward new generations of smart biocompatible materials. *Journal of Polymer Science Part A: Polymer Chemistry*, **46**, 3459-3470, (2008).

10 Erk, K. A., Henderson, K. J. & Shull, K. R. Strain Stiffening in Synthetic and Biopolymer Networks. *Biomacromolecules*, **11**, 1358-1363, (2010).

11 Boral, S., Saxena, A. & Bohidar, H. B. Syneresis in agar hydrogels. *International Journal of Biological Macromolecules*, **46**, 232-236, (2010).

12 Gan, T., Guan, Y. & Zhang, Y. Thermogelable PNIPAM microgel dispersion as 3D cell scaffold: effect of syneresis. *Journal of Materials Chemistry*, **20**, 5937-5944, (2010).

13 Tanaka, T. & Fillmore, D. J. Kinetics of swelling of gels. *The Journal of Chemical Physics*, **70**, 1214-1218, (1979).

14 Huglin, M. B. & Yip, D. C. F. Microsyneresis region in poly(2-hydroxyethyl methacrylate) hydrogels. *Macromolecules*, **25**, 1333-1337, (1992).

15 Kang, H. *et al.* Nonlinear Elasticity of Stiff Filament Networks: Strain Stiffening, Negative Normal Stress, and Filament Alignment in Fibrin Gels†. *The Journal of Physical Chemistry B*, **113**, 3799-3805, (2009).

16 Janmey, P. A. *et al.* Negative normal stress in semiflexible biopolymer gels. *Nat Mater*, **6**, 48-51, (2007).

17 Schneider, C. A., Rasband, W. S. & Eliceiri, K. W. NIH Image to ImageJ: 25 years of image analysis. *Nat Methods*, **9**, 671-675, (2012).

18 van Beijnen, A. J. M. *et al.* Helical Configuration of Poly(iminomethylenes). Screw Sense of Polymers Derived from Optically Active Alkyl Isocyanides. *Macromolecules*, **13**, 1386-1391, (1980).

Chapter 4 : Crosslinking PIC as a means to increase bulk stiffness

Abstract
The influence of mechanical stiffness of fibrous gels on the cellular fate was shown and discussed in previous chapters. It has been shown that for the PIC system bulk stiffness can be controlled through the concentration of polymer in solution. It would be desirable to access even higher bulk stiffness, therefore crosslinking as a means to increase this bulk stiffness was investigated using both covalent and physical crosslinking strategies. The covalent chemistries investigated were: copper catalyzed and thiolyne click chemistry, SPAAC, dithiobridge and Schiff base formation, and the Schmidt reaction. The physical crosslinking strategies investigated were: pore blockage with gelatine spheres, Host-guest chemistry and ionic interactions. There was no significant increase in stiffness observed for any of the applied crosslinking strategies. It is fair to conclude that even in the bundle dominant state (crosslinking above sol-gel temperature) inter polymer fibre crosslink was dominant resulting in "frayed" bundles that adversely affected bulk stiffness.

Introduction

As highlighted in previous chapters the PIC hydrogel closely resembles in many ways the mechanics and architecture of an extra cellular matrix (ECM), but the bulk stiffness at 37 °C resides well within brain tissue matrix stiffness. If the differentiation of cells involves integrin cluster formation, then it would hold that to access muscle and bone phenotypes, the PIC bulk stiffness Pa range [1] would need to be increased to the kPa range [2]. The stiffness of the initial family of PIC hydrogels is depended on the concentration of the material in solution and the stiffness ranges from 10-10^2 Pa. The stiffness of the ECM however can range from 10^2 -10^4 Pa [3]. Stiffer gels are expected to have more physical interactions and different dynamics with the cell affecting proliferation and differentiation [4-5]. It was hypothesized that the addition of crosslinks would result in increased bulk

stiffness to approach the ranges possible in ECM. In Nature, crosslinks are either covalent or physical, but impermanent as the ECM makes room for the newly formed tissue (enzymatic bond cleavage) [6]. In synthetic materials covalent crosslinks are usually permanent, while physical crosslinks are based on non-covalent interactions between the polymer chains making them dynamic [7]. Physical crosslinking could be investigated by looking into ionic interactions through the addition of suitable counter ions [8-9], the formation of interpenetrating networks [10-11], physical blocking of the pores with suitable particles and dynamic bond formation through host-guest chemistry [12].

In Figure 1 covalent crosslink with and without a spacer (pink), physical blockers (spheres), dynamic crosslinks formed between cucurbit[8]uril (CB8 host) and 2 phenylalanine (guest) molecules and physical entanglements cross bundle crosslinking possibilities are schematically summarized. It is known from previous work that in the PIC system as the distance between crosslinks (l_0) decreases, the bulk stiffness will be increased [1], therefore the introduction of crosslinks should result in change in bulk stiffness (Equation 1).

$$G_0(T) \propto N^3 \frac{c}{l_c^2} RT l_{p,0}^2(T) \quad \text{(Eq 1)}$$

Where N is the bundle number which for this system was experimentally determined to be 9, $l_c^2 \approx l_o$is the length between crosslinks and l_p^2 is the persistence length of the individual polymer (AFM); R is the gas constant, and T is the absolute temperature.

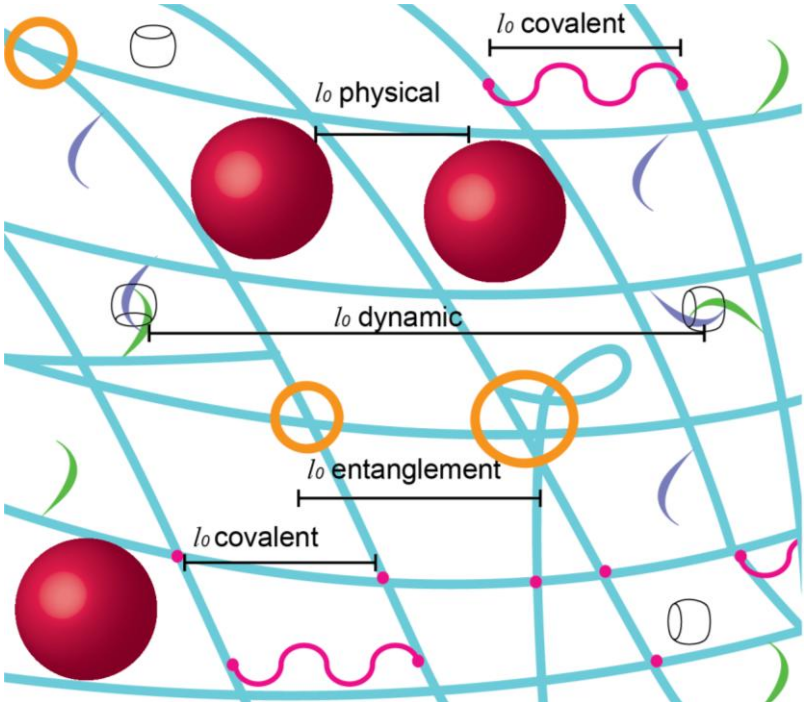

Figure 1. Network structure of PIC showing diverse crosslinks: entanglements, dynamic bonds, covalent bonds and physical blockages [7]

In a system of rigid polymers (such as PIC) with flexible crosslinks, the length and flexibility of these crosslinks strongly affect the network elasticity (Figure 2). Affine theory predicts a linear scaling of bulk stiffness with the crosslink density (Equation 2) [13].

$$G_{1D} = \frac{1}{8} n \frac{k_{cl} K_{EM}}{k_{cl} + K_{EM}} \text{ (Eq 2)}$$

Where G_{1D} is the shear modulus G normalized by the linear modulus G_0 as a function of strain ϵ (1D), n is the number of flexible crosslinkers, k_{cl} is the spring constant of the crosslinker and K_{EM} is the spring constant of the system. Therefore it was expected that if the stiff filament of length (L) has a constant persistence length and the persistent length of

the bundle is the same as for the individual polymers [1] a change in crosslink density should directly affect the bulk stiffness.

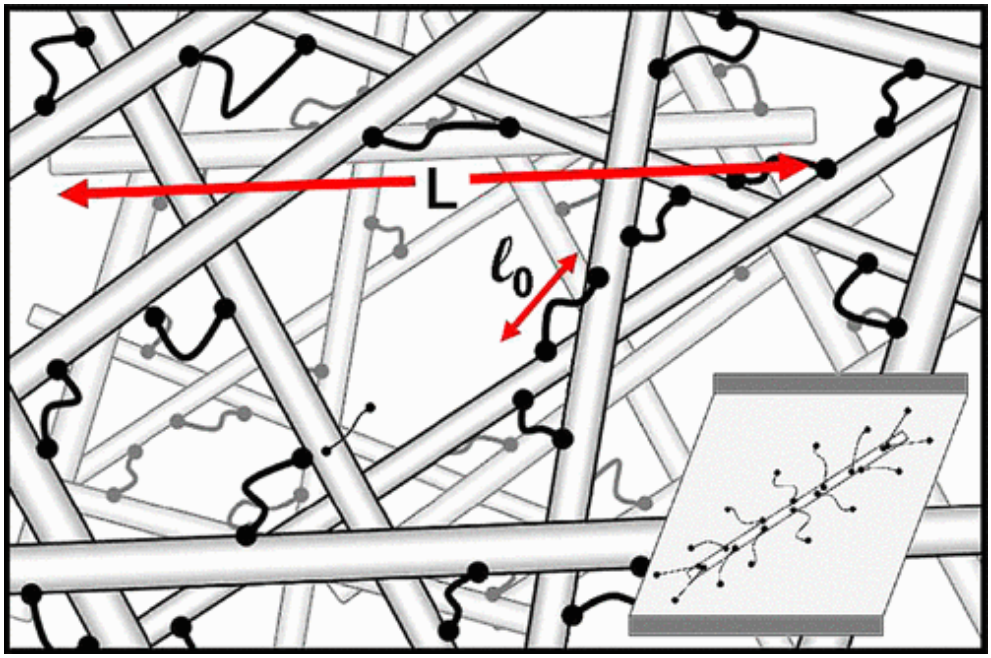

Figure 2. Schematic representation of an isotropic stiff polymer network with highly compliant cross-linkers. The inset illustrates the proposed nonuniform deformation of the crosslinkers on a single filament in a sheared background medium [13].

Results and discussion

To avoid affecting the bundle formation, which is inherent to this system which gels upon heating above its lower critical solution temperature, it would be preferable to form crosslinks in the gelled (bundle dominant) state. However it is not possible to perform the crosslinking reactions since the dynamics of crosslinking in a static system are slow. In addition, it is not possible to transfer a gelled sample to the rheometer as it resulted in sample damage and uneven sample heights were formed which prevents reliable rheology experiments. Crosslinking experiments were therefore performed by mixing the reagents together at 5 °C in its liquid (fibre dominant) state and heating instantly to either 25 °C or 37 °C. As the loading and heating was performed rapidly after the mixing of reactants it was assumed that most of the crosslinking occurred during the gelling process or in the gelled state.

1. Covalent crosslinking:

A variety of covalent bond formation reactions were explored to form crosslinks (Figure 3): A. Schiff base formation [14], B. the Schmidt reaction [15], C/D. dithio-bridge formation [16], E. strain promoted acetylene to azide cycloaddition [17-18] and F. thiolyne UV catalyzed click chemistry[19].

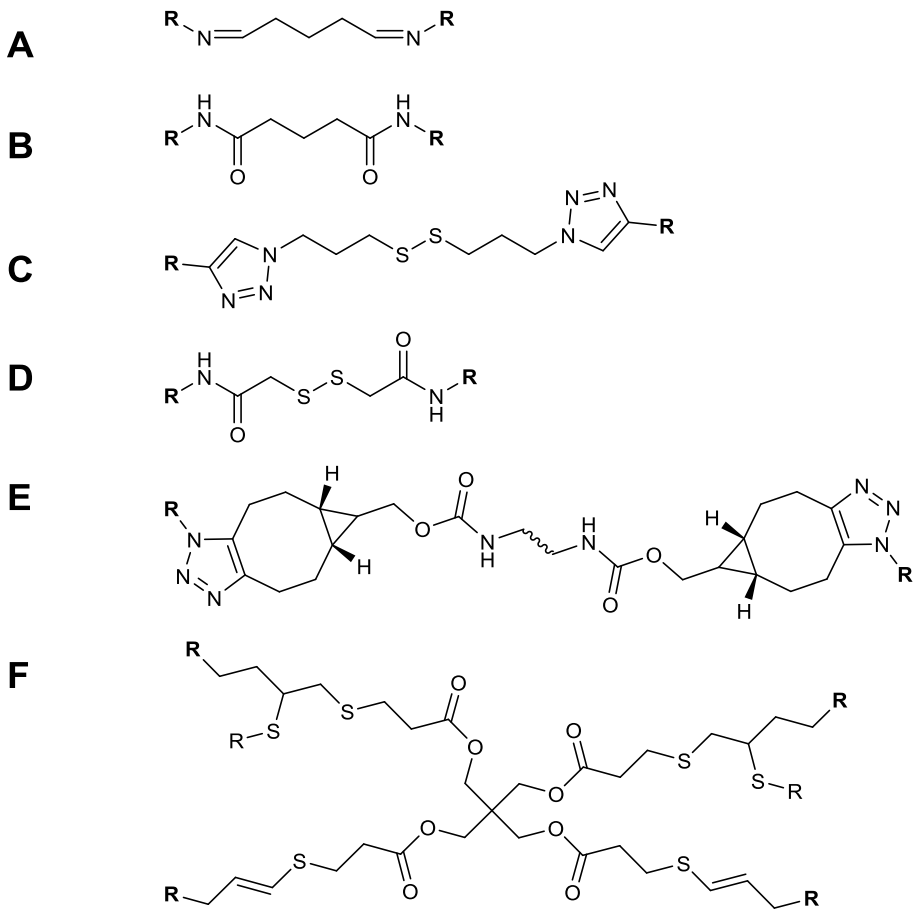

Figure 3. A schematic summary of the covalent crosslinks investigated in this chapter. For individual chemical reactions see the appropriate subsection.

A. Schiff base formation

The formation of a Schiff base as a means of rapidly forming crosslinks has been explored for injectable hydrogel formulation in the past [14,20-21]. The nucleophilic attack of the amine on the aldehyde forms an imine which without the use of a reducing agent forms labile crosslinks.

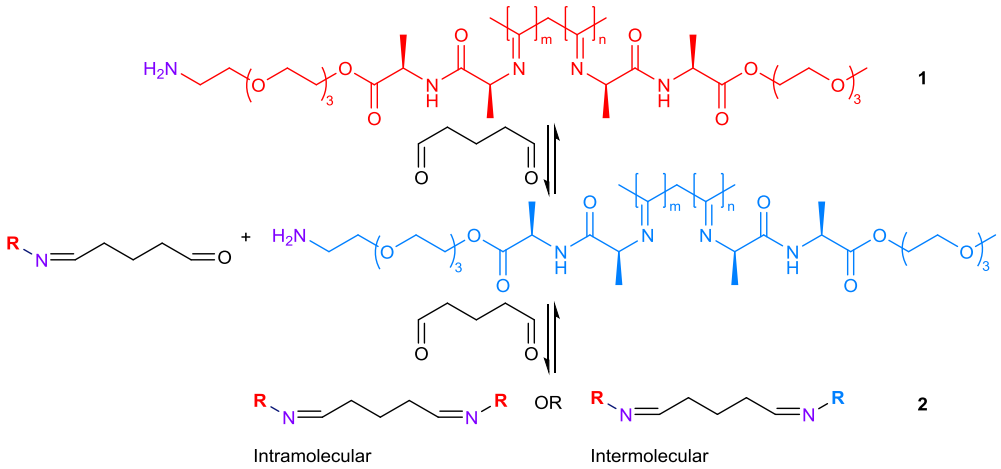

Figure 4. Schematic representation of Schiff base formation between PIC-NH_2 and gluteraldehyde, both inter bundle and intra bundle crosslinking is shown.

In the polyisocyanide system imines were obtained by reacting amine functional polyisocyanide with a bis functional aldehyde. It was opted to use gluteraldehyde as an easily accessible water soluble bis-aldehyde. The amine functional PIC **1** was obtained in good yields 58-87% by the chemical reduction of the azides of azide functional PIC **P36** in the presence of a slight excess of triphenylphospine and water over the course of two weeks at room temperature. The amines were quantified utilizing a fluorescein NHS dye test which revealed conversions ~75 % (Table 1, Experimental section). Nucleophilic attack of the amine on the bis-aldehyde (0.5 molar equivalents relative to amines present), followed by loss of water then forms the imine crosslinked network **2**. Crosslinking may occur either intramolecularly meaning between free amines on the same polymer fibre, which is not likely in the gelled state, due to the long persistence length of the polymer. Intermolecular crosslinking between two different polymer fibres is possible but it is more likely that crosslinking would occur predominantly in the bundled state due to proximity. In the

bundled state two different possibilities (not depicted in Figure 3) arise either crosslinking will occur between two different bundles or within the same bundle as the crosslinking reaction was performed above the sol-gel temperature.

The polymer **1** (n/m of 1:625; triethylene glycol based; 835 kg/mol) the ratio of "spacer" monomers was 625 to every 1 amine. The polymer was dissolved in a slightly acidic pH 6 phosphate buffer over night at 0 °C. Once dissolved, the gluteraldehyde was added, the mixture loaded onto a cooled (5 °C) plate-plate geometry and heated rapidly to 25 °C at which temperature the time sweep experiment was performed. Somewhat surprisingly the storage modulus of the sample was lower as a result of the presence of gluteraldehyde when compared to the **1** without gluteraldehyde under the same reaction conditions (Figure 5). It was hypothesized that the intra bundle crosslinking was dominating; a consequence of the short length of the gluteraldehyde spacer. A possible solution for this would be to use a longer bis-functional aldehyde crosslinker which would allow for inter-bundle crosslinking. In addition it is also possible that the crosslinking reaction was not complete within 3 h.

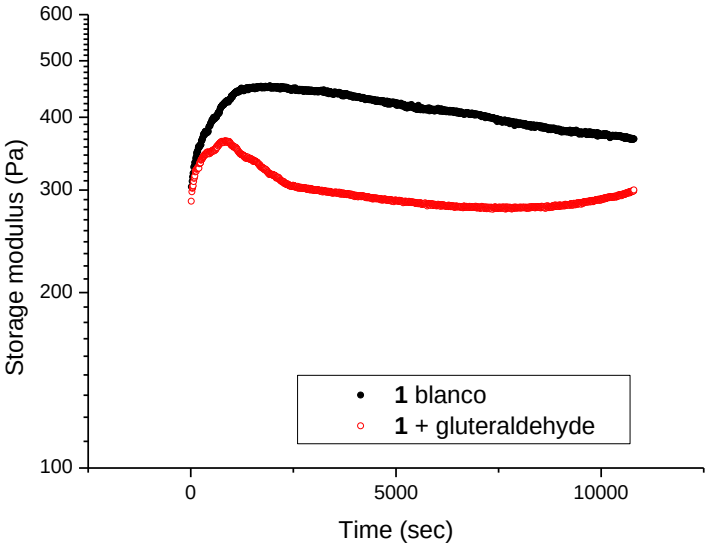

Figure 5. Storage modulus as a function of time at 25 °C for 1 in pH 6 phosphate buffer with gluteraldehyde (0.5 equivalent) and without. Both samples were at a concentration of 1.6 mg/mL.

B. Azide-gluteraldehyde

Aubé *et al*. [15] showed that the covalent bond formation between azides and aldehydes can give high yields and that the reactivity of the reaction can be increased by warming or by the addition of an acid. The reactions were carried out with the water soluble gluteraldehyde as a bis-aldehyde linker in a pH 6 phosphate buffer to activate the aldehydes for nucleophilic attack. The mechanism is shown in Figure 6.

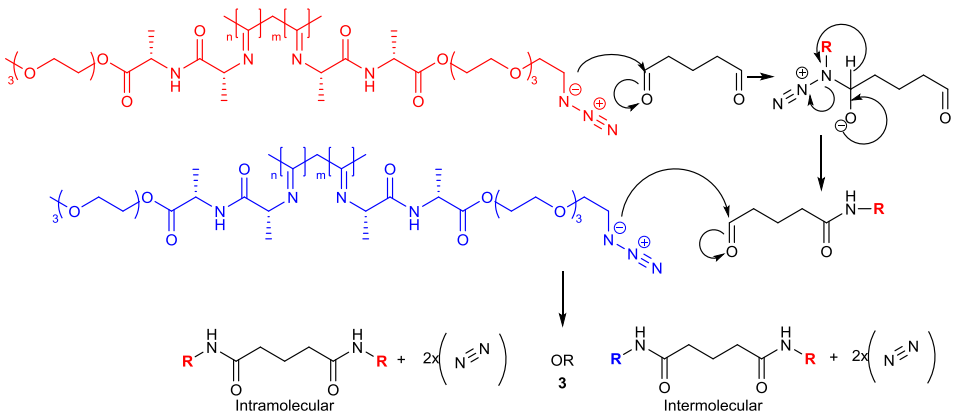

Figure 6. Schmidt reaction between PIC-azide and gluteraldehyde. The azide first attacks the carbonyl, followed by a hydride transfer that causes nitrogen to leave.

As with the Schiff base reaction the rheology experiment was performed by cooling the polymer solution (**P30**; m/n of 1:128; triethylene glycol based; 361 kg/mol) on ice and placing the solution (with and without gluteraldehyde) in plate-plate geometry at 5 °C. The mixture was heated rapidly to the measuring temperature of 37 °C for 3 h. An increase in stiffness was initially observed in both samples during the time sweep experiment (after rapid temperature ramp 5- 37 °C), it was postulated that this was due to the dynamic rearrangement of the lower molecular weight polymers into stable bundled state at 37 °C (Figure 7). If this "blanco" behaviour is ignored it is still clear that the crosslinked polymer **3** has the same stiffness as the blanco at 0 s (~ 50 Pa), higher stiffness at 2500 s (96 vs. 86 Pa) and a lower stiffness at 7500 s (86 vs. 92 Pa). This was interpreted as a change in crosslink sites from a predominantly inter bundle crosslinked system to a predominantly inter polymer crosslinking system which would result in a false assumption about the persistence length of the bundle being equal to that of the single polymer.

Solving this problem by increasing the temperature to increase reactivity of the reaction was felt not to be ideal as the effect of syneresis could not be excluded at higher temperatures and increasing the acidity of the solution could result in destabilization of the helix itself. Therefore this reaction does not appear to be suitable for the design constrains of the PIC system.

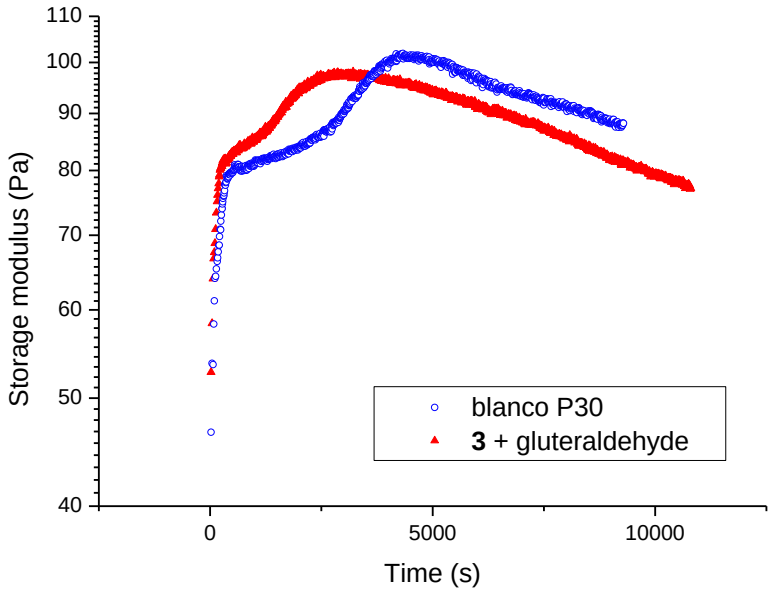

Figure 7. Storage modulus as a function of time at 37 °C for P30 in pH 6 phosphate buffer with gluteraldehyde (0.5 molar equivalent) and without. All samples were measured at a concentration of 1.6 mg/mL.

In conclusion to understand what exactly happened to the architecture of the bundles during crosslinking it would be advisable to compare the two samples either by AFM or multi angle light scattering.

Dithio bridges:

The advantage of utilizing dithio bridges as a dynamic covalent crosslinking strategy is that although the bonds are strong, the system is still tailorable through external stimuli. It is therefore possible to cleave dithio bridges with light, heat or mechanical force and to exchange them with other thiols dependent on external stimuli such as the pH, temperature and redox potential [22]. Palumbo *et al*. showed that for hyaluronic acids hydrogels that the formation of dithio bridges through oxidative crosslinking was an effective biocompatible crosslinking strategy [16]. The formation of di-thiol bridges were investigated through two different strategies. The first was by decorating acetylene polyisocyandes with thiols through the Huisgen cycloaddition to a short azide functional thiol. The second by the decoration of amine functional polyisocyanides with *N*-succinimidyl *S*-acetylthioacetate (SATA) is subsequently converted to a free thiol when required [23]. The formation of the dithio bridge can be obtained by air oxidation or induced by the addition of either hydrogen peroxide or a molar equivalent of DMSO.

1.1. C. Free thiols

Acetylene functional polyisocyanide (**P46**; m/n of 1:128; tetraethylene glycol based; 169 kg/mol) was decorated with thiols through the copper catalyzed click reaction with 3-azidopropane-1-thiol (Figure 8). The molecular weight as determined via the viscometery technique was unchanged after the introduction of thiols giving polymer **5** (169 kg/mol vs.

160 kg/mol), however after the formation of the disulphide bridges the molecular weight increased substantially for polymer **6** (169 kg/mol vs. 197 kg/mol).

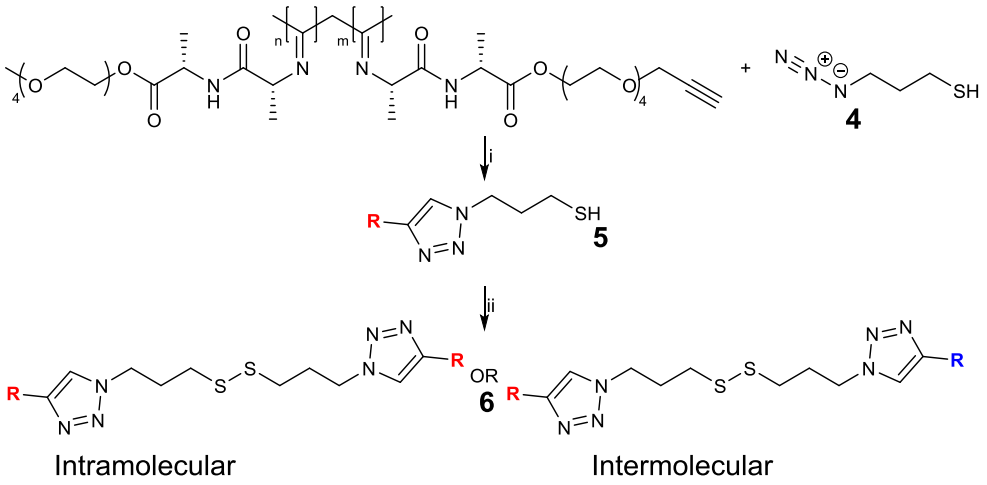

Figure 8. Reaction scheme of the formation dithio-crosslinked PIC, i) CuBr, TBTA under argon atmosphere, stirring 72 h, 60 % yield, ii) DMSO, DCM stirring at room temperature for 5 h, 90 % yield.

The crosslinking samples were prepared by first dissolving the polymer in PBS at 1 mg/mL and standard rheological experiments were performed (temperature ramp, frequency sweep, logarithmic amplitude sweep, linear amplitude sweep) upon warming. The sol-gel transition observed in the temperature ramp experiment of the acetylene tetra ethylene based polyisocyanide **P46** and its relating dithio-crosslinked polymer **6** was essentially unchanged showing the characteristic sol-gel transition temperature of 42 °C (Figure 9).

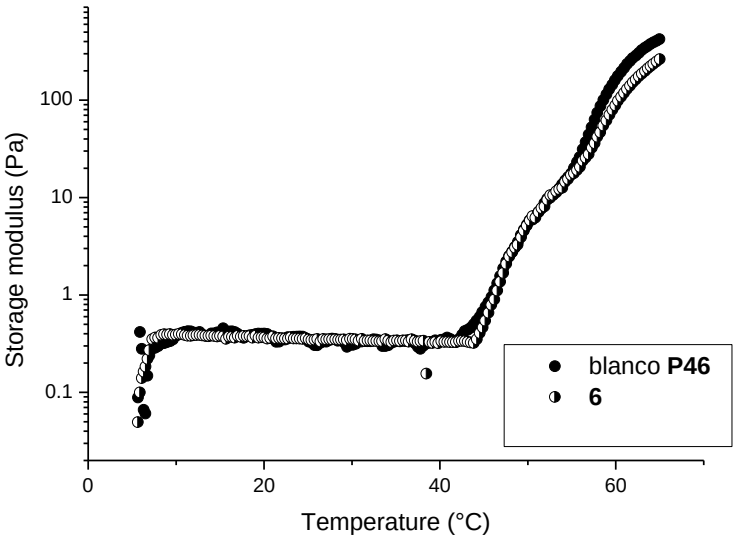

Figure 9. Storage modulus as a function of temperature, before and after crosslinking , for P46 via dithio bridge formation.

It is only in the linear amplitude sweep that **6** appeared to be stiffer initially and able to resist breaking for longer than the blanco (Figure 10).

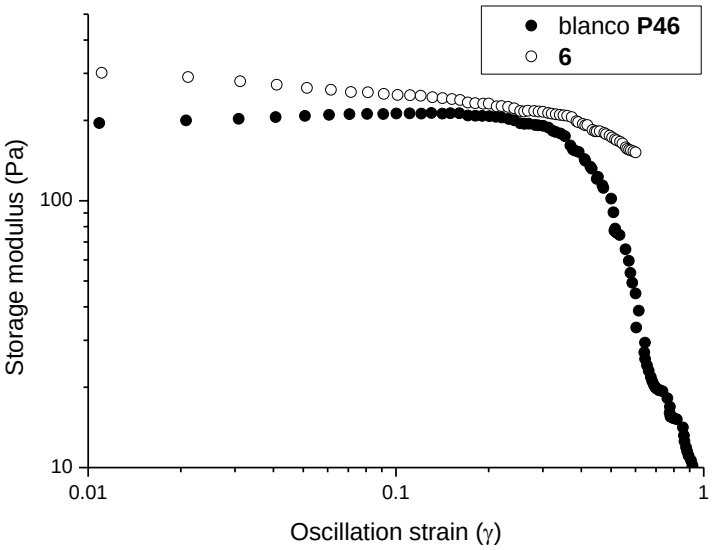

Figure 10. Storage modulus as a function of strain (linear amplitude sweep of 0.001-1 strain at increments 0.1 at 10 rad/s) of dithiobridge crosslinked polymer.

This interesting increase in ultimate fail strength indicates that the complexity of the system has changed through the addition of crosslinks, but that ultimately the stiffness was unaffected.

1.2. D. Protected thiols

The idea behind using a protected thiol was that crosslinking could be induced at a defined time point. As seen in Figure 11, the protection group was introduced by conjugating *N*-succinimidyl S-acetylthioacetate (SATA) to amine appended polyisocyanide **1**. To determine the conversion of amine to thiol a small sample of **7** was deprotected with the deacetylation buffer and quantified via an Ellmans test. The conversion was assumed to

be complete as m/n from the Ellmans test was 1:330 thiols (twice the initial concentration of amines). The deprotected solution was oxidized to obtain the dithio hydrogel by the addition of a small percentage of hydrogen peroxide and allowed to react at room temperature for one week.

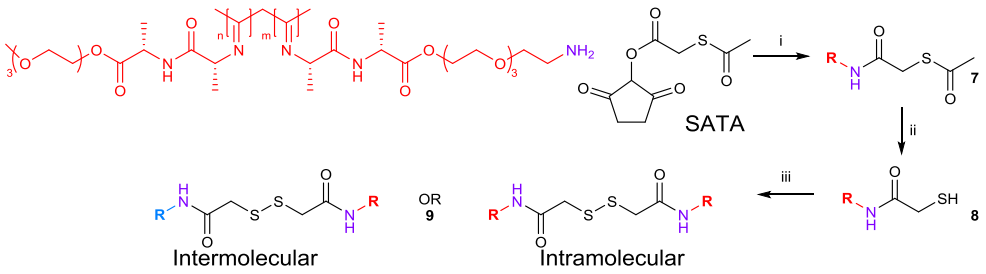

Figure 11. Reaction steps required to convert PIC-NH2 to dithio crosslinked hydrogel i)SATA-NHS, DMF, 7 days; ii) deacetylation buffer 2 h, 100 % conversion; iii) 10% H_2O_2, rt, 1 week.

The samples were loaded onto the rheometer and heated to 37 °C. A standard frequency sweep, amplitude sweep and finally time sweep was performed at 37 °C. Figure 12 shows the time sweep rheology overlay of crosslinked PIC **9**, SATA protected PIC **7** and deprotected free thiol PIC **8**. It is clear that **9** had a higher storage modulus than **8** and 7 (18 vs. 11 Pa) respectively.

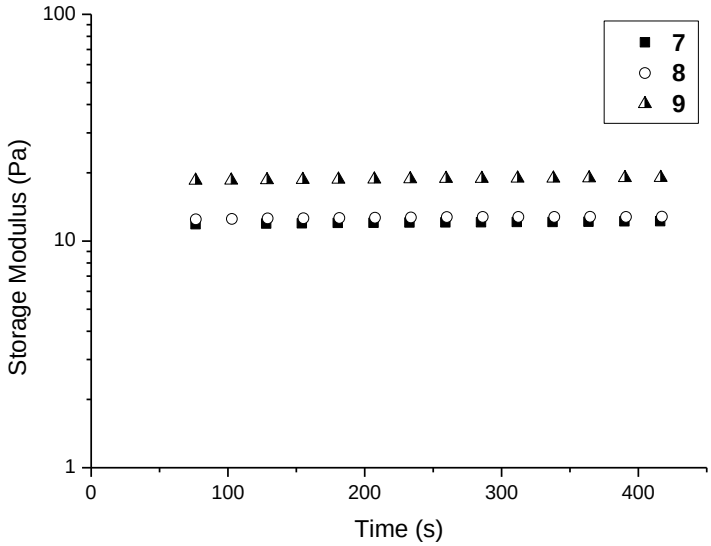

Figure 12. Storage modulus as a function of time of dithio crosslinked polymer before and after crosslinking (7-9) at 37 °C in a concentration of 6.75 mg/mL in PBS.

The route of dithio bridge formation is therefore promising as crosslinking strategy. An optimum loading of thiols per PIC still needs to be obtained as a m/n of 1 in 1000 of **6** seemed too few and even though a much clearer increase in bulk stiffness was observed with the higher ratio of m/n of 1 in 625 of **9**, it still did not result in significant increases of the bulk stiffness.

E. Strain promoted acetylene azide click chemistry (SPAAC)

The strain promoted acetylene azide click reaction is known to be biocompatible, highly reactive, non toxic and a relatively simple way of introducing complexity to biological molecules [24-25]. The SPAAC reaction has been used successfully to introduce crosslinks into PEG hydrogels [17]. It was postulated that this method would also be

translatable into the PIC system as the use of bisfunctional PEG bicyclononyne crosslinker could be used to crosslinking of azide functional polyisocyanides. The linker opted for was a bisfunctional polyethylene glycol (10,000 g/mol, ca. 135 nm) which would be water soluble and long enough to cross the PIC pore size of ca. 100 nm. In Figure 13 the SPAAC crosslinking reaction, which is biologically inert, high yielding and rapid under physiological reaction conditions [26] is depicted.

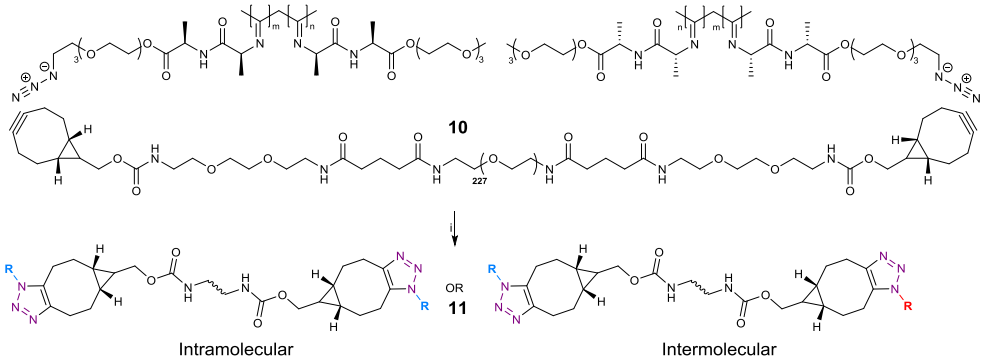

Figure 13. Schematic representation of crosslinking PIC with bis functional PEG i) PBS at 37 °C for 1 h.

The functionalization of bis-functional PEG-amine with BCN-NHS to result in **10** was successful as the molecular weight increased on average with the mass of two BCN-units as seen in the MALDI-ToF spectrum (Figure 14, Experimental section).

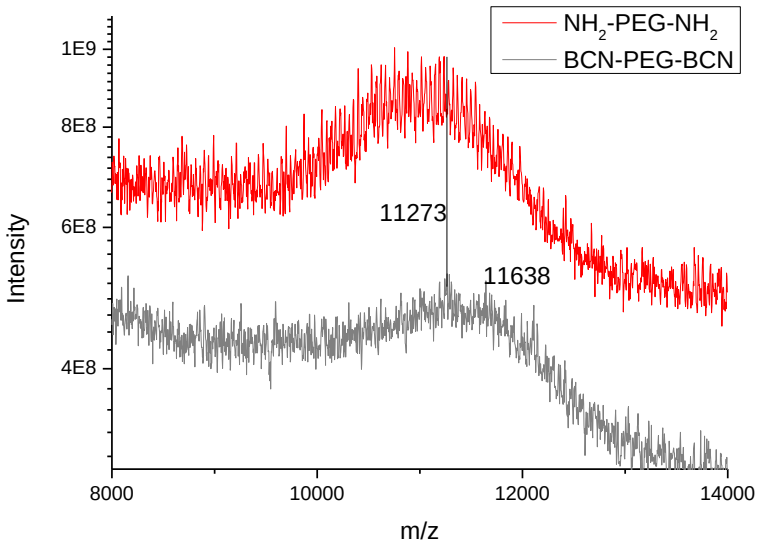

Figure 14. MALDI-ToF of starting PEG-bis-amine versus PEG-bis-BCN.

The effect of crosslinking via the SPAAC reaction between a bis-BCN-PEG (**10**) to the azide PIC (**P30**; m/n of 1:128; triethylene glycol based; 361 kg/mol) on the bulk stiffness was investigated. A time sweep rheology experiment at 37 °C showed no noticeable change in storage modulus occurred (Figure 15). The overall stiffness has decreased as was observed in the blanco experiment with non-functional PEG, but no other effects were visible.

The time of the reaction (1 h) was possibly to short as the decoration of PIC with BCN-peptides requires at least 4 h to reach full conversion. Longer experiments were not possible inside the rheometer as syneresis affected the sample volume and the experiment could not be adjusted to compensate for this. All attempts at transferring externally crosslinked gelled

samples onto the rheometer failed as, even when the sample was not broken, uneven sample surface resulted in irregular results. Another possibility for the lack of success with this method could be that the PEG might be in its more disordered coiled state in solution and therefore much shorter than expected.

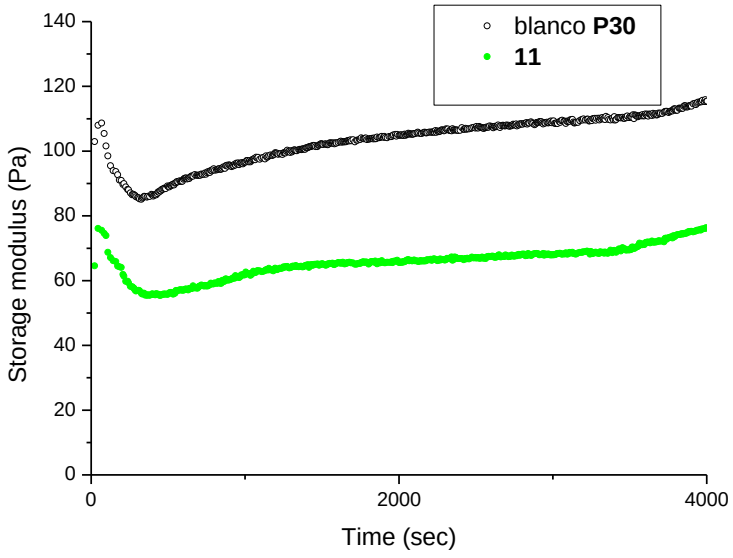

Figure 15. Storage modulus as a function of time at 37 °C for P30 in PBS with and without 11 at PIC concentration of 1.6 mg/mL.

The solution therefore would be a longer PEG crosslinker. It is known that crosslinking with bisfunctional crosslinkers are kinetically slower than utilizing star morphologies [27]. From literature it is known that the rate and efficacy of the crosslinking hydrogel networks based on synthetic and hybrid materials is increased by the use of eight arm star PEG [28-29].

F. Thiolyne "click" chemistry

Thiole(y)ne click chemistries have been used successfully by several groups to add permanent crosslinks and ligands to synthetic and hybrid hydrogels [10,30-31]. After dissolving the polymer (**P58**; m/n of 1:570; triethylene glycol based; 688 kg/mol) in DMF and adding the crosslinking reagents the samples were placed in the UV irradiation chamber and irradiated for 2 h. The crosslinked PIC **12** was purified via dialysis for 3 days (Figure 16).

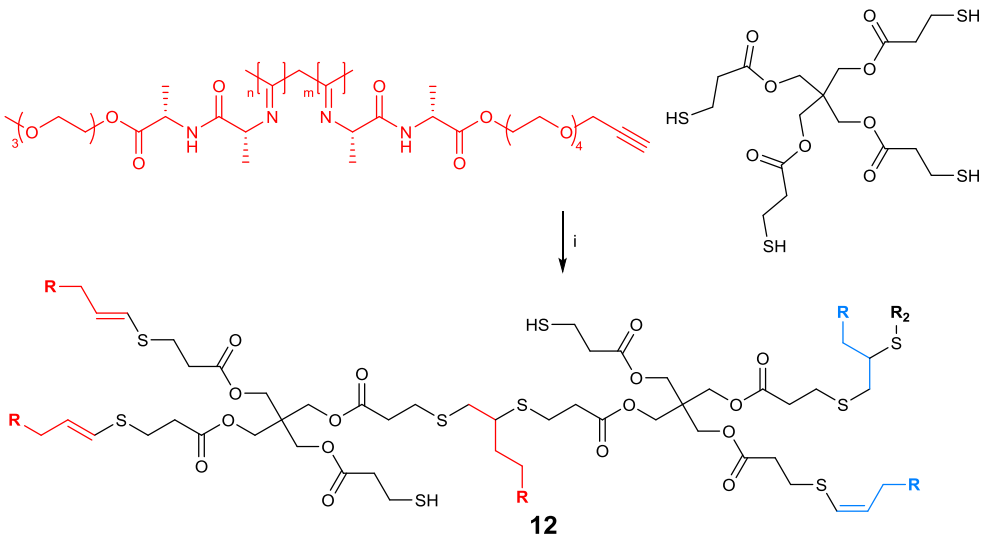

Figure 16. Crosslinking via thiolyne click chemistry of acetylene functional PIC (10 mg/mL) with pentaerythritol tetra(3-mercaptopropionate) as crosslinking agent i) Irgacure, room temperature, UV cure at 365 nm, 2 h

A standard set of rheology experiments were performed on the sample before and after crosslinking to investigate if there was any noticeable difference between the two samples.

From the temperature ramp experiment it was clear that after crosslinking the stiffness and sol-gel transition temperature were unchanged (Figure 17).

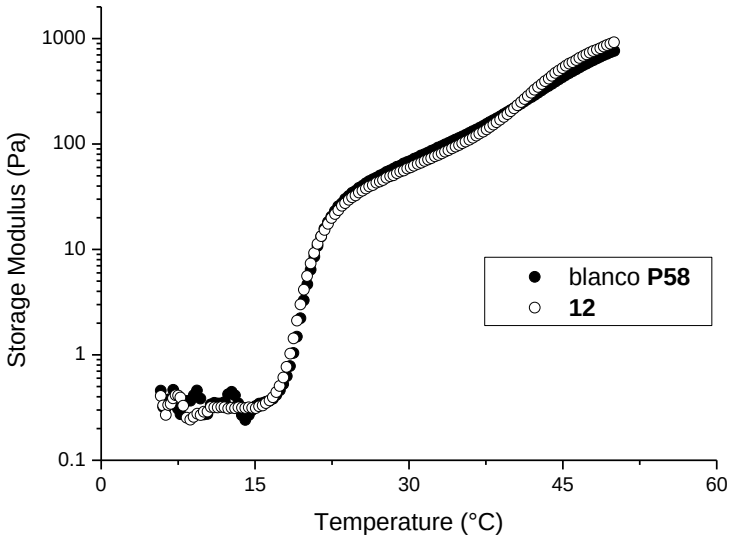

Figure 17. Storage modulus as a function of temperature for P58 before and after UV induced thiolyne click crosslinking, in PBS at 1.6 mg/mL.

In the linear amplitude sweep experiment as the strain increased incrementally the crosslinked sample exhibited a more complex response to increased strain as did not break at the same strain as blanco (Figure 18 red arrow indicates break point).

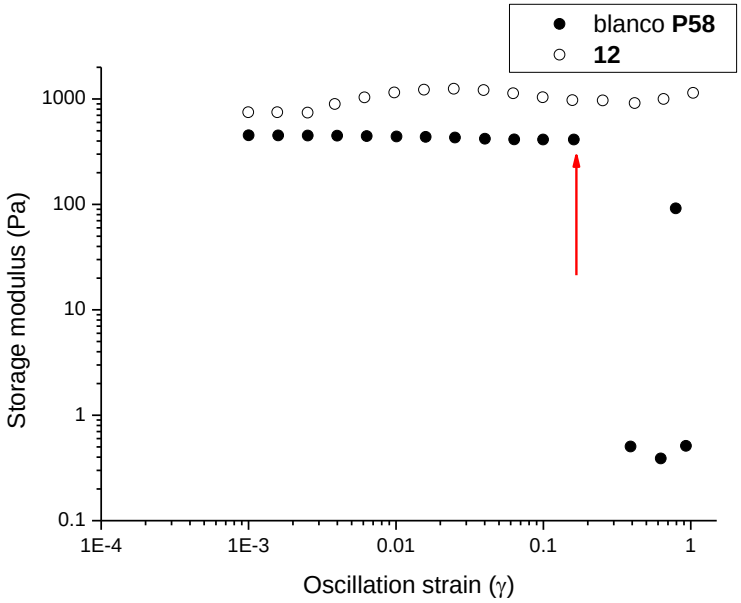

Figure 18. Storage modulus as a function of strain (Linear amplitude sweep 0.001-10 strain at increments 0.1 at 10 rad/s) at 37 °C before and after UV induced thiolyne click crosslinking.

Therefore it is fair to conclude that even though the stiffness was unaffected by the formation of crosslinks, network complexity has increased. As to why the stiffness did not increase perhaps the formation of inter polymer fibre crosslinking was dominant, but as no loss of stiffness was observed it would be fair to assume that bundle formation as a whole was not adversely affected due to the presence of the crosslinks.

2. Physical crosslinking

2.1. Ionic crosslinking

2.1.1. The Hofmeister effect - Salt bridges

In natural systems the use of a suitable counter ion has been used extensively to enable protein precipitation and stabilization, this is known as the Hofmeister effect [32].The efficiency of anions in promoting the hydrophobic interactions and thereby the self assembly of peptide stacking gels was shown to be consistent with the Hofmeister anion series affecting both the strength of gels obtained and macroscopic fibre structure [8]. In synthetic system of poly(*N*-isopropylacrylamide) this effect has also been used to successfully alter the lower critical solution temperature (LCST) [9]. As the PIC closely resembles these two systems in that it is also fibrillar in nature and thermo responsive it was deemed interesting to investigate the effect of the Hofmeister series on the solubility of the PIC fibres through complexation of the counterions with the hydrophobic core of the polymer (Figure 19). At the LCST, the PIC become hydrophobic and form a network of entangled semi-flexible bundles of polymer chains. The mechanical properties of the PIC hydrogels mimic those of the of biological gels, and are readily tuned by changing concentration, temperature and polymer length [see Chapter 3]. It was hoped that the addition of salt bridges would increase the overall stiffness after the sol-gel temperature.

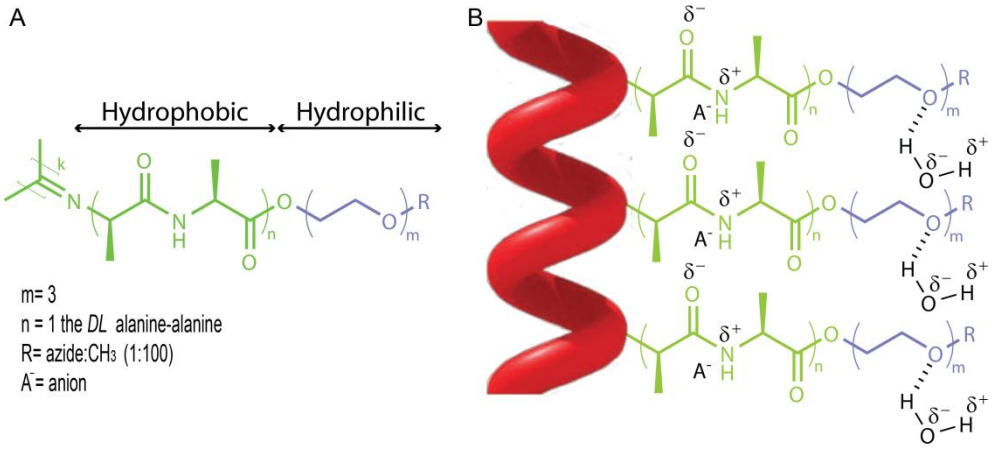

Figure 19. The ethylene glycol-functionalized polyisocyanides in water and the possible effect of anion addition on the polymer scaffold. (A) The polyisocyanide consists of a hydrophobic core and hydrophilic oligoethylene glycol tail (B) Hydrogen bonds between the peptide backbone may be disrupted by the anion A^- and the binding of the anion to the amide group of the alanine.

The experiment of Roy *et al.* [8] was repeated with PIC as pseudo peptide gel in a sodium buffered system with variable counter anions. In Figure 20 the general order of the anions (Hofmeister series) the ions on the left-hand side of the series are kosmotropes, or well-hydrated ions. Kosmotropes decrease the solubility of proteins and decrease the LCST of thermo-responsive polymers [8]. The Hofmeister series was shown to directly affect the LCST of the PIC (**P41**; m/n of 1:144; triethylene glycol based; 516 kg/mol), the ions on the right-hand side are chaotropes, or poorly hydrated ions, which increase polymer solubility and raise the LCST of the PIC fibres.

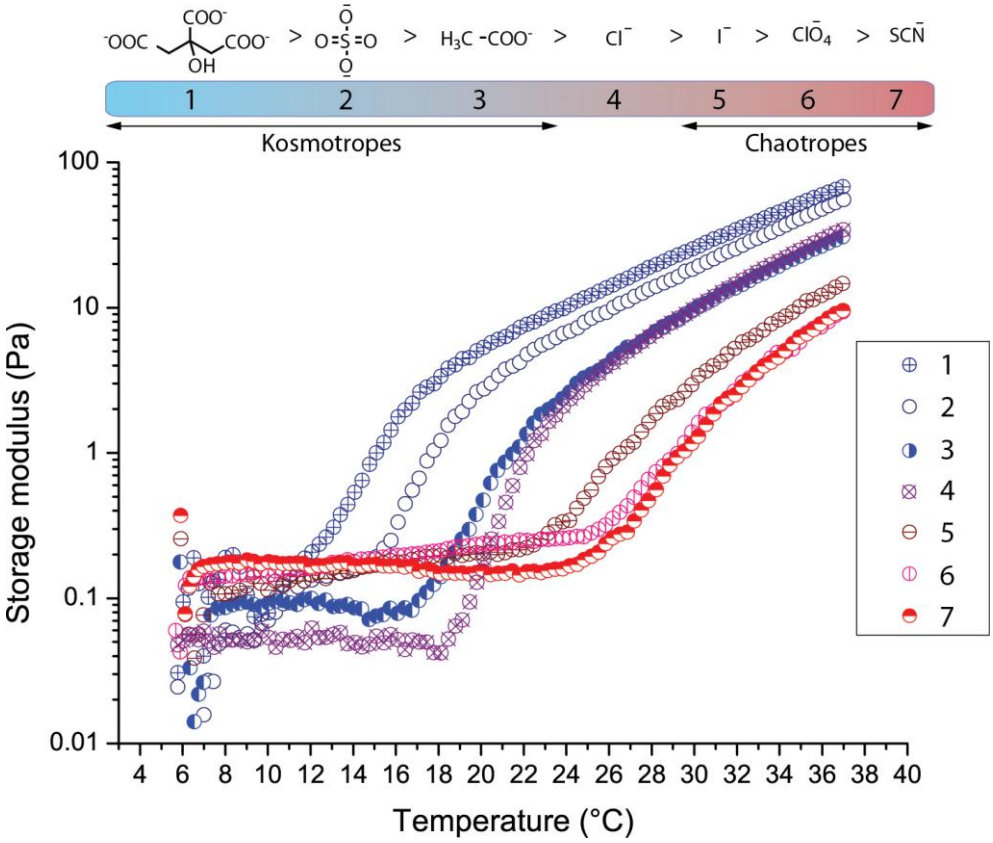

Figure 20. Storage modulus as a function of temperature for copolymer P41 in the presence of various salts in a buffered PBS solution at 1.6 mg/mL.

Not only did the stiffness at 37 °C increase when compared to PBS (Nr.4 from Figure 20) by the addition of kosmotropes, but it also decreased the onset the sol-gel temperature, the inverse was observed with the addition of chaotropes. Therefore, the addition of anions affected the hydrophilic/hydrophobic interface on the PIC, which in turn affects the solubility of the polymer in solution resulting changes in the LCST and stiffness.

Mixed systems and pore fillers

We postulate that by using a filler to block the pores of the matrix it would be possible to change the distance between crosslinks, as the closer the filler density comes to that of the matrix, the smaller the distance between crosslinks become (Figure 21).

$Al_0 \gg Fl_0$ (Eq 3)

Where Al_0 is the length between crosslinks in PIC hydrogel dissolved in water and Fl_0 is the distance between crosslinks in PIC hydrogel mixed with filler. Fillers could be: particles larger than the pore size e.g. gelatine spheres; water soluble polymers e.g. PEG or PVA.

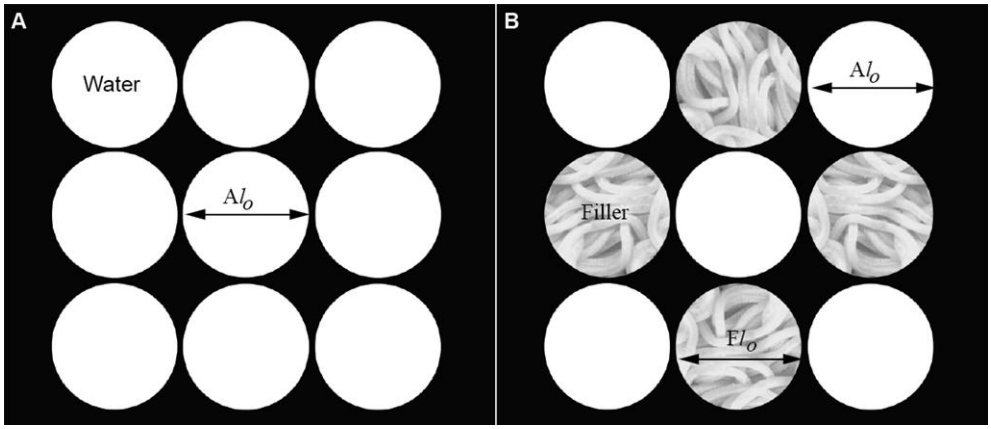

Figure 21. Schematic representation of polymer network pores filled with A) water or B) water and filler.

2.1.2. Pore blocking via spherical particles

Gelatine spheres (FutureChemistry) of 217 nm (PDI determined by DLS to be 0.1 and therefore narrowly distributed) in size were dissolved in PBS at 60 g/L were combined with a PIC (**P41**; m/n of 1:144; triethylene glycol based; 516 kg/mol**)** to obtain a 1.6 mg/mL solution containing 27 g/L gelatine spheres. A standard set of rheological experiments were performed (Figure 22a). From the temperature ramp it was concluded that the PIC containing gelatine spheres did not increase in stiffness. Interestingly, during the linear amplitude sweep, the PIC containing gelatine spheres still exhibited strain stiffening characteristics (Figure 22b).

In conclusion, although the addition of gelatine spheres did not effectively increase the bulk stiffness of the hydrogel, it did not inhibit sol-gel transition. This strategy could be used to add complexity to the PIC system in the form of drug molecules or additional cellular signals (e.g. growth factors). The gelatine spheres could also act as pseudo focal adhesion points to induce vasculogenesis [33] or be used as a carrier for drugs or biological molecules [34].

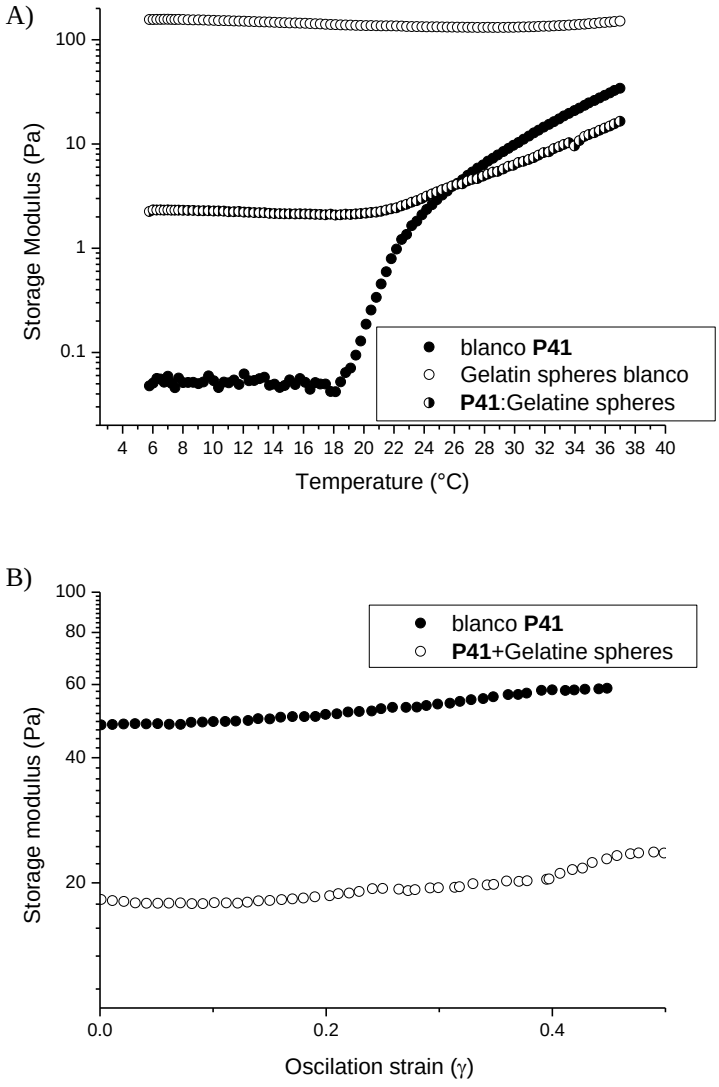

Figure 22. Rheology of polymer P41 with gelatine spheres (a) Storage modulus as a function of temperature, (b) Storage modulus as a function of strain at 37 °C (linear amplitude sweep at 0.001-10 strain increments 0.1 at 10 rad/s)

2.1.3. Polymers as fillers

2.1.3.1. Polyethylene glycol

To investigate what effect the addition of polyethylene glycol (PEG) itself would have on the sol-gel transition of PIC, increasing weight percentages of non functional solutions of PEG (0.6 – 10 wt %) were added to a fixed concentration of 1.6 mg/mL PIC (**P41**; m/n of 1:144; triethylene glycol based; 516 kg/mol). In the temperature rheological experiments, the PIC system (sol-gel transition) seems unaffected by the addition of PEG up to 5 weight percent (Figure 23).

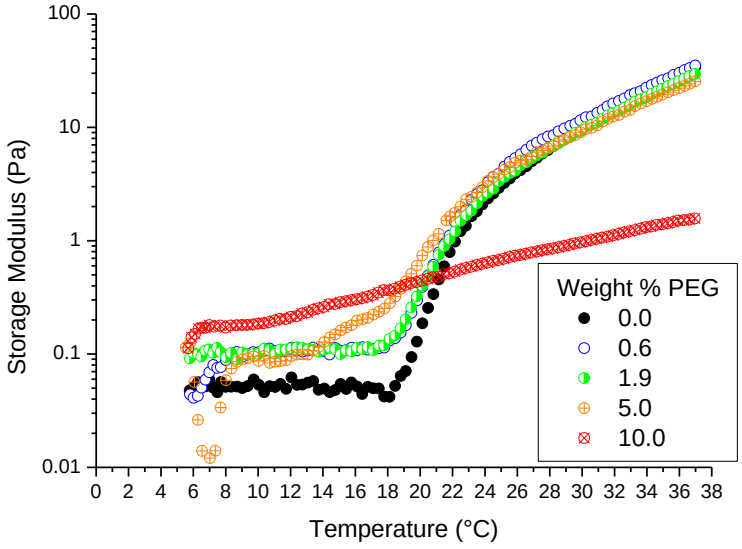

Figure 23. Storage modulus as a function of temperature for polymer P41 (1.6 mg/mL PBS) with increasing percentages of polyethylene glycol.

In Figure 24 the linear amplitude sweep indicate that as the % PEG increases the behaviour of the PIC deters from the blanco, at 5 weight percent it even seems to be able to resist breaking for longer than the reference material (red arrows indicate breaking points). The sample containing 10 weight percent PEG has retained no PIC characteristics and upon increased strain breaks down completely

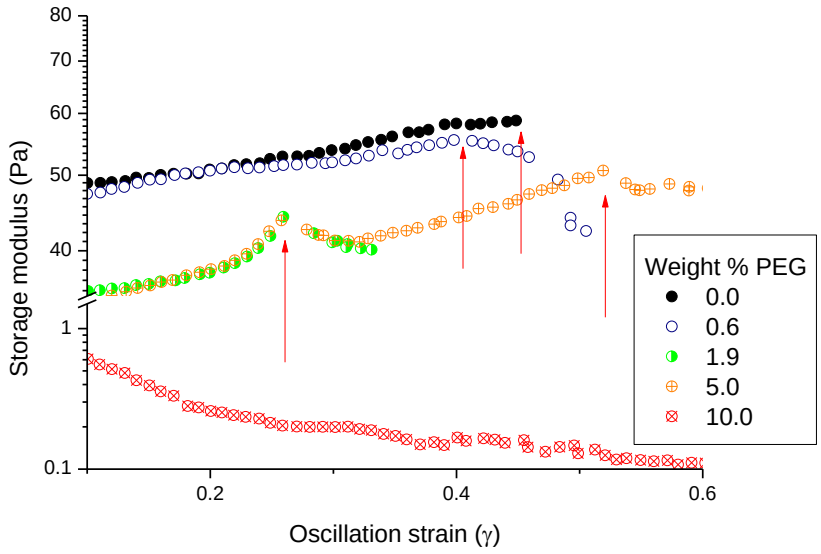

Figure 24. Storage modulus as a function of strain (linear amplitude sweep 0.001-1 strain at increments 0.1 at 10 rad/s) at 37 °C of polymer P41 with increasing percentages of polyethylene glycol.

To conclude, the addition of a PEG does not increase the overall stiffness, in fact a decrease in stiffness was observed for samples containing more than 1.9 weight % PEG. The sol-gel transition temperature was unaffected by the addition of PEG up to 5 weight %.

2.1.3.2. Polyvinylalcohol

The maximum amount of polyvinylalcohol (PVA) added to PIC that still results in a convincing sol-gel transition was determined by mixing increasing amounts of PVA with PIC (**P41**; m/n of 1:144; triethylene glycol based; 516 kg/mol) and measuring the sol-gel transition using rheology. At a mass ratio of PVA to PIC of 1:0.6 the solution was viscous and gel like, but the sol-gel transition was no longer present (Figure 25, Table 8).

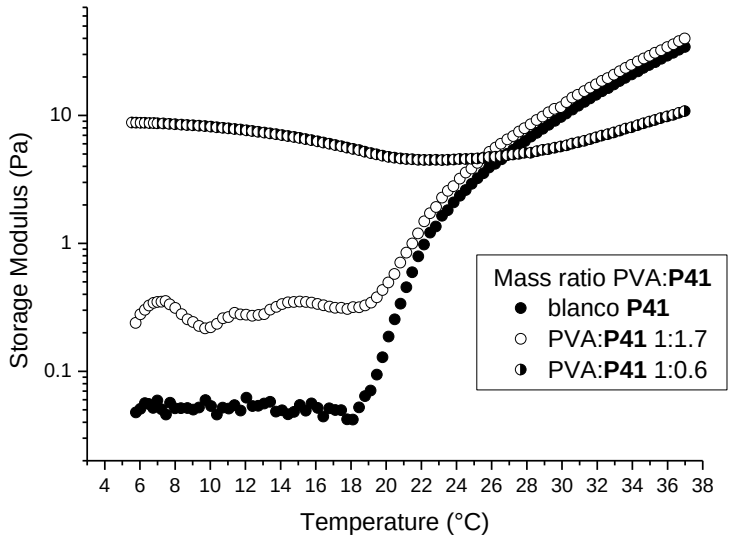

Figure 25. Storage modulus as a function of temperature for polymer P41 in the presence of PVA, the concentration of P41 was kept constant at 1.6 mg/mL in PBS.

During the linear amplitude sweep it appears that the addition of PVA has positively affected the strain resistance properties of the mixture. This can be seen delayed break-off points indicated with red arrows on Figure 26.

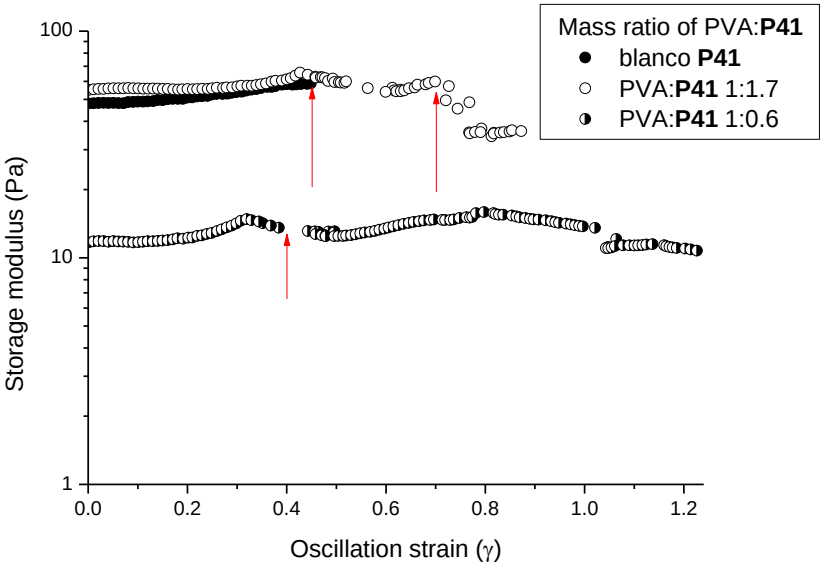

Figure 26. Storage modulus as a function of strain(linear amplitude sweep 0.001-1 strain at increments 0.1 at 10 rad/s) at 37 °C of polymer P41 with PVA at two different mass ratio.

In conclusion, the addition of PVA to PIC does not increase the overall stiffness or the sol-gel transition up to mass ratios of PVA to PIC 1:0.6. A delayed onset of break upon increased stain and multiple break points was observed in the mixture.

3. Dynamic crosslinking

3.1. Host-guest chemistry

Host-guest chemistry has been used as a successful strategy to form hydrogels by the rapid crosslinking of cellulosic (naphthalene) biopolymers with polyvinyl alcohol (methyl viologen) in the presence of cucurbit[8]uril [12,35]. It was also shown that by choosing the appropriate amino acid (phenylalanine), supra-molecular hydrogels based on

(vinylbenzyl)trimethylammonium chloride derived polymers could be successfully synthesized in the presence of CB8 [36]. The addition of this dynamic crosslinking strategy could potentially result in a self-healing PIC hydrogel, as was the case in the system of Apple *et al*. [35,37], but with strain stiffening characteristics inherent of the PIC system.

Two routes were employed to investigate this possible dynamic crosslinking strategy for PIC. The first was to decorate the PIC with phenylalanine (Phe) guest moieties and to use CB8 as the host to form a ternary complex filled with only Phe guest molecules. The second strategy was to use a flexible polyvinyl alcohol (PVA) decorated with methyl viologen (MV) to act as the first electron-poor guest for CB8 and add this to PIC-Phe, the electron-rich guest, yielding the dynamic molecular hand cuff complexes (Figure 27). The strength of this crosslinking could then be tuned stoichiometrically.

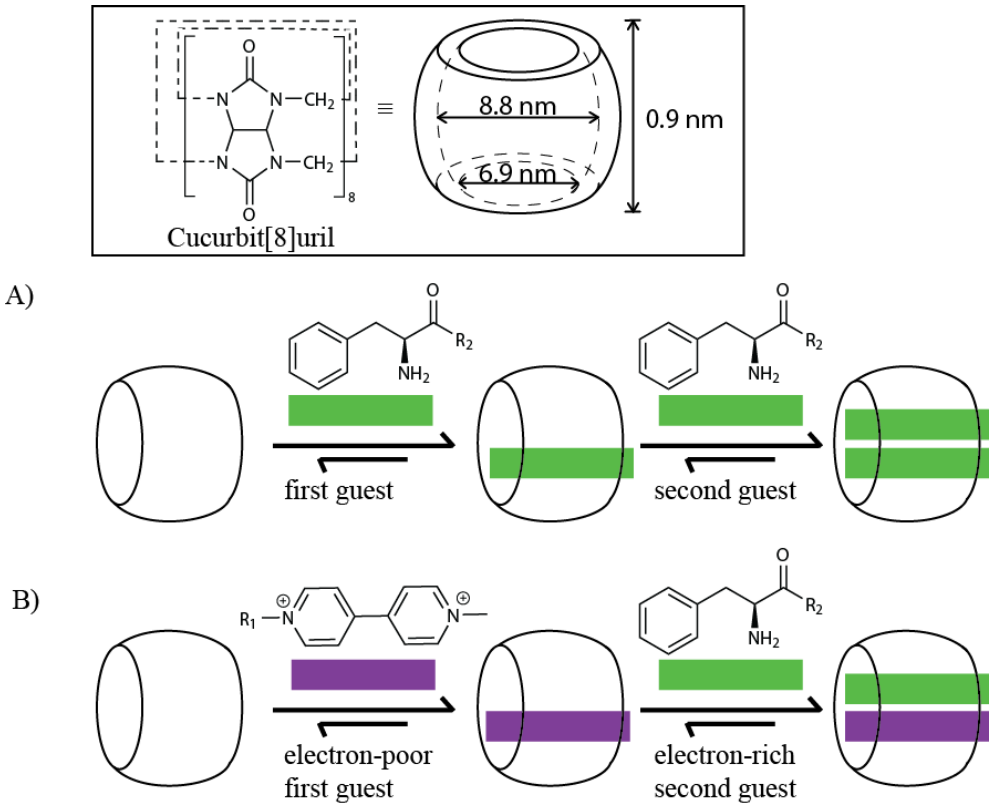

Figure 27. Proposed dynamic crosslinking strategies with cucurbit[8]uril host and A) phenylalanine/phenylalanine or B) phenylanaline/methylviologen guests.

In strategy A, it was thought that the simplest way to obtain PIC-Phe **13** was to decorate amine functional PIC (PIC-NH_2) with phenylalanine (Phe) via condensation reaction of the amine on PIC-NH_2 and carboxylic acid groups on phenylalanine in the presence of 1-ethyl-3-(3-dimethylaminopropyl)carbodiimide (EDC) and N-hydroxysulfosuccinimide (Sulfo-NHS) (Figure 28).

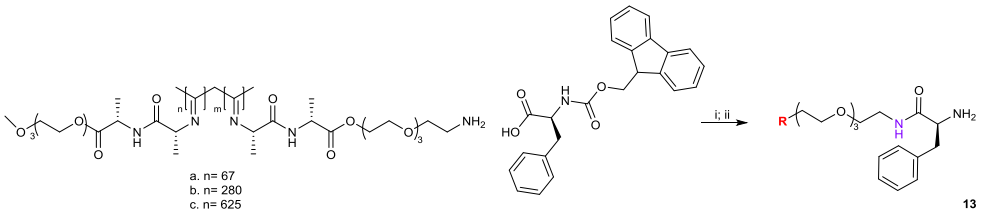

Figure 28. Schematic representation for the synthesis PIC-Phe i) EDC/Sulfo-NHS, DMSO/DMF, 14 days, ii) 16% piperidine/DMF, 9 h, room temperature 35-46 % yield.

^{1}H NMR was used to determine the loading of Phe onto the PIC. What appears to be a doublet of doublets between 8.0 – 7.5 ppm was assigned to the aromatic protons of the Phe and the broad multiplet between 3.75 – 3.25 ppm the CH_2-CH_2 protons of the PIC backbone. The loading of all three polymers and an example of the calculations based on the ^{1}H NMR spectra of **13a** can be seen in Figure 29 (Table 4). It was assumed that the loading of Phe for all other strategies would not be significantly different from these values as the same starting polymers were used.

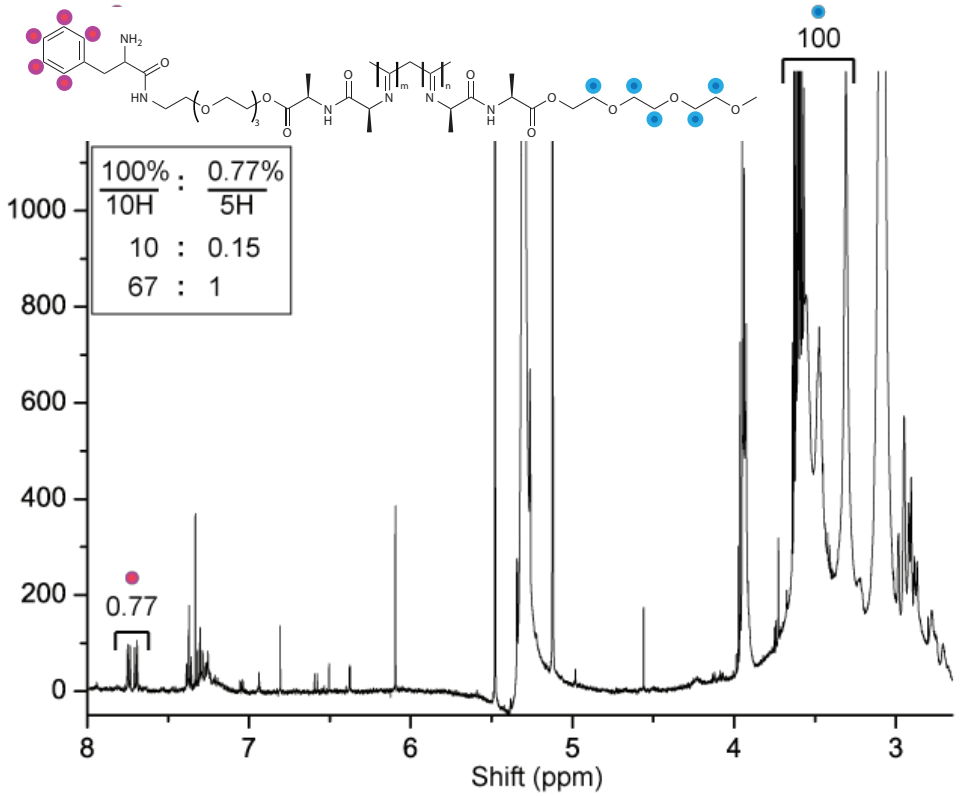

Figure 29. ^{1}H NMR (128 scans) of polymer P38, the peaks used to determine the ratio of m/n are indicated with the coloured circles.

Rheology measurements were performed on the **13 b-c** in the presence of CB8 with a molar ratio of 2 Phe moieties per CB8. The stiffness decreased with the addition of CB8 (Figure 30). This could be that even at densities as low as 1 in 280 or 625 there were still too many phenylalanine groups available for binding.

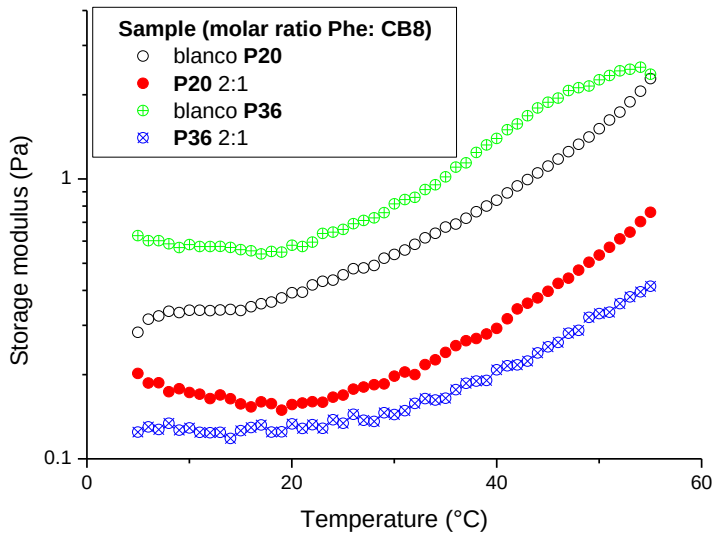

Figure 30. Storage modulus as a function of temperature for PIC-Phe at 2 mg/mL in 50 mM borate buffer pH 8.4 with and without CB8.

It could also be possible that spacer flexibility and length play a role in the efficacy of molecular handcuff formation. Therefore a Phe with a longer more flexible spacer length than **13** was required.

The synthetic strategy opted for was to synthesize a BCN functional PIC with a longer spacer than utilized by the synthesis of **13** (Figure 28). A condensation reaction with Fmoc-phenylanaline and tert-butyl (3-aminopropyl)carbamate with *N,N'*-dicyclohexylcarbodiimide (DCC) in the presence of catalytic amounts of 4-dimethylaminopyridine (DMAP) resulted in **14** (Figure 31). After the successful deprotection, the deprotected compound **14** was then reacted under slightly basic conditions with the activated carboxylic acid of the bicyclononyne N-hydroxysuccinimyl (BCN-NHS)

to yield the Fmoc protected phenylalanine BCN linker **15**. The Fmoc protection group was removed with the mild base piperidine in DMF. After purification, the deprotected BCN-Phe **16** was added to PIC-N_3 and allowed to conjugate for several hours to obtain **17a-c** in good yields (Figure 31, Table 5).

The spacer length of **13** (14.6 Å) **vs. 17** (31.8 Å) was predicted by measuring the distance of Phe from the backbone using a modelled structure energy minimized in ChemDraw3D and rendered in PyMol.

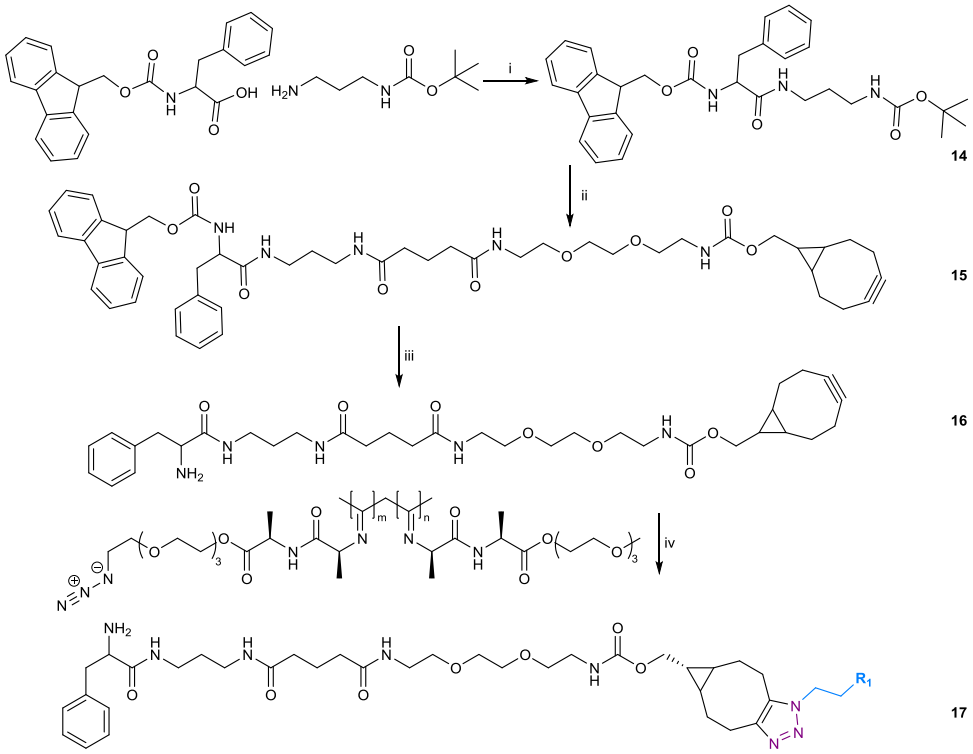

Figure 31. Synthetic scheme of PICR3BCN i) DCM, DCC/DMAP, room temperature16 h ii)a. 2 M HCl/Dioxane, 2 h, b. BCN-NHS, 50 mM Borate buffer pH 8.4 9 h iii) 5 % piperidine/DMF, 1 h, 79 % yield iv) PIC-N3, DCM, 18 h, 82 % yield.

The successful synthesis of **15** was confirmed with ^{1}H NMR, ^{13}C NMR, NOESY, HSQC and LCQ-MS. The HPLC elution profile of compound **15** showed the presence of at least two major products, presumably some residual starting products. Since the desired product was present, it was decided to continue without further purification as this was still an intermediate product (Figure 39).

The successful deprotection of **15** was confirmed by ^{1}H NMR spectroscopy. The characteristic aromatic peaks of the Fmoc protection group disappeared and only the aromatic peaks of the phenyl group were present between 7.5-7.0 ppm. The singlet (1) assigned to the single proton on the bicyclononyne moiety was still present (Figure 47 experimental). The HPLC elution profile of **16** showed one dominant peak at 25.6 min with some minor impurities (Figure 41).

To qualitatively test if product **16** was still active, a test reaction was performed with 7-azido-2-oxo-2H-chromene-4-carboxylic acid, which itself shows only slight fluorescence when excited at 432 nm, but once conjugated, it fluoresces intensely. The 7-azido-2-oxo-2H-chromene-4-carboxylic acid was dissolved in DMSO with a concentration of 1 mg/mL . A small amount of **16** was dissolved in DMSO and to this an equimolar equivalent of 7-azido-2-oxo-2H-chromene-4-carboxylic acid stock solution was added. The combined sample showed increased fluorescence indicating that the bicyclononyne present in **16** was still intact and available for conjugation (Figure 42 experimental).

The SPAAC reaction was performed by dissolving the azide functional polymer (m/n of 1:67; 1: 278; 1:625) in DCM and adding a 20-fold molar excess (relative to azides

present on the PIC) of **16**. The reaction was stirred at room temperature for 18 h. The efficacy of the conjugation was determined to be 81-92 % by the dye test (described previously in Chapter 2.2).

A third BCN-Phe derivative **18** was supplied by SynAffix was also investigated. The distance from the PIC scaffold to the Phe (**19a-c**) was predicted from an energy minimized structure obtained from ChemDraw3D and rendered in PyMol to be 32.3 Å. The **P41** was dissolved in ACN and a 1:1 molar equivalent of **18** was added to the PIC solution and stirred for 4 days at room temperature. The polymer was recovered by precipitation from diisopropyl ether and air dried under nitrogen flow to obtain the Fmoc protected **19** in good yields (Table 6). The polymer **19** was dissolved in borate buffer pH 8.4 at a concentration of 1.2 mg/mL and to this a solution of 5% piperidine in DMF was added. The deprotection was assumed to be quantitative after 16 h of stirring at room temperature (Table 7).

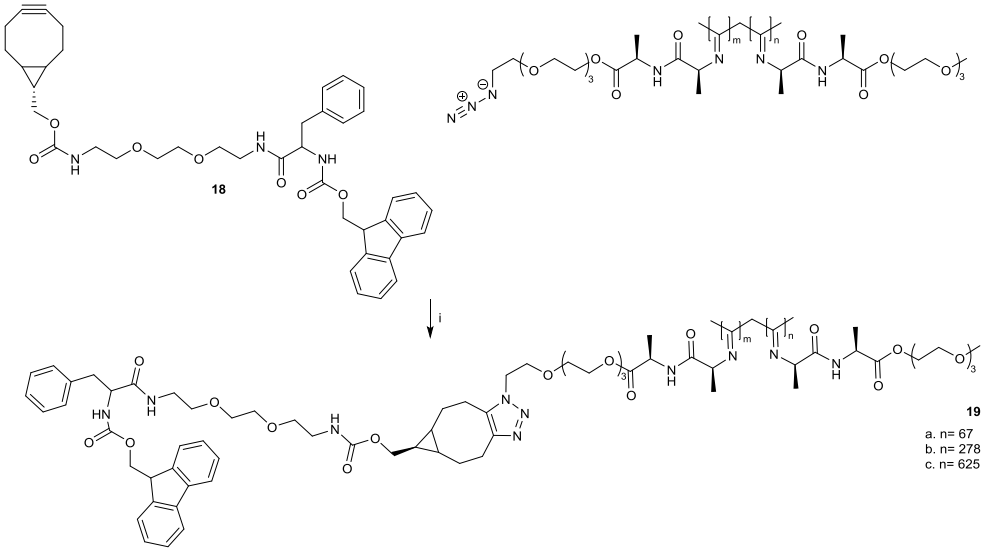

Figure 32. Schematic of the SPAAC functionalization of PIC-N3 with 18: i)ACN, 4 days 40-80 % yield. The m/n was varied 1:67; 1:278; 1:625.

In strategy B to form molecular handcuffs with MV and Phe guest moieties inside a CB8 host, it was decided to use a flexible PVA-MV crosslinker so as to favour interbundle crosslinking over intrabundle crosslinking. It was established in the investigation of physical crosslinking that PVA could be added to the PIC system without adversely affecting the PIC hydrogel sol-gel transition and stiffness below mass ratios of 1:1.7. PVA was functionalized with MV over five steps in an overall yield of 14 %. The final step was performed twice resulting in **24 a-b** loaded with different densities of MV relative to the OH groups (3 and 33 %) on the PVA backbone (Figure 33).

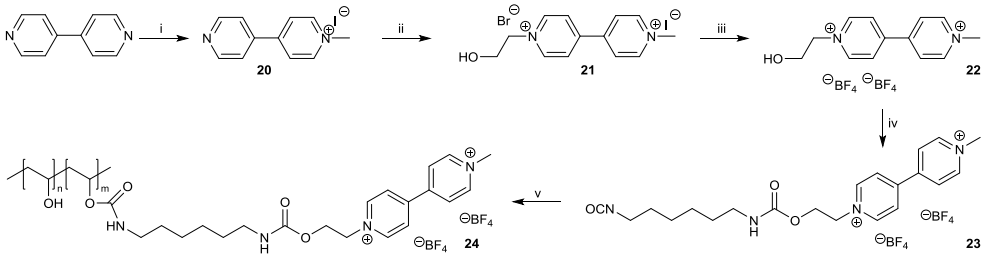

Figure 33. Synthesis of PVA-MV i) MeI, DCM, 25 °C 18 h, 80% yield ii) 2-bromoethan(1)ol, ACN, reflux 48 h, 54 % yield iii) NH_4BF_4, reflux 2 h, 55 % yield iv) 1,6-hexamethylene diisocyanate, dibutyltin dilaurate, ACN, room temperature 24 h, 58 % yield v) PVA, dibutyltin dilaurate, NMP, room temperature 18 h, quantitative.

From the mixed system physical crosslinking investigation, the weight percent at which PVA adversely affects the sol-gel transition was known (Figure 25). Therefore the methyl viologen functional PVA-MV **24a-b** (3% or 33% MV relative to -OH) was mixed with **19a-b** in the presence of CB8 and the mass ratios of PVA to PIC were kept above 1:0.6 (Table 9).

For the PIC sample with the highest loading **19a** Phe (1 in 67) there was no effect on stiffness by adding PVA at different molar concentrations, nor was there any effect on the stiffness due to the presence of PVA-MV in a mass ratio of 1:3 (Figure 34).

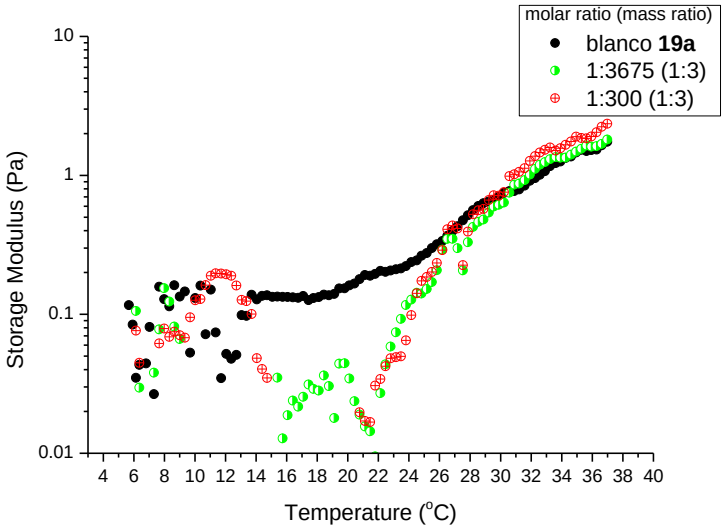

Figure 34. Storage modulus as a function of temperature for 19a at a concentration of 1.1 mg/mL in 50 mM borate buffer pH 8.4 in the presence of PVA-MV and CB8 with varied molar ratios of MV moiety to Phe moiety and a constant mass ratio of 1:3.

The PIC sample with a lower loading of Phe **19b** (1 in 278) exhibited an increase in stiffness in the presence of PVA-MV and CB8. What was clear is that for a sparsely labelled PIC-Phe (1 in 278) at mass ratios above 1:3 an increase in stiffness was observed regardless of the molar ratio MV:Phe (Figure 35a). Interestingly there was a significant difference between the three samples during the linear amplitude sweep, the mixtures resistance to final rupture (as indicated by red arrows Figure 35b) was directly correlated to the amount of PVA-MV present and the slope of the curve is much steeper than that of the control experiment where the dynamic crosslinks were not present (Figure 26). Possibly this could be due to the dynamic nature of the crosslink inducing the polymer with self healing properties under increased strain. In both PIC (**19a** and **19b**) systems the sol-gel transition was unaffected by the reaction conditions.

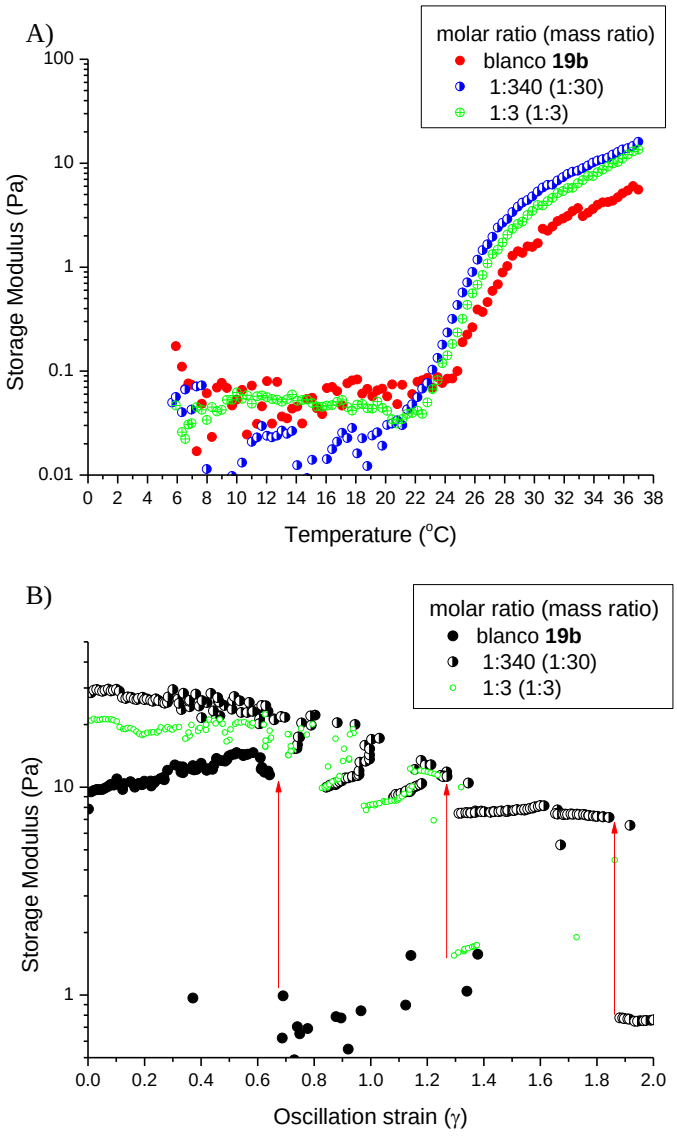

Figure 35. Rheolgy of 19b at a concentration of 1.1 mg/mL in 50 mM borate buffer pH 8.4 in the presence of PVA-MV and CB8 with varied molar ratios of MV moiety a) Storage modulus as a function of temperature, (b) Storage modulus as a function of strain at 37 °C (0.001-10 strain increments 0.1 at 10 rad/s).

Conclusion/Discussion

As a whole, crosslinking did not increase the stiffness of the PIC in gelled state as was expected from previous work [1] which predicts that the storage modulus should increase proportionally as the distance between crosslinks decreases. It was assumed that crosslinking in the gelled state would result in cross bundle linking and that the effect on bundle tightness would be negligible. If the formed crosslinks inhibit PIC fibres from forming tight bundles then the assumption that the persistence length of single chain applies to the bundle is false and as a result unpredictable effects on the storage modulus occur regardless of the decrease in distance between crosslinks, this proposed effect could be referred to as the frayed rope scenario as depicted in Figure 36.

Figure 36. Concept illustration frayed rope, inter polymer crosslink formation results in bundle disruption.

The most promising results on increasing storage modulus of the PIC in gelled state was obtained by adding ionic crosslinks through the addition of kosmotropic anions that stabilize the polymer bundle as a whole and cause precipitation at lower temperatures.

The one covalent crosslinking strategy that resulted in increased stiffness was the addition of dithiobridges. It is postulated that a higher ratio of dithiobridges or bulky spacers will result in increased overall stiffness.

The addition of self healing properties into the PIC system through the formation of molecular handcuffs although not effective in increasing bulk stiffness did result in a PIC that repaired after breaking as a result of increased stress. In the future the effect of pH and varied concentrations of guest concentrations should be explored further.

Perhaps other analytical techniques should be used to measure the effect of crosslinking on the polymer network, like the diffusion of nanoparticles of defined sizes to determine the new pore size. The stiffness could also be measured by surface indentation measurements [38] that would not require the excessive handling of a gelled sample.

Experimental:
Procedures
Rheology
All crosslinking experiments were performed using the same conditions, unless stated otherwise. The crosslinking reagents were prepared prior to the reaction, placed in an ice bath and mixed cold before being rapidly transferred to a cooled plate-plate geometry. At this point either a temperature ramp experiment 2 °C/min 5 – 37 °C or a time experiment at 37 °C (2 % strain) was performed followed by a frequency sweep, logarithmic amplitude sweep (0.1-10 %) and a linear amplitude sweep (0.001-10 strain at 10 rad/s).

Synthesis

1. Covalent Crosslinks

A. Schiff base formation
To quantify the amount of azides prior to the conversion to amines the Tokyo green dye test was performed. Briefly, a Tokyo Green stock solution was made by dissolving BCN-Tokyo Green (2.2 mg, 43.7 µmol) in DMSO (1 mL). The polymer to be tested was dissolved in ACN at a concentration around 3.0 mg/mL, with a total volume of 3 mL. The polymer solution was stirred for one hour at 5 °C to completely dissolve it. A volume of the Tokyo Green stock solution corresponding to 2 equivalent of BCN-Tokyo green per azide was pipetted to the polymer solution. The mixture was stirred overnight at room temperature and was then precipitated in diisopropyl ether (40 mL). The diisopropyl ether was decanted off and the remaining polymer was air dried for one hour. This precipitation process was repeated until the diisopropyl ether was no longer yellow. After the final precipitation the polymer was air dried over night under a nitrogen flow.

To convert azides to amines, the azide functional PIC polymer was dissolved in acetonitrile. To this polymer solution triphenylphosphine (1.2 molar equivalent) and water (1.3 molar equivalent) were added. The mixture was allowed to react for 16 h at 40 °C and then placed in the cold room for 12 days. The polymer was precipitated from diisopropyl ether, the excess solvent decanted and polymer **1** dried under a nitrogen flow.

To quantify the conversion of azides to amines the amount of amines was determined by performing a dye test with an amine reactive dye.

Table 1. Azide conversion to amine. A summary of experimental masses, gravimetric yields and dye test ratio.

	Sample	PIC-N_3 mg	Molar Ratio m/n*	mg Ph_3P	mg PIC-NH_2	% Yield	Molar Ratio Spacer:Amine**
a	**P38**	148.0	1:50	49.0	100.0	68	1:53
b	**P20**	37.0	/	49.0	32.0	87	1:157
c	**P36**	100.0	1:360	49.0	58.0	58	1:478

* As determined by the Tokyo green dye test. **As determined Amine-reactive dye

For the crosslinking experiment the polymer (**1c**) stock solution in pH 6 phosphate buffer was made at a concentration of 3.2 mg/mL by dissolving the polymer overnight at 5 °C. The crosslinking experiments were performed on **1c** at a concentration of 1.6 mg/mL with 0.5 and 50.0 equivalent of crosslinker to amine.

B. Schmidt Reactions

The experiments were performed on **P30** (m/n of 1:128; triethylene glycol based; 361 kg/mol) at 1.6 mg/mL with 0.5 and 50.0 molar equivalent of gluteraldehyde to azide. A polymer stock solution in pH 6 phosphate buffer, at a concentration of 3.2 mg/mL was obtained by dissolving the polymer overnight at 5 °C. The gluteraldehyde was bought as a 25% solution in MQ. From this a 0.6 mM stock solution in pH 6 phosphate buffer was made by pipetting 10.0 µL of the 25%-wt solution into 40 mL of pH 6 phosphate buffer. To 1.1 mL of the **P30** stock solution, 4.0µL of the 0.6 mM gluteraldehyde solution was pipetted. The volume of the added gluteraldehyde stock solution was assumed to be small enough to not change the concentrations significantly. For the control samples the same amount of pH 6 phosphate buffer without gluteraldehyde was added.

Dithiobridge formation

1.1.) C. Unprotected thiols

To 1.0 g (9.0 mmol) of 3-chloropropane-1-thiol and 1.1 g (17.5 mmol) of NaN_3, a solution of H_2O/EtOH (10 mL, 2:1 v/v) was added. The mixture was stirred for 24 h at 100 °C. To the warm solution 50 mL water was added before the product was extracted with diethyl ether. The organic layers were washed with water (3x) and dried with Na_2SO_4. The solvent was evaporated under reduced pressure, resulting in **4** as a yellow oil, 490.0 mg, 46% yield. $\mathbf{R_f}$ = 0.6 (MeOH/n-hexane 3:1 v/v)) **^{1}H NMR ($CDCl_3$, 300 MHz)**: δ = 1.88 (m, 2H, CH_2-C<u>H</u>$_2$- CH_2); 3.43 (m, 2H, , N_3-C<u>H</u>$_2$-CH_2- CH_2-SH*)*, 3.72 (m, 2H, N_3-CH_2-CH_2- C<u>H</u>$_2$-SH*)* **^{13}C NMR ($CDCl_3$, 75 MHz)**: δ = 49.70 (N_3-*C*H_2-CH_2- CH_2-SH*)*, 35.27 (N_3-CH_2-*C*H_2- CH_2-SH*)*, *28.26 (*N_3-CH_2-CH_2- *C*H_2-SH*)* **FT-IR (cm^{-1}, ATR)**: 2926.58 (C-H); 2094.63 (azide).

To 15.0 mL of freshly distilled dichloromethane was added 3.7 mg (7 µmol) TBTA and the solution was degassed by freeze-pump-thaw method (x4). To this solution 1.0 mg CuBr (7

µmol) was added and stirred 16 h under an argon atmosphere. In a separate Schlenk finger, 100.0 mg (0.3 mmol) **P46** was dissolved in 50 mL freshly distilled DCM and the mixture was degassed by purging with argon. To the degassed polymer solution 6.5 mg (0.1 mmol) of **4** was added and the mixture was stirred for 4 h. Finally, 400 µL (0.6 µmol) of the catalyst solution was added to the polymer mixture and was stirred for 72 h at room temperature. The polymer was recovered by precipitation from diisopropyl ether (x3) to obtain 60.1 mg (60% yield).

To a solution of 20.0 mg of polymer **5** in 4 mL dichloromethane was added 0.2 mL DMSO and the mixture was stirred for 5 h at room temperature. The polymer was precipitated in diisopropyl ether and 18.0 mg of **6** was obtained (90% yield).

1.2.) D. Protected thiols

Polymer **1c** (54.5 mg, 172 µmol) was dissolved in 3 mL DMF. N-succinimidyl S-acetylthioacetate (7.2 mg, 31.0 µmol) was added to the polymer solution, the reaction was allowed to react for one week. This solution was diluted with 1.0 mL MQ. The solution was dialysed against water and finally against PBS to obtain 4 mL of **7** a SATA-decorated polymer (13.5 mg/mL).
The deacetylation buffer was prepared separately by adding 40 mL 50 mM phosphate buffer pH 7.2 to 3.8 mL of 200 mM EDTA solution and diluting it with 6.3 mL MQ.
To determine the conversion success a test deprotection reaction was performed on 0.5 mL of the reaction mixture by adding to this 4.5 mL deacetylation solution allow to stir at room temperature for 2 h. An Ellmans test was performed on the deprotected solution to determine the concentration of thiols in solution. The reaction buffer for this was prepared by combining 8.0 mL 250 mM phosphate buffer pH 8.0, 0.1 mL 200 mM EDTA and 11.9 mL MQ. The Ellmans reagent solution was prepared by dissolving 4.0 mg dithiobis(2-nitrobenzoic acid) in 1 mL reaction buffer. The UV analysis test itself was performed on a dilute stock sample which was prepared by combining 50 µL of the deprotected solution with 950 uL of the reaction buffer. From this dilute stock solution a dilution series was prepared and the UV absorption at 412 nm used (ε=14,150 M^{-1} cm^{-1}) to calculate the thiol concentration.

An amount of 500.0 µL of **7** (13.5 mg/mL) was treated with 500.0 µL deacetylation buffer at room temperature for 1 week to obtain the deprotected thiol **8** (6.8 mg/mL). Simultaneously another sample of **7** was treated with 400.0 µL deacetylation buffer and 100.0 µL 30 % hydroxide solution at room temperature for 1 week to obtain a crosslinked dithio PIC **9** (6.8 mg/mL) these solutions were analyzed by rheology.

E. SPAAC crosslinking of PIC-N3 with flexible bifunctional linker

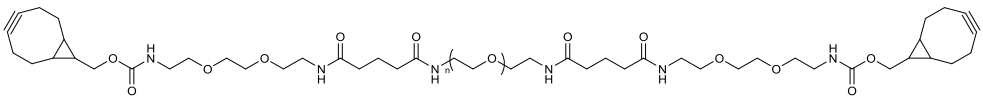

The bis-amine PEG (10 kDa) (450.0 mg, 45.0 µmol) was dissolved in 1 mL ACN. To the PEG solution BCN-NHS (27.5 mg, 94.5 µmol) was added and allowed to conjugate for 4

days at 4 °C on the roller/shaker. The product **10** was precipitated in ice cold diethyl ether and the precipitate dried under nitrogen flow. **MaldiToF** 11638 g/mol

SPAAC crosslinking
The experiments were performed on **P30** at 1.6 mg/mL with 0.5, 5.0 and 50.0 molar equivalent of **10** to azides on the polymer backbone. A polymer stock solution **P30** in PBS (3.2 mg/mL) was made. A stock solution of **10** dissolved in MQ at a concentration of 0.5 g/mL was prepared. For the 0.5 equivalent crosslinking, 10 µL stock solution of **10** was diluted with 8 mL of MQ to obtain a diluted stock solution of **10** with a concentration of 56 µM. Four samples containing the bis-BCN crosslinker were made by mixing the polymer stock solution (0.6 mL) with the bis-BCN stock solution (0.6 mL). For the control samples the polymer stock solution (0.6 mL) was mixed with MQ (0.6 mL). The experiments with 1 and 50 equivalents of crosslinker were carried out in the same way, but with pipetting respectively 20 µL and 100 µL of the 0.5 g/mL bis-BCN solution into 8 mL MQ.

Rheology experiments of PIC in the presence of PEG
A stock solution of PEG 6.0 kDa was prepared by dissolving 40.0 mg in 100 µL of PBS to obtain a 40 wt% solution. Different amounts of this PEG solution were added to PIC 3.4 mg/mL and diluted with PBS to obtain a final concentration 1.6 mg/mL of PIC (Table 2).

Table 2. Rheology experiment of PIC with increasing amount of PEG

wt%	vol PEG µL	µmol PEG	vol PBS µL	vol PIC	µmol PIC	c PIC (mg/mL)
PE 0	0.0	0.0	210.0	190.0	2.0	1.6
PE 0.6	6.0	0.4	204.0	190.0	2.0	1.6
PE 1.9	18.8	1.3	191.0	190.0	2.0	1.6
PE 5	50.0	3.3	160.0	190.0	2.0	1.6
PE 10	100.0	6.6	110.0	190.0	2.0	1.6

F. UV induced thiolyne click chemistry
Dissolve 94.3 mg of the acetylene (1:570) functional polymer **P58** in 10 mL of DMF. A 2.0 mL (17.7 mg, 1.0 pmol acetylene) portion of the stock solution was removed and placed in a glass vial. To the polymer solution 21.3 µL (55.6 µmol) of pentaerythritol tetra(3-mercaptopropionate) (PETMP) and 26.9 µL (1.2 µmol) of an Irgacure solution of 10.0 mg/mL in DMF was added. The sample was placed in the UV irradiation box and isolated with aluminium foil. A custom setup was build with a hand held 365 nm UV Tube Hg source, 4 Watt output (BLE-220B) with 15.9 x 5.1 x 2.5 cm dimensions. Samples were at a fixed distance of 3.0 cm from the source resulting in a radiation of 84.0 mW/cm^2. The light source was turned on and the reaction left for 2 h. The polymer **12** was purified by dialysis using a membrane (snakeskin) with a 1000 g/mol cut off and dialysing against 50:50 DMF:MQ, then plain MQ for 48 h at 37 °C. It is assumed that the polymer concentration does not decrease during the dialysis process as dialysis was performed in the gelled state.

2. Physical crosslinking

2.1. Ionic Crosslinking

2.1.1. Hofmeister Effect

Polymer **P41** was dissolved in 100 mM pH 7.4 PBS to obtain a stock solution of 3.4 mg/mL. The sodium salt solution of all the counter ions depicted in Figure 21 was prepared by dissolving the respective salts in 100 mM pH 7.4 PBS to obtain a 200 mM stock solution. To obtain the working solution, 210 µL of the salt solution was dissolved in 190 µL of polymer stock solution to obtain a 100 mM pH neutral salt solution with a polymer concentration of 1.6 mg/mL.

2.2. Physical crosslinking

2.2.1. Gelatin Spheres

The gelatine particles were dissolved by adding 61.0 mg in 1 mL of 100 mM pH 7.4 PBS by sonicating the mixture for 30 min at 24 °C. The PIC polymer **P41** was dissolved in PBS to obtain a stock solution of 3.4 mg/mL. Prior to the rheological experiment the two solutions were cooled on ice and 59 µL of the gelatine stock solution was combined with 72 µL of the PIC solution. The mixture was aspirated several times to obtain a homogeneous solution before being placed on a 5 °C rheometer for analysis.

3. Dynamic crosslinking

3.1. Host Guest Crosslinking

3.1.1. Synthesis of PIC-Phe (13)

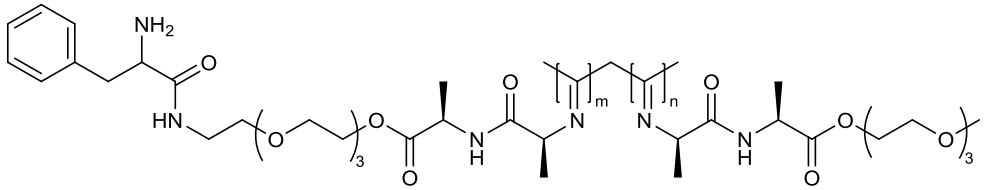

The amine functional polymer was swollen overnight in 1.0 mL DMF. In a separate round bottom flask (((9H-fluoren-9-yl)methoxy)carbonyl)-L-phenylalanine (Fmoc Phe) (110 mg, 0.03 µmol) and EDC (0.1 mg, 0.1 µmol) were dissolved in 2 mL DMSO and 2 mL DMF. To this mixture (130.0 mg, 0.1 µmol) Sulfo-NHS dissolved in 2 mL DMSO was added. Then 2 mL of this mixture was added to each polymer solution and the reaction allowed 14 days to reach completion. Deprotection with 16 % piperidine in DMF was performed on the reaction mixture, stirring for 9 h at room temperature. At this time the solution was dialysed against water for 3 days. The water was removed by co-evaporation with iso-propanol under reduced pressure. The resulting solid was dissolved in DCM and precipitated from diisopropyl ether. The excess solvent was decanted and the polymer **13a-c** was dried under nitrogen flow.

Table 3. PheFmoc conversion to Phe and ratio as determined by ^{1}H NMR.

Compound	mg PIC	mg PheFmoc	mg deprotected PIC	Ratio m:n	% Yield
P38	29.9	36.7	10.6	1:67	35
P20	17.1	30.6	7.9	1:278	46
P36	28.8	36.7	10.0	1:625	35

Table 4. Masses used for the rheology dynamic crosslinking experiment Strategy A.

Compound	Mol ratio	mg PIC	pmol Phe	mg CB8	pmol CB8	concentration PIC (mg/mL)
P38	**0**	2.0	147.0	0.0	0.0	2.0
P38	**2:1**	2.0	147.0	0.1	71.0	2.0
P38	**1:1**	2.0	147.0	0.2	146.0	2.0
P20	**0**	2.0	15.8	0.0	0.0	2.0
P20	**0.5:1**	2.0	15.8	0.04	29.0	2.0

3.1.2. Synthesis of PIC-Phe (17)

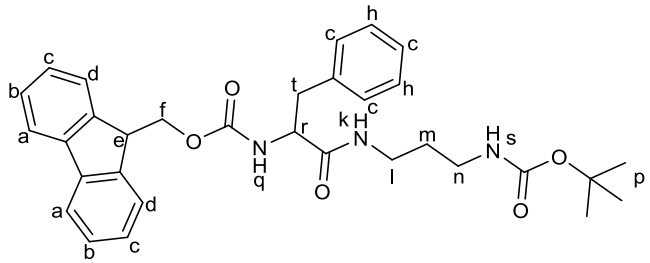

Tert-butyl (3-aminopropyl)carbamate (0.2 g, 0.9 mmol) was dissolved in 50 mL DCM. To this solution Fmoc-Phe (0.3 g, 0.9 mmol), DCC (0.2 g, 1.1 mmol) and a spatula tip of DMAP were added together and allowed to stir at room temperature overnight. The mixture was diluted with 100 mL chloroform and extracted three times with 10 % citric acid solution. The organic layer was concentrated to result in compound **14** as a white powder. **R_f** = 0.5 (DCM) **^{1}H-NMR (400 MHz, $CDCl_3$)** δ 7.75 (d, J= 7.4 Hz, 2H, H_a), 7.55 (t, J=7.6 Hz, 2H, H_d), 7.40 (t, J=7.2 Hz, 2H, H_h), 7.35-7.15 (m , 9H, $H_{b,c}$), 6.40 (s, 1H, H_q), 5.42 (s, 1H, H_k), 4.77 (s, 1H, H_s), 4.47-4.27 (m, 3H, $H_{e,f}$), 4.19 (m, 1H, H_r), 3.30-2.85 (m, 6H, $H_{l,m,n}$), 1.26 (s, 9H, H_p) **^{13}C NMR ($CDCl_3$, 75 MHz)** δ 171.25 (C=O), 144.17(C), 141.70(C), 136.89 (C_{Ar}), 129.73, 129.11, 127.46, 125.45 (CH_c), 120.39 (CH_d), 67.43(CH_2CH_e), 49.58 (CH_r), 47.57 (CH_e), 39.29 (CH_2-C_{Ar}), 36.32 (CH_2), 34.38, 30.36, 28.78 (3-CH_3), 26.04, 25.35 **MS (ESI):** m/z ([M]$^+$: $C_{32}H_{37}N_3O_5Na$), calcd 566.7; found 566.1

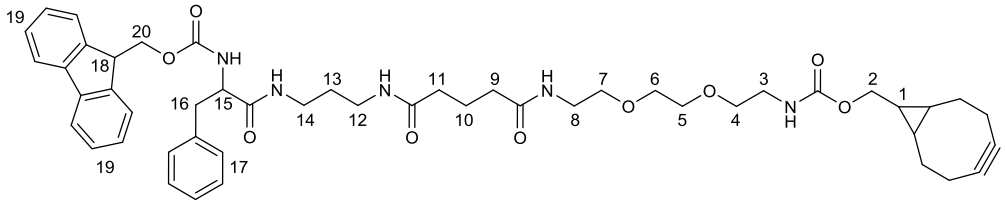

Product **14** (0.1 g, 0.1 mmol) was dissolved in 3 mL DCM. To this mixture 3 mL 4.0 M HCl in dioxane was added. The product formation was traced by TLC and deprotection was deemed complete when only $\mathbf{R}_f$ = 0.88 (DCM) was observed and no peaks corresponding to tert-butyloxycarbonyl (BOC) protons were present in the ^{1}H NMR anymore. Excess acid was removed by removing excess solvent under reduced pressure. To the resulting paste (0.1 g, 0.1 mmol) 10 mL DCM was added and removed under reduced pressure another two times to ensure all acid was removed. The deprotected intermediate was dissolved in 10 mL 50 mM pH 8.4 borate buffer. To this BCN-NHS (0.1 g, 0.1 mmol) in 2 mL DMSO was added. The reaction was allowed to stir at room temperature for 9 h. The solvent was removed by freeze drying to obtain **15** a white powder (0.2 g, 0.2 mmol). **^{1}H-NMR (400 MHz, MeOD)** δ 7.82 (d, *J* = 7.6 Hz, 2H, H_{19}), 7.69 – 7.50 (m, 2H, H_{17}), 7.42 (t, *J* = 7.5 Hz, 2H, H_{19}), 7.27 (dd, *J* = 27.8, 11.4 Hz, 5H, $H_{19/17}$), 4.35 (d, *J* = 7.0 Hz, 1H, H_{18}), 4.28 (s, 1H, H_{15}), 4.23 – 4.08 (m, 2H, H_2), 3.68 – 3.47 (m, 6H), 3.18 (dd, *J* = 21.5, 14.7 Hz, 3H), 2.91 (s, 1H), 2.65 (s, 4H), 2.25 (s, 6H), 1.99 – 1.83 (m, 3H), 1.72 (s, 1H), 1.68 – 1.51 (m, 3H), 1.37 (s, 2H), 1.18 (s, 2H), 0.94 (dd, *J* = 17.8, 8.5 Hz, $1H_1$) **^{13}C NMR ($CDCl_3$, 75 MHz)** δ 172.79 (C=O), 171.90 (C=O), 155.78 (C=O), 143.76 (C=O), 140.67 (C_{fmoc}), 138.16 (C_{fmoc}), 129.22 (2CH), 128.06 (2CH), 127.65(2CH), 127.05(2CH), 125.30 (CH), 120.09 (2CH), 99.02 ($2C_{BCN}$), 69.54 (C_{20}), 69.15 (C_2), 65.67 (CH_{18}), 46.59 (CH_{15}), 36.15, 34.74, 33.38, 30.72, 29.21, 28.62, 25.26 ($2CH_2$), 24.49, 20.88 (C_1), 19.58, 17.68 **MS (ESI):** m/z ($[M]^+$: $C_{49}H_{61}N_5O_9Na$), calc 887.04; found 887.5

To assign the protons with more certainty, 2D NMR strategies such as NOESY and HSQC were used, see Figure 45-46. In NOESY spectra long distance coupling between protons was used to clearly assign protons and with the HSQC it was possible to distinguish peaks that originated from carbon-proton interactions which resulted in the peaks of C*H*$_3$ and C*H*$_2$ protons appearing inverted with regards to C*H* proton peaks.

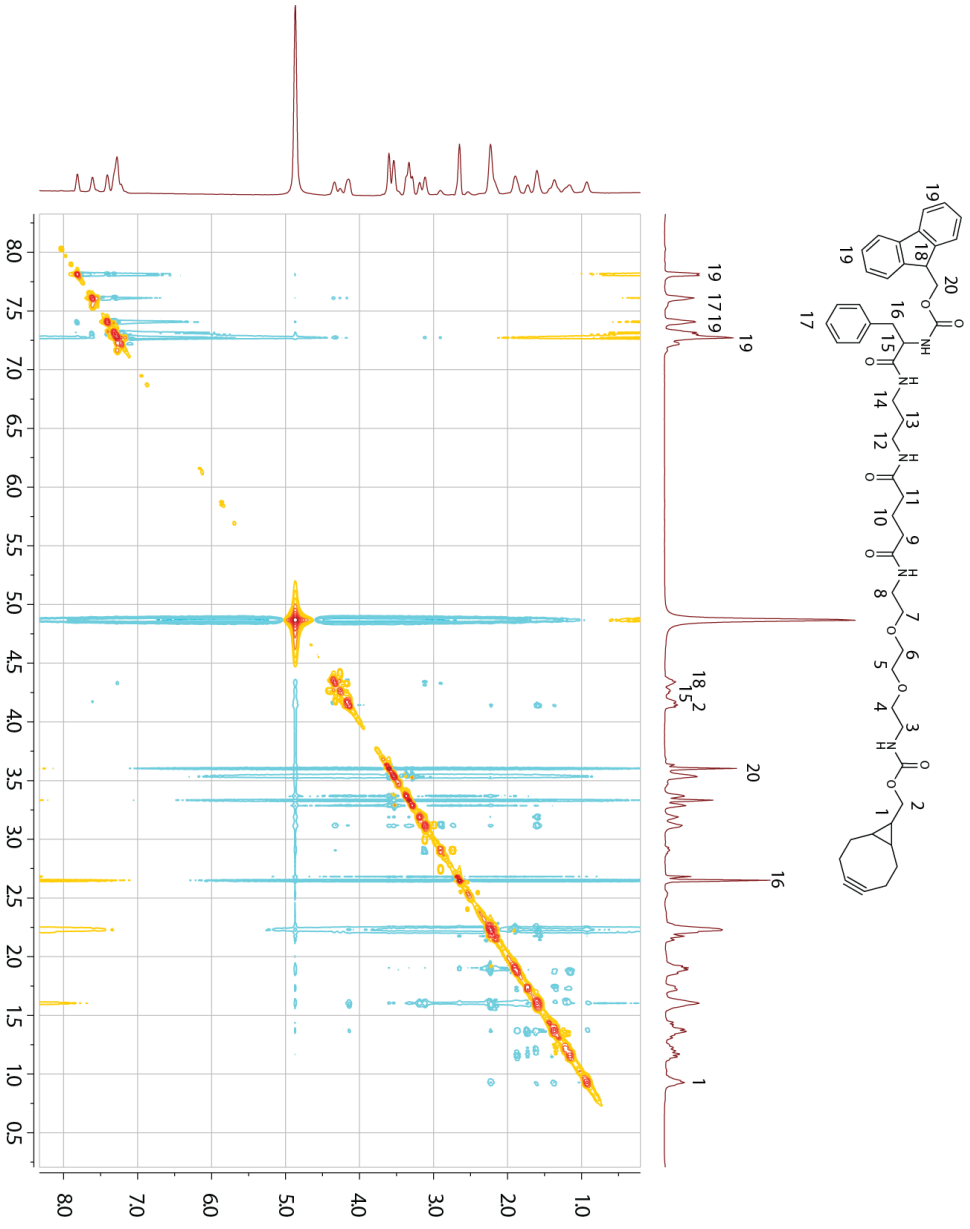

Figure 37. NOESY 2D NMR of FMOC-Phe-BCN

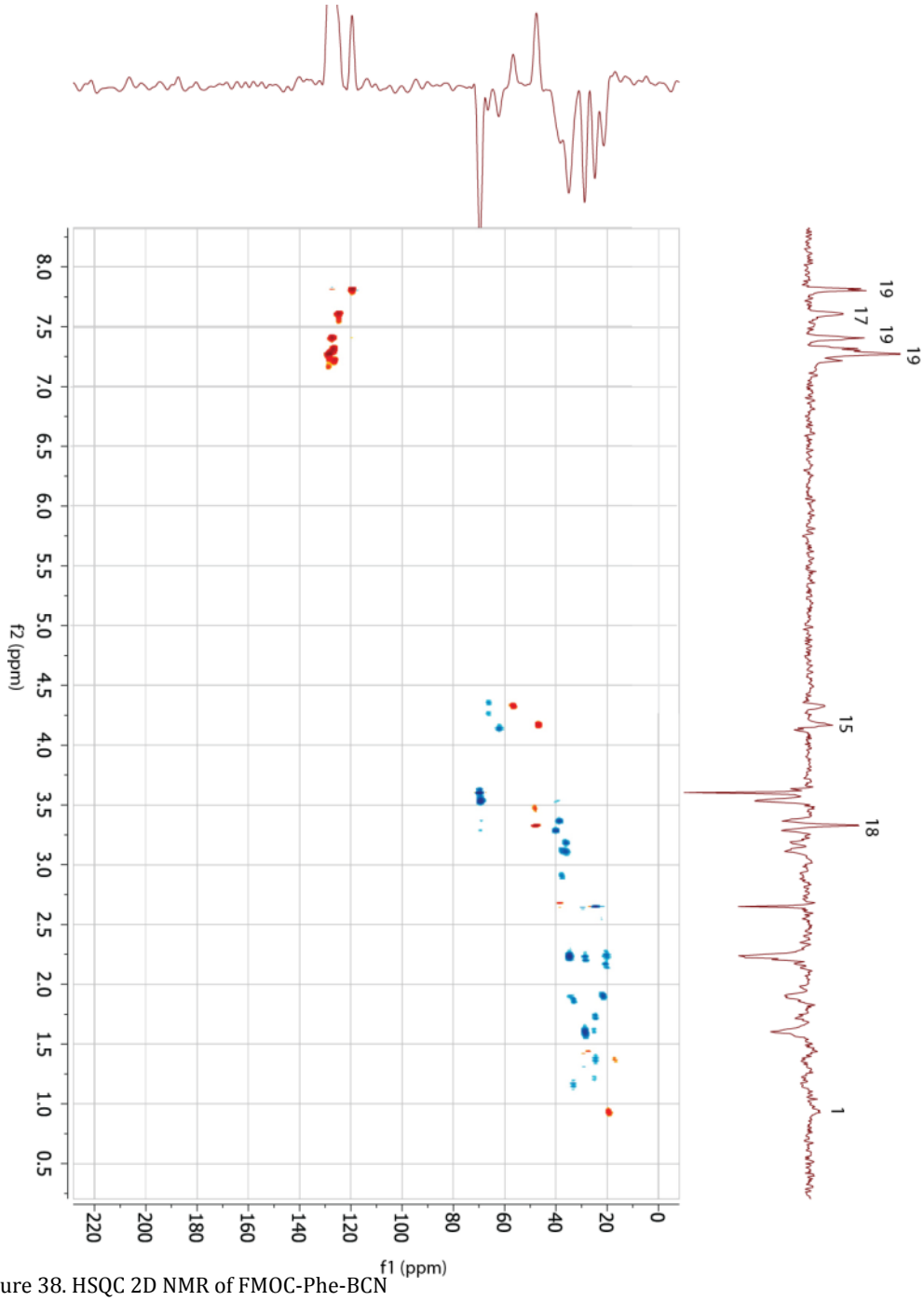

Figure 38. HSQC 2D NMR of FMOC-Phe-BCN

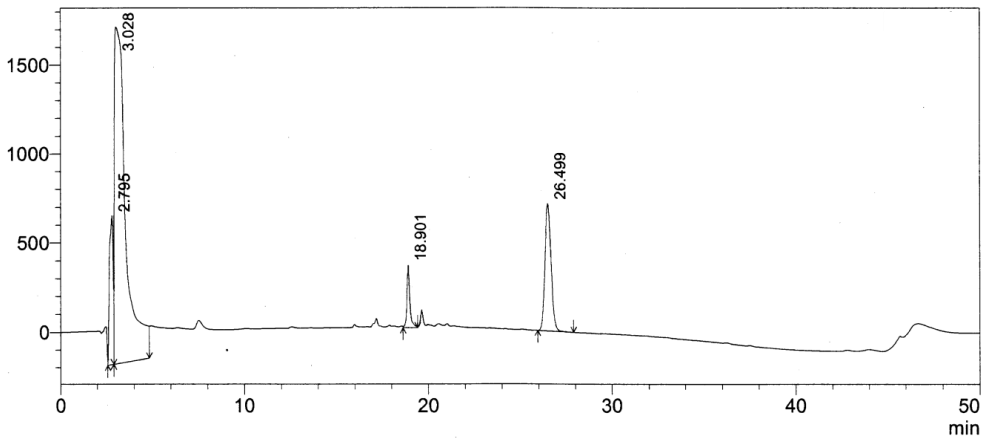

Figure 39. HPLC chromatogram of FMOC-Phe-BCN (15), analyzed with UV detector at λ = 214 nm

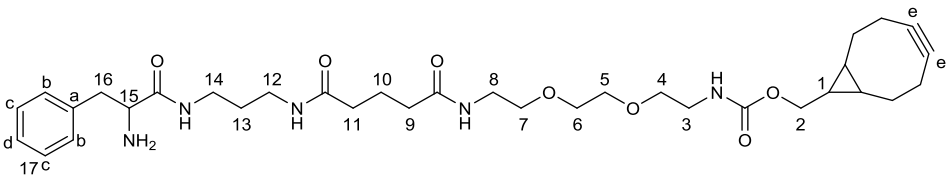

1 mL 5% piperidine/DMF and Fmoc-Phe R3 BCN **15** (0.2 g, 0.2 mmol) was combined and stirred at room temperature for 1 h. Once dissolved 10 mL of MQ was added. A white precipitate formed and was filtered off. The water layer was freeze dried to obtain **16**, colourless oil (0.1 g, 0.1 mmol) in a 79% yield. **^{1}H-NMR (500 MHz, MeOD)** δ 7.34 – 7.18 (m, 5H, H_{17}), 4.13 (d, *J* = 8.1 Hz, 2H, H_2), 3.68 – 3.43 (m, 10H), 3.35 (t, *J* = 5.5 Hz, 2H), 3.21 (s, 1H), 3.16 – 3.03 (m, 12H), 2.72 (dd, *J* = 17.5, 7.2 Hz, 1H), 2.46 – 2.34 (m, 2H), 2.24 (m, 5H), 1.87 (m, 2H), 1.77 (m, 21H), 1.72 – 1.61 (m, 3H), 1.56 (m, 3H), 1.36 (m, 1H), 0.93 (m, 1H, H_1) **^{13}C NMR (126 MHz, MeOD)** δ 182.03 (C=O), 178.14 (C=O), 177.34 (C=O), 138.33 (C_a), 130.02 (C_c), 129.19 (C_b), 127.43 (C_d), 111.95, 99.24 (C_e), 70.87(C_{16}), 70.18 (C_2), 57.57, 45.33, 43.54, 41.88, 40.02, 37.83, 35.86, 33.04, 29.80, 28.55, 27.21, 26.37, 25.11, 23.56, 22.82, 22.43, 21.53, 20.98 (C_1) **MS (ESI):** m/z ($[M]^+$: $C_{34}H_{52}N_5O_7$), calcd 641.4; found 642.4

To assign the protons with more certainty 2D NMR strategies such as NOESY was used see Figure 40. In NOESY spectra long distance coupling, between protons were used to clearly assign protons.

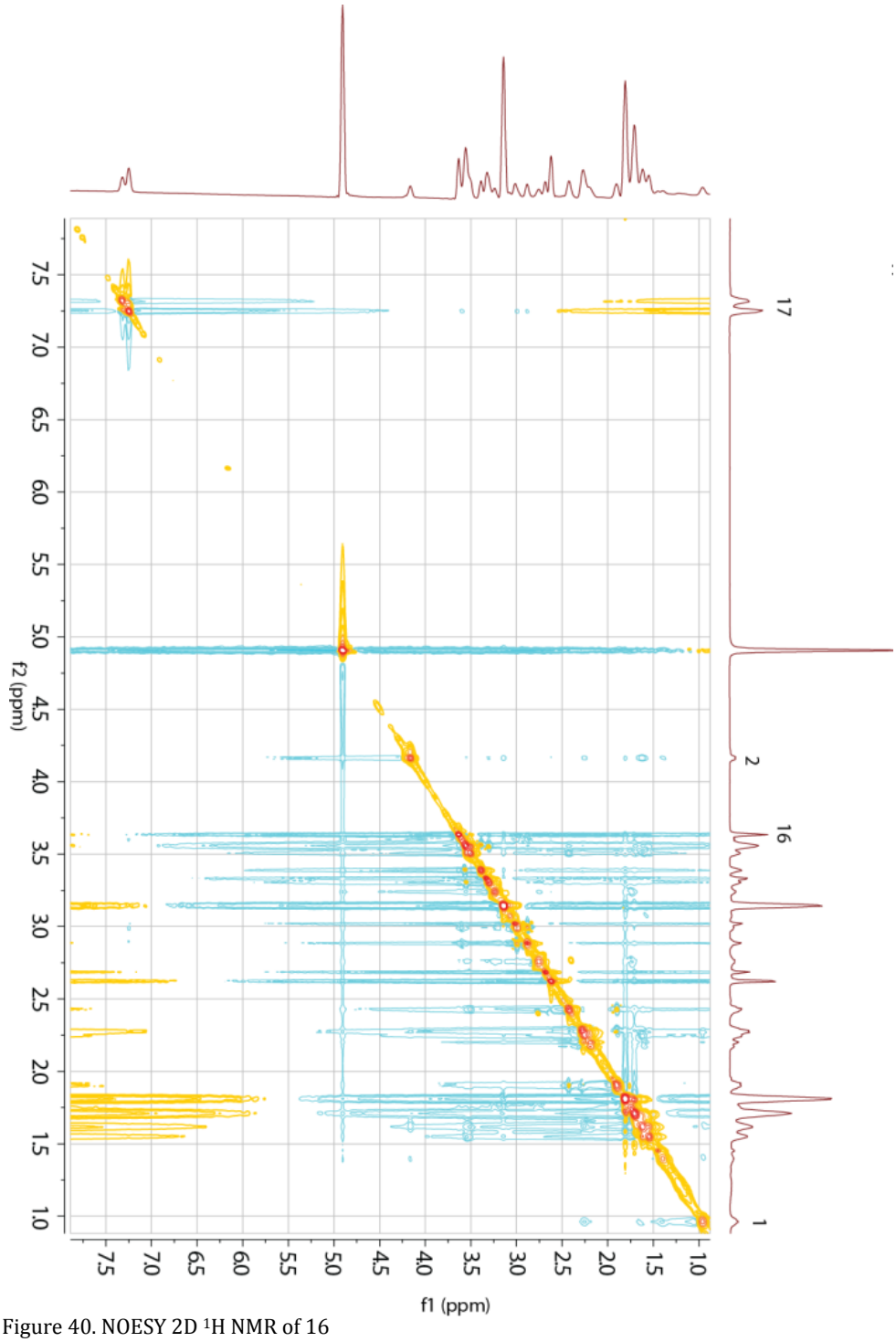

Figure 40. NOESY 2D ^{1}H NMR of 16

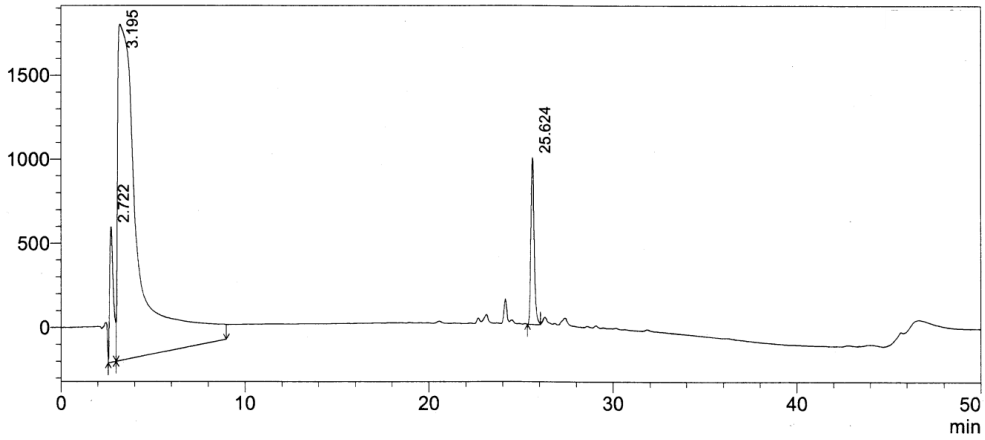

Figure 41. HPLC chromatogram of Phe-BCN (16) analyzed with UV detector 214 nm

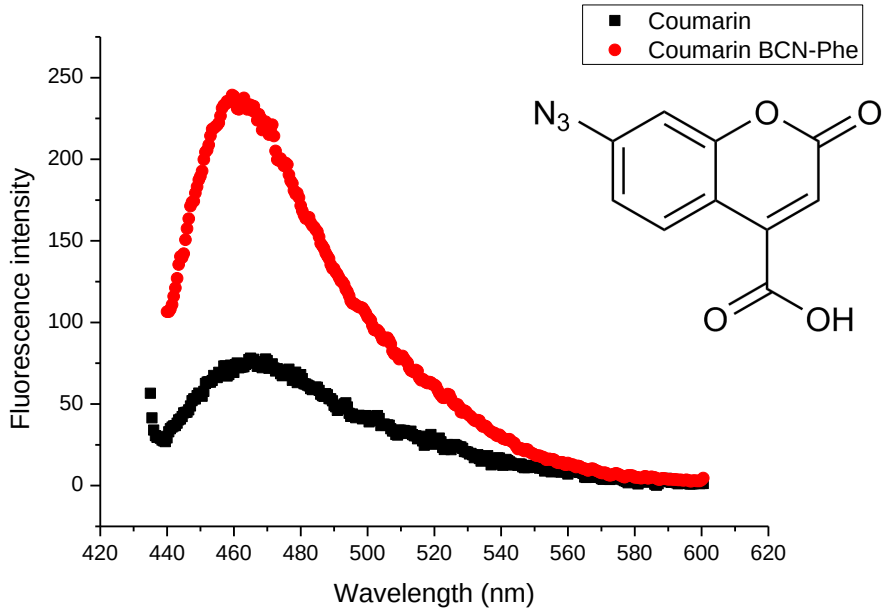

Figure 42. Fluorescence emission of 7-azido-2-oxo-2H-chromene-4-carboxylic acid with and without BCN-Phe (16).

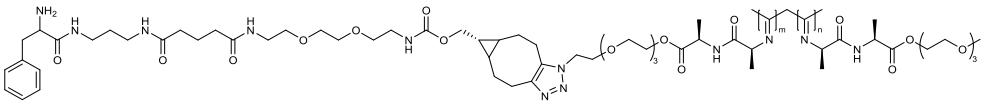

The polymer (see Table 5 for details) was dissolved in DCM, to this 20-fold molar equivalent of **16** was added. The mixture was stirred for 18 h at room temperature. The polymer was obtained by precipitation from diisopropyl ether. The excess solvent was decanted and the polymer dried under reduced pressure to obtain **17a-c**. The remaining azides were measured by dying with BCN-Tokyo green as described previously in Chapter 3 section 1.2.2, if 1:315 azides remained in the PIC with an initial density of 1:67 azides then 79% of the azides were converted to phenylalanine.

Table 5. Experimental masses used for the synthesis of PIC-Phe (17).

	Sample	mg PIC	µmol N_3	mg PIC-Phe	Conversion %	Yield %
a	**P38**	34.0	4.3	28.0	79	82
b	**P20**	35.0	0.3	34.6	87	97
c	**P36**	40.0	0.1	36.8	81	93

3.1.3. Synthesis of PIC-Phe (19)

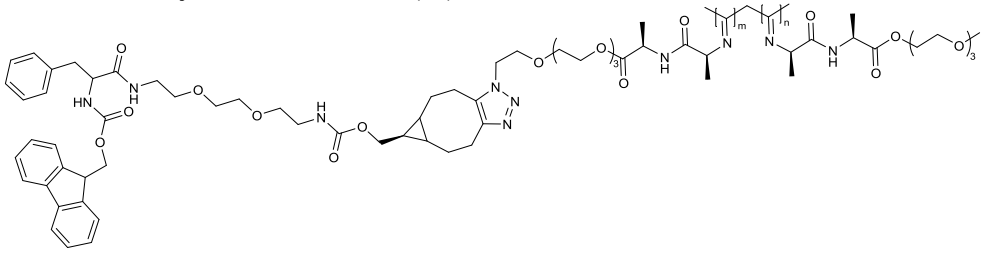

PIC-N_3 (Table 8) was dissolved in ACN, to this an aliquot from a stock solution of 10 mg/mL **18** was added and allowed to react for 4 days at room temperature. The polymer was precipitated from diisopropyl ether. The excess solvent was decanted and dried under nitrogen flow. Samples of Fmoc protected **19a-c** were sent to Cambridge for analysis and rheology experiments.

Table 6. Experimental masses and volumes used for the synthesis of PIC-Phe 19.

	Compound	mg	µmol N_3	BCN-Phe-Fmoc µL	µmol BCN-Phe-Fmoc	% Yield
a	**P38**	23.0	1.7	200.0	2.9	65
b	**P20**	15.0	0.1	70.0	1.0	40
c	**P36**	10.0	0.1	70.0	1.0	80

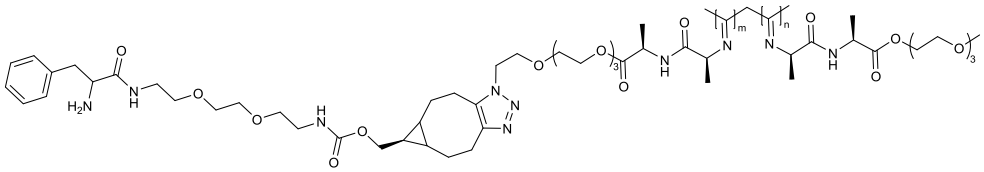

The polymer PIC-N_3 (Table 7) was dissolved in 50 mM borate buffer pH 8.4 to obtain a stock concentration of 4.0 mg/mL. To this a stock solution of 1.1 mg/mL **18** in DMSO was added. The reaction mixture was placed in the heated shaker and allowed to react at 10 °C shaking at 350 rpm overnight. A portion of the reaction mixture was removed for analysis of the intermediate step by rheology. The remaining portion was treated with 5% pipiridine/DMF at 22 °C shaking at 350 rpm for 16 h. The solution was dialysed against MQ and refreshed twice and finally dialysed against 50 mM borate buffer pH 8.4 to obtain a stock concentration of 1.2 mg/mL PIC-Phe **19** in borate buffer.

Table 7. Data summary of PIC-N_3 functionalization and Fmoc deprotection used to synthesize PIC-Phe 19.

Compound	**mg**	**µmol N_3**	**BCN-Phe-Fmoc µL**	**µmol 18**	**µL pipiredine/DMF**
P38	4.0	0.3	160.0	0.3	
P20	4.0	0.03	80.0	0.1	
P36	2.0	0.01	40.0	0.1	
P38-PheFmoc	3.0	0.2			750.0
P20-PheFmoc	3.0	0.02			750.0
P36-PheFmoc	1.0	0.01			250.0

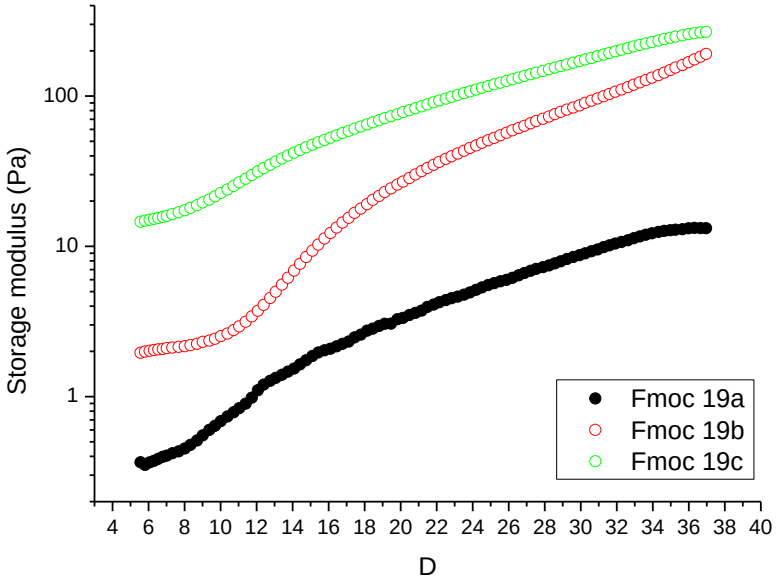

Figure 43. Storage modulus as a function of temperature for Fmoc 19a-c at 1.2 mg/mL in 50 mM borate buffer pH 8.4 .

3.1.4. Synthesis of PVA-MV 24

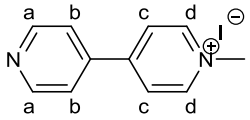

4,4'-Bipyridine (2.50 g, 16.1 mmol) was dissolved in DCM (25 mL). MeI (2.85 g, 20.1 mmol) in DCM (13 mL) was added and the mixture was stirred at 25 °C for 18 h. The resulting yellow precipitate was isolated by vacuum filtration, washed with DCM and dried *in vacuo* to yield 1-methyl-[4,4'-bipyrindin]-1-ium iodide (3.82 g, 12.8 mmol, 80 %) **20** as a yellow solid [35].

^{1}H-NMR (400 MHz, D_2O) δ 8.93 (d, *J* = 6.3 Hz, 2H, H_d), 8.79 (d, *J* = 4.9 Hz, 2H, H_c), 8.41 (d, *J* = 6.3 Hz, 2H, H_b), 7.93 (d, *J* = 4.9 Hz, 2H, H_a), 4.47 (s, CH_3).

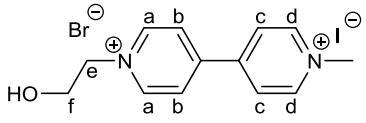

1-methyl-[4,4'-bipyrindin]-1-ium iodide **20** (3.00 g, 10.1 mmol) in acetonitrile (125 mL) was refluxed until a homogenous solution formed. Bromo ethanol (1.8 mL, 25.2 mmol) was added and the mixture was refluxed for 48 h. The resulting precipitate was isolated by vacuum filtration, washed with acetonitrile and dried *in vacuo* to yield 1-(2-hydroxyethyl)-1'-methyl-[4,4'-bipyridine]-1,1'-diium bromide iodide **21** (2.30 g, 5.44 mmol, 54 %) as a yellow solid [35].
^{1}H-NMR (400 MHz, D_2O) δ 9.16 (d, *J* = 6.8, 2H, H_a), 9.09 (d, *J* = 6.7, 2H, H_d), 8.61 (d, *J* = 6.6, 2H, H_b), 8.57 (d, *J* = 6.5, 2H, H_c), 4.89 (m, 2H, H_e), 4.54 (s, CH_3), 4.18 (m, 2H, H_f).

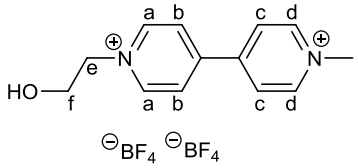

1-(2-hydroxyethyl)-1'-methyl-[4,4'-bipyridine]-1,1'-diium bromide iodide **21** (2.00 g, 4.73 mmol) and NH_4BF_4 (0.99 g, 9.46 mmol) in acetonitrile (50 mL) were refluxed for 2 h. The colourless salt was separated from the brown solution by filtrations. The solvent was removed under reduced pressure to yield 1-(2-hydroxyethyl)-1'-methyl-[4,4'-bipyridine]-1,1'-diium tetrafluoroborate **22** (1.01 g, 2.59 mmol, 55 %) as an orange solid [35].
^{1}H-NMR (400 MHz, D_2O) δ 9.16 (d, *J* = 6.6, 2H, H_a), 9.09 (d, *J* = 6.6, 2H, H_d), 8.61 (d, *J* = 6.4, 2H, H_b), 8.57 (d, *J* = 6.4, 2H, H_c), 4.89 (m, 2H, H_e), 4.54 (s, CH_3), 4.17 (m, 2H, H_f).

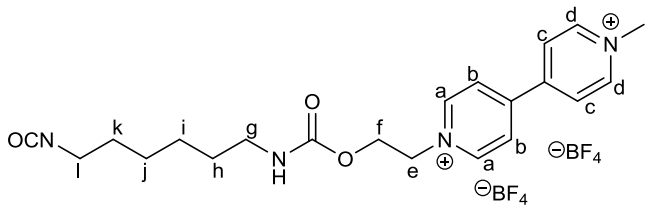

The product **22** (900 mg, 2.31 mmol) was dissolved in dry acetonitrile (250 mL) and 1,6-hexamethylene diisocyanate (3.7 mL, 23.1 mmol) and dibutyltin dilaurate (1 drop) were added. The reaction was stirred for 24 h at room temperature. The solvent was evaporated under reduced pressure to ± 10 mL and 200 mL anhydrous Et_2O was added. This mixture was put to stand in the freezer for 2 h after which the solvent was decanted. The residue was dried *in vacuo* to yield **23** (751 mg, 1.35 mmol, 58 %) as a dark orange solid [35].
^{1}H-NMR (400 MHz, D_2O) δ 9.20 (m, 2H, H_a), 9.11 (d, *J* = 4.7, 2H, H_d), 8.62 (d, *J* = 4.8, 2H, H_b), 8.58 (d, *J* = 4.8, 2H, H_c), 5.05 (m, 2H, H_f), 4.67 (m, 2H, H_e), 4.55 (s, CH_3), 3.04 (m, 4H, $H_{h;g}$), 1.49 (m, 8H, H_{l-i}).

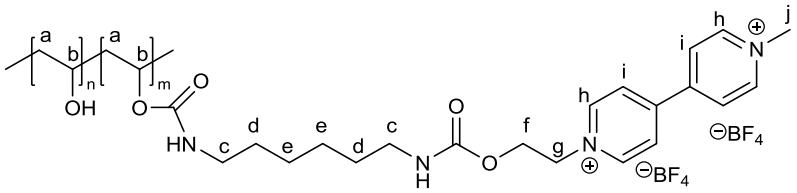

PVA was dried in a vacuum oven at 60 °C for 24 h. Then, PVA (100 mg, 2.44 mmol -OH) was dissolved in dry NMP (6 mL). To this mixture **23** (150 mg, 0.268 mmol) and dibutyltin dilaurate (1 drop) were added and stirred over night at room temperature. The product was purified by precipitation of the reaction mixture into ethyl acetate, filtration and then lyophilized to yield **24** (244 mg, MV:OH = 1:27) as a white solid [35].
^{1}H-NMR (500 MHz, D_2O) δ 9.08 (4H, H_h), 8.57 (4H, H_i), 4.86 (2H, H_f part of H_2O peak), 4.52 (3H, H_j), 4.05 (28H, H_b), 3.87 (2H, H_g), 3.03 (4H, H_c), 1.67 (60H, $H_{a;d}$), 1.23 (4H, H_e).

3.1.5. Synthesis PIC-methyl viologen 26

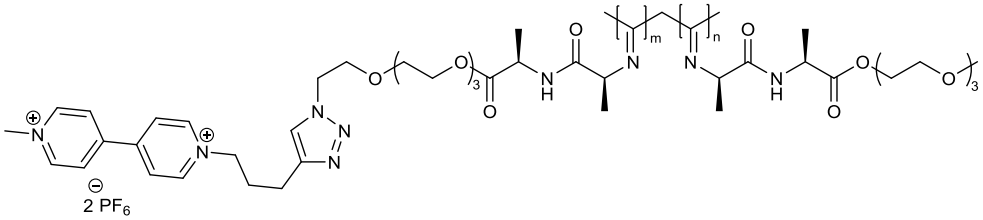

PIC-N_3 **P38** (100 mg, 7.3 µmol $-N_3$) was dissolved in a mixture of DMSO (3 mL) and ACN (5 mL) after which compound **25** (4.0 mg, 7.3 µmol) was added. This viscous solution was degassed for 2 h. $CuPF_6(CH_3CN)_4$ (2.7 mg, 7.3 µmol) was degassed by consecutive flushing with nitrogen gas and a vacuum. Then the solution was added to the copper complex and the mixture was stirred for 4 days between 0 °C and room temperature. The product was purified by dialysis against MQ for 2 days and then isolated by lyophilisation. The polymer was isolated as a white solid **26** (29 mg, 29 %).
^{1}H-NMR (500 MHz, CD_3CN) δ 9.01 (MV), 8.50 (MV), 3.55 (backbone). IR (neat) ν 3268, 2886, 1740, 1657, 1533, 1206, 1106, 955, 862, 755, 695 cm^{-1}. UV-vis λ_{max}=244 nm. Degree of functionalisation has to be determined using displacement studies with acridine orange as described by Urbach [3539] as conventional ^{1}H-NMR ratio determination was not possible.

3.1.6. Synthesis of PVA-phenylalanine 29

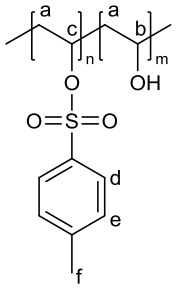

PVA (200.0 mg, 4.9 mmol –OH) was dissolved in DMSO (4 mL) and pyridine was added (0.5 mL). The solution was cooled down to 0 °C and TsCl dissolved in DMSO (2 mL) was added dropwise. The mixture was stirred over night at room temperature. The product was purified by precipitation into ethyl acetate and filtration. The product was dissolved in DMSO and then dialysed against MQ after which it was lyophilized to yield **27** (185.0 mg, OTs:OH = 1:4.5) as a white solid [40].

^{1}H-NMR (400 MHz, D_2O) δ 7.70 (d, *J* = 8.4, 2H, H_d), 7.38 (d, *J* = 8.4, 2H, H_e), 5.08 (s, 0.5H, H_c), 4.02 (s, 4H, H_a), 2.40 (s, 3H, H_f), 1.64 (m, 9H, H_b).

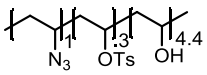

PVA-OTs **27** (100.0 mg, 0.3 mmol –OTs) was dissolved in DMF and NaN_3 (38.0 mg, 0.6 mmol) was added. The resulting solution was allowed to stir at 65 °C for 2 days and precipitated into Et_2O followed by lyophilisation to yield **28** (84.0 mg, N_3:OH = 1:5.6) as a white solid [41].

^{1}H-NMR (400 MHz, D_2O) δ 7.70 (d, *J* = 8.4, 0.6H), 7.38 (d, *J* = 8.4, 0.6H), 5.07 (s, 0.3H), 4.02 (s, 5.4H), 2.41 (s, 0.9H), 1.68 (m, 11.4H). IR (neat) ν 3383, 2940, 2128, 2040, 1657, 1425, 1174, 1094, 1012, 817, 693 cm^{-1}.

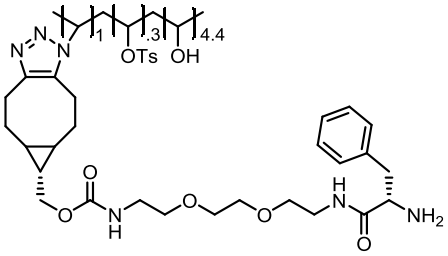

PVA-N_3 **28** (4.2 mg, 14.3 µmol –N_3) was dissolved in DMSO (2.1 mL) after which compound **18** (5.0 mg, 7.2 µmol) in DCM (0.5 mL) was added. The solution was stirred at room temperature for 4 days after which it was dialysed to remove the DMSO followed by lyophilisation to yield a white solid. The white solid was dissolved in DMF (2 mL) and piperidine (1 mL) was added for the deprotection. This mixture was stirred over night at room temperature. The product PVA-Phe **29** was purified by dialysis and isolated by lyophilisation to yield a white solid.

3.1.7. Alternative route to synthesize PVA decorated with phenylalanine 31

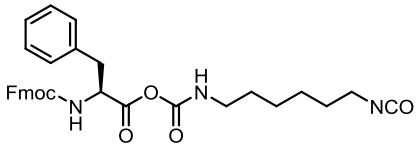

1,6-hexamethylene diisocyanate (2.0 mL, 12.4 mmol) was dissolved in dry toluene (50.0 mL). Fmoc-Phe (1.0 g, 2.6 mmol) was slowly added after which the mixture was heated to 100 °C and stirred over night. Then the solution was allowed to cool down and the solvent was removed *in vacuo*. The resulting mixture was triturated several times with cold, dry diethyl ether to crystallize the product. The Fmoc-Phe-NCO was then washed with diethyl ether on a filter and dried under reduced pressure at 60 °C to yield **30** as a white solid (918.0 mg, 1.7 mmol, 66%, 0.1 equivalents diisocyanate).

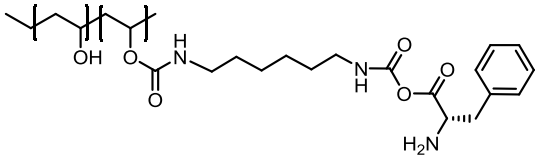

PVA (300.0 mg, 7.3 mmol –OH) was dissolved in dry NMP (15 mL) by heating to 125 °C for 1.5 h. This solution was allowed to cool down after which dibutyltin dilaurate (3 drops) was added. Then **30** (394.0 mg, 0.7 mmol) in dry NMP (2 mL) was added followed by stirring at room temperature for 24 h. Next, piperidine (3 mL) was added and the solution was stirred for another 24 h. The resulting mixture was very viscous and placed in acetone to precipitate the polymers out. The precipitation was stirred for 24 h after which the product was isolated as a white solid by centrifugation. It was not possible to analyze polymer **31** as it was crosslinked most likely due to residual diisocyanate.

Test rheology experiments PIC in presence of PVA

The two polymers were dissolved in 50 mM pH 8.4 borate buffer to obtain their respective stock solutions of 3.2 mg/mL PIC-N_3 **P41** and 44.0 mg/mL PVA. The two solutions were placed on ice prior to the rheology experiment to enable efficient mixing.

Table 8. Rheological crowding experiment of increasing weight ratio PVA in PIC (P41).

mg PVA	mg PIC	w/w	PVA:PIC	Concentration PIC (mg/mL)
0	0.4	0	0	1.6
0.24	0.4	0.6	1:1.7	1.6
0.72	0.4	1.8	1:0.6	1.6

Crosslinking experiments of 19 with flexible linker

Table 9. Ratios used in the rheological mixing experiments of PVA-MV and PIC-Phe (P38 1:67; P20 1:625) in the presence of CB8.

Compound	**PVA: PIC**	**Mol ratio**	**mg PIC**	**pmol Phe**	**mg PVA-MV**	**pmol MV**	**pmol CB8**
P38	**0**	**0**	0.6	44.1	0.0	0	0.0
P38	**1:3**	**1:3675**	0.6	44.1	0.2*	0.01	44.1
P38	**1:3**	**1:300**	0.6	44.1	0.2	1.5	44.1
P20	**0**	**0**	0.6	4.7	0.0	0.0	0.0
P20	**1:3**	**1:3**	0.6	4.7	0.2	1.6	4.7
P20	**1:30**	**1:340**	0.3	2.4	0.01*	$7.1x10^{-3}$	2.4
P20	**1:2**	**1:3**	0.3	2.4	0.2*	0.7	2.4

* 3 % PVA-MV

References

1 Kouwer, P. H. *et al.* Responsive biomimetic networks from polyisocyanopeptide hydrogels. *Nature*, **493**, 651-655, (2013).

2 Discher, D. E., Mooney, D. J. & Zandstra, P. W. Growth Factors, Matrices, and Forces Combine and Control Stem Cells. *Science*, **324**, 1673-1677, (2009).

3 Vanderhooft, J. L. *et al.* Rheological Properties of Cross-Linked Hyaluronan–Gelatin Hydrogels for Tissue Engineering. *Macromolecular Bioscience*, **9**, 20-28, (2009).

4 Winer, J. P., Oake, S. & Janmey, P. A. Non-Linear Elasticity of Extracellular Matrices Enables Contractile Cells to Communicate Local Position and Orientation. *PLoS ONE*, **4**, e6382, (2009).

5 Wells, R. G. The role of matrix stiffness in regulating cell behavior. *Hepatology*, **47**, 1394-1400, (2008).

6 Seiffert, S. & Sprakel, J. Physical chemistry of supramolecular polymer networks. *Chemical Society Reviews*, **41**, 909-930, (2012).

7 Appel, E. A. *et al.* Supramolecular polymeric hydrogels. *Chemical Society Reviews*, **41**, 6195-6214, (2012).

8 Roy, S. *et al.* Dramatic Specific-Ion Effect in Supramolecular Hydrogels. *Chemistry – A European Journal*, **18**, 11723-11731, (2012).

9 Zhang, Y. *et al.* Specific Ion Effects on the Water Solubility of Macromolecules: PNIPAM and the Hofmeister Series. *Journal of the American Chemical Society*, **127**, 14505-14510, (2005).

10 Daniele, M. A. *et al.* Interpenetrating networks based on gelatin methacrylamide and PEG formed using concurrent thiol click chemistries for hydrogel tissue engineering scaffolds. *Biomaterials*, **35**, 1845-1856, (2014).

11 Jiang, B. *et al.* Fibrin-Loaded Porous Poly(Ethylene Glycol) Hydrogels as Scaffold Materials for Vascularized Tissue Formation. *Tissue Engineering Part A*, **19**, 224-234, (2012).

12 Appel, E. A. *et al.* Supramolecular Cross-Linked Networks via Host−Guest Complexation with Cucurbit[8]uril. *Journal of the American Chemical Society*, **132**, 14251-14260, (2010).

13 Broedersz, C., Storm, C. & MacKintosh, F. Nonlinear Elasticity of Composite Networks of Stiff Biopolymers with Flexible Linkers. *Physical Review Letters*, **101**, 118103, (2008).

14 Tan, H. *et al.* Controlled gelation and degradation rates of injectable hyaluronic acid-based hydrogels through a double crosslinking strategy. *Journal of Tissue Engineering and Regenerative Medicine*, **5**, 790-797, (2011).

15 Lee, H.-L. & Aubé, J. Intramolecular and intermolecular Schmidt reactions of alkyl azides with aldehydes. *Tetrahedron*, **63**, 9007-9015, (2007).

16 Palumbo, F. S. *et al.* Self-assembling and auto-crosslinkable hyaluronic acid hydrogels with a fibrillar structure. *Acta Biomaterialia*, **6**, 195-204, (2010).

17 Xu, J. *et al.* Cytocompatible Poly(ethylene glycol)-co-polycarbonate Hydrogels Crosslinked by Copper-free, Strain-promoted "Click" Chemistry. *Chemistry, an Asian journal*, **6**, 2730-2737, (2011).

18 Jonker, A. M. *et al.* A Fast and Activatable Cross-Linking Strategy for Hydrogel Formation. *Advanced Materials*, **27**, 1235-1240, (2015).
19 Akeroyd, N. & Klumperman, B. The combination of living radical polymerization and click chemistry for the synthesis of advanced macromolecular architectures. *European Polymer Journal*, **47**, 1207-1231, (2011).
20 Nishi, K. K. & Jayakrishnan, A. Self-Gelling Primaquine−Gum Arabic Conjugate: An Injectable Controlled Delivery System for Primaquine. *Biomacromolecules*, **8**, 84-90, (2007).
21 Jia, X. *et al.* Hyaluronic Acid-Based Microgels and Microgel Networks for Vocal Fold Regeneration. *Biomacromolecules*, **7**, 3336-3344, (2006).
22 Barcan, G. A., Zhang, X. & Waymouth, R. M. Structurally Dynamic Hydrogels Derived from 1,2-Dithiolanes. *Journal of the American Chemical Society*, **137**, 5650-5653, (2015).
23 Duncan, R. J. S., Weston, P. D. & Wrigglesworth, R. A new reagent which may be used to introduce sulfhydryl groups into proteins, and its use in the preparation of conjugates for immunoassay. *Analytical Biochemistry*, **132**, 68-73, (1983).
24 Dommerholt, J. *et al.* Readily Accessible Bicyclononynes for Bioorthogonal Labeling and Three-Dimensional Imaging of Living Cells. *Angewandte Chemie International Edition*, **49**, 9422-9425, (2010).
25 Jewett, J. C., Sletten, E. M. & Bertozzi, C. R. Rapid Cu-free click chemistry with readily synthesized biarylazacyclooctynones. *Journal of the American Chemical Society*, **132**, 3688-3690, (2010).
26 Sletten, E. M. & Bertozzi, C. R. From Mechanism to Mouse: A Tale of Two Bioorthogonal Reactions. *Accounts of Chemical Research*, **44**, 666-676, (2011).
27 Eksteen, Z.-H. *Hybrid hydrogels based on RAFT mediated poly(N-vinyl pyrrolidone)* Masters thesis, University of Stellenbosch, (2009).
28 Tan, H. *et al.* Novel Multi-arm PEG-based Hydrogels for Tissue Engineering. *Journal of biomedical materials research. Part A*, **92**, 979-987, (2010).
29 Mahou, R. *et al.* Alginate-Poly(ethylene glycol) Hybrid Microspheres for Primary Cell Microencapsulation. *Materials*, **7**, 275, (2014).
30 Boyd, D. A. *et al.* Hydrodynamic shaping, polymerization, and subsequent modification of thiol click fibers. *ACS Appl Mater Interfaces*, **5**, 114-119, (2013).
31 DeForest, C. A., Polizzotti, B. D. & Anseth, K. S. Sequential click reactions for synthesizing and patterning three-dimensional cell microenvironments. *Nat Mater*, **8**, 659-664, (2009).
32 Hofmeister, F. Zur lehre der wirkung der salze. Zweite mittheilung. *Arch. Exp. Pathol. Pharmakol.* , **24**, 247-260, (1888).
33 Huss, F. R. M. *et al.* Use of macroporous gelatine spheres as a biodegradable scaffold for guided tissue regeneration of healthy dermis in humans: An in vivo study. *Journal of Plastic, Reconstructive & Aesthetic Surgery*, **63**, 848-857, (2010).
34 Impellitteri, N. A. *et al.* Specific VEGF sequestering and release using peptide-functionalized hydrogel microspheres. *Biomaterials*, **33**, 3475-3484, (2012).

35 Appel, E. A. *et al.* Ultrahigh-Water-Content Supramolecular Hydrogels Exhibiting Multistimuli Responsiveness. *Journal of the American Chemical Society*, **134**, 11767-11773, (2012).
36 Rowland, M. J. *et al.* Dynamically crosslinked materials via recognition of amino acids by cucurbit[8]uril. *Journal of Materials Chemistry B*, **1**, 2904-2910, (2013).
37 Appel, E. A. *et al.* Sustained release of proteins from high water content supramolecular polymer hydrogels. *Biomaterials*, **33**, 4646-4652, (2012).
38 Drira, Z. & Yadavalli, V. K. Nanomechanical measurements of polyethylene glycol hydrogels using atomic force microscopy. *Journal of the Mechanical Behavior of Biomedical Materials*, **18**, 20-28, (2013).
39 Ghale, G. *et al.* Determining Protease Substrate Selectivity and Inhibition by Label-Free Supramolecular Tandem Enzyme Assays. *Journal of the American Chemical Society*, **133**, 7528-7535, (2011).
40 Argade, A. B. & Peppas, N. A. Poly(acrylic acid)–poly(vinyl alcohol) copolymers with superabsorbent properties. *Journal of Applied Polymer Science*, **70**, 817-829, (1998).
41 Gacal, B. N. *et al.* Pyrene functional poly(vinyl alcohol) by "click" chemistry. *Journal of Polymer Science Part A: Polymer Chemistry*, **47**, 1317-1326, (2009).

Chapter 5 : Potential therapeutic properties of Poly(isocyanopeptides) as synthetic Dendritic Cells

Abstract
In this chapter the use of PIC-based potential therapeutic agents was investigated. A new class of antibody-functionalized, semi-flexible and filamentous polymer (diameter 5-10 nm, length ~200nm) with a controlled persistence length, a high degree of stereoregularity and the potential for multiple simultaneous receptor interactions was developed. These highly controlled, semi-stiff polymers were decorated with T cell activating anti-CD3 antibodies and were analyzed for application as potential synthetic dendritic cells (sDCs). The sDCs do *not only activate* T cells at significantly lower concentrations than free antibodies or rigid sphere-like counterparts (PLGA particles) but also induce a more robust T-cell response. These novel sDCs are further biocompatible and non-toxic. The observed increased efficacy highlights the importance of architectural flexibility and multivalency to modulate T cell response and cellular function in general.

Introduction

The innate immune system is the body's first line of defense against invaders like pathogens and cancerous cells. Among the various cell types of the innate immune system, dendritic cells (DCs), also known as "professional" antigen-presenting cells (APCs) are of prime importance[1]. The knowledge about dendritic cells (DCs) has increased tremendously in the last 30 years[2] and their applicability for cancer immunotherapy has been investigated. *Ex-vivo* generated DCs, when loaded with tumor lysates, tumor antigen-derived peptides or whole tumor proteins, have demonstrated enhanced anti-cancer immune responses[3]. Clinical studies have shown the potential of DCs as an autologous vaccine for cancer therapy[4-5]. In spite of their potency, the application of *ex-vivo* DCs is so far limited by their availability. Growth of *ex-vivo* DCs is both labor and resource intensive. The requirement to generate a tailor made vaccine for every patient[6-7] means that *ex-vivo*

DCs are not economically sustainable. The aforementioned inefficiencies in production of *ex-vivo* DCs have inspired investigators to design artificial antigen-presenting cells (aAPC) as alternatives.

Extensive studies on DC/T cell interactions *in vitro* have shown that the activation of T cells proceeds via a pre-clustering of MHC-peptide complexes. The formed micro-domains subsequently cluster into the so-called 'immune synapse' (IS)[8-9]. Similar to many extracellular biological recognition processes, T cell activation consequently requires the simultaneous multivalent interaction of a number of receptors to initiate clustering. Molecular constructs that are able to mimic this simultaneous multivalent binding have a higher efficacy by increasing the avidity[10]. Further, activation does not only involve one type of receptor but instead multiple receptors that interact with different activation-inducing molecules (*i.e.* MHC/peptides, co-stimulatory adhesion molecules, *etc.*).

The first generation of aAPCs, microbead-based DCs, have shown a marked advantage in expanding specific T cells under laboratory conditions compared to free MHC peptide complexes. Their efficacy for long-term T cell expansion has been limited, however[11]. Unlike aAPCs, natural APCs have the ability to conform to the cell surface topography and allow the dynamic movement of receptor-ligand complexes to form the IS site that ultimately causes T cell activation. Most likely the rigid sphere morphology of these first generation aAPCs hinders the efficient formation of multivalent interactions with the T cells[12-13]. The aAPCs lack the plasma membrane fluidity of natural DCs that allows for the dynamic movement of these complexes to the IS site[14]. Soft spherical aAPCs such as liposomes[15], have overcome the membrane fluidity constraint enhancing activation of T

cells over and above that observed for the rigid sphere models, suggesting that the IS can form more efficiently if a dynamic movement of both binding partners can take place (Figure 1).

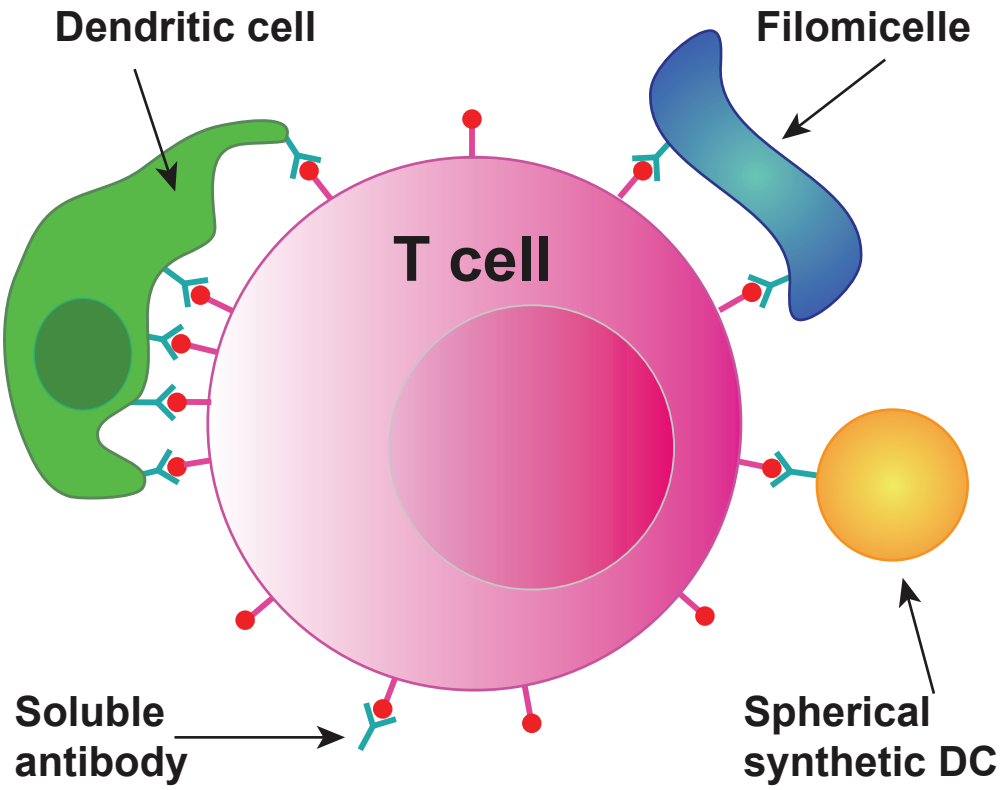

Figure 1. Schematic diagram illustrating different systems available for T cell activation.

Besides an efficient formation of the IS, also the number of receptor-ligand interactions involved in IS formation is thought to play an important role in T cell activation. The number of interactions is dictated by the size and the morphology of the particle. In general, for rigid spherical particles the number of ligands available to participate in the required simultaneous interaction is limited by its topology [15-17]. Second generation

immunotherapeutic delivery vehicles have, therefore, explored extended aspect ratio topologies such as filamentous or rod-like particles. These extended aspect ratio structures have utilized either copolymer filomicelles[18] or decorated carbon nanotubes (CNTs)[19]. Filomicelles have demonstrated a higher anti-tumor activity compared to their spherical counterparts[19-20]. This marked increase in efficacy is most likely a result of the larger surface-to-volume ratio that allows a more effective loading. If the micelle area is held constant for a given mass of copolymer, their effective loading is increased by 50% compared to the corresponding sphere[18]. Besides the increased effective loading that may aid in enhancing multivalent binding, filamentous or rod-like particles also show longer circulation times that might play an additional advantageous role in T cell activation[18].

The design criteria for an ideal synthetic dendritic cell (sDC) should incorporate the described knowledge gained from aAPCs and commonly used therapeutic delivery vehicles. It should combine the above characteristics of high aspect ratio, flexible architecture and multiple interactions to achieve highly efficient T cell activation. The sDCs should further possess an extended half-life and a low systemic toxicity[21-23].

Here, we propose a fundamentally new design of sDCs that have the potential to fulfill all of the above criteria. Our strategy to building these novel delivery vehicles is based on a new class of rod-like, semi-stiff and water-soluble polymers derived from oligoethylene glycol substituted poly(isocyanopeptides). Poly(isocyanopeptides) consist of a helical polyisocyanide backbone carrying peptide functionalized side chains attached to every carbon that stabilize the helix through hydrogen bonding[24-26]. These polymers can be up to 2 μm long and exhibit a well-defined stereoregularity[27] as well as a controlled stiffness

that can be tuned between persistence lengths (l_p) of 5 nm to 200 nm. Since in principle every individual monomer can be substituted with a functional unit, a versatile synthon for the design of multivalent filamentous sDCs is easily obtained (Figure 2). Our hypothesis is that such a semi-stiff poly(isocyanopeptide) decorated with effector molecules rapidly docks on T cells (Figure 2a/b). Subsequently, in contrast to a spherical bead or a random-coil polymer, the semi-stiffness of the poly(isocyanopeptide) will allow it to bind to neighboring receptors on the same cell (Figure 2c). Further, these receptor sites will be able to cluster with a concomitant contraction of the polymer backbone to form the IS while retaining the activated state (Figure 2d). To test our design strategy, we functionalized these sDCs with anti-CD3 antibodies (αCD3-sDC) that are known to cause T cell activation and compared their efficacy with free αCD3 antibodies.

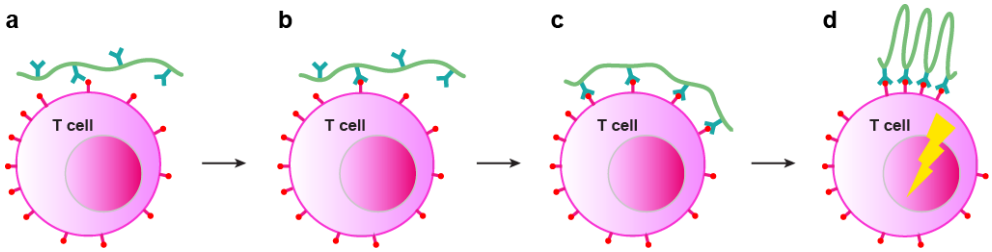

Figure 2. Stages of sDC binding and T cell activation. (a) the mobility of the sDC helps to locate the T cell, (b) sDC docks onto the T cell, (c) attachment to multiple recognition sites, (d) sDC contracting/clustering at the recognition sites, IS formation.

Results and Discussion

1.1. Synthesis and Characterization of the αCD3-sDCs

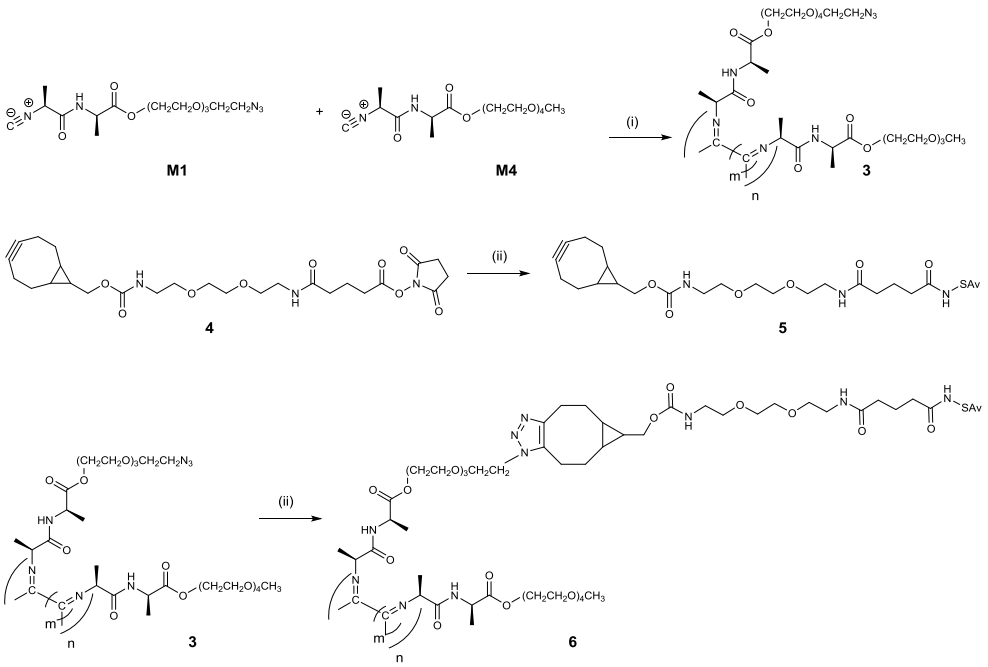

Scheme 1. Synthetic scheme to obtain Streptavidin (SAv) functionalized poly(isocyanopeptides). (a) random co-polymerization of the azide (1) and the methoxy (2) monomers to obtain the azide-functionalized polymer (3), i) $Ni(Cl_2O_4)_2 \bullet 6\ H_2O$, toluene, (b) coupling of BCN-NHS (4) to SAv, ii) 4 days at 4 ˚C in 10 mM borate buffer pH 8.5, (c) synthesis of the SAv-polymer bioconjugate (6), iii) 4 days at 4 °C in 10 mM borate buffer pH 8.5.

Synthetic dendritic cells (sDCs) carrying T cell stimulating αCD3 antibodies have been synthesized from semi-stiff poly(isocyanopeptides). To obtain these sDCs, an azide containing poly(isocyanopeptide) was synthesized in the first step. This was achieved by copolymerizing a mixture of an azide-functionalized monomer and a methoxy-

functionalized monomer using a 1:100 molar ratio resulting in a random copolymer (Scheme 1). The obtained polymers have a degree of polymerization DP = 1633 and a length between 150 nm and 200 nm (Table 1 experimental). The average spacing between azide groups is 10 nm. These azide groups were subsequently used to couple BCN-functionalized streptavidin (SAv) to the polymer backbone using a strain-promoted azide alkyne click (SPAAC) reaction[28].

The obtained SAv-functionalized polymer contains on average one SAv molecule every 50 nm (Figure 3), as determined with AFM. sDCs were obtained by adding biotinylated αCD3 antibodies yielding αCD3-sDC. When preparing the αCD3-sDC, the ratio of αCD3 to SAv on the polymer was adjusted such that on average every SAv was bound to one αCD3 antibody (Figure 14). Consequently, an average polymer contains between 3 and 5 αCD3 antibodies.

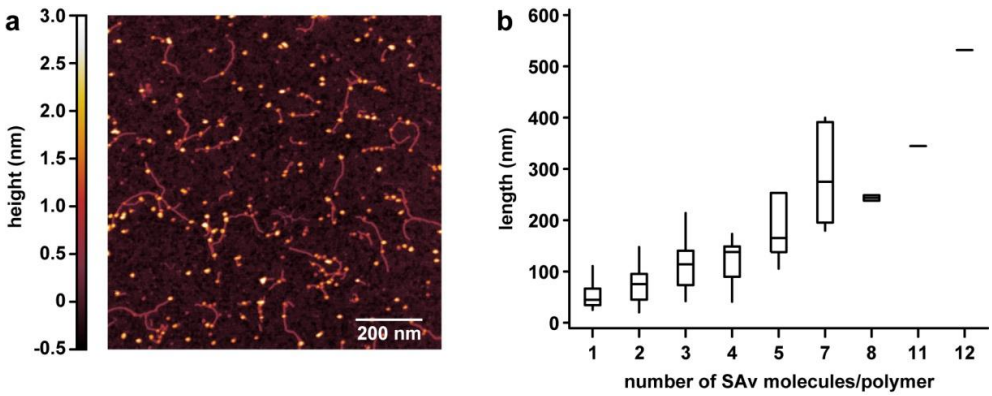

Figure 3. AFM analysis of polymer 6. (a) representative AFM image clearly showing the SAv molecules (bright dots) attached to the polymer, (b) number of SAv molecules per polymer.

1.2. Cell viability measurements

Before testing the efficacy of these novel sDCs on peripheral blood lymphocytes (PBLs), cell viability studies were carried out to study their biocompatibility. PBLs exposed to αCD3-sDC or free αCD3 at different concentrations exhibited no significant decrease in cell viability (MTT assay; Figure 4a). At higher αCD3 concentrations even an increase in the number of cells was observed, which could be explained by induction of T cell proliferation by the αCD3 antibodies (*vide infra*). Even after prolonged incubation times, cell viability remained constant between 90 – 100 % even up to 72 hours (Trypan Blue assay; Figure 4b).

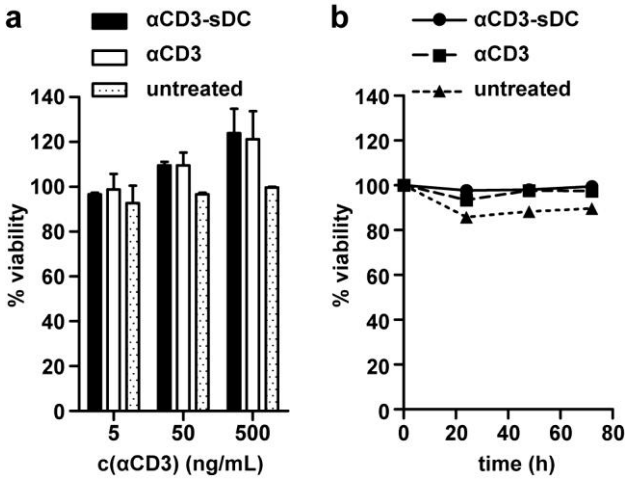

Figure 4. Viability of PBL cells exposed to αCD3-sDC. (a) MTT assay showing cell viability as a function of αCD3 concentration (incubation time 24 h), (b) Trypan Blue assay showing cell viability as a function of incubation time (αCD3 concentration of 200 ng/mL for both αCD3-sDC and free αCD3). The results represent the mean ± s.e.m. (n = 3).

1.3. T cell activation

In subsequent experiments, the capacity of αCD3-sDC to activate T cells was determined, in comparison to free αCD3. After clustering of CD3 on the T cells,

intracellular signaling results in direct activation as demonstrated by expression of the early T cell activation marker CD69[29]. Activated T cells further show enhanced secretion of IFNγ as a late activation event[30] and eventual T cell proliferation is observed[31]. At saturating conditions (> 50 ng/mL) CD69 expression was maximum, for both the αCD3-sDC and the free αCD3 treatment (Figure 5a). At low concentrations (1 - 20 ng/mL), however, the αCD3-sDCs were ~2.5 fold more effective in inducing T cell activation when compared to free αCD3 treatment. Similarly, the αCD3-sDC activated T cells released 2-3 fold higher amounts of IFNγ (Figure 5b). This indicates a more robust T cell activation in comparison to T cells exposed to free αCD3.

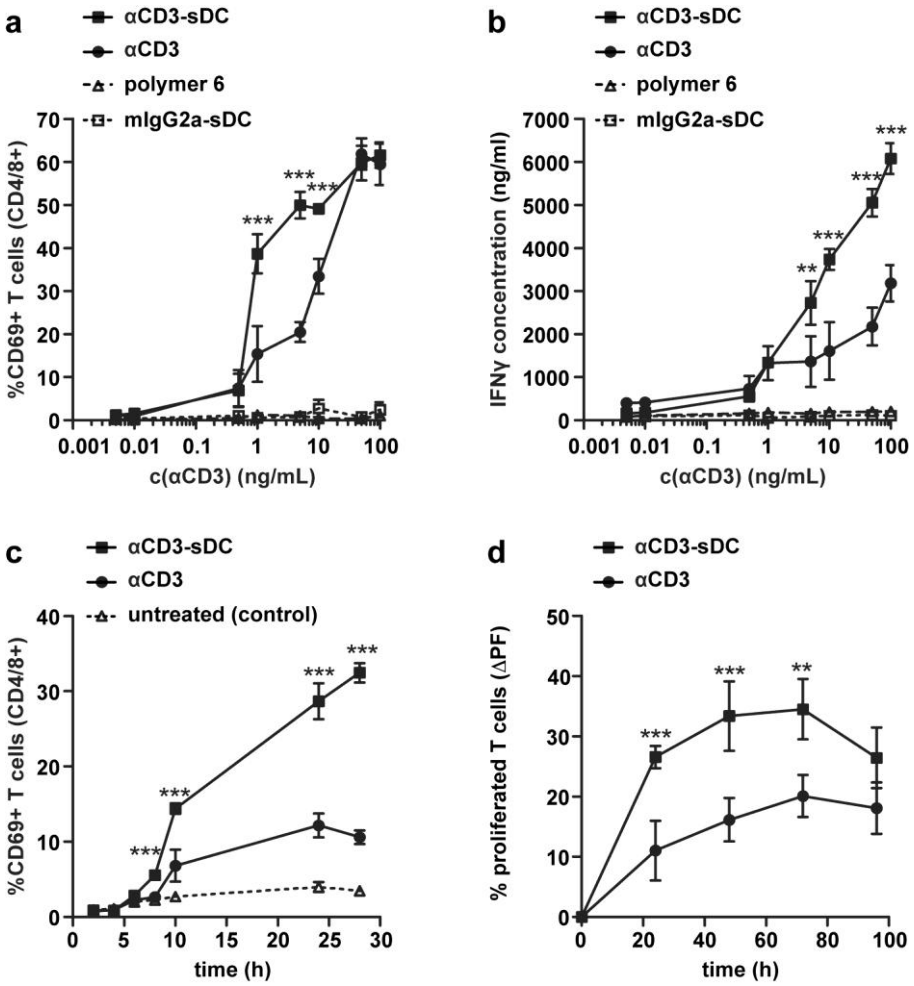

Figure 5. T cell activation upon treatment at different concentrations. (a) percentage of T cells showing CD69 expression and (b) IFNγ release at different αCD3 concentrations (incubation time 24 h), (c) percentage of T cells showing CD69 expression after different incubation times (αCD3 concentration 5 ng/mL), (d) T-cell proliferation measured with an CFSE assay (αCD3 concentrations 50 ng/mL). In (a) the values were normalized against the untreated control and represent the mean ± s.e.m. (n = 4). The asterisks (*) indicate the statistical significance (*, **, *** p≤ 0.05, 0.01, 0.001) of αCD3-sDC compared to αCD3.

To substantiate the above findings, T cell activation was followed over time at a low effective treatment concentration (5 ng/mL αCD3 for both αCD3-sDC and free αCD3). The

αCD3-sDC treated T cells were activated at significantly earlier time points (Figure 5c). Over prolonged exposure, T cell activation increased up to ~35%. In comparison, T cell activation following treatment with free αCD3 shows a delay in T cell activation (10 hours *vs.* 7 hours for αCD3-sDC) and a lower percentage of activated T cells (only ~10-15%). Finally, the ability of αCD3-sDC to induce T cell proliferation was tested (50 ng/mL αCD3 for both αCD3-sDC and free αCD3). In line with the above results, a 2-3 fold higher number of proliferated T cells was detected when the T cells were treated with αCD3-sDC (Figure 5d). Treatment with αCD3-sDC leads to a constant increase in the proliferation rate until 72 h of treatment. The observed decrease in the number of T cells at 96 h is likely resulting from nutrient depletion in the growth medium at high cell concentration.

To investigate the importance of the structural architecture of our novel sDCs, their efficacy was compared to that of spherical αCD3-PLGA particles (1.8 μm diameter, see experimental section 2.1-2.3). The worm-like αCD3-sDCs were ~7 fold more efficient in stimulating T cell activation (CD69 expression) when compared to αCD3-PLGA spheres, even at concentrations as low as 1 ng/mL (Figure 6a). Also the production of IFNγ was ~3 fold higher when compared to αCD3-PLGA spheres (Figure 6b). Together these observations indicate that our αCD3-sDCs do not only activate T cells significantly better at lower concentrations. They also induce the highest IFNγ production when compared with solid particle based DCs.

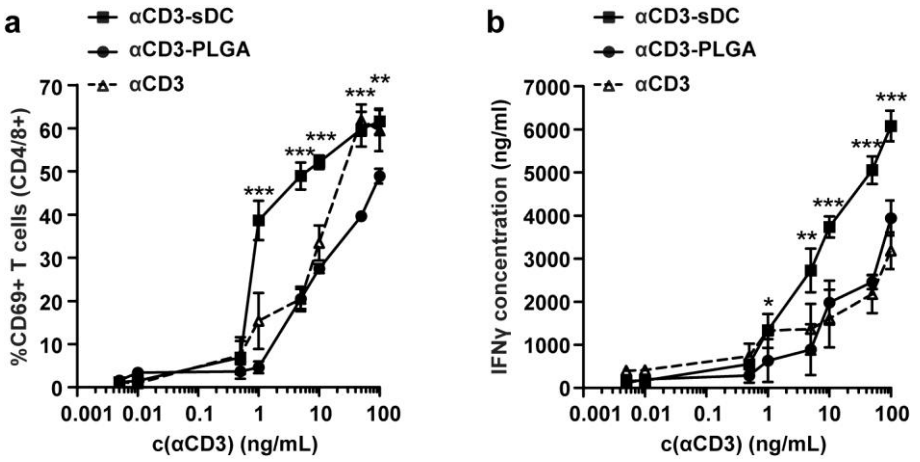

Figure 6. Comparison of αCD3-sDC with spherical αCD3-PLGA. (a) percentage of T cells showing CD69 expression and (b) IFNγ release at different αCD3 concentrations (incubation time 24 h); The results represent the mean ± s.e.m. (n = 3). The asterisks (*, **, *** p= < 0.05, 0.01, 0.001) indicate the statistical significance of αCD3-sDC compared to αCD3.

This difference cannot be explained with the number of receptor-ligand interactions established between the αCD3-sDCs (max. 3-5 interactions) or the αCD3-PLGA spheres (approximately 150 interactions; see Materials and Methods). The comparison of αCD3-sDC with the hard-sphere PLGA particles clearly suggests that it is not only the density of αCD3 but more importantly the ability to flexibly adjust to the spacing of receptors and to dynamically form the immune synapse that leads to the superior activity of our sDCs. In other words, multiple static interactions are not sufficient. We postulate that a more dynamic anisotropic interaction between the binding partners is required to induce and enhance T cell activation[32-33]. Unlike the static shape of the hard sphere model, the controlled stiffness of the αCD3-sDC filament has the capacity to 'concertina' in response to the receptor clustering events associated with the formation of the immune synapse.

1.4. Localization of αCD3-sDC on the cell surface

To investigate the molecular process in more detail and to understand how the sDCs interact with T cells, binding studies were performed with fluorescently labeled αCD3-sDCs. The PBLs were incubated with different concentrations of either fluorescein labeled αCD3-sDCs (FαCD3-sDC) or with free αCD3 (FαCD3) for 24 hours. Subsequently, the number of fluorescent cells was determined using a laser scanning confocal microscope (Figure 7).

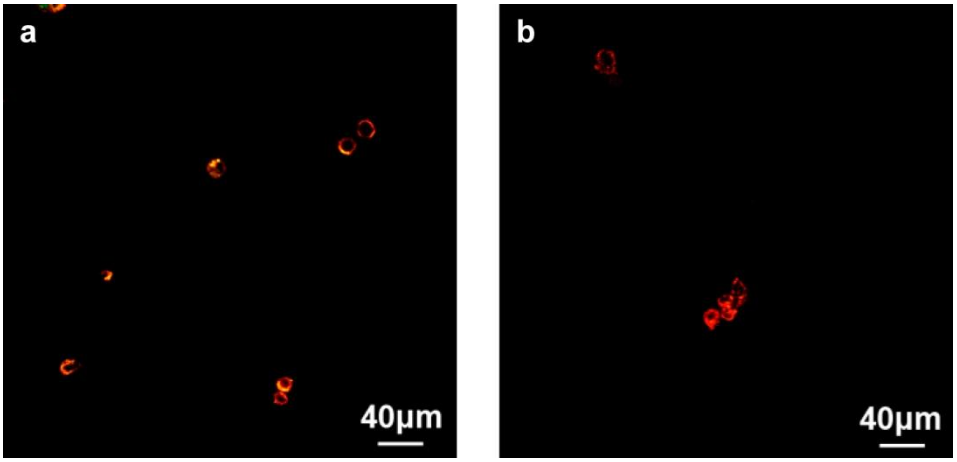

Figure 7. Overview images illustrating co-localization (yellow) of (a) Fluorescein-labelled FαCD3-sDCs and (b) FαCD3 on the PBL membrane (stained with the membrane specific dye PKH26, red)

At high concentrations (50 and 100 ng/mL) the relative number of T cells that show binding of FαCD3-sDC on their surface was comparable to the percentage of cells that have bound free FαCD3. In the low concentration range (≤ 20 ng/mL), however, a higher fraction of PBLs carrying FαCD3-sDC was observed when compared to the cells treated with free FαCD3. This result clearly explains the higher efficacy of the αCD3-sDCs in the

low concentration range (Figure 8a). Besides more efficient binding, 3D images taken after 24 hours further reveal that FαCD3-sDC remained co-localized on the membrane indicating that no receptor internalization has been taking place (Figure 8b).

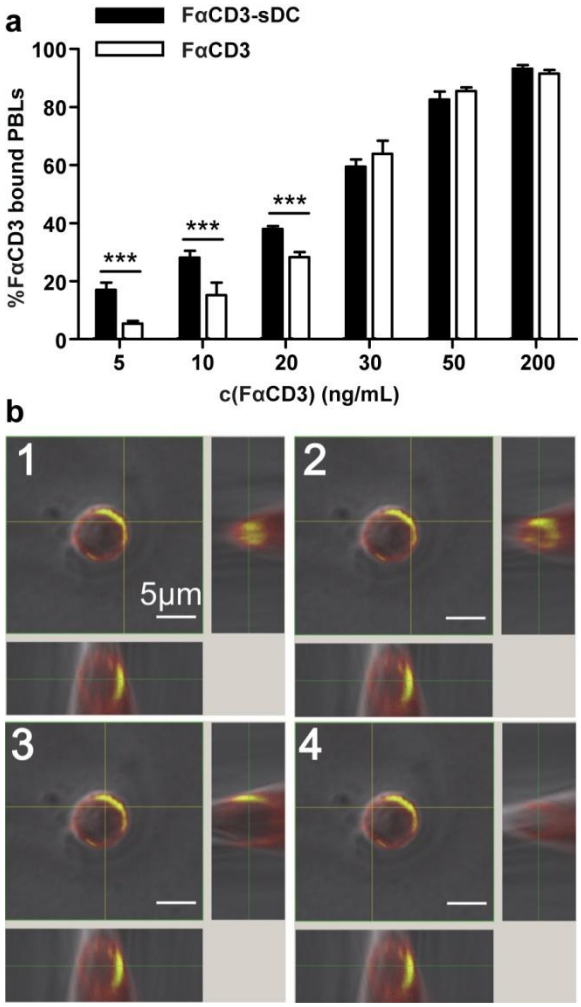

Figure 8. αCD3-sDC binding and location on the cell. (a) percentage of PBLs showing bound FαCD3 or FαCD3-sDC after 24 hours of treatment. The result shows the mean ± s.e.m. (n = 3). The significance of αCD3-sDC compared to αCD3 is indicated by the asterisks (*** p≤ 0.001). b) Orthographic projection of one PBL illustrating αCD3-sDC clustering/binding (yellow; co-

localization of red and green fluorescence). The fluorescence image is merged with a DIC image. The series represent images with varying y-coordinate (x- and z-coordinate constant) over an entire cell showing the αCD3-sDC distribution in the optical plane.

Summarizing the above results, this new class of semi-stiff and filamentous polymers serves as an ideal scaffold for functionalization with antibodies to allow for multiple, simultaneous receptor interactions. These novel sDCs *do not only activate* T cells at significantly lower concentrations than free antibodies and their rigid sphere-like PLGA counterparts but also induce a faster T cell response. Docking of the first antibody to the T cell increases the effective molarity of αCD3 at the cell surface thereby increasing the probability for the remaining antibodies to bind (Figure 2b). It is known that T cell stimulation by αCD3 in solution causes internalization of the CD3 and prevents a further T cell response[34]. The experiments with fluorescently labeled αCD3-sDC have indicated that αCD3-sDC remains bound on the T cell surface even for 24 h after treatment. The semi-stiff, filamentous morphology of the αCD3-sDCs consequently does not only lead to a significantly higher and earlier (CD69 expression) but also to a more sustained T cell response compared to the free antibody and the spherical geometry. This result is supported by the expression of the late stage activation marker INFγ and the associated higher T cell proliferation rates.

Despite their clearly proven potential, a number of open questions remain. Compared to the structural perfection of biomacromolecules, our sDCs show a relatively high polydispersity. Further, the loading with effector molecules is rather low compared to hard spheres. Still, a plurality of valences per molecule is clearly present and exhibits a dramatic effect at extremely low concentrations of αCD3-sDC in inducing T cell activation.

Experiments are currently underway to investigate the role of the polymer length, the polymer stiffness and the effector molecule loading on T cell activation.

Conclusions

In this chapter we demonstrate that multivalency in combination with a controlled semi-stiffness are key parameters for designing potentially therapeutically active vehicles that closely mimic natural DCs. Using the novel sDC design, a more efficient as well as more sustained T cell response is observed. This enhanced activity clearly validates the final stage of the proposed binding mechanism (Figure 2d) that requires the sDC to react to the processes occurring on the T cell surface during formation of the immune synapse. Having shown the potential of this sDCs, the next steps are a more detailed investigation of the activation mechanism allowing for increasing their efficacy even further. Instead of αCD3, MHC-peptide complexes will be coupled to the polymer backbone and co-stimulatory molecules, necessary for efficient T cell activation, as well as cytokines will be added to further shape the T cell response. Ultimately, after characterization of their *in vivo* behavior, our sDCs have the potential to become highly efficient and cost-effective sDCs for cancer immunotherapy.

1. Materials and Methods

1.1. Materials

Unless otherwise stated, all chemicals were obtained from Sigma Aldrich and used without further purification. Toluene was distilled over sodium. Dichloromethane was distilled over phosphorous pentoxide. Column chromatography was performed using silica gel (0.060 - 0.200 mm) provided by Baker. Thin layer chromatography (TLC) analyses were carried out on silica 60 F_{254} coated glass obtained from Merck Millipore. The compounds were visualized using ninhydrin or basic aqueous $KMnO_4$ solutions. All glassware was soaked in 0.5 M NaOH for 3 hours before use.

Peripheral Blood Lymphocytes (PBLs) were isolated from the buffy-coat obtained from a healthy volunteer via Ficoll density gradient centrifugation (Lucron Bioproducts). The PBLs and OKT3 hybridoma were always maintained in RPMI-1640 medium (Life Technologies) containing 10% Fetal Bovine Serum (FBS) (Greiner Bio-One B.V.), 1% glutamine (Lonza) and 1x Antibiotic-Antimycotic (Life Technologies). For the αCD3 production, OKT3 hybridoma cells (at confluence) were transferred into Protein Free Hybridoma Medium (PFHM-II, Life Technologies). These cells were cultured for 3-4 days in PFHM-II before purifying the αCD3 monoclonal antibodies using HiTrap™ Protein G HP Columns (GE healthcare).

1.2. Polymer synthesis

Azide monomers (compound M1; Scheme 1a) and methoxy monomers (compound M4; Scheme 1a) were synthesized as described previously [35]. ^{1}H NMR and ^{13}C NMR spectra were recorded on a Bruker AC-300 MHz instrument operating at 300 MHz and 75 MHz, respectively. FT-infrared spectra of the compounds were recorded using a Thermo Nicolet IR300 FT-IR spectrometer (Thermo Fisher Scientific) equipped with a Harrick ATR unit. UV measurements were done using a Varian Cary 50 spectrometer (Agilent Technologies). For mass spectrometry a LCQ Advantage MAX instrument (Thermo Fisher Scientific) was used.

Compound **M1** (3.1 mg, $8.3 \cdot 10^{-3}$ mmol) and compound **M4** (300 mg, $8.3 \cdot 10^{-1}$ mmol) were dissolved in 30 mL of distilled toluene yielding a ratio of azide-functionalized monomers to methoxy-functionalized monomers of 1:100. The catalyst stock solution was prepared separately by dissolving $Ni(Cl_2O_4)_2 \bullet 6\ H_2O$ (30.7 mg, $8.4 \cdot 10^{-2}$ mmol) in 10 mL of absolute ethanol and 90 mL of toluene. From the catalyst stock solution 83 µL ($8.3 \cdot 10^{-5}$ mmol) was added to the reaction mixture. The mixture was stirred for 3 days at room temperature (RT) and followed by IR until all isocyanide was consumed. The polymer (compound **3**) was isolated via precipitation into diisopropylether. This precipitation cycle was repeated thrice to obtain 299.6 mg, 78 % yield.

1.3. Viscosity measurements

To obtain the intrinsic viscosity of polymer **3**, an Ubbelohde viscometer (Schott Instruments) was used. A stock solution **(**4 mg/mL) of polymer **3** was prepared in acetonitrile. From this stock solution, 4 mL of the following concentrations were prepared: 0.6; 0.5; 0.4; 0.3; 0.2 and 0.1 mg/mL. The solutions were loaded into a viscometry tube (nr. 1053431; Schott Instruments). The tube was placed into the water bath (25 ˚C) and allowed to equilibrate for 15 min before the measurement was started. The flow speed for each sample was measured four times and used to determine the kinematic viscosity ν. From this data, the reduced viscosity η_{red} and the inherent viscosity η_{inh} were calculated[36] and plotted against the polymer concentration. The intrinsic viscosity $[\eta]$ represents the limiting value of η_{red} or η_{inh} at infinite dilution of the polymer, *i.e.* $[\eta] = \lim_{c\to 0} \eta_{inh}$. From extrapolation of η_{red} to c = 0, $[\eta]$ = 9.64 dL · g^{-1} was obtained (Figure 9). Based on $[\eta]$, a molecular weight of 421 kg/mol was determined using the Mark-Houwink equation $[\eta] = K\bar{M}_v^a$. The constants K = 1.4 · 10^{-9} dL · mol^a · g$^{-(1+a)}$ and a = 1.75 for a rigid polyisocyanide have been reported previously[37]. The average polymer length was calculated to be 123 nm (Table 1).

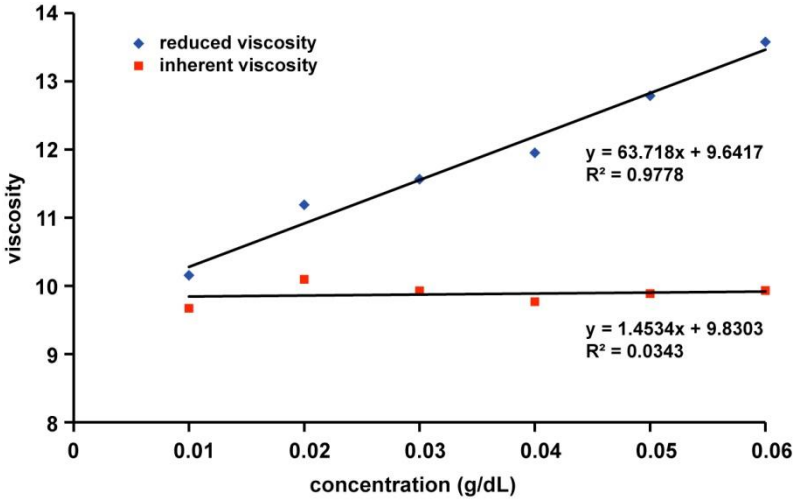

Figure 9. Ostwald viscosity measurement. The intrinsic viscosity was determined experimentally from both the reduced viscosity and the inherent viscosity for different concentrations of the polymer in acetonitrile. The value for the intrinsic viscosity was obtained from extrapolation to c = 0 g/dL. The molecular weight $\overline{\boldsymbol{M_v}}$ was calculated to be 421 kg/mol using the Mark-Houwink equation (with K=1.4x10^{-9} dL mol^a g$^{-(1+a)}$ and a=1.75).

Table 1. Summary of molecular weight and polymer length

	molecular weight M_w (kg/mol)	**apparent polymer length l (nm)**
$\overline{M_v}$ viscosity	421	123[a]
M_w SEC	588	172[a]
AFM	677[b]	197

[a]The apparent polymer length l was calculated from the measured molecular weight:
$l = M_w \times \frac{1}{4} x \frac{1}{360\ g/mol} \times 0.42nm$

[b]The molecular weight M_w was calculated from the experimentally determined polymer length: $M_w = 1 \times 4 \times 360\ g/mol \times \frac{1}{0.42\ nm}$

1.4. Size exclusion chromatography

Polymer **3** was further analyzed by size exclusion chromatography (SEC) to determine its hydrodynamic radius. The SEC system was equipped with a Waters 1515 Isocratic HPLC pump, a Waters 2414 refractive index detector, a Waters 2707 autosampler, a PSS PFG guard column followed by 2 PFG-linear-XL (7 µm, 8*300 mm) columns in series. The system was run at 40 °C. Hexafluoroisopropanol (HFIP, Biosolve) with potassium trifluoro acetate (3 g/L) was used as eluent at a flow rate of 0.8 mL/min. The molecular weights were calculated against poly(methyl methacrylate) standards (M_p = 580 g/mol up to M_p = 7100 kg/mol; Agilent). The measurement yielded a molecular weight of 588 kg/mol and the average polymer length was calculated to be 172 nm (Figure 10 and Table 1).

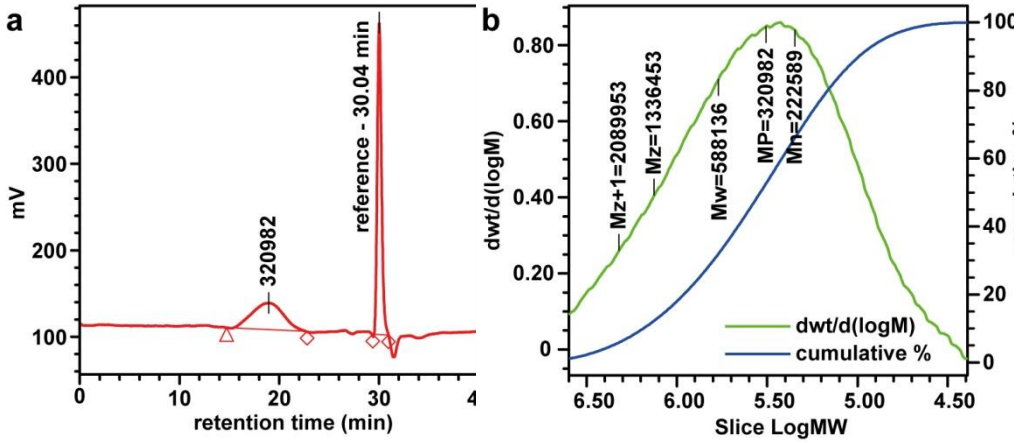

Figure 10. Size exclusion chromatography. a) Compound 3 eluted at 18.5 min. b) This corresponds to a weight average molecular weight M_w of 588 kg/mol (PMMA standards) and a $Đ$ of 2.6.

1.5. AFM measurements

The polymer sample was diluted in 1 mM sodium acetate buffer pH 4.5 to obtain a concentration between 0.5 µg/mL and 5 µg/mL. The samples were drop casted onto freshly cleaved and polylysine coated mica and incubated for 10 minutes. The remaining liquid was then removed and the sample was dried in a stream of N_2. AFM images were recorded in tapping mode in air using a Nanoscope IV instrument (Bruker) and NSG-10 tapping mode tips (NT-MDT, Limerick). The polymer length was determined by hand using the program ImageJ[38] (Figure 11 and Table 1).

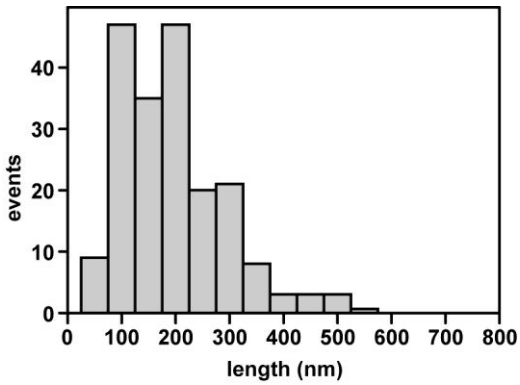

Figure 11. Measurement of the polymer length with AFM. The mean value obtained from *n* = 198 polymers is 197 nm.

1.6. Functionalization of Streptavidin with BCN-NHS

Streptavidin (SAv) was obtained from Thermo Fisher Scientific and bicyclo[6.1.0]nonyne - POE_3-NH-C(O)$CH_2CH_2CH_2$C(O)OSu (BCN-NHS; compound **4**) was obtained from Synaffix. SAv (34.5 mg, $5.2 \cdot 10^{-4}$ mmol) was dissolved in 7 mL borate buffer (10 mM, pH 8.5). BCN-NHS (1.7 mg, $3.1 \cdot 10^{-3}$ mmol) was added to the SAv solution to yield BCN-NHS:SAv = 5:1. The mixture was kept at 4 ˚C for four days. BCN-functionalized SAv (compound **5)** was purified by gel filtration (PD 10 column, GE Healthcare). The eluent was further purified by ultrafiltration (Amicon Ultra-4, 10 kDA; Merck Millipore). The final yield of **5** was determined by measuring absorption at 280 nm. Using an extinction coefficient of $\mathcal{E}$ = 167280 mol^{-1} cm^{-1}, the final yield was determined to be 26.1 mg, 76 %. The conjugate was further characterized using MALDI-ToF to obtain the labeling ratio. MALDI-ToF was performed using a Bruker Biflex III MALDI-ToF spectrometer. SAv and SAv-BCN samples were prepared using α-cyano-4-hydroxycinnamic acid as the matrix. The mass obtained for SAv (monomer) was determined to be 13280 Da [M+ H^+]. This served as a reference for **5**. Compound **5** shows both the peak of the non-functionalized monomer 13280 Da [M + H^+] as well as the mass of **5** carrying one BCN-group coupled to the SAv monomer: 13783 Da [M + $2K^+$] (Figure 12). No peak corresponding to a doubly labeled monomer was visible. Consequently, the degree of functionalization is between 0 and 4 BCN-groups for the SAv tetramer.

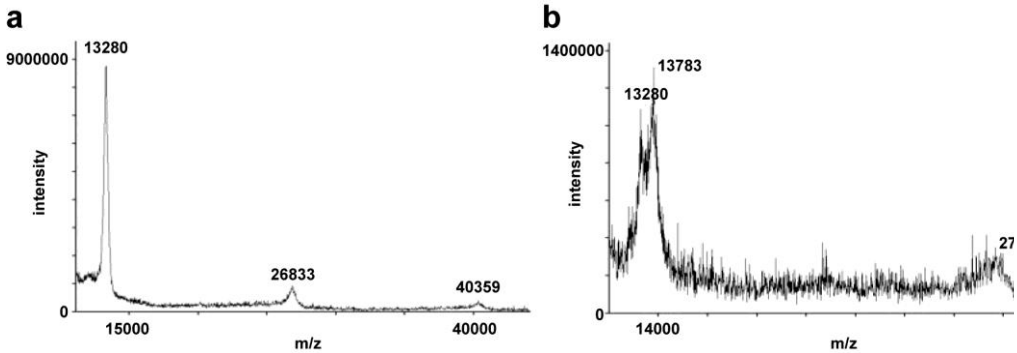

Figure 12. MALDI-ToF analysis. a) SAv before addition of BCN-NHS; b) BCN-functionalized SAv.

1.7. Synthesis and characterization of the SAv-polymer bioconjugate (6)

Polymer **3** in 10 mL 10 mM borate buffer (10 mg, 2.7 x 10^{-5} mmol) was mixed with SAv-BCN (26 mg, 3.9 x 10^{-7} mmol) in 4 mL 10 mM borate buffer. The mixture was incubated at 4 ˚C for four days. Polymer **6** was purified by dialysis against water at 4 °C for 2 days with a membrane with cut-off of 100 kDa.

To ensure that the bioconjugation does not affect the structure of the poly(isocyanopeptide) polymer, circular dichroism spectra were recorded for both polymer **3** and polymer **6**. The measurements were performed at 20 °C at a concentration of 1 mg/mL in 50 mM borate buffer pH 8.5 using a Jasco J-810 CD spectrometer. Both polymers showed identical spectra (Figure 13) clearly indicating that the coupling of SAv does not influence the secondary structure of the SAv-polymer conjugate. The SAv loading of **6** was determined with AFM using the same procedure as for polymer **3**.

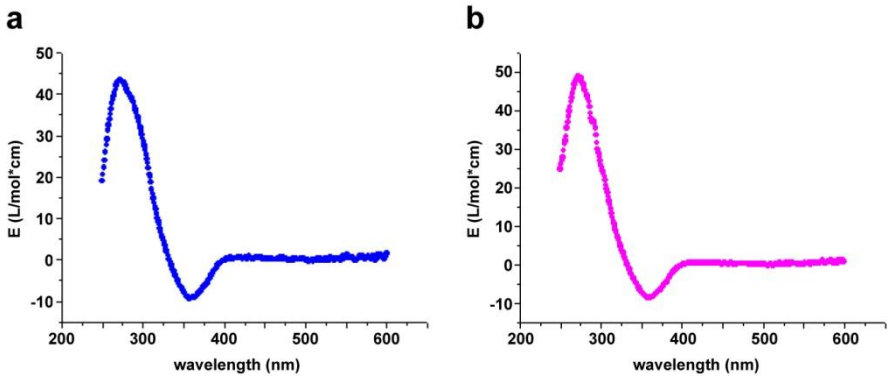

Figure 13. Circular dichroism spectra. a) polymer 3; b) SAv-polymer conjugate 6. Both measurements were done at a concentration of 1 mg/mL in 10 mM borate buffer pH 8.5 at 20 °C.

1.8. Synthesis and characterization of αCD3-sDCs

To obtain the aCD3-sDCs, the aCD3 antibodies were first biotinylated with EZ-Link Sulfo-NHS-LB-Biotin (Thermo Fisher Scientific) to allow for binding to SAv on polymer **6**. Before preparing the aCD3-sDCs, the molecular ratio of aCD3:SAv was optimized using a biotinylated AlexaFluor488-labelled aCD3 antibody. Using the fluorescently labeled antibody, it was possible to determine the aCD3 concentration while measuring the total protein concentration in the same sample.

First the SAv concentration on polymer **6** was determined using a BCA micro assay (Thermo Fisher Scientific). Then polymer **6** was mixed with the AlexaFluor488-labeled and biotinylated αCD3 antibody using 4:1, 6:1 and 8:1 molar ratios of αCD3:SAv. The mixture was left at 4 °C for 24 h. After removing the free αCD3 by ultrafiltration (Nanosep Omega, cut-off of 300 kDa, PALL Life Sciences) the total protein concentration was again determined using the BCA assay. In addition, the fluorescence originating from the AlexaFluor488-labeled antibody was determined from a fluorescence measurement in a microplate reader (Cytofluor II, PerSeptive Biosystems). The aCD3 concentration was calculated using a standard curve of AlexaFluor488-labeled aCD3. Subtracting the Alexa488-αCD3 concentration from the total protein concentration allowed for calculating the SAv concentration as well as the αCD3:SAv ratio. For a 4:1 ratio of αCD3:SAv approximately one αCD antibody was bound per SAv molecule (Figure 14).

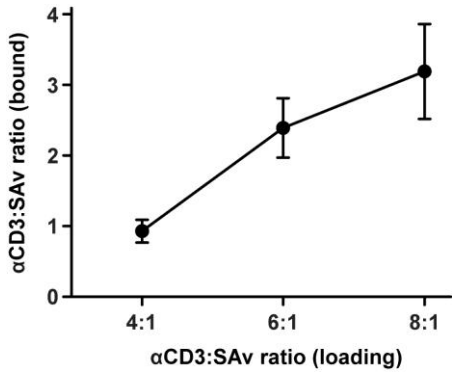

Figure 14. Loading of polymer 6 with αCD3 antibodies. Different ratios of biotinylated, Atto488-labeled αCD3 were added to polymer 6 (αCD3:SAv ratio = 4:1, 6:1 and 8:1). For a ratio of 4:1, an average number of 0.93 αCD3 molecules were obtained per SAv molecule. For 6:1 and 8:1, a final ratio of 2.69 and 3.37 αCD molecules were bound per SAv molecule, respectively. A ratio of 4:1 was used for the T cell experiments.

To prepare the sDCs for the T cell experiments, a 4:1 ratio was used following exactly the same protocol as used in the preliminary experiment. Assuming that the ratio of bound αCD3:SAv will be identical, the concentration of αCD3 could now be determined from the total protein concentration without the need for fluorescently labeling the αCD3 antibody. For the T cell experiments, all the treatment concentrations were based on the concentration of αCD3 present on the sDC backbone, on the micro-bead system or as free αCD3.

1.9. MTT assay

The cytotoxic effect of the αCD3-sDCs was determined using a standard MTT assay[39]. PBLs (10^5 cells/well) were treated with αCD3-sDC, αCD3 or left untreated (control) for 24 h using different concentrations (5, 50, 500 ng/mL) of the respective molecules. After washing twice, the cells were incubated with MTT (5 mg/mL; Sigma Aldrich) for 2 h. The medium was then replaced with 100 µl of DMSO. After solubilization, the microplates were read at 550 nm using a microplate reader (iMark, Bio-Rad). The results were derived from three independent experiments (with three replicates per experiment).

1.10. Trypan Blue assay

In addition, the cell viability was estimated over time. Viable and non-viable cells were counted after αCD3-sDC treatment using the hemacytometer method by means of a Trypan Blue assay[40]. The percentage of viable cells was determined upon exposure to αCD3-sDC, αCD3, and untreated (control) in a concentration of 200 ng/mL and incubation times of 0, 24 and 72 h. The percentage was calculated according to the formula: 100 × (number of viable cells in treated samples/total number of cell counted). The results were obtained from three independent experiments (with three replicates per experiment).

1.11. Flow cytometry (CD69 expression)

The estimation of activated T cells (CD69+ T cells) upon αCD3-sDC treatment was determined using Fluorescence Activated Cell Scanning (FACS). FACS analysis was performed for cells treated with αCD3-sDC and for the following controls: αCD3, αCD3-PLGA (Figure 16), polymer **3**, mIgG2a-sDC and untreated. Briefly, PBLs (10^5/well) were treated with the respective molecules for 24 h at different concentrations (0.005, 0.01, 1, 5, 10, 50, 100 ng/mL). In addition to these concentration dependent experiments also time dependent T cell activation studies were performed. The T cells were treated with αCD3-sDC and αCD3 using a concentration of 5 ng/mL and incubation times of 2, 4, 6, 8, 10, 24, 28 and 30 h. The treated cells were washed with PBS containing 10% BSA (PBA; Sigma Aldrich). Subsequently, the cells were incubated with fluorescein-labeled mouse anti-human CD69 mAb (activated T cell marker, BD Biosciences) and APC-labeled mouse anti-human CD4/8 mAb (T cell marker, BD Biosciences). After washing twice with PBA, FACS analysis was performed using a CyAn™ ADP Analyzer instrument (Beckman Coulter). The results were analyzed using Flow-Jo ver. 9.2 software (Tree Star Inc.). The above experiment was repeated four independent times (with three replicates per experiment).

1.12. Enzyme-linked immunosorbent assay (ELISA; IFNg secretion)

The level of secreted IFNγ was determined in the culture supernatants using a standard sandwich ELISA method. After coating overnight at 4°C with mouse anti-human IFNγ antibody (Thermo Fisher Scientific), the 96-well microplates (Nunc Immunomodules; Thermo Fisher Scientific) were washed with PBS/Tween (0.05%) and blocked with PBS-1% BSA. Subsequently, the IFNγ standards (Thermo Fisher Scientific) and the supernatants were added into the wells and incubated for 1 hour at room temperature. Following washing with PBA for three times, the presence of IFNγ was detected using a biotinylated mouse anti-human IFNγ antibody (Thermo Fisher Scientific) and a streptavidin-horseradish peroxidase (HRP) conjugate (Life Technologies). HRP activity was detected using tetramethyl benzidine (TMB; Sigma Aldrich). The absorption was measured at 450 nm using an iMark Microplate Reader (Bio-Rad). The experiments were conducted for four independent times.

1.13. CFSE assay

T cell proliferation induced by αCD3-sDC was assessed using a CFSE assay[41]. PBLs (10^5) were pre-labeled with 5 µM CFSE (Life Technologies). Free CFSE was quenched with FBS. αCD3-sDC and αCD3 was added to the CFSE-labeled PBLs (10^5/well) at a concentration of 5 ng/mL. Treated cells were incubated overnight along with untreated control cells. After incubation times of 0, 24, 48, 72 and 96 h, the treated cells were used for FACS analysis. T cells were identified based on labeling with a mouse APC-labeled anti-human CD4/8 antibody. T cell proliferation was assessed from determining the CFSE staining intensity. The results were interpreted by considering the % decrease in fluorescence intensity as a corresponding % increase in T cell proliferation. The % difference in T cell proliferation (%ΔPF) was determined by normalizing the treated value against the untreated (control) value. Cyton software was utilized to analyze the number of cells proliferated per generation[42] (Figure 15). The results were derived from four independent experiments (with three replicates per experiment).

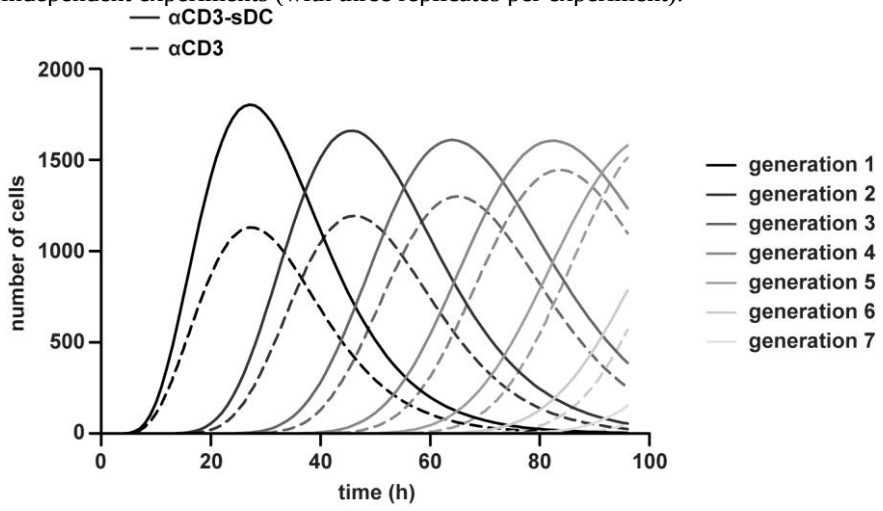

Figure 15. T cell proliferation determined with a CFSE assay. Shown is the increase in the

number of T cells per generation after treatment with αCD3-sDC and soluble αCD3, respectively. In the case of the αCD3-sDC treatment, the cell proliferation rate increases to a maximum in the first generation. This proliferation rate was maintained over the following generations (for the complete time period analyzed). When treating the T cells with soluble αCD3, the cell number only gradually increases per generation.

1.14. Confocal imaging

The binding of αCD3-sDC on the T cell surface was analyzed by confocal imaging using sDCs carrying a fluorescein-labeled αCD3 antibody (FαCD3-sDC). PBLs (10^5/well) were treated for 24 h with FαCD3-sDC and FαCD3 (F-Fluorescein, λ_{ex} = 488 nm, λ_{em} = 520 nm) at different concentrations (5, 10, 20, 30, 50, 200 ng/mL). Further, these cells were labeled with the membrane dye PKH26 (λ_{ex} = 551 nm, λ_{em} = 567 nm; Sigma Aldrich) following the manufacturer's protocol. These labeled PBLs were fixed in 4% paraformaldehyde. The fixed cells were quenched with glycine (0.1 mM) in PBS. The cover slips were mounted onto microscope slides (Thermo Fisher Scientific) using MOWIOL (Merck Millipore). The slides were imaged using a Confocal Laser Scanning Microscope (Olympus FV1000) equipped with a 63x oil immersion objective. The cells that show bound FαCD3-sDC were counted manually and compared to the number of FαCD3-sDC-free cells (Figure 16) using the program ImageJ[38]. All the experiments were repeated three independent times using PBLs from three different healthy donors.

1.15. Statistical analysis

Two-way ANOVA and Bonferroni post-tests were performed for a pair wise comparison between the variables using Graphpad Prism 5 software. The statistical significance is defined as $p < 0.05$. The asterisk '*', '**', '***' represents p values <0.05, <0.01 and <0.001.

2. Comparison of aCD3-sDC efficacy with aCD3-PLGA particles

2.1. Synthesis of αCD3-PLGA particles

A particle based DC system was prepared using PLGA particles as described previously[43] with the following modifications. To attach the αCD3 antibody to PLGA via the SAv-biotin interaction, SAv was covalently coupled to the PLGA particles (PLGA-SAv). In brief, protected sulfhydryl groups were introduced into SAv using N-Succinimidyl S-Acetylthiopropionate (SATP; Thermo Scientific) and deprotected with hydroxylamine hydrochloride (Thermo Scientific) using the manufacturer's protocol. Thereafter, the free thiol-groups on the SAv were reacted with the maleimide group of the DSPE-PEG-maleimide (M_w = 2000 g/mol) that is present on the PLGA surface. After washing with PBS, the biotinylated αCD3 antibody was bound to PLGA-SAv to obtain αCD3-PLGA.

2.2. Characterization of αCD3-PLGA particles

The size and concentration of the SAv-PLGA and αCD3-PLGA were determined using Transmission Electron Microscopy (TEM; JEOL TEM 1010) (Figure 16a and 16b) and

Differential Interference Contrast (DIC; Figure 16c) using a confocal microscope (FluoView FV1000, Olympus).
To obtain the particle concentration, the particle suspension was imaged using a Bürker chamber. The suspension was imaged under semi-dried conditions on the Bürker chamber grid to ensure that all particles had settled on the grid surface. The number of particles on the square grid was counted using the program Image J[44]. For the αCD3-PLGA particles, the concentration was calculated to be $1.24x10^{17}$ particles per mL. To estimate the amount of αCD3 bound per αCD3-PLGA particle, a biotinylated and AlexaFluor488-labeled αCD3 antibody was used in the same way as described for the αCD3-sDCs in the main text. This experiment yielded an amount of 3795 αCD3 antibodies per PLGA particle. For the T cell experiments, where no fluorescently labeled antibody was used, it was assumed that the amount of bound αCD3 will be the same for identical experimental conditions.

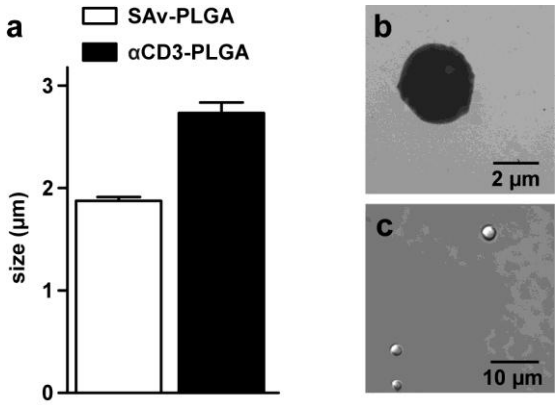

Figure 16. Characterization of αCD3-PLGA particles. a) Particle size obtained from TEM. The result represents mean ± s.e.m. (*n* = 300 particles); b) representative TEM image of αCD3-PLGA; c) representative DIC image of αCD3-PLGA.

2.3. Estimation of the contact area and the number of possible interactions

Based on the above measurements also the number of αCD3 antibodies on a PLGA particle as well as their surface density can be calculated. The number of αCD3 molecules per αCD3-PLGA particle was estimated to be on average 3795, corresponding to 0.3287 αCD3 antibodies per nm^2. This in turn allows us to obtain the number of possible interactions with the cell surface. Before this number can be calculated, the contact area of the PLGA particle with the cell has to be determined first.

The calculation of the contact area is based on Hertz theory[45]:

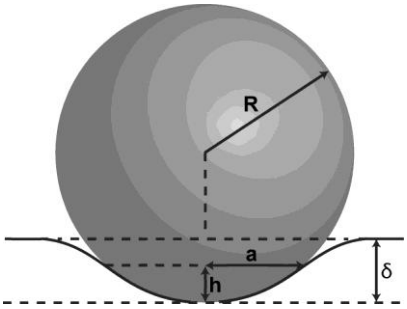

Figure 17. Geometry of the particle membrane interaction; with R - particle radius, d - indentation depth, a - radius of the contact area.

The contact area *A* is described by $A = 2\pi Rh = 2\pi R^2\left(1 - \sqrt{1 - \frac{a^2}{R^2}}\right)$ (Eq 1)

with $a^2 = R\delta$.

To obtain the contact area, first the force *F* that the particle exerts on the cell surface and the corresponding indentation depth d are calculated:

The indentation depth d and the Force *F* are related by the following equations:

$F = \frac{4}{3}E * R^{\frac{1}{2}}\delta^{\frac{3}{2}}$ (Eq 2)

and

$\delta = \left(\frac{3}{4}\frac{F}{E^*}\right)^{\frac{2}{3}} \times R^{-\frac{1}{3}}$ (Eq 3)

with the combined elastic modulus $\frac{1}{E^*} = \frac{1-v_{cell}^2}{E_{cell}} + \frac{1-v_{particle}^2}{E_{particle}}$ (Eq 4)

First, we estimate the force as a function of gravity to model the natural "bouncing" of the sphere into the cell membrane in an aqueous environment. A radius of R = 0.9 µM has been determined for the SAv-PLGA particles (Figure 16). These particles have a density that is 1.2x larger than the density of water. Using equation (5)[46] the maximum speed v_a that a PLGA particle can reach in an aqueous environment can be calculated:

$v_a = \frac{2R^2\Delta D_r g}{9\eta}$ (Eq 5)

with DD_r - difference in density, g – gravitational acceleration, η – viscosity of water

For the PLGA particles we find:

$v_a = 0.353\ \mu m/s$

The corresponding force can then be calculated for low Reynolds number (Re << 1):

$F = f \times v$ (Eq 6)

where *f* depends on the particle radius *R* and the viscosity of the environment η via

$f = 6\pi\eta R$ (Eq 7)

In this way the force exerted by the particle on a cell can be estimated as

$F = 6 \times 10^{-15} N$ for $v = v_a$

Cells are known to have a Young's Modulus of ≈ 400 Pa – 2500 Pa[47], which is much smaller than that of PLGA particles. Therefore, E^* can be simplified as:

$$\frac{1}{E^*} = \frac{1-v_{cell}^2}{E_{cell}} + \frac{1-v_{particle}^2}{E_{particle}} \approx \frac{1-v_{cell}^2}{E_{cell}} \quad \text{(Eq 8)}$$

Using equations (1) – (8), a PLGA particle indents a cell by δ=0.16 nm. The corresponding contact area is A=450 nm^2. Using the experimentally determined value of 0.3287 antibodies/nm^2, a number of 150 antibodies can potentially interact with the cell surface. Based on these results it can be concluded that multivalent interactions can take place when using αCD3-PLGA particles.

References

1 Banchereau, J. & Steinman, R. M. Dendritic cells and the control of immunity. *Nature*, **392**, 245-252, (1998).

2 Steinman, R. M. & Cohn, Z. A. Identification of a novel cell type in peripheral lymphoid organs of mice. I. Morphology, quantitation, tissue distribution. *J Exp Med*, **137**, 1142-1162, (1973).

3 Fong, L. & Engleman, E. G. Dendritic cells in cancer immunotherapy. *Annu Rev Immunol*, **18**, 245-273 (2000).

4 Ballestrero, A. *et al.* Immunotherapy with dendritic cells for cancer. *Adv Drug Delivery Rev*, **60**, 173-183, (2008).

5 Houtenbos, I. *et al.* Feasibility of clinical dendritic cell vaccination in acute myeloid leukemia. *Immunobiology*, **211**, 677-685, (2006).

6 Oelke, M. *et al.* Artificial antigen-presenting cells: artificial solutions for real diseases. *Trends Mol Med*, **11**, 412-420, (2005).

7 Gong, W. *et al.* Establishment and Characterization of a Cell Based Artificial Antigen-Presenting Cell for Expansion and Activation of $CD8^+$ T Cells *Ex Vivo*. *Cell Mol Immunol*, **5**, 47-53, (2008).

8 Giannoni, F. *et al.* Clustering of T cell ligands on artificial APC membranes influences T cell activation and protein kinase C theta translocation to the T cell plasma membrane. *J Immunol*, **174**, 3204-3211, (2005).

9 Dustin, M. L. Stop and go traffic to tune T cell responses. *Immunity*, **21**, 305-314, (2004).

10 Liu, S., Maheshwari, R. & Kiick, K. L. Polymer-Based Therapeutics. *Macromolecules*, **42**, 3-13, (2009).

11 Laux, I. *et al.* Response Differences between Human CD4+ and CD8+ T-Cells during CD28 Costimulation: Implications for Immune Cell-Based Therapies and Studies Related to the Expansion of Double-Positive T-Cells during Aging. *Clin Immunol*, **96**, 187-197, (2000).

12 Anderson, H. A., Hiltbold, E. M. & Roche, P. A. Concentration of MHC class II molecules in lipid rafts facilitates antigen presentation. *Nat Immunol*, **1**, 156-162 (2000).

13 Vogt, A. B., Spindeldreher, S. & Kropshofer, H. Clustering of MHC–peptide complexes prior to their engagement in the immunological synapse: lipid raft and tetraspan microdomains. *Immunol Rev*, **189**, 136-151, (2002).

14 Prakken, B. *et al.* Artificial antigen-presenting cells as a tool to exploit the immune `synapse'. *Nat Med*, **6**, 1406-1410 (2000).

15 Zappasodi, R. *et al.* The effect of artificial antigen-presenting cells with preclustered anti-CD28/-CD3/-LFA-1 monoclonal antibodies on the induction of ex vivo expansion of functional human antitumor T cells. *Haematologica*, **93**, 1523-1534, (2008).

16 Koffeman, E. *et al.* Identification and manipulation of antigen specific T-cells with artificial antigen presenting cells. *Methods Mol Med*, **136**, 69-86, (2007).

17 Schütz, C. *et al.* Killer artificial antigen-presenting cells: the synthetic embodiment of a 'guided missile'. *Immunotherapy*, **2**, 539-550, (2010).

18 Cai, S. *et al.* Micelles of Different Morphologies - Advantages of Worm-like Filomicelles of PEO-PCL in Paclitaxel Delivery. *Pharm Res*, **24**, 2099-2109, (2007).
19 Liu, Z. *et al.* Drug Delivery with Carbon Nanotubes for In vivo Cancer Treatment. *Cancer Res*, **68**, 6652-6660, (2008).
20 Geng, Y. *et al.* Shape effects of filaments versus spherical particles in flow and drug delivery. *Nat Nanotechnol*, **2**, 249-255, (2007).
21 Heister, E. *et al.* Triple functionalisation of single-walled carbon nanotubes with doxorubicin, a monoclonal antibody, and a fluorescent marker for targeted cancer therapy. *Carbon*, **47**, 2152-2160, (2009).
22 Rajagopal, K. *et al.* Polymersomes and Wormlike Micelles Made Fluorescent by Direct Modifications of Block Copolymer Amphiphiles. *Int J Polym Sci*, ID 379286, (2010).
23 Shuvaev, V. V. *et al.* Endothelial Targeting of Antibody-Decorated Polymeric Filomicelles. *ACS Nano*, **5**, 6991-6999, (2011).
24 Visser, H. G. J., Nolte, R. J. M. & Drenth, W. Polymers and copolymers of imidazole-containing isocyanides. Esterolytic activity and enantioselectivity. *Macromolecules*, **18**, 1818-1825, (1985).
25 van der Eijk, J. M. *et al.* Optically Active Polyampholytes Derived from L- and D-Carbylanayl-L-histidine. *Macromolecules*, **13**, 1391-1397, (1980).
26 Cornelissen, J. J. *et al.* Beta-helical polymers from isocyanopeptides. *Science*, **293**, 676-680, (2001).
27 Wu, Z. Q. *et al.* Enantiomer-Selective and Helix-Sense-Selective Living Block Copolymerization of Isocyanide Enantiomers Initiated by Single-Handed Helical Poly(phenyl isocyanide)s. *J Am Chem Soc*, **131**, 6708-6718, (2009).
28 Dommerholt, J. *et al.* Readily Accessible Bicyclononynes for Bioorthogonal Labeling and Three-Dimensional Imaging of Living Cells. *Angew Chem Int Ed Engl*, **49**, 9422-9425, (2010).
29 Yamashita, I. *et al.* CD69 cell surface expression identifies developing thymocytes which audition for T cell antigen receptor-mediated positive selection. *Int Immunol*, **5**, 1139-1150, (1993).
30 Murphy, M. *et al.* Gamma interferon and lymphotoxin, released by activated T cells, synergize to inhibit granulocyte/monocyte colony formation. *J Exp Med*, **164**, 263-279, (1986).
31 Kay, J. E. Mechanisms of T lymphocyte activation. *Immunol Lett*, **29**, 51-54, (1991).
32 Zanders, E. D. *et al.* Tolerance of T-cell clones is associated with membrane antigen changes. *Nature*, **303**, 625-627, (1983).
33 Balmert, S. C. & Little, S. R. Biomimetic Delivery with Micro- and Nanoparticles. *Adv Mater*, **24**, 3757-3778, (2012).
34 Ledbetter, J. A. *et al.* Valency of CD3 binding and internalization of the CD3 cell surface complex control T cell responses to second signals: distinction between effects on protein kinase C, cytoplasmic free calcium, and proliferation. *J Immunol*, **136**, 3945-3952, (1986).

35 Rowan, A. E. *et al.* Method for the preparation of high molecular weight oligo(alkylene glycol) functionalized polyisocyanopeptides. EP2287221 (2011).
36 Teraoka, I. *Polymer Solutions: An Introduction to Physical Properties*. (John Wiley & Sons, 2002).
37 van Beijnen, A. J. M. *et al.* Helical Configuration of Poly(Iminomethylenes) - Screw Sense of Polymers Derived from Optically-Active Alkyl Isocyanides. *Macromolecules*, **13**, 1386-1391, (1980).
38 Schneider, C. A., Rasband, W. S. & Eliceiri, K. W. NIH Image to ImageJ: 25 years of image analysis. *Nat Methods*, **9**, 671-675, (2012).
39 Supino, R. in *In Vitro Toxicity Testing Protocols* Vol. 43 *Methods in Molecular Biology* eds S. O'Hare & C. K. Atterwill) Ch. 16, 137-149 (Humana Press, 1995).
40 Freshney, R. I. in *Culture of Animal Cells: A Manual of Basic Techniques* (ed R. Ian Freshney) Ch. Primary Culture, 173 (Alan R. Liss 2000).
41 Wells, A. D., Gudmundsdottir, H. & Turka, L. A. Following the fate of individual T cells throughout activation and clonal expansion. Signals from T cell receptor and CD28 differentially regulate the induction and duration of a proliferative response. *J Clin Invest*, **100**, 3173-3183, (1997).
42 Hawkins, E. D. *et al.* Measuring lymphocyte proliferation, survival and differentiation using CFSE time-series data. *Nat Protoc*, **2**, 2057-2067, (2007).
43 Cruza, L. J. *et al.* Targeted PLGA nano- but not microparticles specifically deliver antigen to human dendritic cells via DC-SIGN in vitro. *J Controlled Release*, **144**, 118-126, (2010).
44 Schneider, C. A., Rasband, W. S. & Eliceiri, K. W. NIH Image to ImageJ: 25 years of image analysis. *Nat Methods*, **9**, 671-675, (2012).
45 Popov, V. L. *Contact Mechanics and Friction: Physical Principles and Applications*. (Springer, 2010).
46 Newman, J. (Springer, New York, 2008).
47 Shimizu, Y. *et al.* Simple Display System of Mechanical Properties of Cells and Their Dispersion. *PLoS ONE*, **7**, e34305, (2012).

Chapter 6 : Polyisocyanide hydrogels as synthetic extracellular matrix for vasculogenesis

Abstract
Cell fate is a coordinated response caused by biomechanical and biochemical interactions with the extracellular matrix (ECM). The ECM as discussed in Chapter 1 comprises of the following components: insoluble hydrated scaffolds e.g. fibrillar polymers such as fibrin and collagen (biomechanical signals), proteins/ligands on the surfaces of neighbouring cells and soluble macromolecules (biochemical signals). Hydrogels are uniquely suited for synthetic extracellular matrix (sECM) as wet 3D networks with tuneable stiffness, viscosity, porosity, interconnective pores and cell adhesion through introduction of ligands. PICs are a unique type of hydrogels as they consist of extremely stiff fibrillar polyisocyanopeptides with oligo(ethylene glycol) side chains, which show finite bundling, strain stiffening under mechanical deformation and thermo-responsive super hydrogelation [1]. In the PIC matrix structural control at the nanometer level with modular introduction of ligands e.g. GRGDS (Gly-Arg-Gly-Asp-Ser) and controlling stiffness in the range from 10-1000 Pa through stoichiometry is possible. I*n vitro* vasculogenesis of human bladder smooth muscle cells (hbSMCs) with human umbilical endothelial cells (HUVECs) co-cultured in soft PIC (<100 Pa) covalently decorated with GRGDS or physically mixed with low concentrations of fibrin will be presented.

Introduction

Controlling cellular fate in 3D remains the holy grail of tissue engineering. A large range of natural, synthetic and hybrid hydrogel materials have been used to imitate the ECM with varying degrees of success [2-12]. Ultimately there still seems to be a crucial modular element missing from the design arsenal of the synthetic chemist. Cellular fate is a coordinated response influenced by biomechanical and biochemical interactions with the ECM [13]. In response to a series of external triggers a cell may differentiate, proliferate, migrate, die or perform other specific functions. The engineering properties desired in a biomimetic sECM include high water retention capacity, support of cell anchorage and growth, porosity or interconnectivity allowing cells to grow/migrate in 3D and the free flow

of nutrients and oxygen, the presentation of chemical signals like receptor-binding ligands, biodegradability or rather remodelling to create space for new vasculature [14].

In the tissue engineering of thick complex constructs (e.g. organs) it is vital to obtain vasculature to bring nutrients and oxygen to the newly formed tissue and remove waste products [15]. To date this has only been possible in thin skin and cartilage, meaning that once damaged, thick tissue like organs need to be replaced and cannot be regenerated [16-18]. Therefore it is vital to continue the search of sECM mimics that once introduced into damaged or diseased tissue would result in vasculogenesis of the native tissue and ultimately complete repair of the damaged tissue without the need for donor organs and invasive surgery. The generation of new tissue occurs by either sprouting from existing vessels or it is initiated by vasculogenesis. Vasculogenesis may be defined as the *de novo* formation of endothelial cells from mesoderm cell precursors whereas angiogenesis is the process through which new blood vessels are formed from pre-existing vessels. In nature sprouting angiogenesis occurs in clear stages: angiogenic growth factors activate receptors on endothelial cells in blood vessels; the activated endothelial cells then release proteases that degrade the basement membrane to allow endothelial cells to escape from the original vessel walls; endothelial cells proliferate into the surrounding matrix and form solid sprouts or tubules connecting neighbouring vessels. As tubules extend toward the source of the angiogenic stimulus, endothelial cells migrate in tandem, through integrins, reinforcing tubules until finally a full-fledged vessel lumen is formed at the angiogenesis site [19]. Lutolf and Hubbell summarized the vascularisation process for endothelial cells in morphogenetic steps: endothelial progenitor cells become endothelial cells, which in turn

form a vacuole, the vacuole starts to branch or sprout, the tubes connect to form a capillary network and the network itself recruits smooth muscle cells to stabilize the newly formed network (Figure 1) [14].

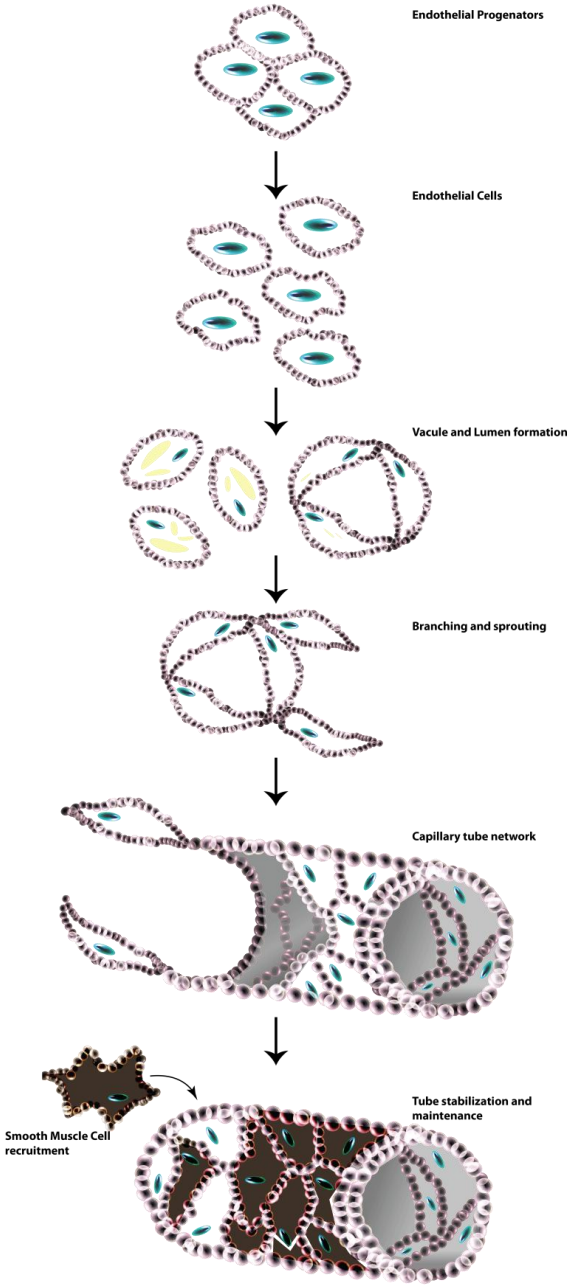

Figure 1. Morphogenic steps required for tubule formation of endothelial cells.

Controlling cellular fate of cells encapsulated in a sECM requires bulk mechanical properties of similar stiffness to that of the matrix of origin with the same amount of tethering points (e.g. RGD). This approach resulted in similar cellular fates e.g. neurite out growth in culture [20-21]. Endothelial cells however are known to be an exception to this rule as it has been shown by Shroff *et al.* that hydrogels with the same stiffness but different architectures (strain stiffening fibronectin elements) and ligand densities catalyzed different cellular fates [22]. Smooth muscle cells have a matrix of origin of stiffness ranging in the kPa [23]. Therefore it is expected that in a soft sECM the hbSMC will remain dormant and HUVEC will exhibit different fates when the critical stress and RGD density of the sECM is varied.

Hydrogels are uniquely suited as sECM for vascularisation, because of their innate similarities to the ECM as a wet 3D framework. A summary of properties that hydrogels for successful vascularisation require are: 3D environment; tuneable stiffness of bulk gel; tuneable viscosity; porosity and inter connectivity pores; cell adhesion through ligands; dynamic change in material properties over time making room for newly formed tissue [14,24-26]. Natural and hybrid hydrogel systems usually contain strain stiffening behaviour, that to date has not been easily mimicked by purely synthetic materials in biologically relevant media [27-30]. Natural (collagen; fibrin; Matrigel) and hybrid (hyaluronic acid-polyethylene glycol-gelatin) hydrogels utilizing extracts from native ECM can actively support cell proliferation, migration and differentiation; however, these materials are mechanically weak, have compositional inconsistency and could be a potential contamination source [31].

In the hybrid sECM, thiolated hyaluronic acid (HA) cross-linked with denatured thiolated collagen encapsulated embryonic endothelial progenitor cells (EPC) were successfully mobilized to kidneys when compared to those delivered in buffer and after implantation showed renal regeneration and promoted vasculogenesis [32]. A commercially available hybrid system based on HA, gelatine and polyethylene glycol has shown EPC tubulogenesis but only in the presence of 50 ng/mL vascular endothelial growth factor [33]. Although promising results are obtainable in the hybrid ECM systems they suffer from the same limitations as natural systems, being batch to batch variation, a source of possible contamination and fixed mechanical properties.

Synthetic ECM materials that have been explored for vascularisation are polyethylene glycol (PEG) and poly(lactic acid-*co*-glycolic acid) (PLGA). For 3D tissue in vitro vasculogenesis, PLGA has been primarily used as a scaffolding material to provide mechanical strength and 3D structure. PLGA seeded with mesenchymal stem cells and kidney vascular endothelial cells formed a vascularized network upon implantation into a rat thigh. Compared to non-prevascularized PLGA scaffold, there was about a twofold increase in the bone density [34]. The biggest drawback of the PLGA system as a whole is the degradation by-product poly(α-hydroxy acids), which lowers the pH and causes local acidosis [35] and inflammatory responses [36]. The co-culture of endothelial cells and mouse pericyte precursor cells (pericytes wrap around blood vessels and can differentiate into SMCs) onto PEG-RGDS resulted in slight tubulogenesis with a cobblestone-like appearance within 18 days [13]. In another study of HUVECs cultured on top of a PEG-RGDS gel slab, slight tubule formation was observed within 19 days [9,37]. On surface

coated with PEG-RGD hydrogels containing matrix metalloproteinase (MMP) cleavable sequences no spreading and complete release of the endothelial cell construct off the hydrogel surface was observed within 3 days [3]. In 3D studies of HUVECs imbedded in a matrix of PEG-RGDSP (containing *no* additional growth factors) no vascular-like networks were observed within 12 h [38], but embedded in PEG-RGDS they did exhibit limited cell-cell interaction and mobility within 29 h [9,37].

Recently a new synthetic hydrogel based on polyisocyanopeptides with oligo(ethylene glycol) side chains (PIC) was developed. This super hydrogelator exhibits: finite bundling, 100-150 nm pores, long persistence lengths l_p and strain stiffening behaviour [1]. This behaviour of PIC hydrogels closely mimics that of natural ECM fibres such as fibrin, in that it contains helical fibrous polymer bundle that respond nonlinearly to applied forces. To the knowledge of the authors there is no other synthetic material that exhibits this behaviour in biologically relevant media. To make cells interact with PIC, a biologically relevant peptide is needed e.g. RGD. This is accomplished by clicking bicyclononyne functionalized RGD to the side chains of the PIC. The degree of RGD functionalization on the PIC as well as the average distance between RGD units can be controlled due to this system's inherent highly organized 4_1 helical structure and ease of functionalization through stoichiometric copolymerization. Strain promoted acetylene azide cycloaddition (SPAAC) was chosen for ligand attachment. By synthesizing an azide-functional monomer and copolymerizing it with the spacer monomer it is possible to decorate these polymers with any biological recognition element desired. A similar strategy was successfully used to decorate the PIC with the streptavidin protein at well defined intervals of ca 50 nm [39]. The spatial control

of the RGD has been shown to be critical on 2D surfaces with respect to integrin clustering (50 - 70 nm) and eliciting cellular responses [40-41]. The specific cell adhesive ligand opted for was the GRGDS peptide (Figure 2) as it has been used successfully in a sECM hydrogel to obtain vascularised constructs in the past [42-43]. Alternatively, cell adhesion can be obtained by mixing PIC with fibrin to obtain a hybrid system that is compatible with HUVEC culture [44]. The co-culture of hbSMCs and HUVECs encapsulated in a soft sECM consisting of PIC either covalently decorated with GRGDS or mixed with fibrin was investigated as possible matrix to elicit vasculogenesis *in vitro* 3D vasculogenesis and *in vivo* after subcutaneous injections in mice whether cell penetration of the native results in vasculogenesis of the sECM.

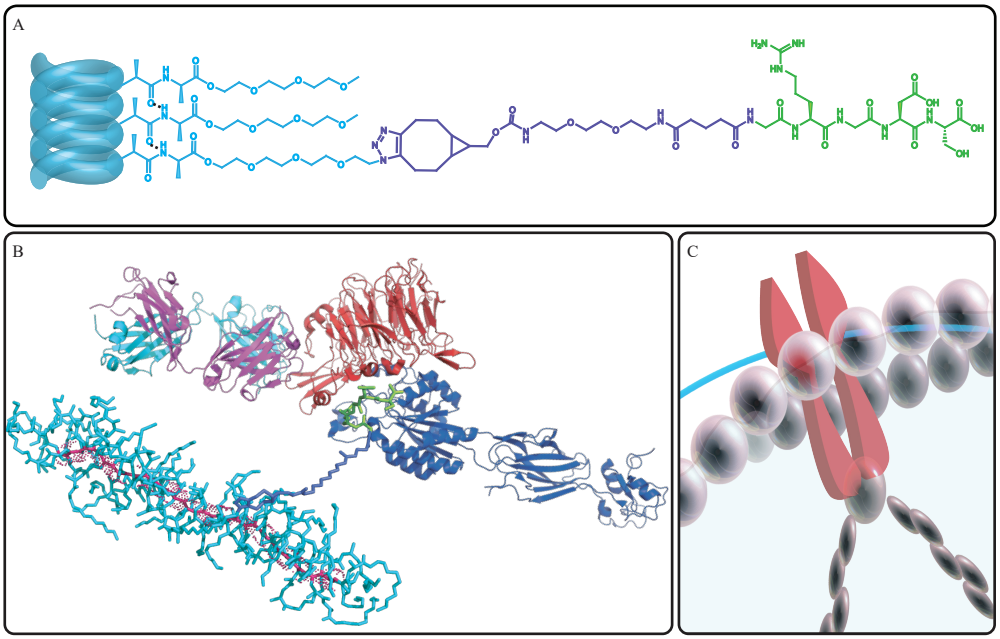

Figure 2. Schematic representation of (a) polyisocyanopeptide decorated with GRGDS (PIC-GRGDS), (b) the binding of a short model PIC-GRGDS segment into integrin cavity based on the structure of the PIC-GRGDS segment optimized in ChemDraw3D and combined with the PDB

structure of integran-$\alpha_{IIb}\beta_3$ [37] rendered in PyMol, (c) schematic representation of integrin-GRGDS-PIC complex through the cellular membrane

Results and Discussion

To investigate the effect of different densities of cell adhesion sites in the PIC to induce vasculogenesis, a range of polymers with different distance between neighbouring azides of (2 – 55 nm) and molecular weights were synthesized (Table 1). The GRGDS peptide was functionalized with a BCN-NHS (SynAffix) in biologically relevant media, the conjugation was confirmed by LC-MS. The BCN-GRGDS conjugate was added to a solution of the azide-functional PIC in equivalent molar amounts based on the azides present and allowed four days to reach full conversion. The success of the labelling was confirmed by determining the azide still available by conjugation through a BCN-Tokyo green dye test. The conversion was consistently between 80-95 %. The conjugate will hereafter be referred to as PIC-GRGDS, and the homopolymer containing no azide monomer will be referred to as PIC. To simplify the results only samples highlighted in Table 1 will be discussed. For more information on synthetic and hybrid mixtures used, see experimental section (Table 5).

Table 1. The molecular weight, storage modulus of PIC used as sECM

Compound	**M1: M2** (mol Azide:CH_3)**	**Yield wt%**	**$\overline{M_v}$ (kg/mol)**	**G' (Pa) 1.6 mg/mL PBS @ 37 °C**
P3	0	80	491	79*
P41	1:144	91	516	80
P40	1:126	50	674	28
P28/29	1:98	70	425	26
P19	1:187	67	866	21

*concentration of the hydrogel was 3.2 mg/mL; ** as determined by the dye test

The linear rheology of the PIC-GRGDS exhibited a slightly lower storage modulus than the azide-functional polymer (Figure 3), most likely due to sample memory effect from the additional processing step of conjugation at 4 °C over several days. In Chapter 3 the effect of prolonged periods in solvated state below the sol-gel temperature was shown to affect the storage modules of PIC. The sol-gel temperature was however unaffected after the conjugated of GRGDS. Interestingly in PIC-GRGDS polymers where syneresis was present, this effect appeared to be delayed by the presence of GRGDS (Figure 23).

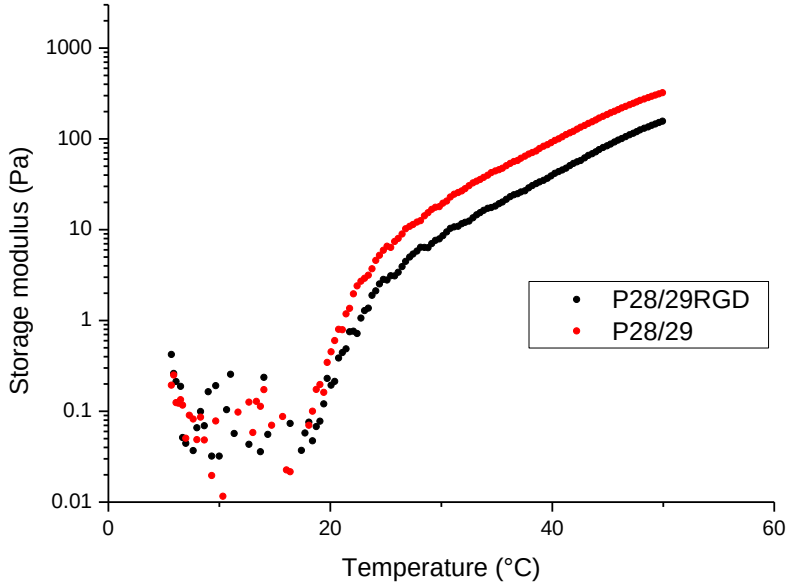

Figure 3. Storage modulus as a function of temperature for P28/29 and P28/29RGD at 1.6 mg/mL in PBS.

Nonlinear behaviour of the PIC was measured with rheology. The samples were equilibrated for 25 minutes at 37 °C prior to starting the measurement. Samples were

exposed to a pre-stress protocol and superimposing a small oscillatory stress with an amplitude of $|\delta\sigma| < 0.1\sigma$ at a frequency of $0.1 - 10$ Hz [45] and allowed to equilibrate between incremental stress steps for 3 min. The differential modulus (K') was calculated from the oscillatory strain response $\delta\gamma$, as

$$K' = \frac{\partial\sigma}{\partial y} = \frac{\delta\sigma}{\delta y} \quad \text{(Eq 1)}$$

$$K' = A\sigma^B \text{ (Eq 2)}$$

$$\sigma_C = \left(\frac{G'}{A}\right)^{\left(\frac{1}{B}\right)} \text{ (Eq 3)}$$

Where σ_C is the critical stress, G' is the storage modulus in Pa and A and B values derived from the linear fitting of the differential modulus plotted against the stress. For example for sample **P39** (Figure 4), the initial storage modulus was 85.5 Pa, A= 13.2 and B = 1.1, a critical stress value of $\sigma_C = 5.7$

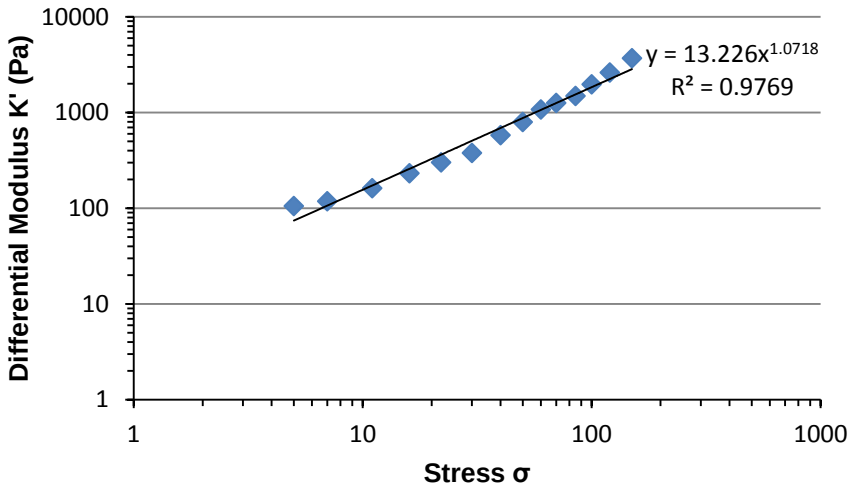

Figure 4. Differential modulus plotted against stress of P39 in MQ (1 mg/mL) at 37 °C.

By measuring the differential modulus relative stress and using Eq 3 it was possible to determine the critical stress values of PIC with a range of molecular weights (Table 2).

Table 2. The critical stress values of a range of PIC dissolved in MQ at 1.0 mg/mL used to construct the calibration curve (Eq 1)

Compound	**M_η (kg/mol)**	**critical stress σ_c**
P21	948	12.5
P37	791	10.2
P38	733	7.9
P39	569	5.7
P28/29	425	1.6

From the data summarized in Table 2 it appeared as if the critical stress values scaled with molecular weight. A calibration curve based on the measured critical stresses based on Eq 3 of a range of PIC consisting of a broad range of molecular weights was constructed

(Figure 5). A linear relationship between molecular weight and critical stress was observed and a trendline $y = 0.0202x - 6.423$ (Eq 4), with a $R^2 = 0.99$ was derived from the data. Where x is the molecular weight and y is the critical stress.

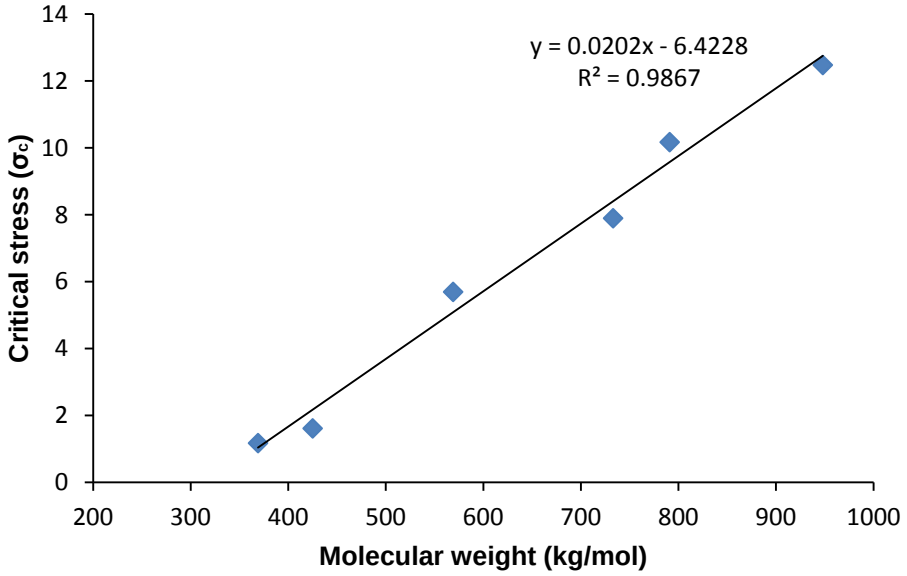

Figure 5. Critical stress vs. molecular weight at a concentration of 1 mg/mL in MQ at 37 °C.

The R^2 of Eq 4 was very good at 0.99 as seen in Figure 5. The calculated and measured critical stress was summerized in Table 3. The average critical stresses compared well with the average calculated critical stress of 5.6 ±3.0 and average measured critical stress of 4.6±3.6. The two data sets that of calculated critical stress and the measured critical stress were both normally distributed (see, Figure 6) and when the two sets were compared using the two sample t-test a P value = 0.6 was obtained indicating that there was no statistical difference between the two. Therefore Eq 4 can be used to predict critical stress of PIC based on its molecular weight.

Table 3. Critical stress measured vs. calculated values at a concentration of 1 mg/mL in MQ.

Compound	M_η (kg/mol)	calculated critical stress	critical stress 1 mg/mL	Difference
P28/29	425	2.2	1.6	0.6
P39	569	5.1	5.7	-0.6
P38	733	8.4	7.9	0.5
P41	516	4.0	1.1*	2.9
P7	796	9.7	10	-0.3
P28/29RGD	425	2.2	0.8	1.4
P18RGD	688	7.5	4.8	2.7

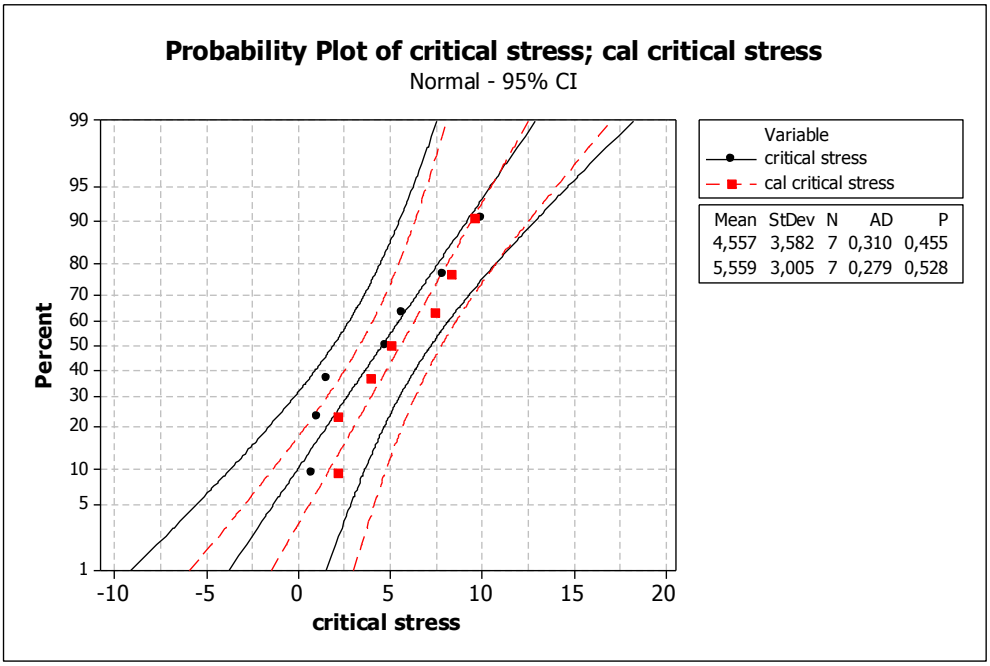

Figure 6. Probability Plot at 95% confidence interval of measured critical stress and the calculated critical stress (Eq 4).

The stiffness of the PIC hydrogel is important but as discussed in Chapter 1, the porosity is also very important when designing a sECM as it affects cellular motility. It was suspected

that cellular motility would be limited or hampered in the PIC system as it consists of nm pore sizes. Therefore, cellular motility was investigated by culturing hbSMCs or HUVECs in PIC for three days and observed with time lapse microscope for 50 h. The small pores did not appear to hamper hbSMC motility however, where hbSMCs moved freely through the PIC, HUVECs on the other hand only migrated when encapsulated in PIC-GRGDS. This behaviour would suggest another mode of migration than one purely driven by passive diffusion through pores (Movie 1-2). This behaviour of unhampered motility in hydrogels with nm scale pores has been observed before by Zaman *et al.* in cells immersed in Matrigel, an ECM extract. In Matrigel, the cells deformed the matrix and created spaces to migrate through, therefore mobility in this system was thought to be regulated by mechanical stiffness, proteolysis and integrin expression [46]. In the sECM of PIC the exact mode of migration still needs to be investigated, but it is clear that in stiffness of <200 Pa motility is unaffected by pore size.

The hybrid fibrin-PIC was easily prepared by mixing different volume ratios of fibrin with PIC (1:1, 1:5, 1:10, and 1:50 (v/v)). Fibrin gel was prepared as described [38]. Fibrinogen from bovine plasma (Sigma-Aldrich, Schnelldorf, Germany) was reconstituted in 0.9% NaCl to final concentration of 10 mg/mL and thrombin (50 U/mL, Sigma-Aldrich) was added to polymerize fibrin gel at varied concentrations in the presence of PIC (2.5 mg/mL). The linear rheology of the 1:5 fibrin-PIC mixture exhibited similar sol-gel transition temperatures but lower overall storage moduli (Figure 24). The non-linear behaviour of the mixture also matches that of the PIC (Figure 16).

First the initiation of vasculogenesis was investigated by evaluating light microscopy images of PIC-GRGDS (**P28/29RGD**; **P19RGD**), PIC (**P3**) and PIC-fibrin mixtures and compared to control fibrin gel (10 mg/mL) (Figure 7). The control fibrin experiments have a fivefold concentration when compared to the hybrid PIC:fibrin mixtures as at the concentrations used in hybrid system fibrin did not form gels. Within 24 h sprouting was observed in all the hydrogels containing cell adhesion ligands whether it be from fibrin or synthetically introduced. No vasculogenesis was observed in pure PIC as no anchor points extended from single cells (Figure 7f). The combination of fibrin-PIC resulted in faster vasculogenesis than in PIC-GRGDS.

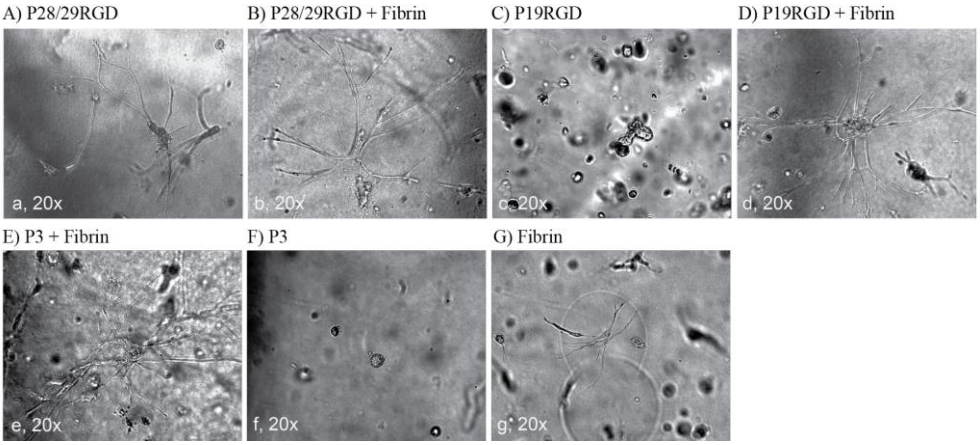

Figure 7. Initiation of vasculogenesis. Bright field images of HUVEC and hbSMC in hydrogels were taken after 24 h. a)P28/29RGD (1 in 10 GRGDS); b) P28/29RGD +Fibrin; c) P19RGD (1 in 23 GRGDS); d)P19RGD+Fibrin; e) P3+Fibrin (5:1); f) P3; g) Fibrin (positive control 10 mg/mL).

Next, the effect of culturing hbSMCs/HUVECs in PIC over extended periods of time (up to two weeks) was investigated (Figure 8). Vasculogenesis was monitored with light microscopy every 3 days over this period. In PIC hydrogels mixed with fibrin (**P3 +** fibrin 5:1) the newly formed structures/sprouts were complex and endothelial tubes were

substantial as early as four days after initiation (Day 4 scale bar is 500 μm). After 14 days, sprouts/construct were too condensed to observe via light microscopy. This is remarkable as the concentration of fibrin in PIC:fibrin is only 2 mg/mL and this sprouting would not occur in fibrin gels at 2 mg/mL as it does not form an efficient hydrogel at these concentrations. The cells still showed characteristic sprouting similar to that observed in 5 fold higher concentration of fibrin gels at 10 mg/mL (Figure 7- 9). In **P41RGD** and **P19RGD**, co-cultured cells formed clusters and endothelial tubes sprouted in a radial fashion. In **P1** (without GRGDS or fibrin) cells formed clusters that increased in size and stained positively for propagation markers, but no sprouting was observed (Appendix Figure 25, 28-29). In **P1** supplemented with unbound GRGDS at similar concentrations to the **P41,** no sprouts formed, only cellular clusters (Figure 8).

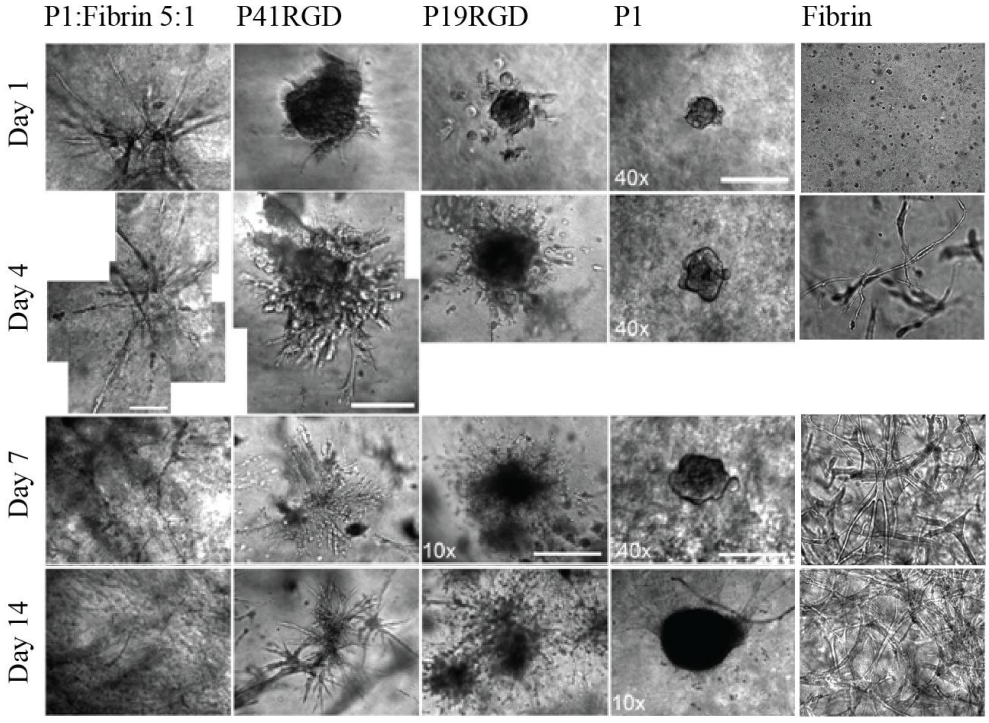

Figure 8. Vasculogenesis in hydrogels over incubation of two weeks. (Scale bars at first and second rows are 175 μm for magnification x40. Scale bar at third column and third row is 500 μm for magnification x10. Fibrin at x20 magnification.

To explore the effect on vasculogenesis purely induced by changing the molecular weight the GRGDS density was kept constant and the PIC concentration constant and the stiffness low (below 100 Pa, Table 1). The onset and degree of vasculogenesis was controlled in this manner (Figure 9) irrelevant of hydrogel stiffness. In **P28/29RGD** the cells showed faster tubule formation than in **P40RGD** from day 1-7 and by day 12 the cells have formed a dense structure.

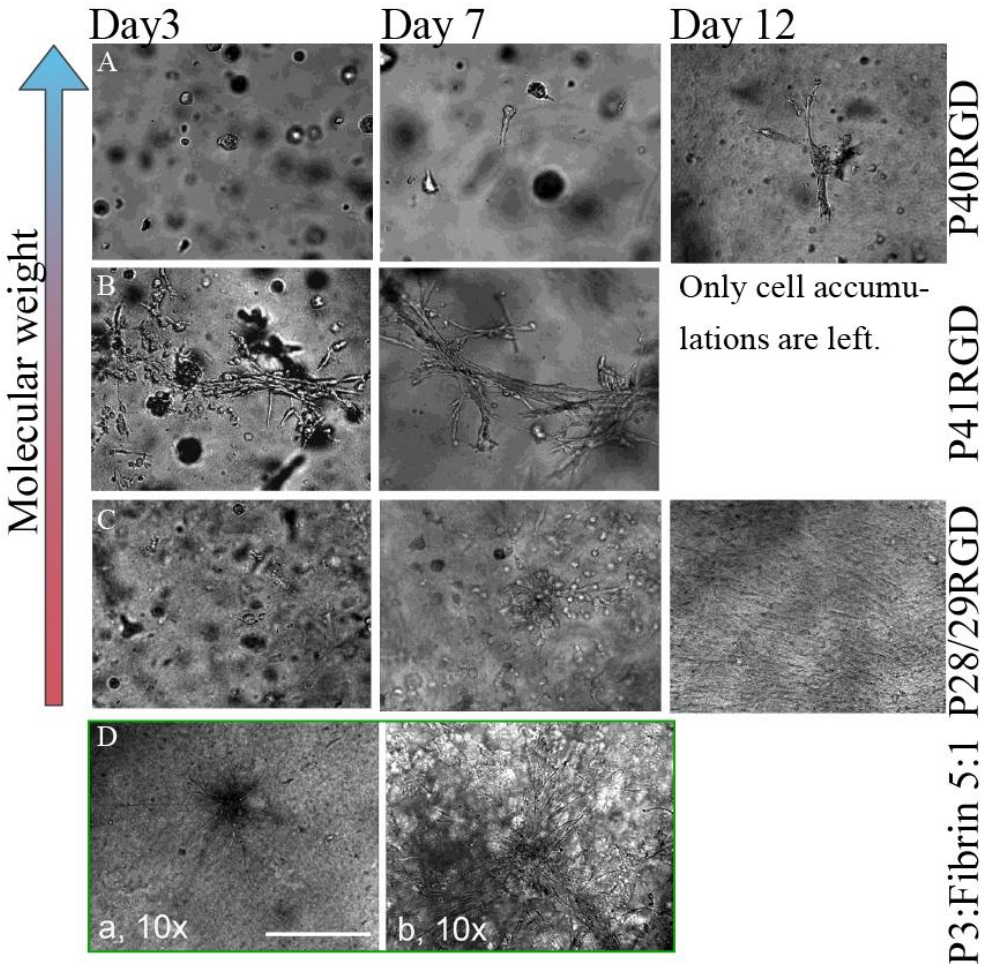

Figure 9. (a-c) Light microscopy of HUVEC/hbSMC in PIC-GRGDS 1 in 10 nm at a concentration of 1.6 mg/mL with decreasing molecular weights at x20 magnification, (d) Vasculogenesis with P3:Fibrin 5:1 from day 1 to day 3. a: on day 1, vasculogenesis initiated. Distance of sprouting is around 500 μm. b: on day 3, complex vasculature formed. (Scale bar is 500 μm.)

To investigate the optimal density of cell adhesion ligands required on PIC, PICs were decorated with a range of GRGDS densities from as high as 1 in 2 nm to as low as 1 in 55 nm (Figure 10). The highest density of 1 in 2 nm GRGDS (**P38RGD**) resulted in undefined

cellular response that did not appear to be tubular in any way and the lowest density of 1 in 55 nm (**P36RGD**) showed similar results as pure PIC hydrogels containing no GRGDS.

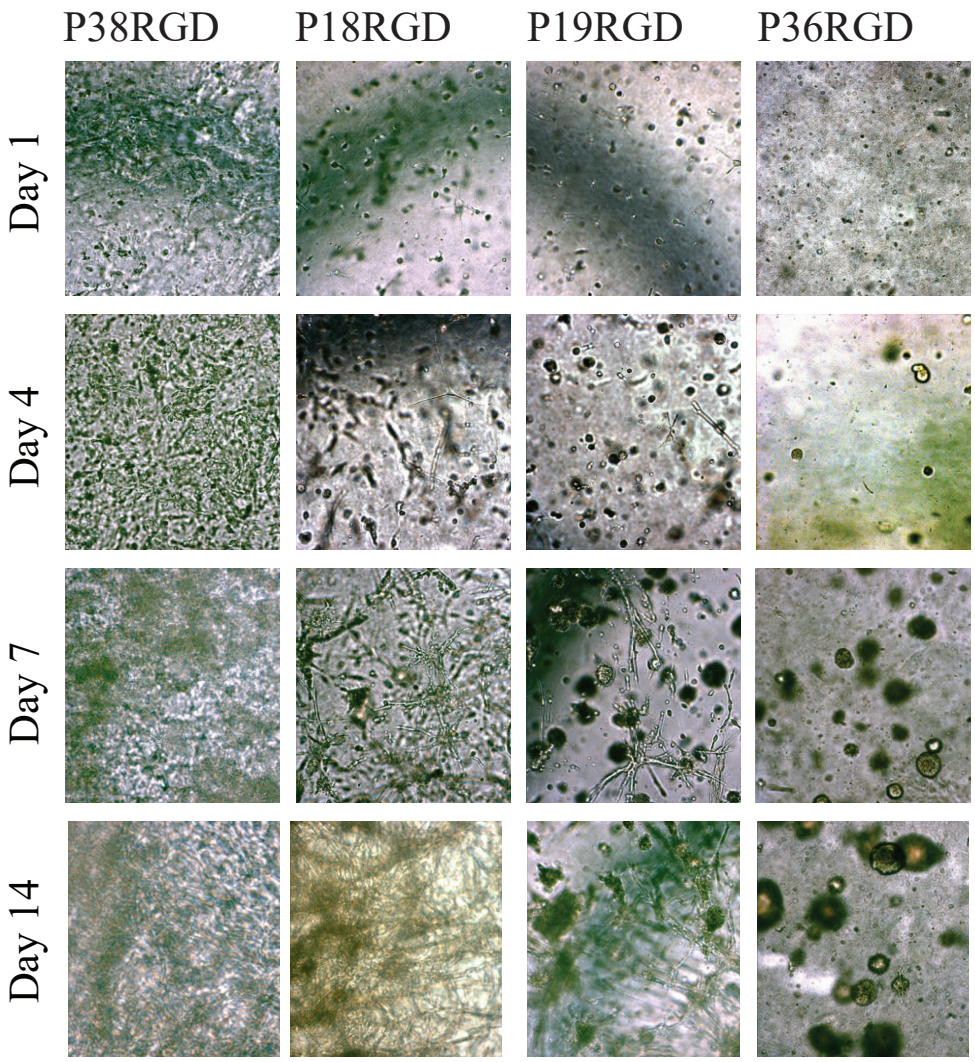

Figure 10. Light microscopy of hbSMC/HUVEC co-culture over two weeks in 3D, PIC with decreasing density of GRGDS: P38RGD (1 in 2 nm); P18RGD (1 in 10 nm); P19RGD (1 in 20 nm); P36RGD (1 in 55 nm).

Vascularisation in mixed systems of PIC and fibrin were investigated by mixing volume ratios of the two: 1:1 v/v was equal to 1 mg/mL PIC to 5 mg/mL fibrin, 1:5 v/v was equal to 2 mg/mL PIC to 2 mg/mL fibrin, 1:10 v/v was equal to 2 mg/mL PIC to 1 mg/mL fibrin and 1:50 v/v was equal to 2 mg/mL PIC to 0.2 mg/mL fibrin. In samples containing fibrin, sprouting was evident in all the mixtures except 1:50 within a 14 day incubation period (Figure 11). In the mixed PIC:fibrin systems the lowest concentration of RGD from the fibrin required for vascularisation (1 mg/mL fibrin) was calculated to be 13.2 µM, but the best results were obtained in the PIC:fibrin 1:5 containing 2 mg/mL fibrin which is equal to 23.4 µM RGD (Figure 12 and 27).

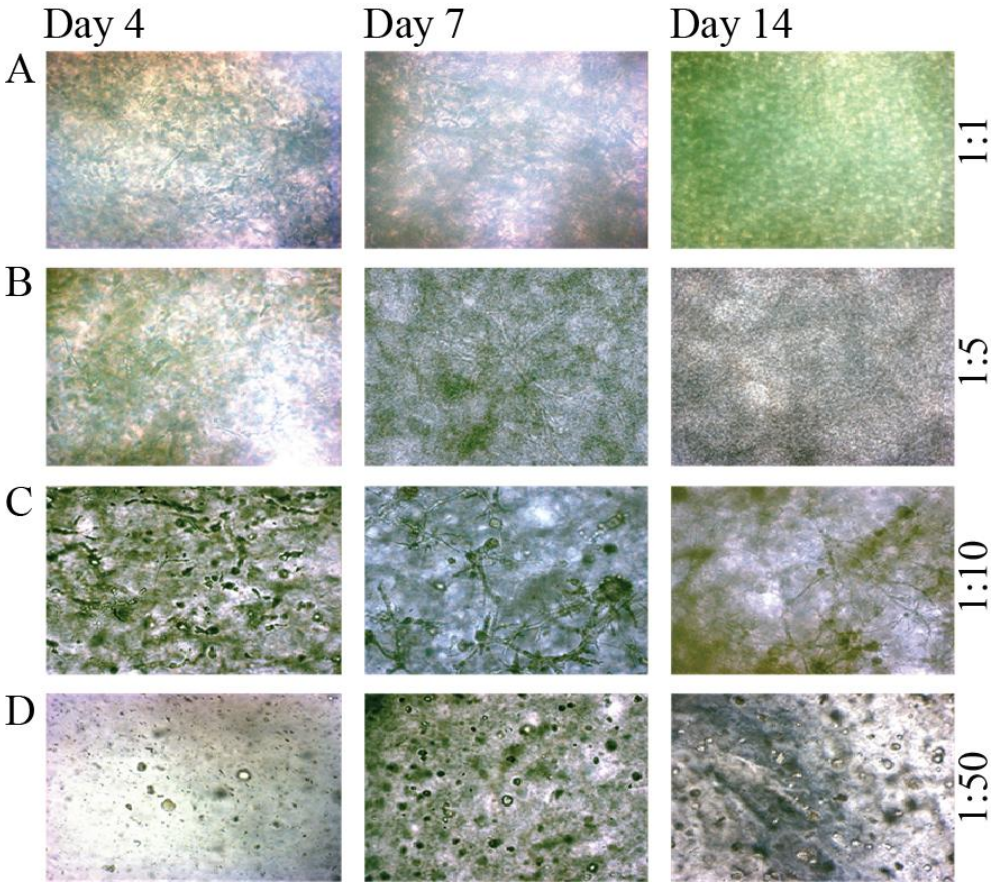

Figure 11. Light microscopy of hbSMC/HUVEC over time in the 3D hydrogel constructs containing decreasing concentration of fibrin relative to PIC (magnification 10x) a) 1:1, b) 1:5, c) 1:10, d) 1:50.

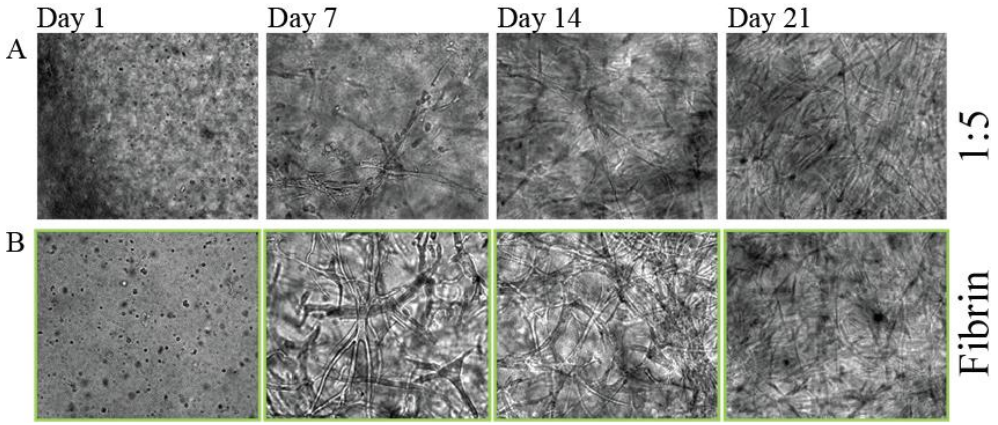

Figure 12. Light microscopy images (magnification 20x)a) P41:fibrin 1:5 (2 mg/mL) b) Fibrin 10 mg/mL.

In conclusion, the optimal density of GRGDS on the PIC backbone was one every 10 nm on average which in stoichiometric terms is 63.3 µM. On closer examination of PIC-GRGDS 1 in 10 nm against 1 in 23 nm, vasculogenesis was observed in both samples over a week and half. In **P41RGD** on day 1, cells started to anchor in the hydrogel. On day 4, cells clustered and started to sprout. On day 9, large cell clusters formed (diameter of cell cluster is around 500 µm), and communication formed between clusters (Figure 8; 9b). The behaviour in **P19RGD** (1 in 23 nm) over the same time period was comparable but with a lower degree of complexity of the formed sprouts (Figure 8). If we now compare the PIC-GRGDS system to the PIC-fibrin system where fibrin was simply mixed with PIC (**P3**) vasculogenesis was observed within three days. On day 1, vasculogenesis initiated and the distance of sprouting was around 500 µm. By day 3, complex vasculature formed (Figure 9d). Therefore it is clear that the synthetic PIC system requires optimization, possibly by the inclusion of additional cell adhesion ligands (e.g. KQAGDV) and covalent attachment of growth factors that are present in the fibrin mixed system.

The growth of vasculature was followed with light microscopy for 14 days. To confirm whether the formed sprouts were indeed vasculature, immunohistochemical (IHC) analysis was performed to identify vasculature orientation with specific markers. Von Willebrand factor (vWF) is a glycoprotein and CD31 is a protein for adhesion on the membrane. The expression of vWF and CD31 in endothelial cells is different but both markers are often used to identify vasculature [47]. All constructs formed in various sECM (pure fibrin; **P3**:Fibrin 5:1, **P28/29RGD** and **P19RGD**) were evaluated and the presence of 3D sprouting and branching confirmed (Figure 13). Endothelial tubes were stained against vWF or CD31. Tubular structures were supported with smooth muscle cells (SMA or vimentin positive). Endothelial tubes sprouted and extended from a cell cluster to communicate with other clusters (Figure 13a). Connection of endothelial tubes indicated an initiation of vasculature network in hydrogels (Figure 13b). In hybrid sECM with fibrin as cell adhesion component dispersed in PIC, vascularisation was observed (Figure 13c). The presence of CD31 positive vascular-like structures, surrounded by vimentin positive cells and even some luminal structures were identified in **P3:fibrin** 1:5 similar to those observed in the fibrin positive control where observed (Figure 26).

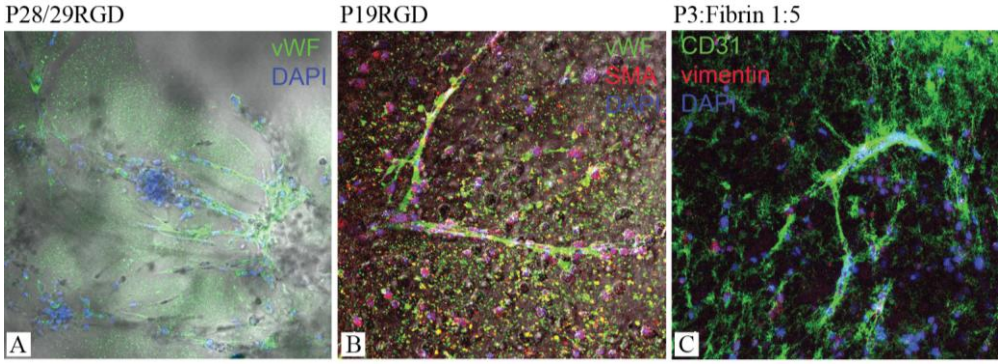

Figure 13. Confocal images of vasculatures after two weeks incubated in hydrogels. Vasculature was stained with vWF/α-SMA or CD31/vimentin. Endothelial tubes were clearly showed with Alexa 488. Supporting smooth muscle cells were either scattering in hydrogel or surrounding endothelial tubes. a) P28/29RGD, b) P19RGD, d) P3:fibrin [5:1]. Magnification is x20.

To summarize, it was observed that some vasculogenesis of HUVEC/hbSMC does occur in PIC-GRGDS over a two week period, but the structures that most closely resemble those obtained in the fibrin control were observed in the hybrid mixture of fibrin:PIC (1:5).

Once formed it would be advantageous to remove formed vasculature for possible implantation applications. Skardal *et al.* have reported the non enzymatic harvesting of cellular clusters from HA-gelatin coated beads of a range of cells including endothelial cells (HUVECs) excellent viability and growth during 3D expansion and the following cell recovery by gentle centrifugation. The use of excessive force or enzymatic degradation could result in construct damage and undesired cell surface modification [48]. The use of beads is an attractive solution but ideally it would be desirable to simply melt the hydrogel away without any chemical or enzymatic degradation. Due to its thermo-responsive properties, it was possible to harvest cell clusters from pure PIC by cooling the hydrogel down and carefully removing them. The pre-formed clusters could consequently be induced

to sprout when immersed in PIC-GRGDS and incubated for three days (Figure 14). To my knowledge this is a unique characteristic of PIC sECM and not possible in any other ECM mimic. This strategy should be transferable to harvesting sprouted structures from the hydrogel after two weeks of incubation, but as the goal of this particular study was to obtain vasculogenesis *in vivo*, the ex situ harvesting of sprouts was not investigated further.

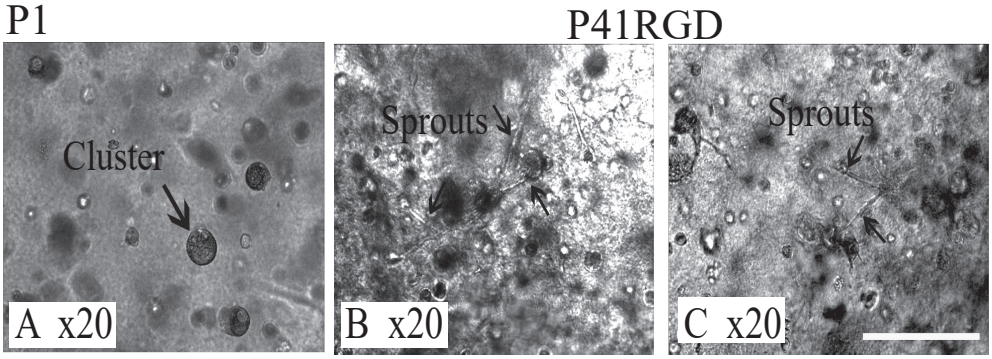

Figure 14. Harvest of 3D cell culture. First HUVEC and hbSMC were co-cultured in P1 and then transferred to P41RGD. a) Day 3, cells formed spheres/clusters, b&c) Clusters were harvested via pipette tips and transferred to P41RGD, 3 days after transferring to P41RGD, cell clusters started to sprout. (scale bar is 250 μm).

The vasculogenesis of native tissue in the presence of PIC-GRGDS *in vivo* by cellular infiltration of the host tissue was investigated by the subcutaneous injection of PIC into mice. It was hypothesized that native tissue would infiltrate the PIC-GRGDS and just as observed *in vitro* initiate vasculogenesis inside the hydrogel. The material properties of the *in vivo* experiment were reconstructed (0 °C solution, injection and rapid heating to 37 °C Figure 15) in a rheological environment. A significant decrease in stiffness after injection was observed in PIC and PIC-GRGDS (34 Pa for the **P28/29** and 6 Pa for the **P28/29RGD)** see Figure 15. To counteract the decreased stiffness after injection, the sample concentration was increased from 1.6 mg/mL *in vitro* to 2.0 mg/mL *in vivo*.

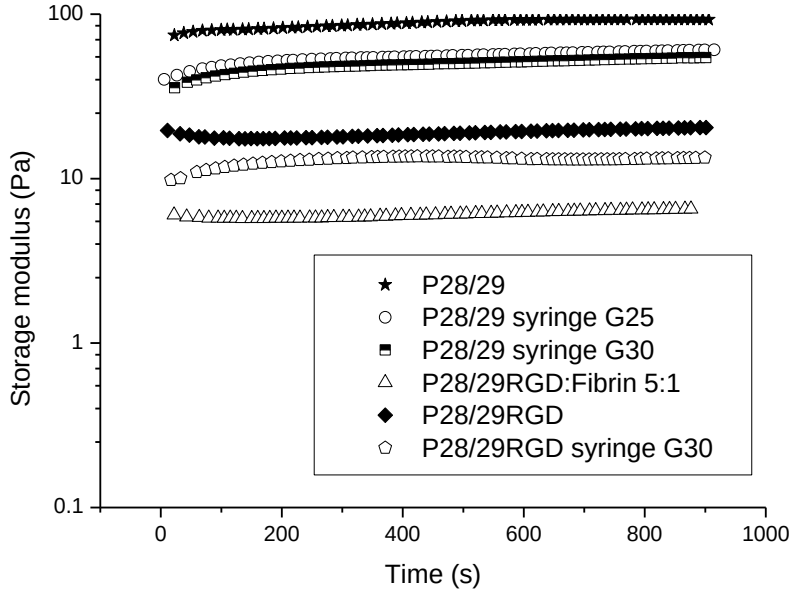

Figure 15. Storage modulus as a function of time for PIC samples at 1.6 mg/mL (medium) for 900 s at 37 °C (2 % strain, 1 Hz).

To determine the critical stress values of the samples used for animal studies, the differential modulus was measured with increasing stress for sECM samples at 2 mg/mL in cell culture medium (Figure 16).

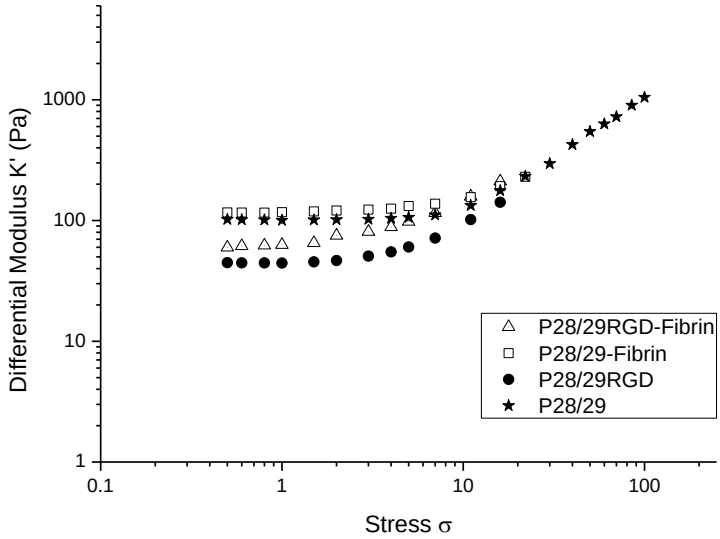

Figure 16. The differential modulus as a function of stress for P28/29 (Azide; GRGDS), fibrin-PIC (Azide; GRGDS) in cell culture medium at 2 mg/mL. Fibrin at 2 mg/mL did not form a hydrogel and was therefore not included in this graph.

The strain stiffening characteristics of the PIC were retained regardless of the presence of fibrin at 2.0 mg/mL. The fibrin itself did not form a hydrogel at 2.0 mg/mL. From these curves it was possible to derive the critical stress of the aECM used using Eq 3 (Table 4).

Table 4. Critical stiffness and storage modulus of aECM at 2 mg/mL in cell culture medium at 37 °C

Sample name	**Critical stiffness σ_c**	**Storage Modulas (Pa)**
P28/29	9.1	103.4
P28/29RGD	2.9	45.3
Fibrin-P28/29	2.1	60.5
Fibrin-P28/29RGD	5.2	116.7

The penetration of native tissue into PIC-GRGDS was visualized by staining of the hydrogel construct one and two weeks after subcutaneous injection with haematoxylin and eosin (HE) and Masson staining. In Figure 17 partial cellular penetration was observed in **P3**, but more so in **P28/29RGD.** The penetrated cells are indicated by the arrows, the deposition of native ECM was directly correlated to the degree of cellular penetration and moderate immune response from surrounding native tissue was observed from the **P28/29RGD** injections.

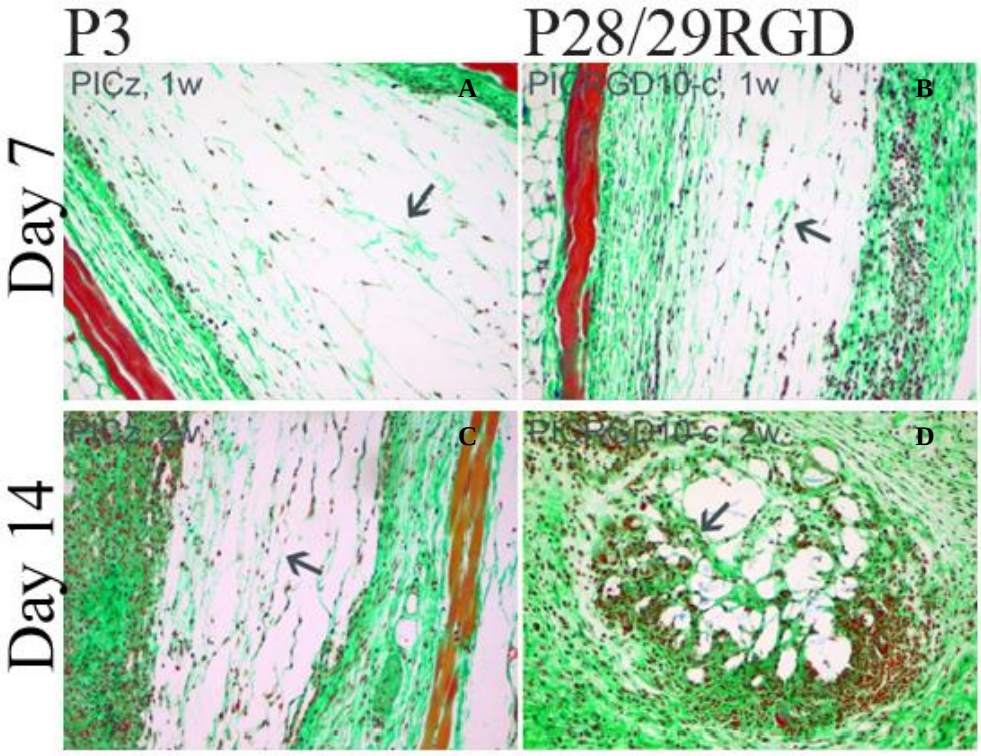

Figure 17. Microscopic images (magnification 20x) of the haematoxylin and eosin (HE) and Masson staining showing: (a) the P3 construct after one week, (b) P28/29RGD construct after one week, (c) P3 construct after two weeks , (d) P28/29RGD after two weeks.

Microscopic evaluation indicated a moderate inflammatory response in all constructs one and two weeks after injection. The cellular response was scored semi-quantitatively (Figure 18 and Table 9). Representative images of the different constructs, which were used for the scoring, are shown in Figure 17 and Figure 31. After two weeks, cell infiltration and native ECM production was clearly present, but no vascular structures were observed. These are still very promising results as pure fibrin hydrogels do not survive longer than a week *in vivo* as they are highly susceptible to fibrinolysis [10].

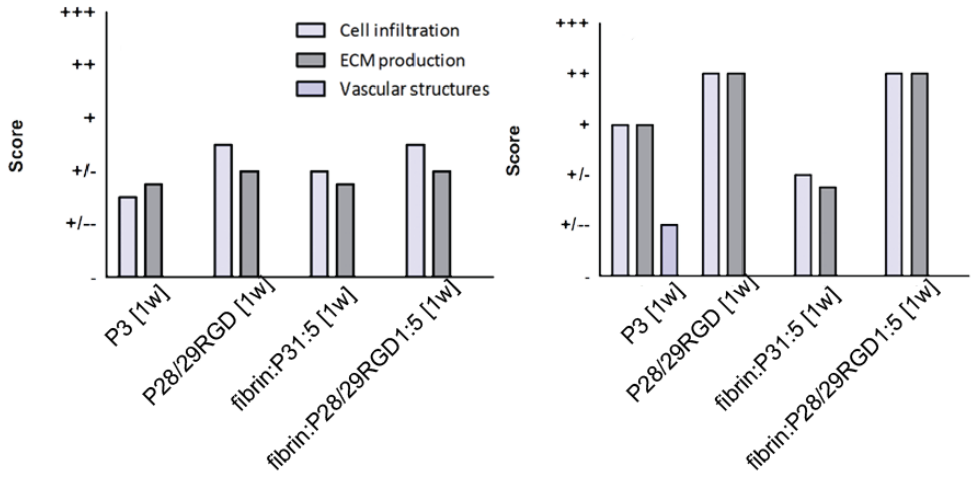

Figure 18. Histograms showing the average score (±SEM) assigned to the cell infiltration, ECM production and vascular structures seen in the different PIC constructs evaluated one (left) and two (right) weeks after injection. Figures represent the scores assigned to the PIC constructs injected (n=1). Scoring: - = not present, +/- - = sporadically present, +/- = a little bit present, + = present, ++ = clearly present, +++= abundantly present.

Conclusion

It was shown that polyisocyanides as sECM can be used to induce vasculogenesis *in vitro* if a cell adhesion ligand GRGDS is covalently attached to it in an optimum concentration of 63.3 μM. At this optimum peptide concentration, the polymer itself should have a molecular weight of 425-516 kg/mol to ensure initial sprouting occurs within three days. The sECM (synthetic and hybrid materials) used *in vivo* had stiffness of <100 Pa and a critical stress of 2.0-2.9. It was also shown that vasculogenesis *in vitro* was possible without the covalent attachment of GRGDS to the PIC but by simply mixing fibrin with PIC at concentration as low as 1.0 mg/mL, the best results were however obtained in mixtures containing 2.0 mg/mL of fibrin. This result was surprising in that the fibrin concentration is 10 fold lower than those previously reported in mixed sECM of PEG [49]. Minimal inflammatory response was observed, mice thrived and cellular invasion was observed into the hydrogel during the *in vivo* experiments, however no vasculogenesis was observed and no difference was observed between the PIC-RGD and mixed PIC:fibrin system. The poor results obtained in the mixed fibrin-PIC system could be as a result of rapid fibrin degradation resulting in loss sample of volume and mechanical stability [49]. Perhaps the mode of PIC introduction subcutaneously into the mice for both systems needs to be re-evaluated opting for a cooled injection setup [NanoCool^{TM}, Harvard Apparatus] or larger needle diameter to avoid loss of material integrity through the mode of introduction.

Materials and Methods

Synthesis and Analysis of PIC

The synthesis and analysis of the polymers were discussed in Chapter 2. In Table 5 the analytical data of the polymers used in this chapter are summarized.

Table 5. Data summary of M_v, AFM and rheology

Sample name	**M_v (kg/mol)**	**dye test* to determine azide to CH_3**	**1.6 mg/mL G' @ T = 37 °C**	**1.0 mg/mL G' @ T = 37 °C**
P41	516	1:144	34	11
P40	674	1:126	28	
P28/29	425	1:97	60	16
P18	688	1:115		
P19	866	1:225	21	
P39	569	1:250	58	86
P38	733	1:50	162	184
P36	835	1:575	184	
P31	755	1:62	481	
P32	735	1:98	279	
P33	714	1:556	395	
P18RGD	688			34
P19RGD	866		11	
P41RGD	516		80	
P40RGD	674	1:4601	347**	
P39RGD	569	1:1804	615**	
P28/29RGD	425	1:1872	26	5
P1	498			
P3	491		8	

* See page 6-33 for details on procedure; ** the G' at a concentration of 3.2 mg/mL

Synthesis and characterization PIC-GRGDS

Synthesis of 1-(bicyclo[6.1.0]non-4-yn-9-yl)-29-(carboxymethyl)-23-(3-guanidinopropyl)-32-(hydroxymethyl)-3,14,18,21,24,27,30-heptaoxo-2,7,10-trioxa-4,13,19,22,25,28,31-heptaazatritriacontan-33-oic acid (BCN-GRGDS)

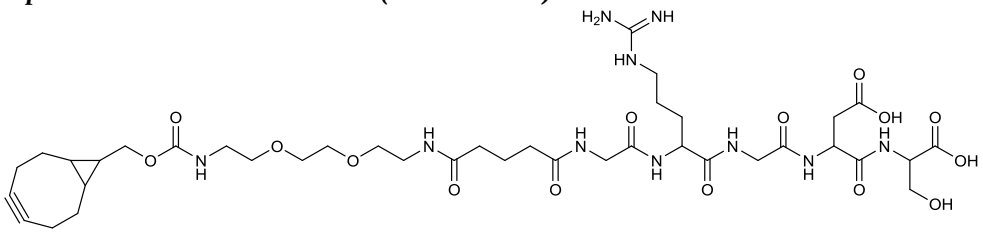

Figure 19. The chemical structure of the BCN-GRGDS

The GRGDS [Bachem] was dissolved in a 50 mM borate buffer pH 8.4 to a final concentration of 2 mg/mL. The 2,5-dioxopyrrolidin-1-yl 1-(bicyclo[6.1.0]non-4-yn-9-yl)-3,14-dioxo-2,7,10-trioxa-4,13-diazaoctadecan-18-oate (BCN-NHS) [SynAffix] dissolved in DMSO was added in a 1:1 molar ratio to the peptide solution and mixed 300 rpm at 18 °C for one hour before being frozen in 100 µL aliquots. MS calc [$C_{39}H_{62}N_{10}O_{15}$]: 910.4 obtained: 911.5

Dye test for determining azide concentration

The azide-functional polyisocyanide was dissolved in ACN at 2 mg/mL. To this PIC solution, a 2 molar (azide) equivalent of BCN-GRGDS (Figure 19) was added. The mixture was allowed to stir for 72 h at 4 °C. The PIC-peptide was purified by precipitation from diisopropyl ether. The precipitant was decanted, re-dissolved and precipitated from DCM into diisopropyl ether. No further purification was performed. The conversion of azides to peptide was determined by determining the residual azide concentration by coupling BCN-TokyoGreen [SynAffix] dye.

To determine the remaining azide density on the PIC, a colorimetric test was performed by conjugating BCN-TokyoGreen (Figure 20) to a known amount of PIC-peptide and calculating the concentration from the Law of Beer Lambert. A BCN-TokyoGreen stock solution of 2.2 mM in DMSO was prepared. The polymer was dissolved on ice in acetonitrile (ACN) with rapid stirring until dissolved (5 mg/mL). An excess (10) of BCN-TokyoGreen based on the mols of azide expected was added to polymer solution. The mixture was stirred for 3 h at room temperature. The dyed polymer was precipitated from diisopropyl ether, the diisopropyl ether was decanted from the polymer and the polymer redissolved in DCM. This step was repeated once more. The diisopropyl ether was decanted from the polymer precipitate which was subsequently dried in vacuo. For UV analysis a 1 mg/mL solution in a mixture of 0.75 ACN: 0.25 DMSO: 1.0 H_2O was prepared. The stock solution was measured against a background of the same mixture of solvents in a quartz-cuvet with a path length of 1 cm on a Cary UV-vis spectrometer. Multiple measurements were made over a range of (1.0 -0.01 mg/mL) polymer concentrations by diluting the stock

solution with H_2O. The extinction coefficient of the BCN-tokyoGreen in this mixture was determined to be 35493 $M^{-1} cm^{-1}$ by measuring the free dye at different concentrations and calculating the slope of the curve at 506 nm. The ratio of azides still present after BCN-GRGDS conjugation was determined in this way.

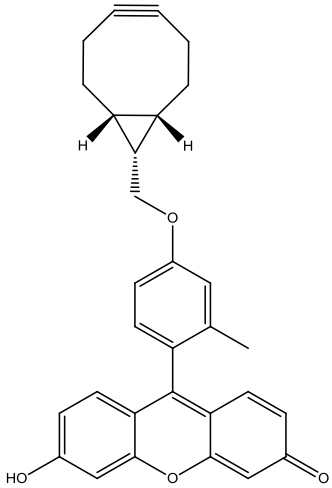

Figure 20. Chemical structure of 9-(4-(((1R,8S,9s)-bicyclo[6.1.0]non-4-yn-9-yl)methoxy)-2-methylphenyl)-6-hydroxy-3H-xanthen-3-one (BCN-TokyoGreen)

Table 6. Dye test results to determine the efficacy of the BCN-GRGDS conjugation

Sample name	**Equivalent of peptide used**	**Yield of conjugation (%)**
P28/29RGD	2	88
P31RGD	2	98
P32RGD	2	94
P33RGD	2	89

From this point forward, care was taken to ensure that the polyisocyanopeptide remained sterile. All equipment was sprayed with ethanol before use. The PIC-GRGDS was weighted directly into a sterile centrifuge tube. The tubes were further sterilized by exposing them to UV radiation for a period of 5 minutes. The PIC-GRGDS was covered with sterile cell culture medium to obtain the final dilution of polymer in media of 3.2 mg/mL and allowed to swell for 24 h at 4 °C. After 24 h a swollen gel-like substance was obtained at the bottom of the centrifuge tube. The swollen PIC-GRGDS conjugate was stirred until dissolved for up to 72 h at 4 °C. The solution exhibited a sharp transition in viscosity above the sol-gel temperature. For the preparation of the constructs of appropriate stiffness and concentration a stock solution of PIC at 3.2 mg/mL in cell culture medium was supplied to the cell culture laboratory.

Rheology
For gel studies, the polymer was dissolved in purified water (MQ); PBS; cell culture medium by first swelling the polymer in a cooled solution before stirring for 16-72 h at 4 °C. Samples were placed in the rheometer at 5 °C (i.e. as a liquid) and gelation occurred between the parallel plates by raising the temperature (2 °C/min). Drying of the sample was prevented by maintaining a moist atmosphere.

Non-linear rheology

The nonlinear rheology of the aECM at 2 mg/mL in cell culture medium was measured. The differential modulus (K') is calculated from the oscillatory strain response δγ, as

$K' = \frac{\partial \sigma}{\partial y} = \frac{\delta \sigma}{\delta y}$ (Eq 1)

$K' = A\sigma^B$ (Eq 2)

$\sigma_C = \left(\frac{G'}{A}\right)^{\left(\frac{1}{B}\right)}$ (Eq 3)

Where σ_C is the critical stress, G' is the storage modulus in Pa. A and B values derived from the linear fitting of the differential modulus plotted against the stress. For example for sample **P19**, at a concentration of 1 mg/mL in MQ, the initial storage modulus was 85.5 Pa, A= 13.2 and B = 1.1, a critical stress value of $\sigma_C = 5.7$

Statistical analysis

Table 7. Two-sample t-test for calculated critical stress vs. measured critical stress

Data set	N	Mean	StDev	SE Mean
Calculated critical stress	7	5.6	3.0	1.1
Measured critical stress	7	4.6	3.6	1.4

Difference = μ (Calculated critical stress) - μ (Measured critical stress)
Estimate for difference: 1.0
95% CI for difference: (-2.9; 4.9)
t-test of difference = 0 (vs ≠): t-value = 0.6 P-Value = 0.5 DF = 11

In vitro:

Cell culture

Human umbilical vein endothelial cells (HUVEC) were expanded in microvascular endothelial cell growth medium-2 (EBM-2MV, Lonza, Basal, Switzerland) with supplements (Lonza, CC-4147) and penicillin/streptomycin solution (p/s). Human bladder smooth muscle cells (hbSMC) were expanded in smooth muscle cell medium (SMCM, Sciencell, Carlsbad, USA) with growth supplement (SMCGS), fetal bovine serum (FBS),

and p/s. The medium was changed three times per week. Cells were maintained at 37 °C, 5% CO_2.
To prevascularized hydrogels, HUVEC (2.5×10^4 cells/mL) and hbSMC (1×10^4 cells/mL) were mixed with different hydrogels and cultured in 3D in insert rings for 24-well plate (0.4 μm polyester membranes, Costar, NY, USA). Mixed hydrogels were incubated at 37 °C for 1 hour in a humidified incubator containing 5% CO_2 to ensure the solidity of hydrogels. In the end of incubation, EGM-2MV: SMCM (1:1 (v/v)) was added on the lower chamber of the transwell plate (Costar, NY, USA).

Cell mobility
HUVEC ($2.5x10^4$ cells/mL) and hbSMC ($1x10^4$ cells/mL) were mixed with different hydrogels and cultured in inserts (ibidi, Martinsried, Germany). After three days, cell mobility was observed with a time lapse microscope for 50 h (Nikon Diaphot 300 with Hamamatsu C8484-05G CCD Camera, Japan; Okolab 4 well CO_2 stage incubator and Okolab 2D time lapse software, Italy).

Harvesting of 3D construct
HUVEC ($2.5x10^5$ cells/mL) and hbSMC ($1x10^5$ cells/mL) were cultured in PIC. After three days culturing in PIC, cell clusters were collected from cooled liquid hydrogel without damaging them and transferred to RGD 1:10. The volume ratio of PIC and PIC-GRGDS was 1:4 (v/v). Three days after transferring, cell clusters started to sprout (Figure 14).

Immunohistochemistry and immunofluorescent staining
At different time points, samples were collected and either embedded in O.C.T. compound TissueTek (Sakura) and snap frozen in liquid nitrogen, or fixed in paraformaldehyde and embedded in paraffin. Frozen specimen were cut as 5 μm and fixed with methanol for 10 minutes at 21 °C. Paraffin embed specimen were cut as 4 μm. For antigen retrieval, slides were incubated with boiling sodium citrate buffer (10 mM, pH 6) for 10 minutes and cooled down to 21 °C for 1 hour. Non-specific antigens were blocked with 10% normal goat serum (NGS) and 1% bovine serum albumin (BSA) in phosphate-buffered saline (PBS) for 1 hour at 21 °C. In Table 8, the antibodies used are summarized. Primary antibodies were incubated in 1% NGS 1% BSA in PBS for 1 hour at 21 °C. Non-specific binding was washed away with PBS 5 minutes in 3 times. Secondary antibodies conjugated with Alexa fluor probes were incubated in 1% NGS 1% BSA in PBS for 30 minutes at 21 °C. Non-specific binding was washed away with PBS 5 minutes in 3 times. Slides were mounted with Prolong Gold mount medium with DAPI (Invitrogen). Slides were evaluated with fluorescence microscopy (LEICA DC 300F, Germany).
For whole gel staining, hydrogels were washed with PBS 5 minutes in three times. Nuclei were stained with Hoechst 33342 (1:2000, 5 μg/mL, Invitrogen). The whole gel staining was analyzed with confocal laser scanning microscope (Olympus FV1000, Tokyo, Japan).

Table 8. Summary of antibodies

Antibody	**Origin**	**Clone**	**React**	**Stock Concentration**	**Dilution, final concentration**	**Company**
Von Willebrand factor	Rabbit	Polyclonal	Human	3.1 mg/ml	1:400 (7.8 µg/mL)	Dako
CD31	Mouse	JC70A	Human	n. a.	1:100	Dako
α-SMA	Mouse	1A4	Human and mouse	6 mg/ml	1:8000 (0.8 µg/mL)	Sigma
Vimentin	Rabbit	n. a.	Human, mouse, and rat	n. a.	1:400	Abcam
Ki67	Rabbit	SP6	Human	n. a.	1:200	Thermo Scientific
Type 1 collagen	Rabbit	Polyclonal	Bovine	1.0 mg/ml	1:100 (1.0 µg/mL)	Millipore
Fibrin/Fibrinogen	Mouse	MFB-HB	Human and canine	0.5 mg/ml	1:50 (10.0 µg/mL)	Thermo Scientific
Alexa-488	Goat		Mouse		1:200	Invitrogen
Alexa-568	Goat		Rabbit		1:200	Invitrogen
Alexa-488	Donkey		Mouse		1:200	Invitrogen
Alexa-594	Donkey		Rabbit		1:200	Invitrogen

Appendix

Comparing PIC with PIC-GRGDS

The circular dichroism spectra of dilute solutions of PIC in acetonitrile were measured to confirm the β-helical conformation of the polymer. After decoration with GRGDS the orientation of the helix was retained, but at the same concentration it is somewhat diminished in intensity (Figure 21).

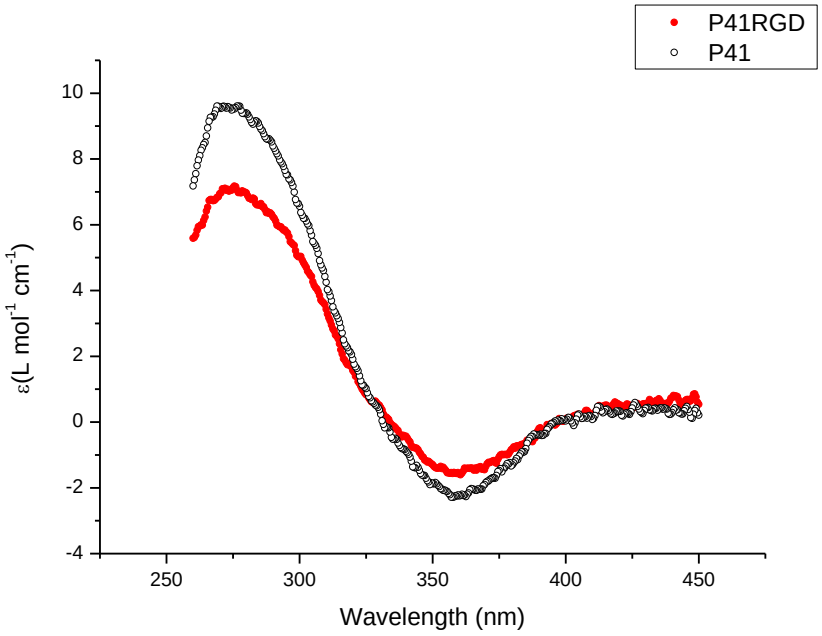

Figure 21. CD spectra of P41 and P41RGD 1 mg/mL in PBS at 22 °C

The infrared spectrum of the PIC samples appears very similar except for a weak azide signal in the region of 2100 cm^{-1}. This peak only becomes pronounced in the highest loading of 1 in 25 azides or rather one azide every 3 nm. It is clear however that after conjugation with BCNGRGDS this broad peak disappears completely indicating that the azides were completely consumed (Figure 22)**.**

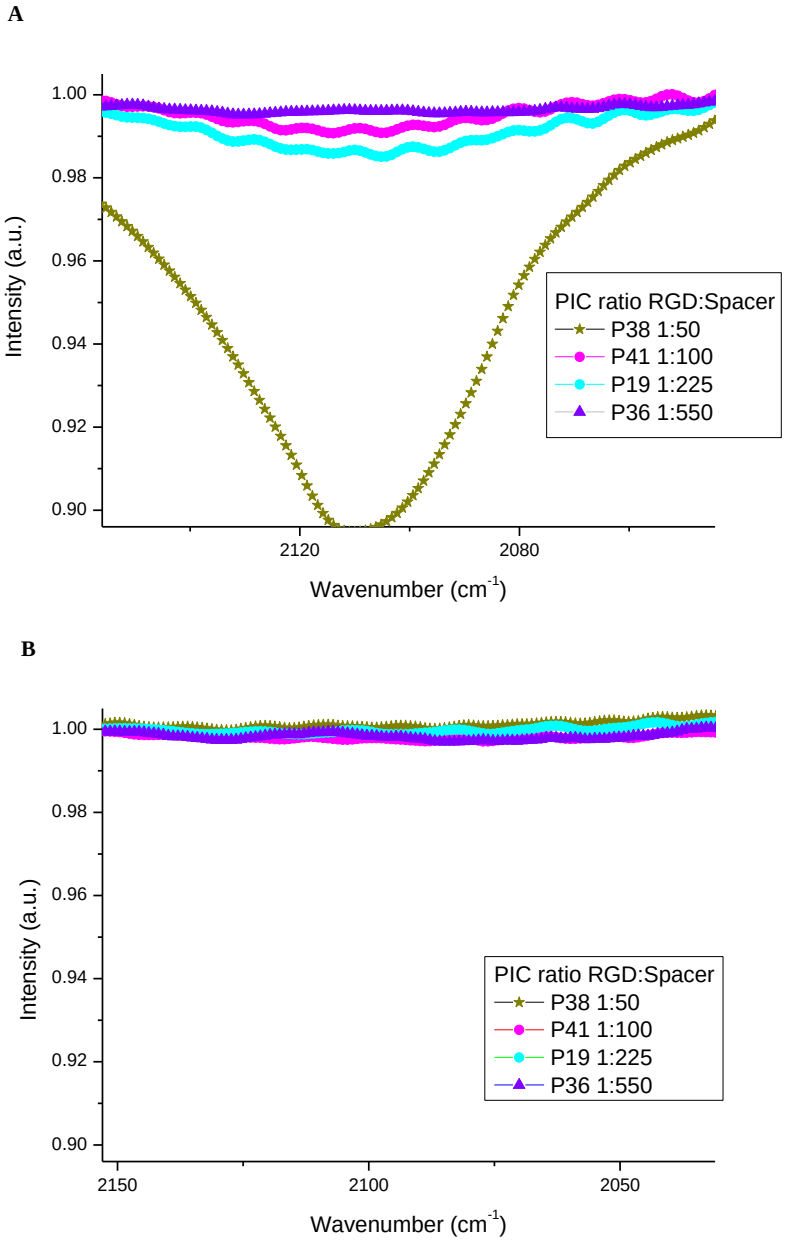

Figure 22. a) IR spectrum before and b) after conjugation BCN-GRGDS. Notice the disappearance of the azide peak at 2100 cm^{-1}.

Linear rheology

To investigate the effect of RGD conjugation on the PIC, linear rheology before and after conjugation was performed on a set of PIC with known sample history (see, Figure 23). The measurements in the linear response regime were conducted at 2 % strain at a frequency of 1 Hz. Temperature sweeps were recorded at a heating or cooling rate of 2 °C/min.

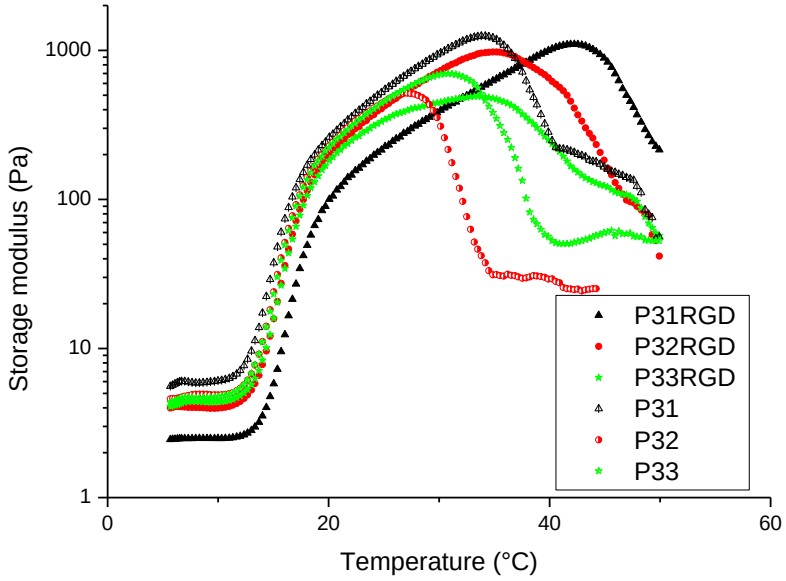

Figure 23. Storage modulus as a function of temperature comparing PIC before and after GRGDS functionalization 1.6 mg/mL in PBS (1 Hz, 2 % strain, 2 deg/min) same sample history.

To mimic animal experiments, the dissolved samples were placed on ice, sucked up via syringe through a needle (G25/30) and ejected on a 5 °C peltier plate. The sample temperature was raised to 37 °C rapidly and time sweep performed 15 min at 37 °C under 1 Hz, 2 % strain. For subcutaneous injection a cooled solution of PIC needed to be passed through a syringe. Interestingly the material did recover after 15 min incubation at 5 °C, before running a temperature sweep from 5 – 37 °C (Figure 24).

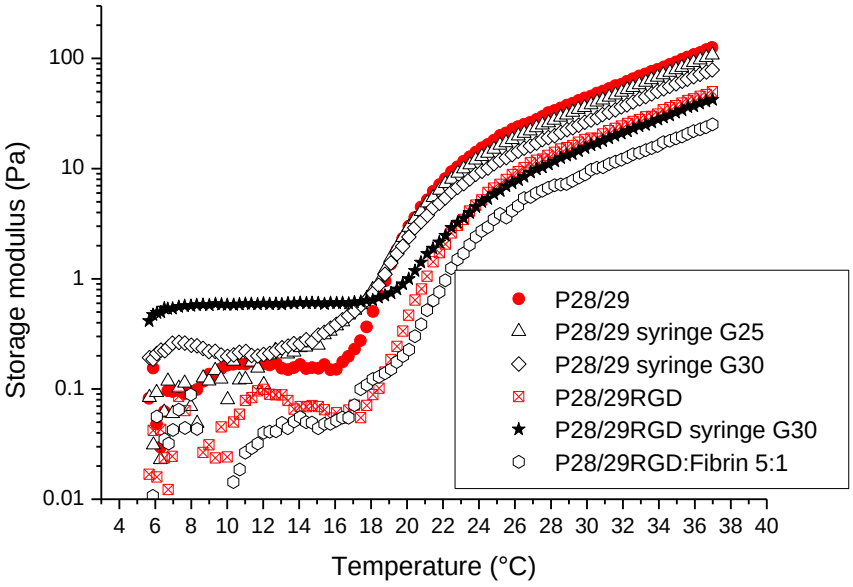

Figure 24. Storage modulus as a function of temperature comparing different sample history effects at 1.6 mg/mL (1 Hz, 2 % strain, 2 deg/min)

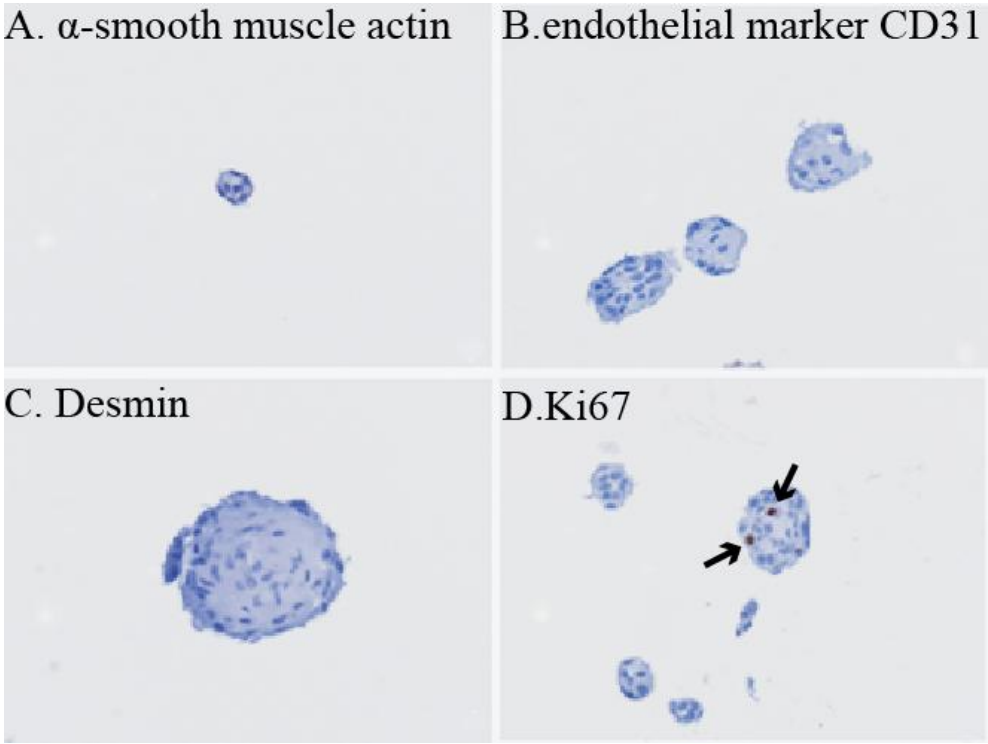

Figure 25. Immunohistochemistry of clusters for (a) α-smooth muscle actin, (b) endothelial marker CD31, (c) desmin, (d) Ki67 after 28 days. The nuclei of the cells were stained by haematoxylin appear in blue. Markers were stained with diaminobenzidine (DAB) and appear in brown. The clusters were both CD 31 and desmin negative (b and c). Weak positive signal of α-smooth muscle actin was observed within the cluster (a). The arrow points to the Ki67 positive cells (brown) present in one cluster (d). Magnification 40x.

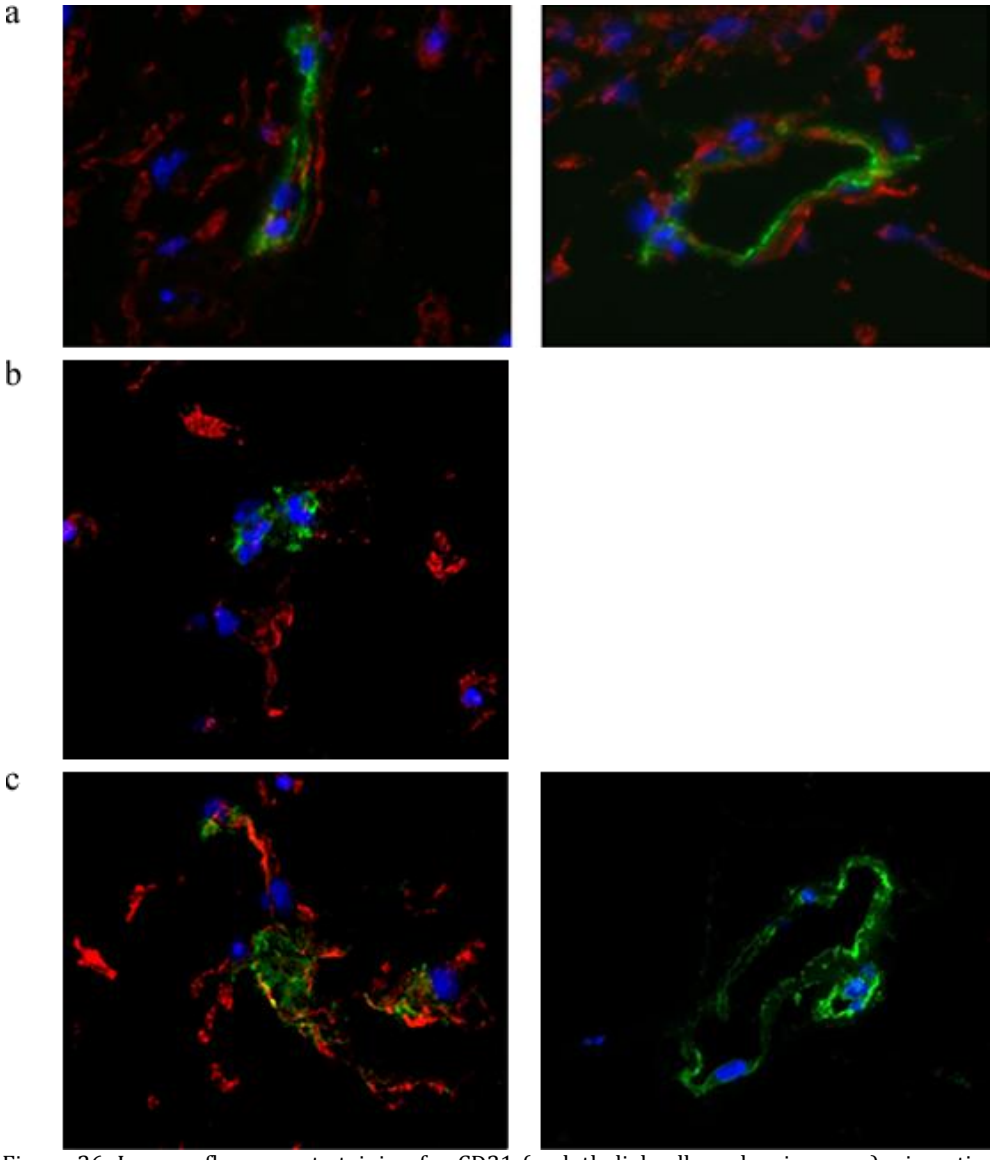

Figure 26. Immunofluorescent staining for CD31 (endothelial cell marker in green), vimentin (mesenchymal cell marker in red) and nuclei (blue) of (a) Fibrin:P3 1:5, (b) Fibrin:P28/29RGD 1:5, (c) Fibrin control (10 mg/mL) after 21 days. Images were taken with a 40x magnification.

Light microscopy:

The vasculogenesis of constructs were followed with light microscopy (LEICA, Germany) during cell culturing.

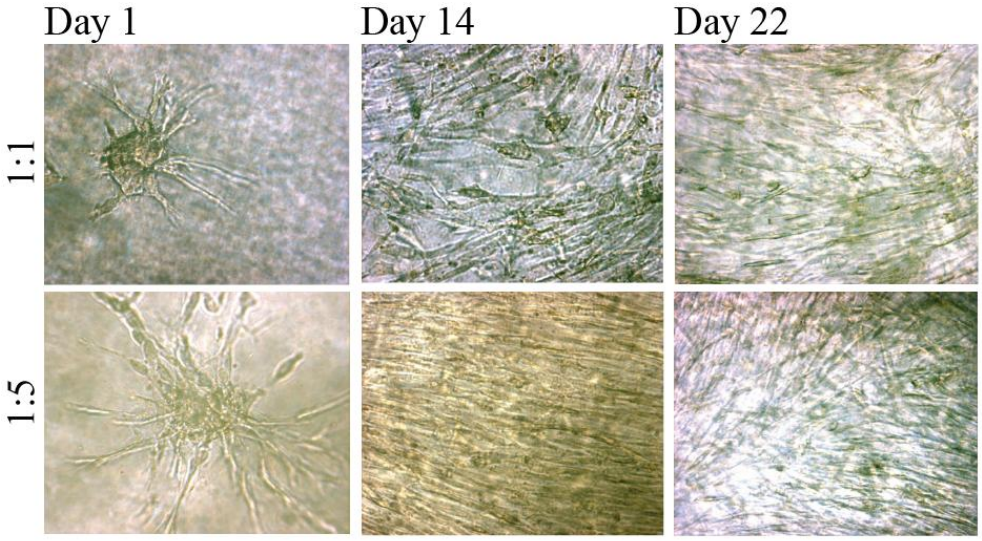

Figure 27. Light microscopy images (a) P1:fibrin 1:1 and (b) P1:fibrin 1:5 . Magnification 40x.

In the fibrin:PIC mixtures, branch formation was observed as early as day 1 and vessel-like structures were observed at day 14 and day 22. At day 14, sprouts increased and connected with each other in mixtures is comparable with pure fibrinogen gels (Figure 10-12).

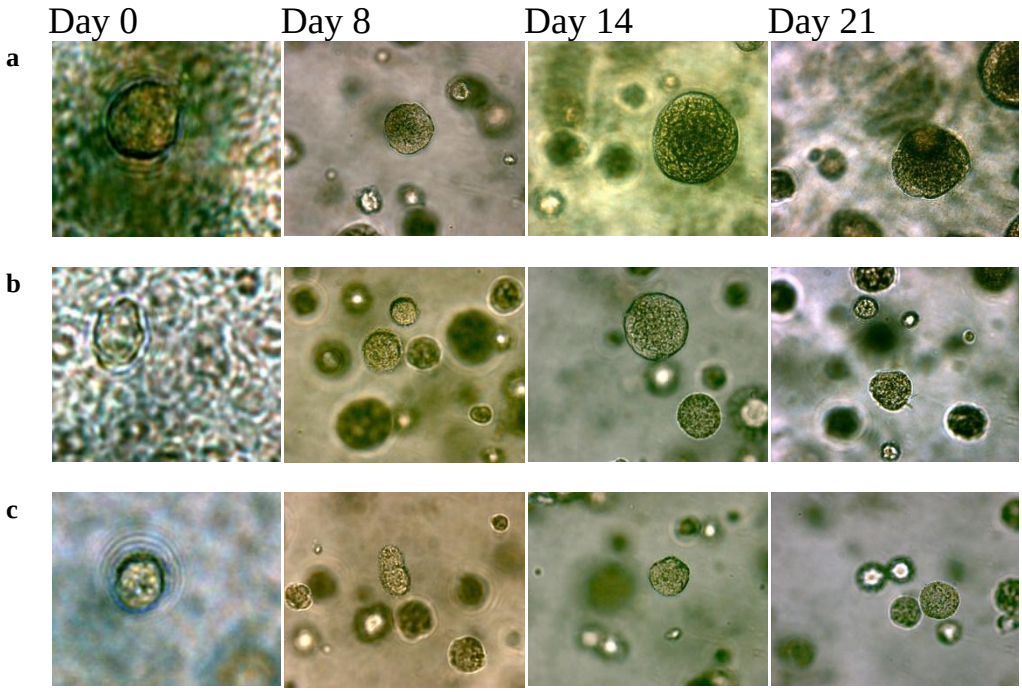

Figure 28. Light microscopy (a) P36 plus free GRGDS 2mg/mL, (b) P1 plus free GRGDS 2 mg/mL, (c) P1 *without* GRGDS Magnification 40x.

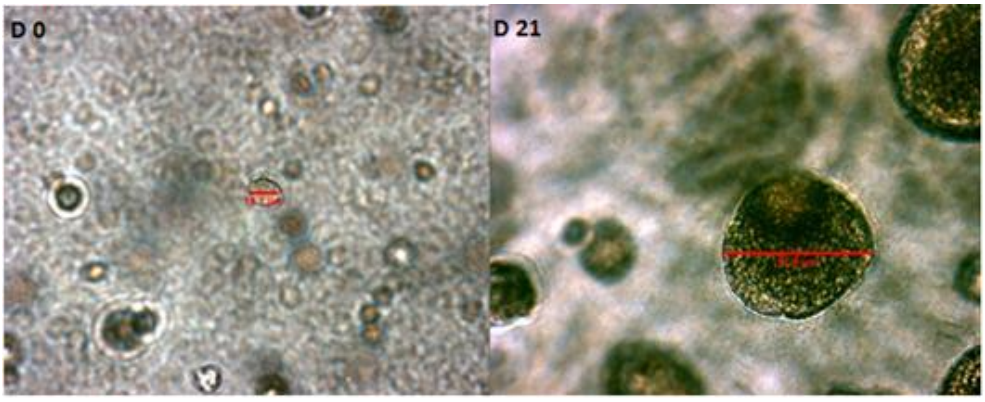

Figure 29. Light microscopy of clusters in P1. the diameter of one single individual cell at day 0 is 18.1 µm and the diameter of one cluster at day 21 is about 93.8 µm. Magnification 40x.

In Vivo:

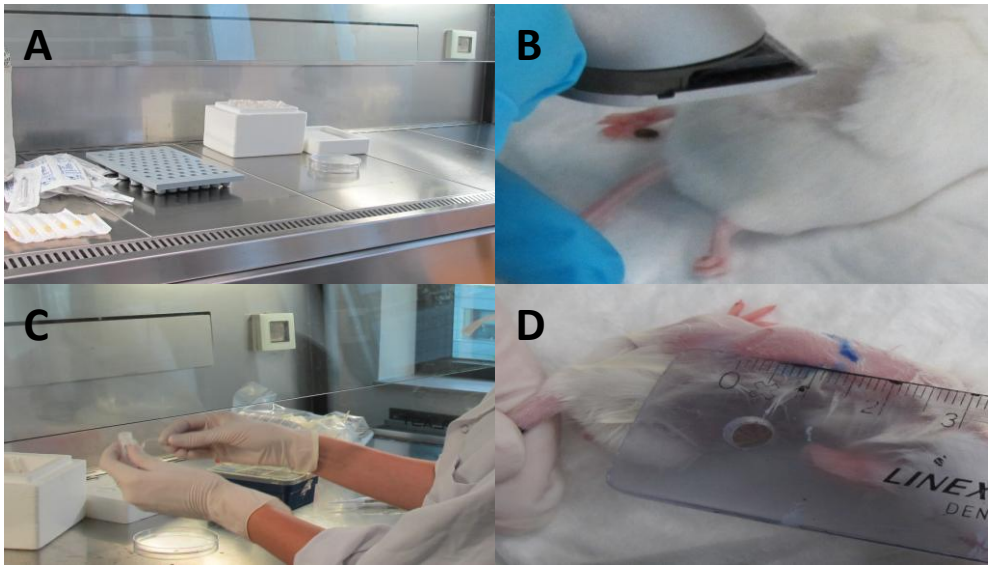

Figure 30. Injection procedure. Aliquots of the PIC or PIC-fibrinogen suspension were placed on ice for a minimum of 30 minutes (a) Prior to subcutaneous injections the implant area was shaved, (b) and disinfected with 70% EtOH. The syringes used for injection were prepared under semi-sterile conditions, (c) 100 µL of the PIC or PIC-fibrin was directly injected subcutaneously, either on the left or right side of the back of the mouse. Implant areas were marked with a waterproof marker, (d) Subsequently, mice were placed in a heating chamber at 37 °C for a minimum of 10 minutes to ameliorate hydrogel solidification.

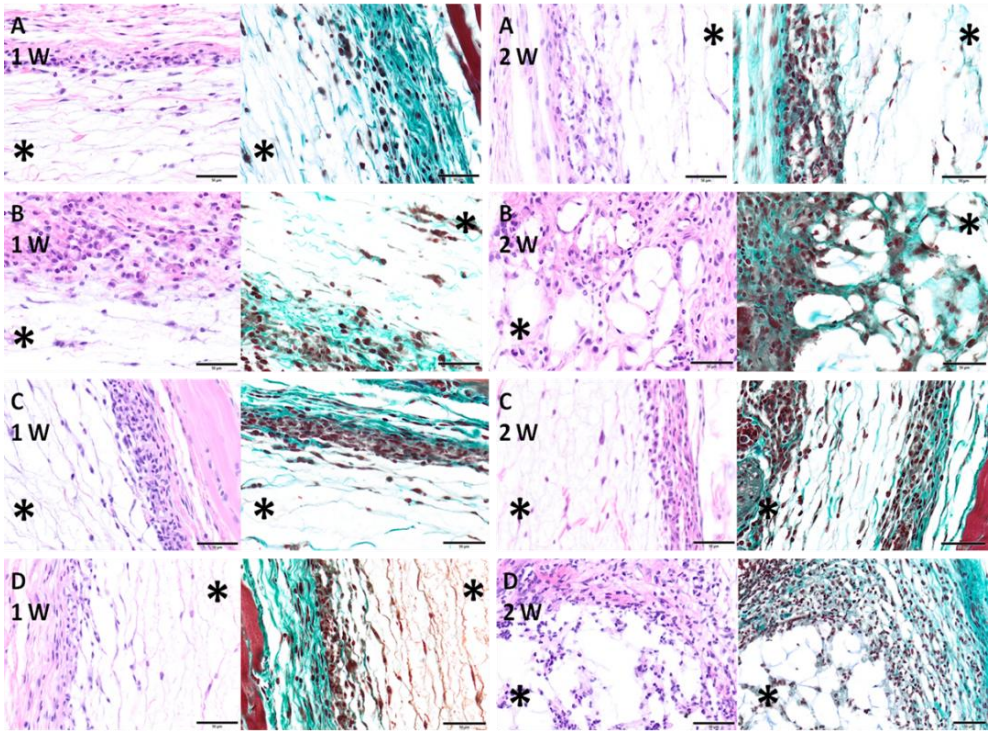

Figure 31. Microscopic images (magnification 20x) of the HE and Masson staining showing the rim of the P3 construct (a) P28/29RGD construct, (b) Fibrin:P3 construct, (c) and the fibrin:P28/29RGD construct, (d) one and two weeks after injection. The * indicates the area of the construct.

Table 9. *Overview of the semi-quantitative scoring of the cellular response to the constructs. The scores assigned to the PIC constructs are based on one sample (n=1).*

Samples:	**A**	**B**	**C**	**D**	**E**	**F**	**G**	**H**	**I**	**J**	**K**
P3	*1*	1.5	2	1.5	0	2	0	2	0	1.75	2
	2	3	2.5	2	1	3	1	3	1	3	3
P28/29RGD	*1*	2.5	2.5	1	1	2.5	0	2.5	0	2	2
	2	4	4	2.5	1.5	3.5	1	3	0	4	4
Fibrin-**P3**[1:5]	*1*	2	1	0.5	0.5	2	0	2	0	1.75	1
	2	2	2	0.5	0.5	2	0	2	0	1.75	1
Fibrin-**P28/29RGD** [1:5]	*1*	2.5	2.5	0.5	0	2	0	2	0	2	1
	2	4	4	2	2.5	4	1	2.5	0	4	4

Titles:
A) Evaluation point (weeks)
B) Cell infiltration
C)Cells in scaffold centre
D) Granulocytes
E) Lymphocytes
F) Macrophages
G) Giant cells
H) Fibroblasts
I) Vasc. Structures
J) ECM product
K) Incorporation in surrounding tissue

Scoring:
0=not present [-]
1=sporadically present [+/- -]
2=a little bit present [+/-]
3=present [+]
4=clearly present [++]
5=abundantly present [+++]

References

1 Kouwer, P. H. *et al.* Responsive biomimetic networks from polyisocyanopeptide hydrogels. *Nature*, **493**, 651-655, (2013).

2 Adelöw, C. *et al.* The effect of enzymatically degradable poly(ethylene glycol) hydrogels on smooth muscle cell phenotype. *Biomaterials*, **29**, 314-326, (2008).

3 Seliktar, D. *et al.* MMP-2 sensitive, VEGF-bearing bioactive hydrogels for promotion of vascular healing. *Journal of Biomedical Materials Research Part A*, **68A**, 704-716, (2004).

4 DeLong, S. A., Moon, J. J. & West, J. L. Covalently immobilized gradients of bFGF on hydrogel scaffolds for directed cell migration. *Biomaterials*, **26**, 3227-3234, (2005).

5 Porter, A. M., Klinge, C. M. & Gobin, A. S. Biomimetic Hydrogels with VEGF Induce Angiogenic Processes in Both hUVEC and hMEC. *Biomacromolecules*, **12**, 242-246, (2011).

6 Liu, Y. *et al.* Impact of Endothelial Cells on 3D Cultured Smooth Muscle Cells in a Biomimetic Hydrogel. *ACS Applied Materials & Interfaces*, **4**, 1378-1387, (2012).

7 Aizawa, Y. & Shoichet, M. S. The role of endothelial cells in the retinal stem and progenitor cell niche within a 3D engineered hydrogel matrix. *Biomaterials*, **33**, 5198-5205, (2012).

8 Khetan, S. *et al.* Degradation-mediated cellular traction directs stem cell fate in covalently crosslinked three-dimensional hydrogels. *Nat Mater*, **12**, 458-465, (2013).

9 Leslie-Barbick, J. E., Moon, J. J. & West, J. L. Covalently-Immobilized Vascular Endothelial Growth Factor Promotes Endothelial Cell Tubulogenesis in Poly(ethylene glycol) Diacrylate Hydrogels. *Journal of Biomaterials Science, Polymer Edition*, **20**, 1763-1779, (2009).

10 Dikovsky, D., Bianco-Peled, H. & Seliktar, D. The effect of structural alterations of PEG-fibrinogen hydrogel scaffolds on 3-D cellular morphology and cellular migration. *Biomaterials*, **27**, 1496-1506, (2006).

11 Ekaputra, A. K. *et al.* The three-dimensional vascularization of growth factor-releasing hybrid scaffold of poly (ε-caprolactone)/collagen fibers and hyaluronic acid hydrogel. *Biomaterials*, **32**, 8108-8117, (2011).

12 Rouwkema, J., Rivron, N. C. & van Blitterswijk, C. A. Vascularization in tissue engineering. *Trends in Biotechnology*, **26**, 434-441, (2008).

13 Saik, J. E. *et al.* Covalently immobilized platelet-derived growth factor-BB promotes angiogenesis in biomimetic poly(ethylene glycol) hydrogels. *Acta Biomaterialia*, **7**, 133-143, (2011).

14 Lutolf, M. P. & Hubbell, J. A. Synthetic biomaterials as instructive extracellular microenvironments for morphogenesis in tissue engineering. *Nat Biotechnol*, **23**, 47-55, (2005).

15 Griffith, L. G. & Naughton, G. Tissue Engineering--Current Challenges and Expanding Opportunities. *Science*, **295**, 1009-1014, (2002).

16 Mansbridge, J. Skin tissue engineering. *Journal of Biomaterials Science, Polymer Edition*, **19**, 955-968, (2008).
17 Temenoff, J. S. & Mikos, A. G. Review: tissue engineering for regeneration of articular cartilage. *Biomaterials*, **21**, 431-440, (2000).
18 Marler, J. J. *et al.* Transplantation of cells in matrices for tissue regeneration. *Advanced Drug Delivery Reviews*, **33**, 165-182, (1998).
19 Risau, W. & Flamme, I. Vasculogenesis. *Annual Review of Cell and Developmental Biology*, **11**, 73-91, (1995).
20 Trappmann, B. *et al.* Extracellular-matrix tethering regulates stem-cell fate. *Nat Mater*, **11**, 642-649, (2012).
21 Young, J. L. & Engler, A. J. Hydrogels with time-dependent material properties enhance cardiomyocyte differentiation in vitro. *Biomaterials*, **32**, 1002-1009, (2011).
22 Shroff, K. *et al.* Fibronectin-mimetic peptide-amphiphile nanofiber gels support increased cell adhesion and promote ECM production. *Soft Matter*, **6**, 5064-5072, (2010).
23 Levental, I., Georges, P. C. & Janmey, P. A. Soft biological materials and their impact on cell function. *Soft Matter*, **3**, 299-306, (2007).
24 Mann, B. K. *et al.* Smooth muscle cell growth in photopolymerized hydrogels with cell adhesive and proteolytically degradable domains: synthetic ECM analogs for tissue engineering. *Biomaterials*, **22**, 3045-3051, (2001).
25 Horák, D. *et al.* Pentapeptide-modified poly(N,N-diethylacrylamide) hydrogel scaffolds for tissue engineering. *Journal of Biomedical Materials Research Part B: Applied Biomaterials*, **98B**, 54-67, (2011).
26 Sieminski, A. L. *et al.* Primary sequence of ionic self-assembling peptide gels affects endothelial cell adhesion and capillary morphogenesis. *Journal of Biomedical Materials Research Part A*, **87A**, 494-504, (2008).
27 Storm, C. *et al.* Nonlinear elasticity in biological gels. *Nature*, **435**, 191-194, (2005).
28 Winer, J. P., Oake, S. & Janmey, P. A. Non-Linear Elasticity of Extracellular Matrices Enables Contractile Cells to Communicate Local Position and Orientation. *PLoS ONE*, **4**, e6382, (2009).
29 Head, D. A., Levine, A. J. & MacKintosh, F. C. Deformation of Cross-Linked Semiflexible Polymer Networks. *Physical Review Letters*, **91**, 108102, (2003).
30 Broedersz, C. P. & MacKintosh, F. C. Molecular motors stiffen non-affine semiflexible polymer networks. *Soft Matter*, **7**, 3186-3191, (2011).
31 Hansen, K. C. *et al.* An In-solution Ultrasonication-assisted Digestion Method for Improved Extracellular Matrix Proteome Coverage. *Molecular & Cellular Proteomics*, **8**, 1648-1657, (2009).
32 Ratliff, B. B. *et al. Endothelial progenitors encapsulated in bioartificial niches are insulated from systemic cytotoxicity and are angiogenesis competent*. Vol. 299 (2010).
33 Hanjaya-Putra, D. *et al.* Vascular endothelial growth factor and substrate mechanics regulate in vitro tubulogenesis of endothelial progenitor cells. *Journal of Cellular and Molecular Medicine*, **14**, 2436-2447, (2010).

34 Sun, H. *et al.* In vitro and in vivo effects of rat kidney vascular endothelial cells on osteogenesis of rat bone marrow mesenchymal stem cells growing on polylactide-glycoli acid (PLGA) scaffolds. *BioMedical Engineering OnLine*, **6**, 41-41, (2007).
35 Fu, K. *et al.* Visual Evidence of Acidic Environment Within Degrading Poly(lactic-co-glycolic acid) (PLGA) Microspheres. *Pharm Res*, **17**, 100-106, (2000).
36 Boland, E. D. *et al.* Utilizing acid pretreatment and electrospinning to improve biocompatibility of poly(glycolic acid) for tissue engineering. *Journal of Biomedical Materials Research Part B: Applied Biomaterials*, **71B**, 144-152, (2004).
37 Leslie-Barbick, J. E. *et al.* The promotion of microvasculature formation in poly(ethylene glycol) diacrylate hydrogels by an immobilized VEGF-mimetic peptide. *Biomaterials*, **32**, 5782-5789, (2011).
38 Kraehenbuehl, T. P. *et al.* Cell-responsive hydrogel for encapsulation of vascular cells. *Biomaterials*, **30**, 4318-4324, (2009).
39 Mandal, S. *et al.* Therapeutic nanoworms: towards novel synthetic dendritic cells for immunotherapy. *Chemical Science*, **4**, 4168-4174, (2013).
40 Mager, M. D., LaPointe, V. & Stevens, M. M. Exploring and exploiting chemistry at the cell surface. *Nat Chem*, **3**, 582-589, (2011).
41 Wang, X. & Ha, T. Defining Single Molecular Forces Required to Activate Integrin and Notch Signaling. *Science*, **340**, 991-994, (2013).
42 Ferreira, L. S. *et al.* Bioactive hydrogel scaffolds for controllable vascular differentiation of human embryonic stem cells. *Biomaterials*, **28**, 2706-2717, (2007).
43 Hersel, U., Dahmen, C. & Kessler, H. RGD modified polymers: biomaterials for stimulated cell adhesion and beyond. *Biomaterials*, **24**, 4385-4415, (2003).
44 Mason, M. N. & Mahoney, M. J. A novel composite construct increases the vascularization potential of PEG hydrogels through the incorporation of large fibrin ribbons. *Journal of Biomedical Materials Research Part A*, **95A**, 283-293, (2010).
45 Jaspers, M. *et al.* Ultra-responsive soft matter from strain-stiffening hydrogels. *Nat Commun*, **5**, (2014).
46 Zaman, M. H. *et al.* Migration of tumor cells in 3D matrices is governed by matrix stiffness along with cell-matrix adhesion and proteolysis. *Proceedings of the National Academy of Sciences*, **103**, 10889-10894, (2006).
47 Trojan, L. *et al.* Expression of Different Vascular Endothelial Markers in Prostate Cancer and BPH Tissue: An Immunohistochemical and Clinical Evaluation. *Anticancer Research*, **24**, 1651-1656, (2004).
48 Skardal, A. *et al.* The generation of 3-D tissue models based on hyaluronan hydrogel-coated microcarriers within a rotating wall vessel bioreactor. *Biomaterials*, **31**, 8426-8435, (2010).
49 Jiang, B. *et al.* Fibrin-Loaded Porous Poly(Ethylene Glycol) Hydrogels as Scaffold Materials for Vascularized Tissue Formation. *Tissue Engineering Part A*, **19**, 224-234, (2012).

Chapter 7 : Epilogue

Abstract
Conclusions based on the individual chapters of the thesis will be presented separately. Based on these conclusions, suggestions for future projects, and ideas on how to overcome certain shortcomings will be provided along with some preliminary results. Finally the research questions from chapter 1 will be answered.

The aim of this thesis was to explore the possible biomedical applications of polyisocyanopeptide oligoethylene glycol. The biomedical applications investigated were the material in its gelled state as an artificial ECM and in its diluted state as a therapeutic carrier. It is fair to conclude that PIC is extremely suitable for these applications.

Over the course of this research it was sometimes difficult to understand why different batches of polymers resulted in vastly different hydrogels (Storage moduli and sol-gel temperatures). The importance of monomer purity cannot be stressed enough as observed in Chapter 3 with constant catalyst ratios of 1:10,000 and experimental procedure a broad range of molecular weights were obtained. Even small differences in purity of the triethylene glycol monomers affected the polymerisation kinetics, as the average molecular weight achievable utilizing the monomer with an optical rotation of -0.4° was 466 kg/mol compared to 652 kg/mol with a monomer with an optical rotation of -0.3°. Therefore monomer purity is an important key in reproducibly obtaining PIC with the same average molecular weight. One aspect of polymer characterization that was not discussed in great detail was the dispersity (*Đ*) of polyisocyanides. In general the *Đ* values of polymers are obtained from size exclusion chromatography (SEC). The SEC of oligoethylene glycol

polyisocyanides with THF as solvent is not ideal, a better solvent system would be dimethylformamide (DMF) with lithiumchloride, but as this solvent system was not available at the Radboud University alternative methods for determining molecular weight and *Đ* had to be used. It was possible to derive the *Đ* values from the lengths measured on AFM height images. The weighted average length (L_w) and the number average lengths (L_n) can be divided to obtain the *Đ*, under the assumption that the L_w is the same as the weighted average molecular weight and the L_n is the same as the number average molecular weight since it is known that for polyisocyanides length directly correlates to its molecular weight [1]. The average *Đ* obtained using a 1:10,000 catalyst to monomer ratio was 1.5±0.2 (Table 1).

Table 1. Polyisocyanide length and corresponding dispersity index values.

Sample	**Spacer monomer**	**Weighted average length L_w (nm)**	**Number average length L_n (nm)**	***Đ*** **($\frac{L_w}{L_n}$)**
P28	triethylene glycol	296.2	210.0	1.4
P29	triethylene glycol	362.9	221.7	1.6
P32	triethylene glycol	1250.8	816.9	1.5
P54	tetra ethylene glycol	320.9	231.8	1.4
P46	tetra ethylene glycol	610.5	380.3	1.6
P47	tetra ethylene glycol	519.2	415.8	1.2

It was clear that the measurement of the molecular weight of polyisocyanides via non standard techniques such as AFM and viscometry compared very well to SEC in DMF with lithiumchloride, performed at the Stellenbosch University. In the future it should be possible to use field flow fractionation combined with a multi angle laser scattering detector to determine the Mark Houwik parameters of the oligoethylene glycol functional

polyisocyanides. Using a fraction collector attached to the field flow fractionation instrumentation it should be possible to separate long (>1 μm) polymers from the shorter polymers, to enable experiments requiring low signal to noise ratio such as reptation of fluorescently labelled PIC.

In Chapter 4 it became clear that crosslinking was far more complicated than initially expected , the working hypothesis was that intra-bundle crosslinking did not result in increased overall stiffness of the hydrogel as it disrupted the overall persistence length of the bundle itself. Therefore in the future, inter-bundle crosslinking should be forced by crosslinking in the gelled state, with large (> 500 nm) macromolecules that contain multiple crosslinking sites, using crosslinking reactions with high efficiency and low concentrations of the crosslinker itself e.g. eight-arm star vinyl sulfone polyethylene glycol stars to polyisocyanides appended with either thiols or amines.

The use of tetraethylene glycol appended polyisocyanides as stealthy therapeutic devices or synthetic dendritic cells resulted in surprisingly high activity at extremely low concentrations. The most inspiring conclusion from Chapter 5 was showing just how important shape, stiffness and multivalency are in activating cellular activity at extremely low concentrations of the active compound. The multivalent polymer worm effectively formed an artificial synapse with the T-cells surface, inducing the prolonged targeted attack of model pathogen invaders. In the future it would be possible to decorate the synthetic dendritic cell with **combinations** of not only antibodies but even larger cell instructive proteins such as the major histocompatibility complex to mimic natural dendritic cells more closely, enabling targeted immunization of e.g. patient specific cancers.

The stealthy properties of PIC can be further explored to cross the most sought after therapeutic barrier of all, **the blood brain barrier**. In Chapter 5, the use of worm-like PIC as efficient therapeutic delivery vehicles was discussed as it shows increased circulation times and higher activity due to multivalency when compared to spherical carriers. Crossing the blood brain barrier remains a difficult endeavour for current therapeutic strategies as the blood brain barrier is extremely efficient at "protecting" the brain [2]. Serendipitously in a biodistribution study Dr Lambeck observed that PIC labelled with indium showed up in brain tissue (Figure 1).

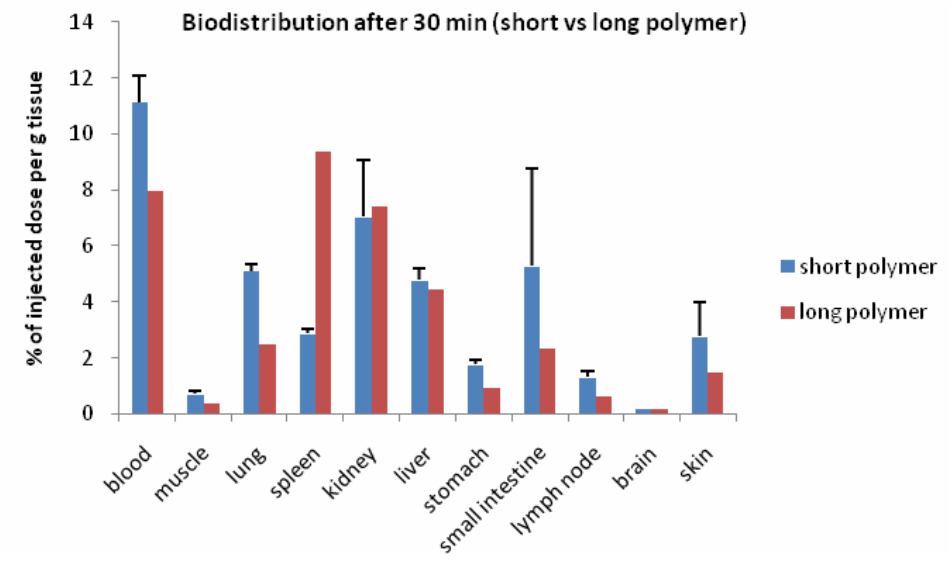

Figure 1. Biodistribution of ^{111}Indium labelled polyisocyanide short = 95 nm and long = 518 nm (unpublished work)

Preliminary experiments beyond the scope of this thesis were used to investigate if this would also be possible in a controlled blood brain barrier experiment as illustrated in Figure 2.

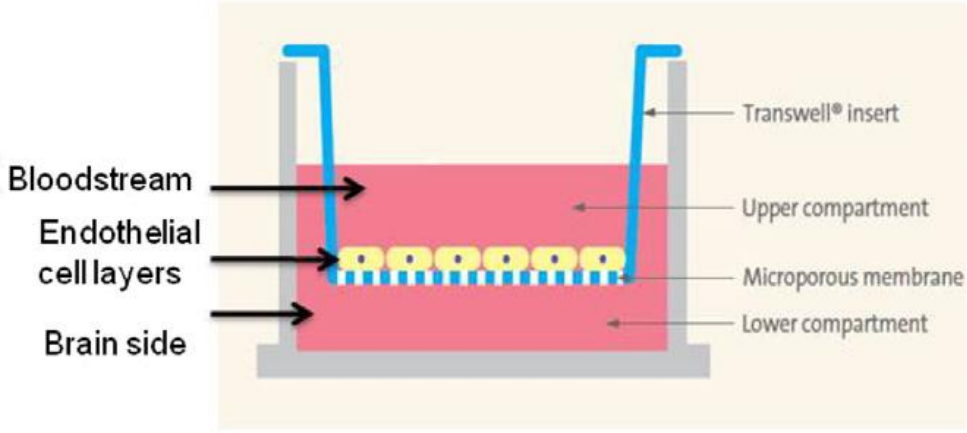

Figure 2. Schematic of the in vitro blood–brain barrier model

In this preliminary experiments two PICs with different lengths were prepared and coated with a fluorescent dye (Tokyo Green). The cell biology experiments were performed by Dr Stojanov [3]. The short (86 nm) PIC crossed the membrane more efficiently when compared to the long (208 nm) PIC (Figure 3).

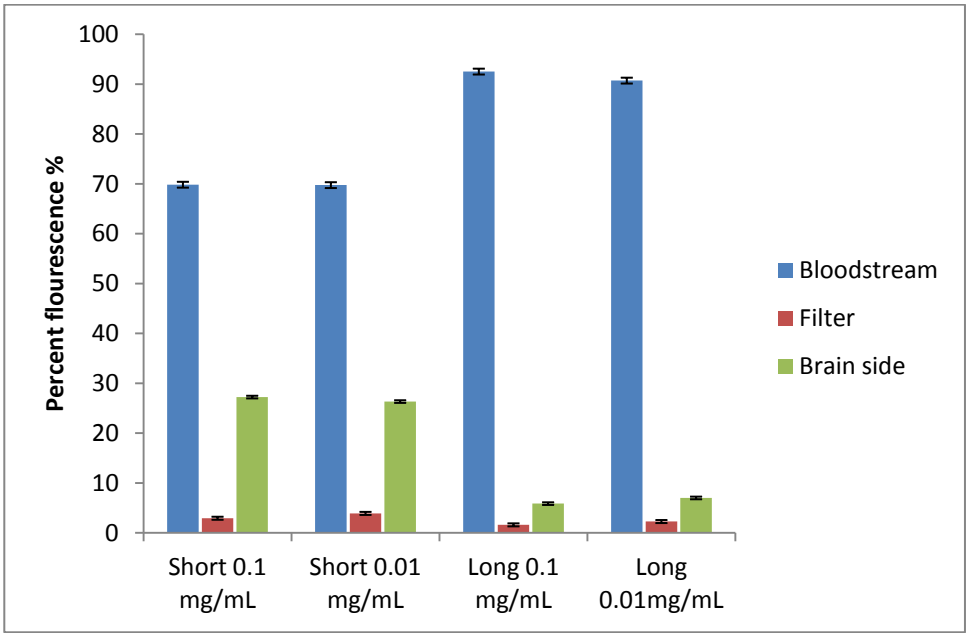

Figure 3. Direct comparisons of effects of polymer length and concentration on the percentages of fluorescence counts found in the different compartments of the experiment. Short = 86 nm and Long 208 nm based on size measurements via Nanosight.

In the future these experiments should be repeated on a range of polymer lengths, but it does seem very promising as the values obtained in these first experiments already match those observed for the spherical polymersome counterparts [3].

In Chapter 6 Tissue mimetic materials for vasculogenesis were made and the following essential parameters defined: the stiffness of the hydrogel should be between 10-300 Pa, cell adhesion peptides should be present at an average spacing of 1 in 10 nm, with a molar concentration of 63.3 µM and as the rate of vasculogenesis is affected by the stiffness of the polymer fibre through the molecular weight, the molecular weight should be between 425-516 kg/mol. Tissue mimetic materials are expected to mimic

extremely complex and crowded environments as is beautifully illustrated in the work by Goodsell *et al* (Figure 4). It should be simple to introduce larger biomolecules such as antibodies (Chapter 5), growth factors (GF) and enzymes as those utilized in Chapter 5&6.

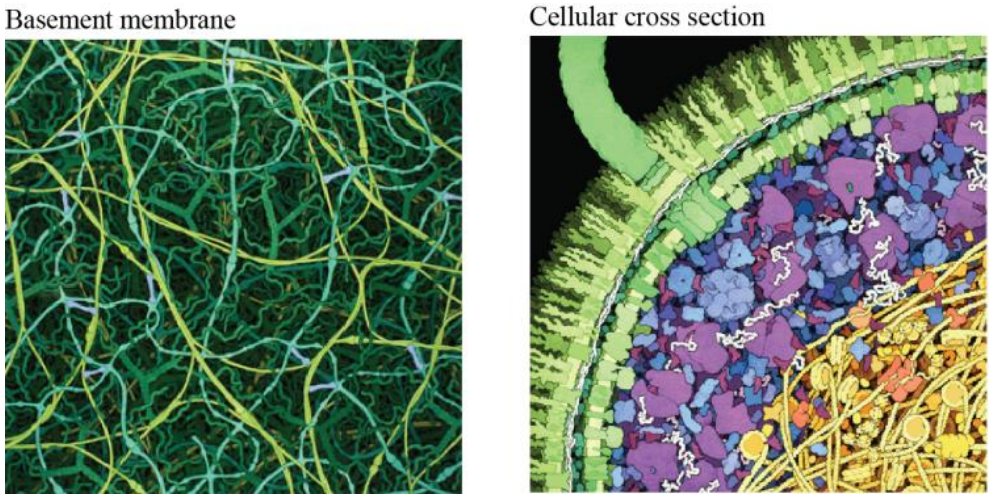

Figure 4. Cellular complexity and crowding form an integral part of biological platforms, as seen in these illustrations of basement membrane and cellular cross section by Goodsell [12]. The basement membrane acts as a support between tissues filled with fibrillar proteins and larger biomolecules.

Vascularisation by the introduction of growth factors: In Chapter 6, vasculogenesis was discussed and investigated in tissue-mimetic polyisocyanide. In the formation of vasculature, both vasculogenesis and angiogenesis occur. Angiogenesis relates to the formation of new capillaries from pre-existing vessels to further expand and complete the vasculature [13-15]. It was speculated in the conclusion of Chapter 6 that to truly mimic tissue, the combinations of different cell adhesion ligands and the presence of additional cellular signals must be

incorporated. Vascular endothelial growth factor (VEGF) and basic fibroblast growth factor (bFGF) are the most important growth factors for vasculogenesis and angiogenesis [16]. In the state of the art in synthetic tissue mimetic materials containing VEGF and bFGF have been used as angiogenic growth factors, resulting in an improved environment for endothelial cells leading to vessel formation [17-22]. The addition of either VEGF or bFGF to tissue mimetic materials resulted in increased blood vessels density [23-24]. Asahara *et al* reported that for the creation of well-developed mature vessels in an ischemic hind limb model **both** VEGF and FGF are required [25]. The way growth factors are immobilized onto the tissue mimetic material may either be non-covalently linked [26-27], covalently linked [17,28-29] or encased in the hydrogel [30]. Controlled slow growth factor release can be desirable because this creates a gradient that stimulates endothelial cell migration towards the implants [31]. Preliminary experiments beyond the scope of this thesis showed that the SPAAC bioconjugation strategy utilized in Chapter 6 could easily be adapted to covalently attach growth factors decorated with bicyclononyne (BCN-NHS was non-specifically coupled to the lysine residues present on the growth factor, see Figure 5). Linde Zhou performed the initial cell culture experiments, the results of which will be discussed below.

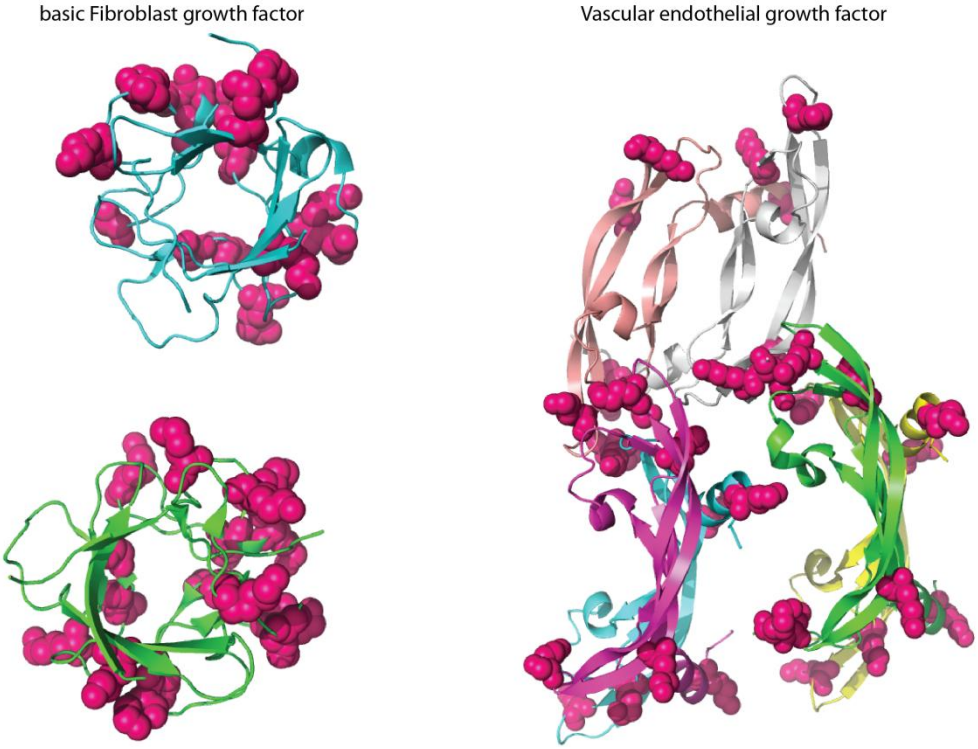

Figure 5. Structures based on the protein data bank files for VEGF [32] and bFGF [33] with lysine residues coloured pink rendered in Pymol.

After conjugation with bicyclononyne the growth factors did show a slight loss of activity, in the future this might be mitigated by using a lower molar ratio of BCN-NHS to growth factor (Figure 6).

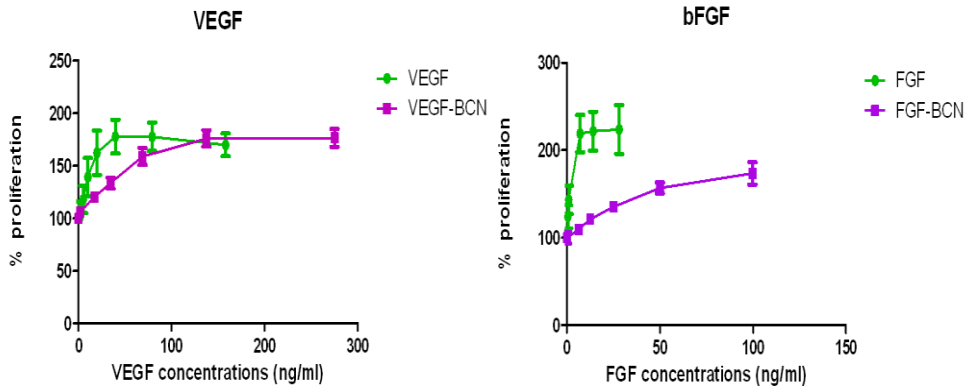

Figure 6. Biological activity after non-specific conjugation with BCN-NHS to lysine residues present on the growth factors (molar ratio 10:1). Proliferation with HUVEC cells at day 3. The proliferation without added growth factors was set to 100%. Results are mean ± SD for 3 separate experiments.

Polyisocyanide (**P28/29**) containing 1 in a 100 nm GRGDS, but still contain *ca* 20 % free azides were covalently decorated with bicyclononyne functional VEGF, bFGF and both VEGF-bFGF (Table 3).

Table 2. Concentration of PIC to GRGDS and growth factors used to study vasculogenesis.

Sample	**PIC concentration (mg/mL)**	**GRGDS concentration (nmol/mL)**	**bFGF concentration (ng/mL)**	**VEGF concentration (ng/mL)**
PIC_RGD	2.5	79	0	0
PIC_RGD_FGF	2.5	78	100	0
PIC_RGD_VEGF	2.5	77	0	200
PIC_RGD_FGF_VEGF	2.5	76	100	200
PIC_RGD free VEGF and FGF	2.5	77	10	100

The viability and metabolic activity of the HUVECs and SMCs after incorporation in different hydrogels were investigated by a proliferation assay. Cell viability was determined with CellTiter-Glo luminescent viability assay according to the manufacturer's instructions. To measure cell viability of cells encapsulated in the PIC hydrogel, the hydrogels were collected and placed at 0 °C to induce gel-solution transition. The now liquid hydrogels and cells were then transferred from the inserts into 1 mL tubes, equal volume CellTiter-Glo reagent was added into the tubes and allow to react for 10 min. After reaction, the solution was transferred into 96-wel plate and analyzed by fluorescence microscopy. After 4 days, a significant increase in proliferation was present in PIC_RGD with growth factors compared to the PIC_RGD hydrogel on its own. At day 21, this difference was more prominent. Cells mixed in PIC_RGD_VEGF_FGF or PIC_RGD with free growth factors showed almost 3-fold higher proliferation compared to cells within PIC_RGD. Cells mixed in PIC_RGD_VEGF and PIC_RGD_FGF showed a 2- and 1.5-folds increase in proliferation compared to PIC_RGD hydrogel, respectively (see, Figure 7).

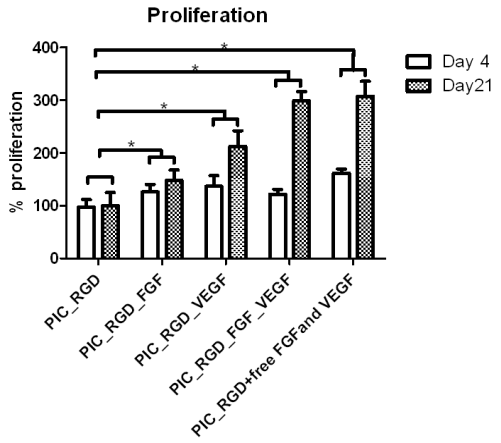

Figure 7. Cell viability at day 4 and day 21. The proliferation of PIC_RGD sample was set to 100% baseline value. Results are mean±SD for 3 separate experiments. * indicates $p<0.05$.

To create a 3D vasculature in the hydrogel, 500,000 cells (SMCM: HUVECs =1:1) per mL were mixed with PIC_RGD_VEGF_FGF and Matrigel^{TM} (n=3 per condition). 200µl cell suspended gel solutions were transferred into a 24-well insert with a membrane pore size of 0.2 µm (Corning Incorporated, Corning, USA). After 1 hour of incubation at 37 °C, 700 µl medium was added to the culture well and cultured for 3 weeks. The culture medium was changed three times per week.

Vascular tube-like structures were visualized on all the samples within 12 h, where the largest tube length was obtained on the sample containing both growth factors (VEGF-bFGF). The immunohistochemistry of the structures formed on the surface of PIC-VEGF-FGF closely resembles those formed on Matrigel surfaces, a naturally sourced tissue mimetic material (Figure 8). Remarkably the proliferation of cells cultured on polyisocyanide GRGDs containing both growth factors matched those obtained on polyisocyanide GRGDS sample that were continuously doped with free growth factor, which means that not only was the growth factors still active after covalent immobilization to the polyisocyanide scaffold they **remained equally potent to free growth factors** over a period of 21 days (Figure 7).

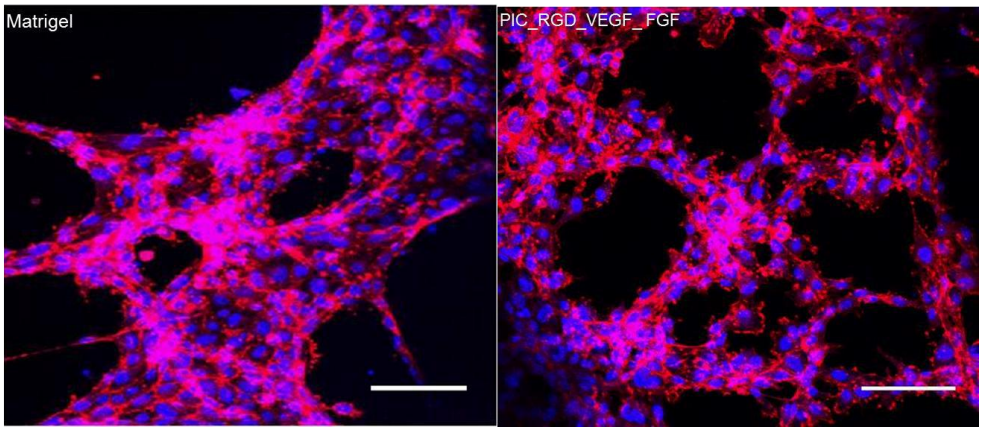

Figure 8. Fluorescence microscopy of tubular structures. Tubular structures on the surface of Matrigel and PIC-VEGF-bFGF. Cells were labelled with phalloidin (red) and DAPI (blue) to visualize the actin cytoskeleton and nuclei, respectively. Scale bar is 50 µm.

In the future it would be interesting to investigate the effect of changing the bulk stiffness, fibre stiffness and stress stiffening on vasculogenesis in the presence of both growth factors covalently immobilized on the same PIC.

Reflection

In this thesis, the chemical and mechanical requirements for a synthetic ECM consisting of polyisocyanide hydrogel were explored. To control cellular fate of HUVEC-SMC for vasculogenesis within 3 days, the presence of a covalently immobilized cell adhesion ligand GRGDS in a concentration range of 23-63 µM was required. From the initial experiments, in addition to cell adhesion ligands, the presence of additional covalently immobilized growth factors greatly enhanced the rate and degree of sprouting within 12 h and tube formation within 4 days when compared to hydrogels containing only

GRGDS. Surprisingly the covalently immobilized growth factors retained and matched the bioactivity of continuously refreshed growth factor imbibed matrices over a period of 21 days. The mechanical properties present in these sECM at 2.0 mg/mL in medium were bulk stiffness <100 Pa and strain stiffening fibres with a critical stress of 2.0-2.9. Literature indications that synthetic matrix stiffness need to match that of target tissue to elicit the desired cellular response does not apply for a strain stiffening matrix. Pore size nm range was also shown to be a non factor for a sECM consisting of PIC in obtaining vasculogenesis. This is likely caused by the network being sufficiently flexible (soft) to facilitate cellular induced matrix remodelling through both cellular cues and native ECM deposition.

Now follows a short overview of the answers to the proposed research topics: Is it possible to synthesize water soluble PIC? Yes, it was possible to synthesise water soluble PIC. Can the gelation temperature be tuned? Yes, it was possible to change the gelation temperature in the range of 18-42 °C either by changing the molecular weight or by making copolymers with different ratios of triethylene glycol to tetraethylene glycol monomers. Is PIC biologically inert? In cell culture material was biologically inert. Is it possible to add copolymers with functional handles and what is the highest tolerable handle loading? Yes it was possible to synthesize copolymers with functional handles, with a monomer molar ratio of up to 1 handle for every 100 spacer monomers. Can PIC be used as therapeutic carriers and how do they compare to the current state of the art? It was possible to use PIC as a therapeutic carrier at extremely low concentrations of polymer with high efficacy and it compared extremely well with current spherical therapeutic carriers. Is it possible to change

the bulk stiffness of PIC hydrogels? It is only possible to increase the bulk stiffness of PIC through concentration, all attempts of significantly increasing the stiffness via chemical or reversible crosslinking experiments were unsuccessful. Can a PIC hydrogel containing GRGDS be used as aECM for vasculogenesis (under cell culture conditions)? Yes cells were grown successfully in this PIC hydrogel and vasculogenesis was observed. What loading of GRGDS was required to induce a cellular response? A GRGDS loading of 1 in 100 was the most effective in inducing vasculogenesis during cell culture. What concentration of PIC results in a hydrogel that is strong enough to suspend cells in 3D? A concentration range of 1.6 mg/mL to 2.0 mg/mL was satisfactory for cell culture purposes. Does the hydrogel itself survive cell culture? The hydrogel remains intact over extended periods of cell culture, but in some samples syneresis was observed. In the animal model PIC is subcutaneously injected; was this the correct technique for administration of the PIC? The hydrogels experienced a reduction in stiffness from passing through the thin syringe needle and as it was extremely difficult to find the hydrogel at the point of injection it would seem that this mode of administration is not advisable. Was the cellular response to the PIC hydrogel *in vivo* similar to that of observed *in vitro*? No vasculogenesis was observed *in vivo*.

References

1 Cornelissen, J. J. L. M. *et al.* Helical Superstructures from Charged Poly(styrene)-Poly(isocyanodipeptide) Block Copolymers. *Science*, **280**, 1427-1430, (1998).

2 Ragnaill, M. N. *et al.* Internal benchmarking of a human blood–brain barrier cell model for screening of nanoparticle uptake and transcytosis. *European Journal of Pharmaceutics and Biopharmaceutics*, **77**, 360-367, (2011).

3 Georgieva, J. V. *et al.* Peptide-Mediated Blood–Brain Barrier Transport of Polymersomes. *Angewandte Chemie*, **124**, 8464-8467, (2012).

4 Chee, P. L. *et al.* Supramolecular cyclodextrin pseudorotaxane hydrogels: A candidate for sustained release? *Materials Science and Engineering: C*, **39**, 6-12, (2014).

5 Lu, D. R., Abu-Izza, K. & Mao, F. Nonlinear data fitting for controlled release devices: An integrated computer program. *International Journal of Pharmaceutics*, **129**, 243-251, (1996).

6 Polli, J. E., Rekhi, G. S. & Shah, V. P. Methods to Compare Dissolution Profiles. *Drug Information Journal*, **30**, 1113-1120, (1996).

7 Chien, Y. W. Controlled release of biologically active agents. By Richard W. Baker. John Wiley & Sons, New York, 1987. vii + 279 pp. 23.8 × 16.5 cm. ISBN 0-471-83724-5. $59.95. *Journal of Pharmaceutical Sciences*, **77**, 371-371, (1988).

8 Peppas, N. A. Analysis of Fickian and non-Fickian drug release from polymers. *Pharm. Acta Helv.*, **60**, 110-111, (1985).

9 Hixson, A. W. & Crowell, J. H. Dependence of Reaction Velocity upon surface and Agitation. *Industrial & Engineering Chemistry*, **23**, 1002-1009, (1931).

10 Higuchi, T. Rate of release of medicaments from ointment bases containing drugs in suspension. *Journal of Pharmaceutical Sciences*, **50**, 874-875, (1961).

11 Shah, M. V., de Gennaro, M. D. & Suryakasuma, H. An evaluation of albumin microcapsules prepared using a multiple emulsion technique. *Journal of Microencapsulation*, **4**, 223-238, (1987).

12 Goodsell, D. S. Eukaryotic cell panorama. *Biochemistry and Molecular Biology Education*, **39**, 91-101, (2011).

13 Risau, W. Mechanisms of angiogenesis. *Nature*, **386**, 671-674, (1997).

14 Shweiki, D. *et al.* Vascular endothelial growth factor induced by hypoxia may mediate hypoxia-initiated angiogenesis. *Nature*, **359**, 843-845, (1992).

15 Li, J., Zhang, Y.-P. & Kirsner, R. S. Angiogenesis in wound repair: Angiogenic growth factors and the extracellular matrix. *Microscopy Research and Technique*, **60**, 107-114, (2003).

16 Chung, J. C. Y. & Shum-Tim, D. Neovascularization in Tissue Engineering. *Cells*, **1**, 1246-1260, (2012).

17 Zisch, A. H. *et al.* Cell-demanded release of VEGF from synthetic, biointeractive cell-ingrowth matrices for vascularized tissue growth. *The FASEB Journal*, (2003).

18 Leslie-Barbick, J. E. *et al.* The promotion of microvasculature formation in poly(ethylene glycol) diacrylate hydrogels by an immobilized VEGF-mimetic peptide. *Biomaterials*, **32**, 5782-5789, (2011).

19 Cai, S. *et al.* Injectable glycosaminoglycan hydrogels for controlled release of human basic fibroblast growth factor. *Biomaterials*, **26**, 6054-6067, (2005).
20 Ferreira, L. S. *et al.* Bioactive hydrogel scaffolds for controllable vascular differentiation of human embryonic stem cells. *Biomaterials*, **28**, 2706-2717, (2007).
21 Hersel, U., Dahmen, C. & Kessler, H. RGD modified polymers: biomaterials for stimulated cell adhesion and beyond. *Biomaterials*, **24**, 4385-4415, (2003).
22 Mason, M. N. & Mahoney, M. J. A novel composite construct increases the vascularization potential of PEG hydrogels through the incorporation of large fibrin ribbons. *Journal of Biomedical Materials Research Part A*, **95A**, 283-293, (2010).
23 Lee, K. Y., Peters, M. C. & Mooney, D. J. Comparison of vascular endothelial growth factor and basic fibroblast growth factor on angiogenesis in SCID mice. *Journal of Controlled Release*, **87**, 49-56, (2003).
24 Peattie, R. A. *et al.* Stimulation of in vivo angiogenesis by cytokine-loaded hyaluronic acid hydrogel implants. *Biomaterials*, **25**, 2789-2798, (2004).
25 Asahara, T. *et al.* Synergistic Effect of Vascular Endothelial Growth Factor and Basic Fibroblast Growth Factor on Angiogenesis In Vivo. *Circulation*, **92**, 365-371, (1995).
26 Zieris, A. *et al.* FGF-2 and VEGF functionalization of starPEG–heparin hydrogels to modulate biomolecular and physical cues of angiogenesis. *Biomaterials*, **31**, 7985-7994, (2010).
27 Anderson, S. M., Siegman, S. N. & Segura, T. The effect of vascular endothelial growth factor (VEGF) presentation within fibrin matrices on endothelial cell branching. *Biomaterials*, **32**, 7432-7443, (2011).
28 Leslie-Barbick, J. E., Moon, J. J. & West, J. L. Covalently-Immobilized Vascular Endothelial Growth Factor Promotes Endothelial Cell Tubulogenesis in Poly(ethylene glycol) Diacrylate Hydrogels. *Journal of Biomaterials Science, Polymer Edition*, **20**, 1763-1779, (2009).
29 Phelps, E. A. *et al.* Bioartificial matrices for therapeutic vascularization. *Proceedings of the National Academy of Sciences*, **107**, 3323-3328, (2010).
30 Ehrbar, M. *et al.* Cell-Demanded Liberation of VEGF121 From Fibrin Implants Induces Local and Controlled Blood Vessel Growth. *Circulation Research*, **94**, 1124-1132, (2004).
31 Kaully, T. *et al.* Vascularization—The Conduit to Viable Engineered Tissues. *Tissue Engineering Part B: Reviews*, **15**, 159-169, (2009).
32 Mandal, K. & Kent, S. B. H. Total Chemical Synthesis of Biologically Active Vascular Endothelial Growth Factor. *Angewandte Chemie International Edition*, **50**, 8029-8033, (2011).
33 Ye, S. *et al.* Structural Basis for Interaction of FGF-1, FGF-2, and FGF-7 with Different Heparan Sulfate Motifs†,‡. *Biochemistry*, **40**, 14429-14439, (2001).

Summary

The aim of this thesis was to explore the possible biomedical applications of polyisocyanopeptide oligoethylene glycol (PIC). The biomedical applications investigated include the material in its gelled state as a synthetic extracellular matrix (sECM) and in its diluted state as a therapeutic carrier. In Chapter 1, the extracellular matrix (ECM) was defined to comprise of the following components: insoluble hydrated scaffolds e.g. fibrillar polymers such as fibrin and collagen (biomechanical signals), proteins/ligands on the surfaces of neighbouring cells and soluble macromolecules (biochemical signals). The design parameters for sECM for vasculogenesis were defined as: 3D network containing cell adhesion ligands (RGD), variable bulk stiffness; fibre stiffness (strain stiffening), porous and cellular remodelling of the matrix is possible. In Chapter 2, the design, synthesis and characterization of isocyanide monomers for the synthesis of polyisocyanodipeptide oligoethylene glycol polymers was performed. Alanine-alanine triethylene glycol isocyanide monomers with varied enantiomers of alanine-alanine (*LD;DL*) were synthesized. Alanine-alanine (*LD*) tetraethylene glycol isocyanide monomer was synthesized. Isocyanide monomers of alanine-alanine (*LD*) oligoethylene glycol containing a functional handle appendage of either acetylene or azide were synthesized. As a whole, all the functional isocyanide monomers were synthesized successfully with overall average total yield of 5%. To increase the yields it would be advisable to investigate the use of different dehydration methods. In Chapter 3, the monomers synthesized in Chapter 2 were used as reactants to synthesize a broad range of (homo-;co-; ter-) polymers. It is possible to synthesize co and terpolymers with targeted sol-gel transition (standard deviation 6.4 °C)

temperatures by varying the ratio of tri- to tetra ethylene glycol monomer. The LCST of tri-ethylene glycol based homo and co-polymers are shown to be effected by up to 5 °C as a direct consequence of the average molecular weight. Polymers with molecular weights of <700 kg/mol show LCST of ~12 °C and between 300-630 kg/mol showing LCST of ~18 °C. The bulk stiffness and critical stress of homo-; co-polymers (at the same concentration) above their sol-gel transition temperature are linearly related to their molecular weights. The addition of azide and acetylene co monomer do not affect the overall mechanical characteristics of the polymers up to densities of 1:50 and 1:100 respectively. It is possible to reliably determine the molecular weight of the synthesized water soluble PIC with two non standard techniques (viscometry and AFM) that compare well with standard size exclusion chromatography (SEC) technique. Crosslinking as a means to increase the bulk stiffness was explored in Chapter 4, by using both covalent and physical crosslinking strategies. The covalent chemistries investigated were: copper catalyzed and thiolyne click chemistry, SPAAC, dithiobridge and Schiff base formation, and the Schmidt reaction. The physical crosslinking strategies investigated were: pore blockage with gelatine spheres, Host-guest chemistry and ionic interactions. There is no significant increase in stiffness observed for any of the applied crosslinking strategies.

The second biomedical application, PIC as therapeutic carrier, was investigated in Chapter 5. A new class of antibody-functionalized, semi-flexible and filamentous polymer (diameter 5-10 nm, length ~200 nm) with a controlled persistence length, a high degree of stereoregularity and the potential for multiple simultaneous receptor interactions was developed. These highly controlled, semi-stiff polymers were decorated with T cell

activating anti-CD3 antibodies and were analyzed for application as potential synthetic dendritic cells (sDCs). The sDCs do *not only activate* T cells at significantly lower concentrations than free antibodies or rigid sphere-like counterparts (PLGA particles) but also induce a more robust T cell response. These novel sDCs are further biocompatible and non-toxic. The observed increased efficacy highlights the importance of architectural flexibility and multivalency to modulate T cell response and cellular function in general.

In Chapter 6, PIC hydrogels, decorated with varying densities of the cell adhesion ligand GRGDS (Gly-Arg-Gly-Asp-Ser) was investigated as sECM both *in vivo* and *in vitro*. PICs are a unique type of soft hydrogels (10-1000 Pa) as they consist of extremely stiff fibrillar polyisocyanopeptides with oligo(ethylene glycol) side chains, which show finite bundling, strain stiffening under mechanical deformation and thermo-responsive super hydrogelation. It is shown that PIC (10-300 Pa) as sECM can induce vasculogenesis *in vitro* if a cell adhesion ligand GRGDS is covalently attached to it at a concentration of 63.3 µM. At this peptide concentration, the polymer itself should have a molecular weight of 425-516 kg/mol to ensure initial sprouting occurs within three days. The sECM used *in vivo* had stiffness of <100 Pa and a critical stress of 2.0-2.9. Minimal inflammatory responses are observed, mice thrive and cellular invasion is observed, however no vasculogenesis is observed. In Chapter 7, the main findings of Chapters 2-6 are discussed and any potential future work briefly highlighted. The initial research questions were answered.

Samenvatting

Het doel van deze thesis was de toepasbaarheid van polyisocyanopetide oligoethyleen glycol (PIC) in het biomedische vakgebied te onderzoeken. Onder andere is de PIC, in een hydrogel formulering, toegepast als synthetisch extracellulair matrix materiaal (sECM) en in een verdunde oplossing is de PIC gebruikt als medicijn drager. In het eerste hoofdstuk werdt extracellulair matrix materiaal beschreven (ECM). Hieruit blijkt dat ECM de volgende componenten bevat: onoplosbare gehydrateerd vormgevend materiaal gebaseerd op vezelachtige polymeren, zoals fibrine en collageen (deze materialen zijn verantwoordelijk voor de biomechanische signalering), en eiwitten/liganden op de oppervlakte van de naburige cellen en oplosbare macromoleculen (voor de biochemische signalering). Een van de toepassingen voor een sECM is de vascularisatie van cellen in gebruik bij *in vitro* cel kweek. De sECM moet de volgende eigenschappen hebben om succesvol te zijn in vascularisatie experimenten: een 3D netwerk dat cel adhesie liganden bevat (zoals RGD peptide); een variabele bulk stijfheid en vezel stijfheid (strain stiffening); sECM moet poreus zijn en een cellulaire her-rankschikking van het matrix materiaal moet mogelijk zijn. In hoofdstuk 2 werdt het ontwerp, de synthese en de analyse van isocyanide monomeren, die nodig zijn voor de synthese van PICs, beschreven. Alanine-alanine triethyleen glycol isocyanide monomeren met verschillende enantiomeren samenstelling van alanine-alanine (*LD; DL*) zijn gemaakt. Als variant hierop is ook alanine-alanine (*LD*) tetraethyleen glycol isocyanide monomeer gesynthetiseerd. Om de verdere modificatie van het eindproduct de PIC mogelijk te maken, zijn isocyanide monomeren van alanine-alanine (*LD*) oligoethylene glycol met een functionele reactieve eindgroep ontwikkeld en als

functionele groep zijn de acetyleen en azide groep gebruikt. Alle hiervoor beschreven monomeren zijn succesvol gesynthetiseerd en geanalyseerd. De gemiddelde opbrengst van deze syntheses was 5% (mol). Om de opbrengst van deze producten te verbeteren wordt aangeraden om verder onderzoek te doen naar de dehydratie stap van de reactie, omdat hier het grootste verlies geleden werd. In hoofdstuk 3 worden de verkregen monomeren uit hoofdstuk 2 gebruikt voor de synthese van een grote variatie aan PICs. Uit de verschillende monomeren zijn homo-, co- en ter-polymeren ontwikkeld. Door te variëren in de ratio tussen tetra- en tri-ethyleen glycol monomeren, van co- en ter-polymeren, was het mogelijk om de sol-gel transitie temperatuur te sturen (met een standaard deviatie van 6.4 °C). De LCST van triethyleen glycol gebaseerde homo- en co- polymeren is ook te beïnvloeden door het mol gewicht van de PIC te veranderen. Een variatie in de LCST van 5 °C is op deze wijze behaald: polymeren met een mol massa <700 kg/mol hebben een LCST van ~12 °C waar hetzelfde polymeer met een mol massa van 300-630 kg/mol een LCST van ~18 °C heeft. Ook bestaat er een lineair verband tussen het mol gewicht van homo- en co-polymeren en de bulk stijfheid, als mede de kritische stress van de verkregen hydrogels (gemeten bij de zelfde polymeer concentratie) bestaande uit deze polymeren. Het toevoegen van azide en acetyleen functioneel monomeer in een ratio van 1:50 of 1:100 heeft geen invloed op de mechanische eigenschappen van de polymeren en gels hiervan. Het mol gewicht van de gesynthetiseerde polymeren is op 3 manieren bepaald. Als eerste zijn de niet conventionele technieken viscometrie en AFM gebruikt voor het bepalen van de mol massa. De uitkomst van deze technieken komt goed overeen met de standaard methode van size exclusion chromatography (SEC). Omdat SEC niet constant beschikbaar was, is voor veel polymeren de molmassa met viscometrie en AFM bepaald. Voor sommige

toepassingen is het belangrijk om een hydrogel te hebben met een hele hoge bulk stijfheid. Om met de PIC gebaseerde hydrogels aan deze eigenschap te kunnen voldoen moet de bulk stijfheid worden verhoogd. In hoofdstuk 4 wordt er onderzoek gedaan naar het verhogen van de bulk stijfheid door middel van crosslinken. In dit hoofdstuk worden twee manieren van crosslinken vergeleken: de eerste is crosslinken door het creëren van chemische bindingen en de tweede methode maakt gebruik van fysische interacties. Voor de eerste methode is er gebruik gemaakt van verschillende chemische reacties: koper(I) gekatalyseerde Huisgen 1, 3 cycloadditie, thiolyn click chemie, SPAAC, disulfide vorming, Schiff base formatie en de Schmidt reactie zijn als crosslink reactie onderzocht. Voor de fysische crosslinking zijn 3 methodes onderzocht: porie blokkade met gelatine bolletjes, host-guest chemie en ionische interacties. Helaas bleek het onmogelijk om de bulk stijfheid van de PIC gels te verhogen door middel van deze geteste crosslink methodes. De toepasbaarheid van PICs als medicijn drager is onderzocht in hoofdstuk 5. In dit hoofdstuk is een nieuw soort antilichaam ontwikkeld: een semi-flexibel en draderig polymeer (diameter 5-10 nm, lengte ~200 nm) met een gecontroleerde persistentie lengte, een hoge mate van stereoregulatie en de potentie voor meerdere simultane receptor interacties. De ontwikkelde, semi-stijve polymere medicijn dragers zijn gedecoreerd met T-cel activerende anti-CD3 antilichamen om gebruikt te worden als synthetische dendritische cellen (sDCs). De nieuwe sDCs activeren niet alleen T cellen bij een significant lagere concentratie als vrije antilichamen of antilichamen geïmmobiliseerd op onbuigzame polymeren bolletjes (PLGA deeltjes), maar introduceren ook een meer robuuste T-cel reactie. Verder bleken de nieuwe sDCs niet toxisch en biocompatibel te zijn. De behaalde resultaten laten duidelijk het voordeel zien van de flexibiliteit in de architectuur van de PICs en de mogelijkheden die

de PICs bieden om T-cellen op meerdere plekken te gelijk te activeren, doordat er op de lange flexibele hoofdketen op verschillende plekken antilichamen kunnen worden geplaatst. In hoofdstuk 6, werdt de toepasbaarheid van PIC hydrogels als sECM onderzocht. Hiervoor zijn de PIC moleculen ontwikkeld met verschillende hoeveelheden cel bindende ligand GRGDS (Gly-Arg-Gly-Asp-Ser). Deze GRGDS ontwikkelde PICs zijn zowel *in vivo* als *in vitro* toegepast als sECM. Deze materiaal zijn zo geschikt as sECM omdat dit zachte hydrogels (10-1000 Pa) zijn die bestaande uit extreem stijve draderige vezels van polyisocyanopeptides met oligo(ethyleen glycol) zijketens, die eindige bundels vormen en stijver worden door mechanische deformatie. Het bleekt dat PICs (10-300 Pa) gebruikt als sECM vasculogenese kunnen induceren *in vitro,* mits er cel bindende GRGDS liganden covalent gebonden zijn aan de PIC in een concentratie van 63.3 µM. Bij deze peptide concentratie gebonden aan een polymeer met een mol massa tussen de 425 en 516 kg/mol werden er initiële kiemen gevonden binnen drie dagen. Voor de *in vivo* studies is een sECM gebruikt met een stijfheid <100 Pa en een kritische stress van 2.0-2.9. Tijdens de studie is er nauwelijks inflammatie gevonden bij de muizen, in het algemeen ging het erg goed met de muizen en leken ze geen last te hebben van het PIC implantaat. Ook kon is er cellulaire invasie van het sECM gevonden, wat betekent dat er cellen van uit de muis in de sECM zijn gemigreerd. Er werd echter geen vasculogenese gevonden *in vivo*. In hoofdstuk 7, zijn de hoofdconclusies uit de hoofdstukken 2-6 samengevat en besproken waarbij ook advies werdt gegeven voor vervolg onderzoek. De allerlaatste conclusie van deze thesis is dat de gestelde onderzoeksvragen zijn beantwoord.

Dankwoord/ Acknowledgements

"For he today that sheds his blood with mine, Shall be my brother"

William Shakespeare ("Quote from King Henry V")

The conclusion of this journey is in sight, and yes at times it did feel like waging war. Alan used to call me his canon, blasting ideas into the darkness and seeing what turns up. Luckily I was not alone in this search for answers, knowledge, publications and applications for these new materials. To these brothers (sisters) I thank you for the camaraderie, assistance and support.

Prof Alan Rowan, I thank you for entrusting this PhD to me, for believing in this project, for listening to my ideas (even when they were mad), for all the cups of coffee and your unwavering loyalty. I will be eternally grateful to you for letting me take compassionate leave when my mom was sick without a moment's hesitation. I hope that you will be proud to have this thesis in your bookcase.

Dr Wilson, I thank you for your time, passionate assistance with idea generation, for finding enthusiastic collaborators and for highlighting the importance of application based end results. Dr Blank, I will always remember the lessons I learned from you, both in science and life. Dr Kouwer, I thank you for the desktop folder labelled "Extra experiments for Paul", it seemed that this folder just kept growing over the years, which was lucky as it lead to a beautiful publication and the meat of quite a few chapters in this thesis. Dr Janssen, I thank you for reading, scrutinizing and correcting this thesis. No one could hope for a better friend and colleague. You will forever be my brother. To Dr D Wilson, thank you for teaching me how to use the nanosight equipment and being such an inspirational role model. Dr Das thank you for your help with the review.

To the people whose work inspired this thesis: Dr Koepf, thank you for answering all my emails rapidly and in great detail. I thank you for the conceptualization of these molecules and I hope that you will be pleased with my modifications. Dr Lambeck, thank you for your initial work on the use of tetraethylene glycol polymers as therapeutic carriers, the results

from the indium labelled polyisocyanides are truly inspirational. Tim, I am sorry we did not finish this together.

I would like to thank the entire Molecular Materials group for the camaraderie in Monday morning meetings, social therapy sessions around coffee and pirate fun during borrels. I will never look at processed meats the same again. To the office mates of the Single Molecule Cluster, thank you for all the lovely lunches and sharing the woes of expats missing home.

Dear supporting staff members: Paula Willems, René Aben, Peter van Dijk, Jan Dommerholt, Peter van Galen, Paul Schlebos, Ad Swolfs, Hans Adams and Theo Peters, thank you for teaching me how to use the university instrumentation, for answering my questions and making me feel genuinely welcome.

I want to thank all the dedicated people at Encapson for helping with the initial discussions and design on up scaling the isocyanide monomer synthesis. I would like to applaud the hard work and excellent synthetic design of Dr Gruijters at Chiralix in successfully up scaling the synthesis of the isocyanide monomer to the purity specifications as instructed by us. I would like to thank Ryan Heesbeen at SynAffix for the consistent synthesis of excellent bicyclononyne molecules and advice on the characterization on a few custom designed variations of my own.

Special thanks to Dr Appel and Prof Scherman at the University of Cambridge, for allowing me to visit your laboratories. Thank you also for both your time and generosity in hosting Colet during her masters internship at your facilities.

To the entire Huck group, thank you for teaching me how to use your instrumentation and sharing a few happy beers. To the promovendi and students of wing one, special thanks go out to Stéphanie, Luuk, Lieke, Ferdi, Britta, Petra, Nanda, Bram, Nico, Jorge, Marjoke, Henri and Sander, for making me feel welcome.

To those who went into the dark with me: Sara, Roel, Laura, Cristina, Aswin, Dion, Tahoora, Niels K, Anna, Welmarie, Colet and Gillian, I cannot thank you enough. Each one of you contributed to this thesis, taught me something and although at times I drove some of you too hard, it is my sincere hope that you will remember our time together fondly.

To all the lovely cell biologists at the NCMLS I'm so glad to have had the privilege to work with you: Linde, Tamar, Bronte, Pedro, Martijn, Cindy and Dorien. Thank you for all the dedication, hard work, discussions and protocol optimization over the four years. Linde I would especially like to applaud your inspiring positivity and your brilliant mind.

To the dear friends I have made during my time at Radboud: Paula, Monique, Johny, Dagmara, Petri, Emilia, Kathleen, Hans, Joris, Onno, Loek, Roy, Dennis, Daniel, Bart, Kate and Khal, I hope that we stay in touch and that there are some cold beers in our future.

Beste Rob en Wilma, hartige dank voor al jullie emotioneel ondersteuning, voor de leuke uitjes, sterk bakjes koffie en dat jullie altijd bereid waren om naar de klaag liederen te luister zonder oordeel en met adviezen.

Mamma, ek is verskriklik dankbaar dat jy nog by ons is! Ek hoop regtig die verdomde melanoom word weer dormant en dat ons nog baie jare saam kan geniet. Johann baie dankie dat jy so mooi na my ma kyk. Liewe Pa en Erita, baie dankie dat julle my gehelp het om Luna in die kinder dag verblyf te sit met die laaste maande se skryf. Sonder julle het hierdie tesis nooit klaar gekom nie, ek is ontsettend dankbaar.

Allerliefste Luna, jy het gebrul soos ‘n leeu tydens groot dele van hierdie boek se skrywery, ons het dit oorleef en jy het gesonde longe gekry. Ek is oneindig dankbaar vir jou my maankind. Niels baie dankie dat jy nie na Alan geluister het nie en begin soek het na ‘n makliker manier om meer monomeer op een slag te maak. Sonder jou metode het ek nooit genoeg van die goed gemaak om al die verskillende projekte van polimeer te verskaf nie. Ek is so innig bly dat ons mekaar gevind het, my beste vriend, my verskietende ster.

List of Publications

Responsive biomimetic networks from polyisocyanopeptide hydrogels.

Kouwer PH, Koepf M, Le Sage VA, Jaspers M, van Buul AM, Eksteen-Akeroyd ZH, Woltinge T, Schwartz E, Kitto HJ, Hoogenboom R, Picken SJ, Nolte RJ, Mendes E, Rowan AE, *Nature*. 2013;493(7434):651-655.

Therapeutic nanoworms: towards novel synthetic dendritic cells for immunotherapy.

Eksteen-Akeroyd ZH, Mandal S, Jacobs MJ, Hammink R, Koepf M, Lambeck AJA, van Hest JCM, Wilson CJ, Blank K, Figdor CG, Rowan AE, *Chemical Science*. 2013;4(11):4168-4174.

Polymer-based synthetic dendritic cells for tailoring robust and multifunctional T cell responses.

Mandal S, Hammink R, Tel J, Eksteen-Akeroyd ZH, Rowan AE, Blank K, Figdor CG, *ACS Chemical Biology*. 2015;10(2):485-492

Polymer suitable for use in cell culture.

Rowan AE, Eksteen Akeroyd ZH, Wilson C, Geutjes PJ, Feitz WF, Oosterwijk E. 2015. WO/2015/007771 and PCT/EP2014/065233

Curriculum Vitae

Zaskia Hillét Eksteen Akeroyd graduated from Paarl Gymnasium high school in 2000 with average grades, convinced she will become an artist of some kind and a keen desire to travel. Between 2001-2002 she went on a working holiday through Europe making many new friends, visiting all the art museums she learned about in art class and learning how to make the perfect sandwich. In 2003 she started studying BSc changing major at least twice (human biological sciences, biochemistry, chemistry) and nearly graduating with two degrees as a result. She obtained her MSc degree (*cum laude*) in 2009 at the Institute of Polymer Sciences, University of Stellenbosch, South Africa. The title of her thesis was Hybrid hydrogels based on RAFT mediated poly(N-vinyl pyrrolidone). In 2010 she started her PhD degree under supervision of Prof. Alan Rowan at the Institute of Molecules and Materials, Radboud University, Nijmegen. The title of her dissertation is: Biomaterial study with polyisocyanide hydrogel. During her PhD she focussed primarily on the synthesis and design of polymer materials for 3D cell culture and as therapeutics carriers. In 2015 she worked as a material scientist designing flexiramic a substrate for flexible electronics that resist extreme temperatures at Eurekite BV, Enschede. In the summer of 2016 she started her own company Serenity Consulting. She still loves to travel, being creative and spending time with friends.